Develop Rapid Quality Control and Assurance Technologies for Pavements: Phase I

Technical Report 0-6874-R1

Cooperative Research Program

TEXAS A&M TRANSPORTATION INSTITUTE
COLLEGE STATION, TEXAS

in cooperation with the
Federal Highway Administration and the
Texas Department of Transportation
http://tti.tamu.edu/documents/0-6874-R1.pdf

Technical Report Documentation Page

1. Report No. FHWA/TX-16/0-6874-R1	2. Government Accession No.	3. Recipient's Catalog No.
4. Title and Subtitle DEVELOP RAPID QUALITY CONTROL AND ASSURANCE TECHNOLOGIES FOR PAVEMENTS: PHASE I		5. Report Date Published: September 2021 6. Performing Organization Code
7. Author(s) Bill Crockford, Fan Gu, Soohyok Im, Alireza Joshaghani, Wenting Liu, Xue Luo, Bob Lytton, Stephen Sebesta, Bryan Wilson, and Dan Zollinger		8. Performing Organization Report No. Report 0-6874-R1
9. Performing Organization Name and Address Texas A&M Transportation Institute College Station, Texas 77843-3135		10. Work Unit No. (TRAIS) 11. Contract or Grant No. Project 0-6874
12. Sponsoring Agency Name and Address Texas Department of Transportation Research and Technology Implementation Office 125 E. 11th Street Austin, Texas 78701-2483		13. Type of Report and Period Covered Technical Report: April 2015–August 2016 14. Sponsoring Agency Code

15. Supplementary Notes
Project performed in cooperation with the Texas Department of Transportation and the Federal Highway Administration.
Project Title: Develop Nondestructive Rapid Pavement Quality Assurance/Quality Control Evaluation Test Methods and Supporting Technology
URL: http://tti.tamu.edu/documents/0-6874-R1.pdf

16. Abstract

Attaining uniform construction of the required specification quality serves to maximize pavement life and minimize life-cycle costs. Often, localized defects govern pavement life. This project evaluated technologies for rapidly verifying attainment of specification and material requirements during flexible base construction, during asphalt mixture construction, and during concrete paving. A common theme throughout this project was the use of non-destructive test technologies to expedite test turnaround time, minimize disruption to traffic, and increase testing coverage to reduce contractor and agency risks.

For flexible base construction, this project demonstrated proof of concept using ground-penetrating radar (GPR) with mechanics-based models to estimate the in-situ resilient modulus. For asphalt mixture construction, this project demonstrated proof of concept for real-time compaction monitoring from the breakdown roller to estimate density in a quality control setting, and proof of concept using GPR to non-destructively measure the density of the finished compacted asphalt mat area. For concrete mixtures, this project demonstrated proof of concept using a curing Effectiveness Index (EI) concept along with GPR to select proper curing compound application rates and verify optimum curing of concrete in the field.

If fully implemented, initial estimates suggest these technologies could save hundreds of million of dollars over 10 years. However, at this time further work to increase the technology readiness is needed before transitioning these technologies to stakeholders.

17. Key Words Quality control, quality assurance, flexible base, resilient modulus, permanent deformation, SWCC, dielectric constant, FWD, GPR, HMA, asphalt mixture, compaction monitoring, concrete curing, concrete maturity, effectiveness index		18. Distribution Statement No restrictions. This document is available to the public through NTIS: National Technical Information Service Alexandria, Virginia http://www.ntis.gov	
19. Security Classif. (of this report) Unclassified	20. Security Classif. (of this page) Unclassified	21. No. of Pages 226	22. Price

Form DOT F 1700.7 (8-72) Reproduction of completed page authorized

DEVELOP RAPID QUALITY CONTROL AND ASSURANCE TECHNOLOGIES FOR PAVEMENTS: PHASE I

by

Bill Crockford, P.E.

Fan Gu, Ph.D.

Soohyok Im, Ph.D., P.E.

Alireza Joshaghani

Wenting Liu, P.E.

Xue Luo, Ph.D.

Bob Lytton, Ph.D., P.E.

Stephen Sebesta

Bryan Wilson

and

Dan Zollinger, Ph.D., P.E.

Report 0-6874-R1
Project 0-6874
Project Title: Develop Nondestructive Rapid Pavement Quality Assurance/Quality Control Evaluation Test Methods and Supporting Technology

Performed in cooperation with the
Texas Department of Transportation
and the
Federal Highway Administration

Published: September 2021

TEXAS A&M TRANSPORTATION INSTITUTE
College Station, Texas 77843-3135

DISCLAIMER

This research was performed in cooperation with the Texas Department of Transportation (TxDOT) and the Federal Highway Administration (FHWA). The contents of this report reflect the views of the authors, who are responsible for the facts and the accuracy of the data presented herein. The contents do not necessarily reflect the official view or policies of the FHWA or TxDOT. This report does not constitute a standard, specification, or regulation.

ACKNOWLEDGMENTS

This project was conducted in cooperation with TxDOT and FHWA. The authors thank the TxDOT Project Manager Sonya Badgley, and members of the TxDOT project team: Dar Hao Chen, Yvette Flores, Miles Garrison, Stephen Kasberg, Joe Leidy, Andy Naranjo, Travis Patton, Jimmy Si, and Stacey Strittmatter.

TABLE OF CONTENTS

Page
List of Figures ... ix
List of Tables ... xiii
Executive Summary ... xiv
Chapter 1. Use of Mechanics Based Models to Measure Flexible Base Quality ... 1
- Background ... 1
  - Resilient Modulus of Flexible Base ... 1
  - Permanent Deformation of Flexible Base ... 3
  - Soil-Water Characteristic Curve of Flexible Base ... 4
  - Moisture Density Curve of Flexible Base ... 4
- Procedures ... 6
  - Development of Resilient Modulus Model for Flexible Base ... 6
  - Development of Mechanistic-Empirical Rutting Model for Flexible Base ... 9
  - Development of Nonlinear Finite Element Program for Flexible Pavement ... 12
  - Laboratory Characterization of Flexible Base ... 13
  - Development of Mechanistic-Based Approach to Evaluate Flexible Base Construction ... 24
- Results ... 27
  - Estimation of Resilient Modulus of Flexible Base in the Lab ... 27
  - Estimation of Permanent Deformation of Flexible Base in the Lab ... 31
  - Estimation of Moisture Density Curve of Flexible Base in the Lab ... 34
  - Estimation of Resilient Modulus of Flexible Base in the Field ... 36
- Conclusion ... 46
  - Conclusions ... 46
  - Recommendations for Future Work ... 47

Chapter 2. Compaction Monitoring for Quality Control during Asphalt Mixture Construction ... 49
- Background ... 49
- Procedures ... 51
  - Compactor Characteristics ... 51
  - PC (Personal Computer/Laptop) System ... 56
  - PLC (Programmable Logic Control) System ... 68
- Results ... 71
  - PLC System ... 71
  - Field Experiments to Demonstrate CMS with PC System ... 78
- Conclusion ... 93
  - Recommendations ... 94

Chapter 3. Quality Assurance of Asphalt Mixture Construction Using Ground-Penetrating Radar ... 95
- Background ... 95
  - Current Quality Assurance Methods ... 95
  - Ground-Penetrating Radar ... 96
- Procedures ... 97
  - Precision and Reproducibility Analysis ... 97

Calibration Procedures between GPR Data and In-Field Density 98
Field Implementation 100
Results 103
Precision and Reproducibility Analysis 103
Calibration Procedures between GPR Data and In-Field Density 114
Field Implementation 116
Conclusion 122
Precision and Reproducibility Analysis 122
Calibration Procedures between GPR Data and In-Field Density 124
Field Implementation 124
Chapter 4. Effectiveness of Concrete Curing Compounds 127
Background 127
Procedure 128
Laboratory Testing and Data Collection Program 128
Field Testing and Data Collection Program 136
Results 139
Curing Effectiveness Lab Test Data Trends 139
Curing Effectiveness Laboratory Reference Curves 155
Special Comparative Studies 156
Testing Program on John Stockbauer Dr. 158
Testing Program on Ball Airport Rd 160
The Proof of Concept behind Protocol 161
Conclusions 163
References 165
Appendix A. PC-Based CMS Instructions 169
Appendix B. Laboratory Effective Index (EI) 193
Appendix C. Laboratory Reference Curves 205

LIST OF FIGURES

Page

Figure 1. Illustration of Moisture Density Curve of Soil. 5
Figure 2. Comparison of Predicted and Measured Resilient Modulus of Unbound Aggregates. 7
Figure 3. Comparison between Predictions by Proposed Model and Generalized Model. 8
Figure 4. Comparison between Predictions by Proposed Model and MEPDG Model. 8
Figure 5. Illustration of the Stress-Related Terms in the MER Model. 10
Figure 6. Comparison of Lab-Measured and Proposed Model-Predicted Permanent Deformation Curves for Granite Aggregates. 11
Figure 7. Comparison of Lab-Measured and Proposed Model-Predicted Permanent Deformation Curves for Limestone Aggregates. 11
Figure 8. Flowchart of Developed Finite Element Program. 13
Figure 9. Configuration of Methylene Blue Test. 14
Figure 10. Configuration of Aggregate Imaging System Test Device. 15
Figure 11. Configuration of Particle-Size Analyzer. 16
Figure 12. Measurement of Dielectric Constant of Flexible Base Using Percometer. 17
Figure 13. Configuration of RLT Test. 18
Figure 14. Location of Identified Pavement Sections. 19
Figure 15. Correlation between MBV and PFC. 19
Figure 16. Illustration of Three-Point Method on Soil-Water Characteristic Curve. 20
Figure 17. Effect of PFC on the Drying Soil-Water Characteristic Curves. 22
Figure 18. Comparison of Measured and Predicted Suction Values for Flexible Base. 23
Figure 19. Concept of the SDCC Model. 23
Figure 20. A Typical SDCC of Flexible Base. 24
Figure 21. Flowchart of Prediction of Resilient Modulus Model Coefficients. 25
Figure 22. Process of Estimation of Moisture Content and Matric Suction of Flexible Base in the Field. 25
Figure 23. Procedure to Estimate Resilient Modulus of In-Situ Flexible Base. 26
Figure 24. Comparison between Predicted K Values by Performance-Related Parameters and Simple Empirical Parameters. 29
Figure 25. Comparison between Model-Predicted Resilient Modulus and Lab-Measured Resilient Modulus of Flexible Base. 30
Figure 26. Comparison of Predicted Permanent Deformation Properties and Measured Permanent Deformation Properties. 33
Figure 27. Comparison of Model-Predicted Dry Density and Lab-Measured Dry Density. 34
Figure 28. Illustration of Three-layered Neural Network Architecture 35
Figure 29. Comparison of Maximum Dry Density of Flexible Base between Model Predictions and Laboratory Measurements 36
Figure 30. Validation of Mechanistic-Based NDT Approach Using Field Project Data 37
Figure 31. Location of Two Identified Pavement Sections in SH 21. 38
Figure 32. Structures of Identified Pavement Sections in SH 21. 39
Figure 33. Surface Conditions of Identified Pavement Sections in SH 21. 40
Figure 34. Results of Laboratory Characterization for Materials A and B. 41

Figure 35. Surface Deflection Basin of Identified Pavement Sections. 42
Figure 36. Comparison of Resilient Moduli of Flexible Base between Model Predictions and FWD Backcalculations. 43
Figure 37. Location of Construction Project in SH 24. 44
Figure 38. Volumetric Water Content Profile of Flexible Base. 44
Figure 39. Matric Suction Profile of Flexible Base. 45
Figure 40. Dry Unit Weight Profile of Flexible Base. 45
Figure 41. Resilient Modulus Profile of Flexible Base. 45
Figure 42. Initial proposed block diagram of CMS. 49
Figure 43. Lab vs. field compaction index (to 8 percent air voids). 50
Figure 44. Bomag approach to reducing negative effects of standard vertical impact vibration (from the Bomag website). 51
Figure 45. The Hamm oscillation approach to reducing negative effects of standard vertical impact vibration (from the Hamm AG website). 52
Figure 46. Belt type rollers (from the Internet). 53
Figure 47. Finite element mesh (full-scale roller drum). 54
Figure 48. Deflection results at bottom of pavement model. 55
Figure 49. Efficiency distribution of the compaction effort across roller width. 57
Figure 50. TTI's CMS. 58
Figure 51. TTI's Old CMS. 60
Figure 52. TTI's New CMS. 61
Figure 53. TTI's New CMS Control box side view. 62
Figure 54. Updated CMS control box, inside view. 63
Figure 55. Old CMS control box inside view. 63
Figure 56. Remove the sensors out of the CMS control box. 66
Figure 57. Accelerometer installed inside the buffer. 67
Figure 58. PLC version mounted on Bomag compactor. 68
Figure 59. Basic PLC circuit (overview). 69
Figure 60. Basic software logic for PLC (overview). 70
Figure 61. First version of PLC system hardware (main HMI screen shown). 72
Figure 62. First version of PLC system hardware (battery, PLC, terminal strip, and GPS unit shown with HMI panel raised). 72
Figure 63. Final Hardware version (small nominal 6" HMI on right, PLC, battery, signal conditioning, GPS unit and on/off switch in left case). 73
Figure 64. Final hardware version (carry cases closed for transport). 73
Figure 65. Second version of HMI main screen (with section status bars and time history plot of vibration and travel speed). 74
Figure 66. Version 3 (final) of HMI main (Home) screen (optimized for 6-inch HMI). 76
Figure 67. Version 3 time history screen. 76
Figure 68. Version 3 compactor-related setup screen. 77
Figure 69. Version 3 setup screen for entering targets and prediction equation parameters. 77
Figure 70. US 183 field project location. 79
Figure 71. US 90 field project location. 79
Figure 72. Assembled PC-based CMS system onto compaction roller. 80
Figure 73. Compaction efforts. 80
Figure 74. Extraction of field cores at different locations in the mat. 81

Figure 75. Compaction curves of US 183 field project. 83
Figure 76. Compaction curves of US 90 field project. 84
Figure 77. Relationship between air voids and number of gyrations in semi-log scale for each project. 85
Figure 78. Relationship between laboratory compaction and field compaction at 8 percent air voids for different mixes 86
Figure 79. ANOVA Project factor summary. 87
Figure 80. Means and interval plot for air voids by project. 88
Figure 81. Model Predictions of air voids versus observed values. 90
Figure 82. Residual plot by compaction (random scatter is desirable). 91
Figure 83. Residual plot by air voids (random scatter is desirable). 91
Figure 84. Residual plot by data row (see text for discussion). 92
Figure 85. Risks of Current QA Method: (a) Agency and (b) Contractor. 95
Figure 86. Materials and associated dielectric constants (U.S. Environmental Protecton Agency n.d.). 96
Figure 87. Test Arrangement for Precision of Radar System. 98
Figure 88. Laser-Alignment System. 99
Figure 89. Measurement Layout. 99
Figure 90. US 183 Project Location. 100
Figure 91. US 90 Field Project Location. 101
Figure 92. Testing and Sampling: (a) Surface Dielectric, (b) Nuclear Density, (c) Cores for Bulk Density 102
Figure 93. Test Section Layout. 102
Figure 94. Potential Relationship between Precision Limit and Material Dielectric. 107
Figure 95. Between-Lab Consistency h for Precision Test of RDM System. 108
Figure 96. Within-Lab Consistency k for Precision Test of RDM System. 109
Figure 97. Example Unstable initial Readings with Antenna 7A. 110
Figure 98. Random Noise from Antenna 7A appears larger than other Antennas 110
Figure 99. Influence of Surface Layer Thickness on Calculated Surface Layer Dielectric. 111
Figure 100. Example Calibration Data from SP 12.5, 1.5 inch Lift. 112
Figure 101. Example Calibration Data from SP 12.5, 2 inch Lift. 112
Figure 102. Example Calibration Data from SP 6.33, 1 inch Lift. 113
Figure 103. Surface Dielectric Results for each Antenna. 115
Figure 104. Dielectric-Voids Calibration Curve from Riverside Test Section. 115
Figure 105. Calibration Curve Error—Core Location within 24 in. 116
Figure 106. Calibration Curve Error—Smaller Sample Size (six cores vs. 10). 116
Figure 107. Correlation of Nuclear Gauge Density to Core Voids—US 183-TOM-F. 117
Figure 108. Correlation of Surface Dielectric to Core Voids—US 183-TOM-F. 117
Figure 109. Density Distribution Results—US 183-TOM-F. 118
Figure 110. Correlation of Surface Dielectric to Flow Time—US 183-TOM-F. 119
Figure 111. Correlation of Nuclear Gauge Density to Core Voids—US 90-Ty D. 120
Figure 112. Correlation of Surface Dielectric to Core Voids—US 90-Ty D. 121
Figure 113. Density Distribution Results—US 90-Ty D. 122
Figure 114. The ACMM system. 131
Figure 115. Top and bottom view of the curing plate 131
Figure 116. The Adek^{TM} Percometer and the probe. 133

Figure 117. Dielectric constant measurement setup. 134
Figure 118. Fluorescent epoxy impregnated thin sections prepared from concrete specimens. 135
Figure 119. Curing plate Components and setup on a pavement surface. 137
Figure 120. Setups of the ACMM system and the mold for DC measuring. 137
Figure 121. GRP used in this study. 138
Figure 122. Weight Loss—Wind Speed 0 mph. 139
Figure 123. Weight Loss—Wind Speed 5 mph. 140
Figure 124. Weight Loss—Wind Speed 10 mph. 140
Figure 125. Weight Loss—Wind Speed 15 mph. 140
Figure 126. Weight Loss in Abrasion Resistance test—Wind Speed 0 mph. 141
Figure 127. Weight Loss in Abrasion Resistance test—Wind Speed 5 mph. 141
Figure 128. Weight Loss in Abrasion Resistance test—Wind Speed 10 mph. 142
Figure 129. Weight Loss in Abrasion Resistance test—Wind Speed 15 mph. 142
Figure 130. EI measurement—Wind Speed 0 mph. 143
Figure 131. EI measurement—Wind Speed 5 mph. 143
Figure 132. EI measurement—Wind Speed 10 mph. 144
Figure 133. 2 EI measurement—Wind Speed 15 mph. 144
Figure 134. Moisture loss vs. EI. 145
Figure 135. Abrasion weight loss vs. EI. 145
Figure 136. EI measurements comparison by different ARs. 146
Figure 137. Dielectric constants for City White compound with AR100. 147
Figure 138. Dielectric constants for City White compound with AR140. 148
Figure 139. Dielectric constants for City White compound with AR200. 148
Figure 140. Dielectric constants for City White compound with AR240. 149
Figure 141. Effects of curing compound rate on porosity of specimens. 150
Figure 142. Total voids content for different AR. 151
Figure 143. Total voids profile content versus depth from the cured surface. 151
Figure 144. Capillary voids content for different AR. 152
Figure 145. Effect of application rate on drying shrinkage in W/C=0.40 and 0.45. 153
Figure 146. EI versus β based on laboratory data. 154
Figure 147. β versus PE based on laboratory data. 155
Figure 148. EI vs. PE in the laboratory. 155
Figure 149. Diagrams from EI, PE, and the Application rate. 156
Figure 150. EI comparison among four curing compounds (W/C=0.4 - Wind speed=0). 158
Figure 151. Regression Curves for DC Measurements in the Field Using the Percometer........ 159
Figure 152. Regression parameters and EI for the four test sections. 160
Figure 153. Sample DC data obtained with the GPR cart. 160
Figure 154. Two DC data traces at separate times. 161
Figure 155. Diagram from Field EI, PE, and Beta Data. 162
Figure 156. Curing Monitoring Protocol. 162

LIST OF TABLES

Page

Table 1. Multiple Regression Analysis of Resilient Modulus Model. 28
Table 2. Multiple Regression Analysis of Permanent Deformation Model. 32
Table 3. Comparison of PC and PLC platforms. 50
Table 4. An incomplete listing of various approaches to intelligent compaction (Brandon Crockett—Sakai). 56
Table 5. Information on asphalt mixes used in this study. 78
Table 6. US 183 field cores' locations, their compaction index, and air voids. 81
Table 7. US 90 field cores' locations, their compaction index, and air voids. 82
Table 8. Analysis of Variance for Air Voids—Type III Sums of Squares. 87
Table 9. Table of Least Squares Means for Air Voids with 95.0 percent Confidence Intervals. 87
Table 10. Multiple Range Tests for Air Voids by Project (Method: 95.0 percent LSD). 88
Table 11. Regression Analysis. 89
Table 12. Unusual Residuals. 92
Table 13. Influential Points. 93
Table 14. Project and Asphalt Mixture Details. 101
Table 15. Paired t-test Results for Computing Dielectric with either 5 or 500 Scans. 104
Table 16. Precision Summary Data using a 5-Scan Average to Measure Dielectric. 105
Table 17. Precision Summary Data using a 500-Scan Average to Measure Dielectric. 106
Table 18. ANOVA Output for Slab 3, Constant On, Average of 500 Scans. 113
Table 19. ANOVA Output for Slab 5, Constant On, Average of 500 Scans. 114
Table 20. Comparison of GPR Measurement Methods. 114
Table 21. HMA Properties from Agency and Contractor Lab Testing—US 183-TOM-F. 118
Table 22. Density Results—US 183-TOM. 119
Table 23. Flow Time Results—US 183-TOM. 120
Table 24. HMA Properties from Agency and Contractor Lab Testing-US 90-Ty D. 121
Table 25. Density Results—US 90-Ty D. 122
Table 26. GPR Precision Statistics for Constant on Condition Averaging 5 scans. 123
Table 27. GPR Precision Statistics for Hard Reset Condition Averaging 5 scans. 123
Table 28. GPR Precision Statistics for Constant on Condition Averaging 500 scans. 123
Table 29. GPR Precision Statistics for Hard Reset Condition Averaging 500 scans. 124
Table 30. Mixture designs. 128
Table 31. Levels of the design variables. 129
Table 32. Specifications for the Percometer. 134
Table 33. Moisture weight loss, surface abrasion weight loss, and EI. 145
Table 34. Correlation coefficients of EI with abrasion weight loss and moisture loss. 146
Table 35. Laboratory data summary. 154
Table 36. Comparison between two curing compounds in related parameters. 156
Table 37. EIs for four compounds under different conditions. 157
Table 38. Curing Treatments for the Victoria Test Sections. 158
Table 39. Regression parameters and EI for the four test sections in the field. 159

EXECUTIVE SUMMARY

Attaining uniform construction of the required specification quality serves to maximize pavement life and minimize life-cycle costs. Often, localized defects govern pavement life. To improve agency's abilities for attaining the most uniform level of quality construction, this project evaluated technologies for rapidly verifying attainment of specification and material requirements during flexible base construction, during asphalt mixture construction, and during concrete paving. A common theme throughout this project was the use of non-destructive test technologies to expedite test turnaround time, minimize disruption to traffic, and increase testing coverage to reduce contractor and agency risks. This project was conducted under a Phase I agreement to conduct proof of concept work on innovative technologies aimed at goals of minimizing disruption to traffic, enhancing safety, and making agency practices best-in-class.

For flexible base construction, this project demonstrated proof of concept using ground-penetrating radar (GPR) with mechanics-based models to estimate the in-situ resilient modulus of flexible base course. This proof of concept demonstrated that several new performance-related laboratory tests can be used to improve mechanistic-empirical pavement design models, and that GPR can be used in the field in conjunction with mechanics-based models to estimate the in-situ flexible base modulus value and moisture content. Additionally, initial work explored and demonstrated feasibility of using the new performance-related tests to estimate the flexible base optimum moisture content and maximum dry density. The findings from the proof of concept with mechanics-based models for flexible base suggest additional validation work should be performed, draft construction specification frameworks should be developed, and work extending the technology to stabilized materials should be performed.

For asphalt mixture construction, this project demonstrated proof of concept for real-time compaction monitoring from the breakdown roller with a compaction monitoring system (CMS) to estimate density in a quality control setting. The proof of concept with the CMS showed that the technology can accurately map roller passes to verify application of the prescribed rolling pattern, and that the compaction index (CI) principle in the CMS does appear viable for use in measuring density in real time. These findings with the CMS open up the possibility of passive inspection, where technology can be used to minimize exposure of inspectors in the work zone while still achieving (and actually increasing) testing coverage. The findings with the CMS did suggest that additional variables need exploration in the density-prediction model to improve the density prediction accuracy.

Also for asphalt mixture construction, this project demonstrated proof of concept for using GPR to measure density of the completed asphalt mat after all finish rolling. This proof of concept effort used a GPR system custom tailored to the application, where the data are processed in real time for potential real-time density measurement. The proof of concept with GPR for asphalt mixture quality assurance showed good to excellent correlation with standard field compaction acceptance measurements, demonstrating the technology could potentially offer a solution for near full-coverage quality assurance with minimum disruption to traffic. The findings using GPR for asphalt mixture quality assurance did suggest additional work is needed to better identify when a new calibration procedure is required or identify how to adjust calibration curves to changes in the job-mix formula.

For concrete mixtures, this project demonstrated proof of concept using a curing Effectiveness Index (EI) concept along with GPR to select proper curing compound application rates and verify optimum curing of concrete in the field. The proof of concept with EI demonstrated that EI is sensitive to curing compound application rate, to concrete mixture abrasion loss and moisture loss, and that laboratory EI curves along with expected field environmental conditions can be used to estimate the required curing compound application rate. The proof of concept with EI also demonstrated that GPR is a viable tool to verify attainment of the required minimum curing effectiveness in the field with near full-coverage testing. Further work needed before transitioning the EI concept to stakeholders includes establishment of more case studies, enabling real time data processing of the GPR data in the field, and evaluation of an automated system for GPR data collection in the field.

Further development of these innovative technologies would offer significant benefits in assuring construction quality. Due to their non-destructive nature, test turnaround time is minimized resulting in minimal disruption to traffic and improved workzone safety. Also due to their non-destructive nature, potential testing coverage is increased resulting in reduced producer (contractor) and consumer (agency) risks. Each of these technologies if furthered and implemented would also significantly advance the state-of-the-practice, consistent with the goal of making agency practices best-in-class. Additionally, if fully implemented, initial estimates suggest these technologies could save hundreds of million of dollars over 10 years. A Phase II work plan, not included in this document, has been submitted to futher the technology readiness of each of these innovations to prepare each technology for transition to stakeholders.

CHAPTER 1. USE OF MECHANICS BASED MODELS TO MEASURE FLEXIBLE BASE QUALITY

BACKGROUND

In flexible pavements, flexible base is applied between an asphalt concrete layer and the subgrade. A flexible base with high quality can provide functional support to the pavement structure and effectively dissipate the stresses induced by the traffic load to the underlying subgrade (Huang, 2004). During construction, the measured properties of flexible base for current quality control (QC) and quality assurance (QA) are the dry unit weight and moisture content. These values are compared with the laboratory moisture-density curve to assure that an adequate level of compaction has been achieved for the flexible base in the field. However, current pavement design is not based upon the dry unit weight and moisture content of flexible base, but based upon the modulus of the base layer. The modulus of each individual pavement layer significantly influences the performance and service life of pavement. To assure the construction quality of flexible base, the modulus values of the base course that are compacted should match as closely as possible the modulus values of base course that are used in design. QA of the compacted flexible base course must also be conducted in a timely and efficient manner so as not to retard the pace of construction. Therefore, it is necessary to develop an efficient nondestructive testing (NDT) approach to measure the resilient modulus and dry unit weight of the compacted flexible base. To evaluate a potential NDT solution for flexible base quality assurance this project performed proof of concept to:

- Develop a quick, accurate, and simple method for determining reliable values of the in-place-as-compacted base course modulus, dry density, and permanent deformation properties.
- Provide mechanistic-based models to characterize the performance properties of unbound base aggregate for a variety of environmental conditions.
- Demonstrate the developed methods as a tool for rapid QA technology.

A falling weight deflectometer (FWD) and a ground-penetrating radar (GPR) are two NDT devices commonly used in pavement engineering. FWD is primarily used to estimate the resilient modulus of each individual pavement layer by measuring the pavement surface deflections at different load levels. The use of FWD normally requires a specific traffic control, which significantly increases the potential-user time-delay costs and the road safety problems. GPR is another NDT device used to measure the dielectric constant of paving materials and to estimate the layer thickness of pavements. The measured dielectric constant profiles are related to the density of asphalt concrete, the density of base course, and the moisture content of base course. Compared to the FWD device, the GPR system can be operated at normal highway speed (e.g., 60 mph); thus, it will not cause any traffic disruptions. According to the aforementioned task objectives, the GPR system-based NDT approach was selected for evaluating flexible base construction.

Resilient Modulus of Flexible Base

The resilient modulus is defined as the ratio of the maximum cyclic stress to the recoverable resilient strain in one repeated dynamic loading cycle. It can be used to describe the response of the base layer under the traffic load. In order to determine the resilient modulus of flexible base, various models have been developed to predict the resilient modulus by the bulk stress or deviatoric stress, or the combination of them (Uzan 1985; Andrei et al. 2004). The most popular one is the generalized model developed in the National Cooperative Highway Research Program (NCHRP) Project 1-28A, which is shown in Equation 1 (NCHRP 2003),

$$E_y = k_1 P_a (\frac{I_1}{P_a})^{k_2} (\frac{\tau_{oct}}{P_a} + 1)^{k_3} \tag{1}$$

where I_1 is the first invariant of the stress tensor; τ_{oct} is the octahedral shear stress; P_a is the atmospheric pressure; and k_1, k_2, and k_3 are regression coefficients. This model indicates that the resilient modulus of granular materials is stress-dependent. However, a number of studies have reported that the resilient modulus of flexible base is not only stress-dependent but also moisture-dependent. For example, Lekarp et al. (2000) showed that the degree of saturation can affect the resilient modulus of flexible base in both laboratory and in-situ conditions. AASHTO (2008) employed an environmental factor to represent the moisture dependence of the resilient modulus. This model is adopted by the current MEPDG, which is shown in Equation 2:

$$\log \frac{M_R}{M_{Ropt}} = a + \frac{b-a}{1+\exp\left[\ln \frac{-b}{a} + k_m \cdot \left(S - S_{opt}\right)\right]} \tag{2}$$

where M_R is the resilient modulus at a given degree of saturation; M_{Ropt} is the resilient modulus at reference condition; a is the minimum of $\log\left(\frac{M_R}{M_{Ropt}}\right)$; b is the maximum of $\log\left(\frac{M_R}{M_{Ropt}}\right)$; k_m is the regression parameter; and $\left(S - S_{opt}\right)$ is the variation of degree of saturation expressed in decimals. Heath et al. (2004) developed a framework to predict the resilient modulus of flexible base at any moisture content by incorporating a normalizing matric suction term into the Uzan model (Uzan 1985). Liang et al. (2008) and Cary and Zapata (2011) also proposed similar models to characterize the moisture dependence of resilient modulus for both subgrade soils and flexible base in terms of matric suction.

According to these existing studies, the resilient modulus model of flexible base should take into account both the stress level and the moisture variation. In addition, the moisture sensitivity of the resilient modulus of flexible base should depend on both the degree of saturation and the matric suction. As a result, the formulation of Equation 1 needs to be improved to characterize the moisture dependence of the resilient modulus by incorporating the degree of saturation and the matric suction term. Furthermore, the values of k_1, k_2, and k_3 must be reinvestigated since they are regression coefficients associated with the formulation of the model.

Currently, there are two common approaches to estimate k_1, k_2 and k_3: one is by conducting laboratory repeated-load triaxial tests on materials used in pavement construction; the other approach is through empirical estimation on the basis of the correlations between unbound aggregate properties and the base course stiffness (Nazzal and Mohammad 2010; Malla and Joshi 2007). The repeated-load triaxial test is complex and time-consuming. It requires experienced personnel to operate the test equipment and to analyze the test data. Contrary to this difficult procedure, the latter method using empirical estimation is simpler and much more efficient in obtaining the resilient modulus of the compacted base course. In this approach, the values of k_1, k_2, and k_3 are usually predicted by their relations with some simple material properties, which are determined from regression analysis. The material properties used in the regression include dry unit weight, water content, plasticity index, liquid limit, and weight percent of aggregates passing through a No. 200 sieve (P_{200}) (Yau and Quintus 2004). However, the resulting correlations are not very accurate because these index properties are not directly related to the pavement performance. In order to accurately estimate k_1, k_2 and k_3, repeatable and reliable performance-related properties would be better employed in the regression model.

Permanent Deformation of Flexible Base

Accumulated permanent deformation is the primary distress for unbound aggregate bases in flexible pavements. Accordingly, understanding the permanent deformation behavior of flexible base plays a significant role in the accurate evaluation and prediction of the performance of an unbound base layer (Epps et al. 2014). In the laboratory, the permanent deformation behavior of the flexible base is characterized by repeated-load triaxial (RLT) tests. The responses of an unbound aggregate specimen under the repeated load include resilient (recoverable) strain and permanent (unrecoverable) strain. The recoverable behavior is characterized by the resilient modulus of the unbound aggregates (Gu et al. 2015).

In order to characterize the permanent deformation properties of flexible base, various models have been developed to determine the relation between the accumulated permanent strain and the number of load cycles. Two commonly used models are the VESYS model and the Tseng-Lytton model, which are shown in Equations 3 and 4, respectively,

$$\frac{1}{\varepsilon_r}\left[\frac{\partial \varepsilon^{p}\left(N\right)}{\partial N}\right]=\mu N^{-\alpha} \tag{3}$$

where ε_r is the resilient strain of the granular aggregate; ε^p is the permanent strain of the granular aggregate; N is the number of load cycles; and μ and α are permanent deformation properties in VESYS model.

$$\varepsilon^{p}=\varepsilon_0^{p}e^{-(\frac{\rho}{N})^{\beta}} \tag{4}$$

where ε^p is the permanent strain of the granular material; ε_0^p is the maximum permanent strain; N is the number of load cycles; ρ is the scale factor; and β is the shape factor. The variables ε_0^p, ρ ,and β are permanent deformation properties in the Tseng-Lytton model, which is implemented in the mechanistic-empirical pavement design program. In both the models, the permanent deformation properties are determined through the regression analysis of test data from RLT tests. However, the test time and experience required to perform RLT tests become major obstacles to applying permanent deformation properties in QC and QA of the construction of flexible base.

Soil-Water Characteristic Curve of Flexible Base

Soil suction is commonly referred to as the free energy state of moisture within the soil. It directly relates the moisture condition of a soil to the engineering behavior. The relationship between soil suction and moisture content is defined as the soil-water characteristic curve (SWCC) (Fredlund and Rahardjo, 1993). The SWCC is an important characteristic used to evaluate the moisture susceptibility for flexible base.

Currently, there are two popular approaches to determine the SWCC for a soil: one is an experimental method of conducting the filter paper test or pressure plate test to measure the suction values at different moisture contents; the other is an estimation method on the basis of the Fredlund and Xing (1994) equation, which is shown in Equations 5 and 6:

$$\theta_w = C(h) \times \left[\frac{\theta_{sat}}{\left[\ln\left[\exp(1) + \left(\frac{h}{a_f} \right)^{b_f} \right] \right]^{c_f}} \right] \tag{5}$$

$$C(h) = \left[1 - \frac{\ln\left(1 + \frac{h}{h_r} \right)}{\ln\left(1 + \frac{10^6}{h_r} \right)} \right] \tag{6}$$

where θ_w is volumetric water content, θ_{sat} is saturated volumetric water content, h is matric suction, and a_f, b_f, c_f, and h_r are regression coefficients. Once the fitting coefficients a_f, b_f, c_f, and h_r are determined, the SWCC for a specific soil can be established automatically. In the current Pavement ME Design (AASHTO, 2008), the fitting coefficients can be predicted by weight percent of material passing sieve No. 200 (P_{200}), effective grain size with 60 percent passing weight (D_{60}), and plasticity index (PI). The filter paper test and the pressure plate tests are time-consuming and material-consuming. In contrast, the estimation method is very simple and efficient in determining the SWCC for a soil. However, the measurements of the predicting variables, including sieve analysis and Atterberg limits, have high variability (Epps et al., 2014). The predicted SWCCs still have a noticeable difference with the measured ones. Under this circumstance, a new estimation method based on the methylene blue value (MBV) and percent fines content (PFC) was proposed by Sahin et al. (2014).

Moisture Density Curve of Flexible Base

Flexible base compaction is an optimization process of air, water, and density. In general, a higher degree of compaction yields a higher shear strength of flexible base. Therefore, achieving the maximum dry density ensures the maximum shear strength of flexible base. Figure 1 illustrates the relationship between the dry unit weight and the moisture content. The maximum dry unit weight occurs at a particular moisture content, which is called the optimum moisture content.

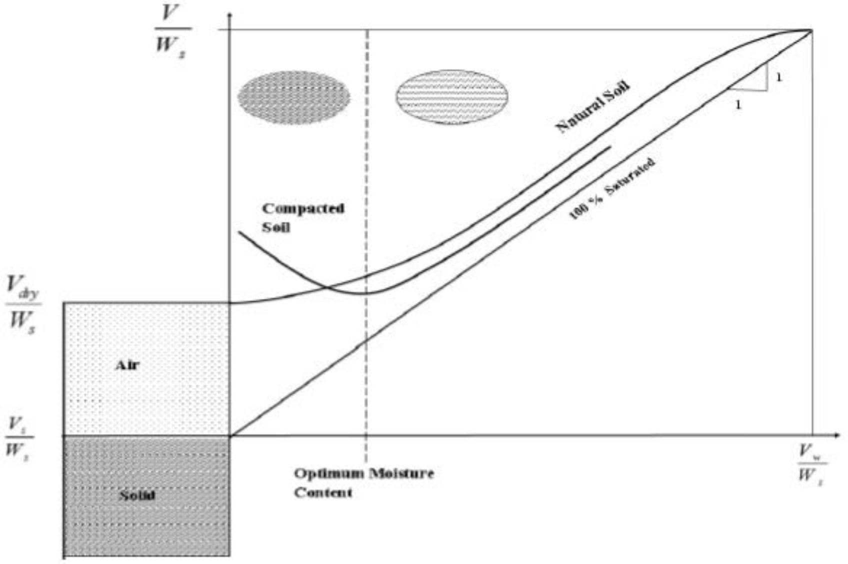
$\frac{V}{W_s}$
Natural Soil
1
1
100 % Saturated
Compacted Soil
$\frac{V_{dry}}{W_s}$
Air
$\frac{V_s}{W_s}$
Solid
Optimum Moisture Content
$\frac{V_w}{W_s}$

Figure 1. Illustration of Moisture Density Curve of Soil.

In the field, the dry density of flexible base is normally measured by the nuclear density gauge. The use of the nuclear gauge has several disadvantages including special licensing, special equipment security procedures, and special staff training and certification. These disadvantages result in a research need for a non-nuclear approach to measure the density of flexible base. Ideally, the procedure should provide rapid test turnaround time and improved testing coverage as compared to current spot test techniques.

PROCEDURES

Development of Resilient Modulus Model for Flexible Base

In order to incorporate the moisture-dependent characteristic of the resilient modulus of unbound aggregates, a new constitutive model was used in this project, as shown in Equation 7, which is able to determine the resilient modulus at any specific stress state and moisture content (Lytton 1995).

$$E_y = k_1 P_a \left(\frac{I_1 - 3\theta f h_m}{P_a}\right)^{k_2} \left(\frac{\tau_{oct}}{P_a}\right)^{k_3} \tag{7}$$

where I_1 = the first invariant of the stress tensor; P_a = the atmospheric pressure; θ = the volumetric water content; h_m = the matric suction in the aggregate matrix; f = the saturation factor, $1 \le f \le \frac{1}{\theta}$; τ_{oct} = the octahedral shear stress; and k_1, k_2, and k_3 are model parameters that are dependent on material properties of the base course. In this model, I_1 and τ_{oct} vary with the stress state, and h_m is related to the moisture content of unbound aggregates. Two critical steps are involved in using Equation 7 to estimate the resilient modulus of unbound aggregates:

- Determining the value of the matric suction h_m and examining the validity of h_m in discriminating different moisture contents.
- Determining the values of k_1, k_2, and k_3 by developing regression models based on performance-related base course properties.

Figure 2 shows the plot of the predicted resilient moduli by Equation 7 versus those measured from the test. A good agreement is observed between the predicted resilient moduli and the measured ones. This result indicates that the resilient modulus model proposed in Equation 7 properly reflects the change of the resilient modulus due to the moisture variations of unbound aggregates.

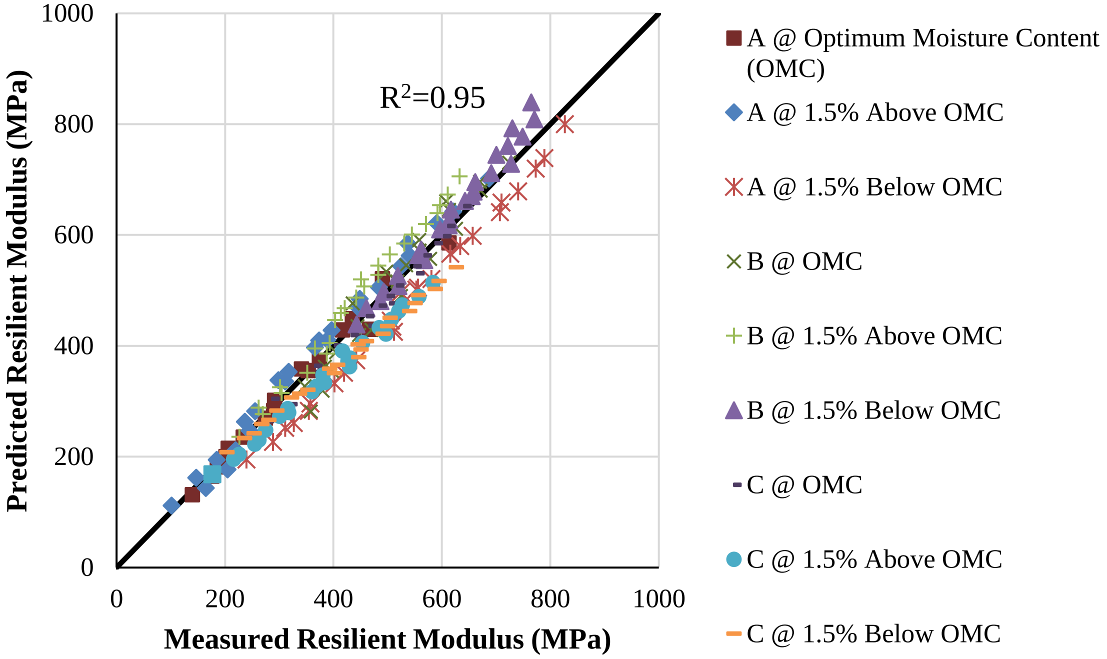

Figure 2. Comparison of Predicted and Measured Resilient Modulus of Unbound Aggregates.

To further examine the accuracy of the proposed resilient modulus model, the predictions by Equation 3 are compared to that of the generalized model (Equation 1) and that of the MEPDG model (Equation 2), respectively. Figure 3 shows an example of the comparison of the prediction between the proposed model and the generalized model in which the matric suction is ignored. The correlation between the predicted resilient moduli and the measured values are significantly improved when the matric suction is included. Figure 4 shows the comparison between the proposed model and the MEPDG model. It is obvious that the proposed model provides a more accurate prediction of the changes in resilient modulus due to changes in moisture. This result is because the MEPDG model assumes the moisture condition and stress state are independent, while the proposed model considers the influence of the moisture variation on the stress state in terms of matric suction.

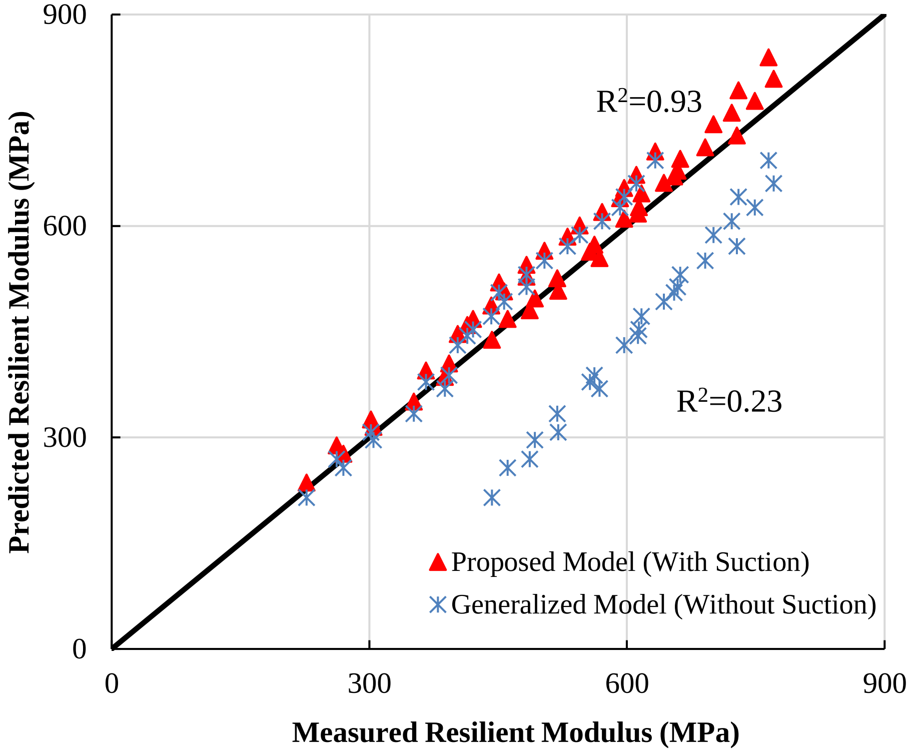

Figure 3. Comparison between Predictions by Proposed Model and Generalized Model.

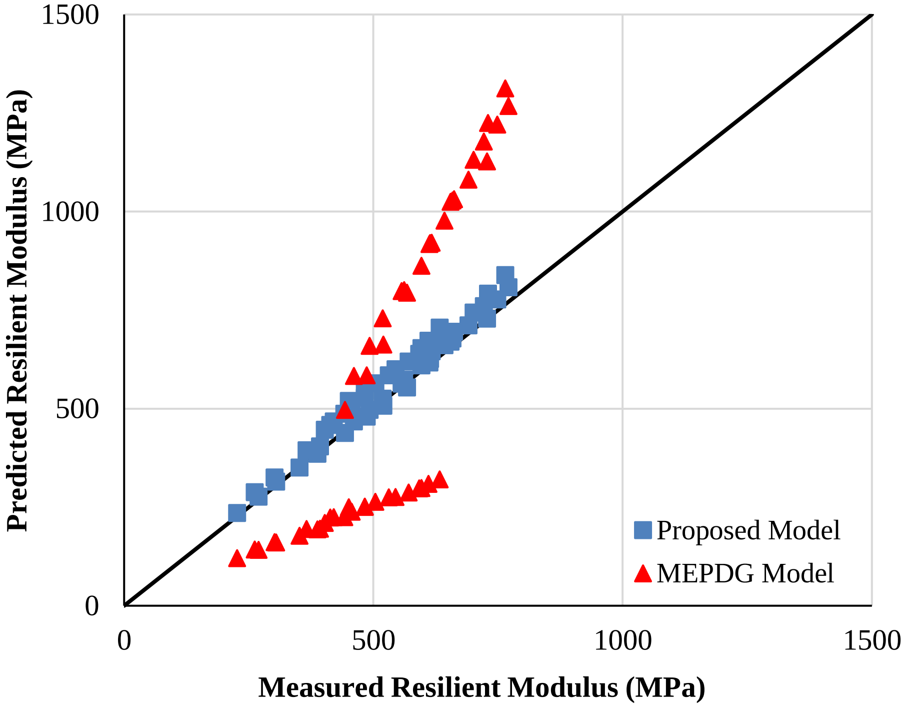

Figure 4. Comparison between Predictions by Proposed Model and MEPDG Model.

Development of Mechanistic-Empirical Rutting Model for Flexible Base

In order to characterize the stress-dependent permanent deformation behavior of flexible base, a new mechanistic-empirical rutting (MER) model is proposed, i.e., the MER model shown in Equation 8. The MER model is able to determine the accumulated permanent deformation at any specific stress state and number of load repetitions (Gu, Zhang, et al. 2016).

$$\varepsilon_p = \varepsilon_0 e^{-\left(\frac{\rho}{N}\right)^{\beta}} \left(\sqrt{J_2}\right)^m \left(\alpha I_1 + K\right)^n \tag{8}$$

$$\alpha = \frac{2\sin\phi}{\sqrt{3}\left(3-\sin\phi\right)} \tag{9}$$

$$K = \frac{c \cdot 6\cos\phi}{\sqrt{3}\left(3-\sin\phi\right)} \tag{10}$$

where J_2 is the second invariant of the deviatoric stress tensor; I_1 is the first invariant of the stress tensor; ε_0, ρ, β, m and n are model coefficients; c and ϕ are cohesion and friction angle, respectively. In this model, the two terms $\sqrt{J_2}$ and $\alpha I_1 + K$ are incorporated into the Tseng-Lytton model, which are used to reflect the influence of a stress state on the permanent deformation of the flexible base.

Figure 5 illustrates the concept of the MER model. The Drucker-Prager plastic yield criterion (Drucker and Prager 1952), which is widely applied to rock, concrete, and other pressure-dependent materials, is used in this study. As shown in Figure 5, the black dot represents the current stress state in the $I_1 - \sqrt{J_2}$ plane. The term $\sqrt{J_2}$ represents the softening effects of the deviatoric shear stress on the UGM, and a higher $\sqrt{J_2}$ yields a larger permanent deformation. Thus, the power coefficient m is always a positive number. In addition, the term $\alpha I_1 + K$ indicates the hardening/strengthening effect of the hydrostatic stress on the unbound granular material (UGM), which is highly affected by the material cohesion and internal friction angle. A higher $\alpha I_1 + K$ value results in a smaller plastic deformation; thus, the power coefficient n is always a negative number. Note that by using the same concept but different plastic yield criterion, the MER model can be extended to address more mechanical properties of the granular materials, such as the anisotropy, convexity of the yield surface, extensive yielding, and more (Zhang et al. 2014; Matsuoka and Nakai 1985).

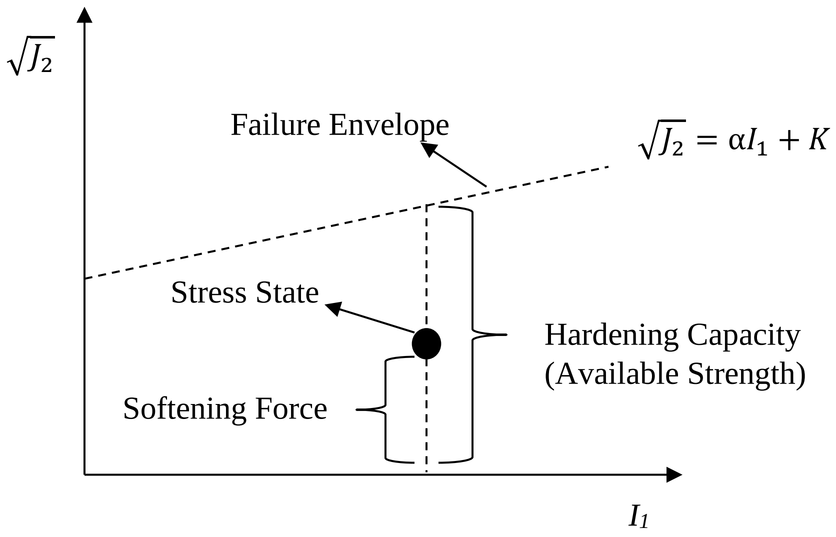

Figure 5. Illustration of the Stress-Related Terms in the MER Model.

Two critical steps are involved in using Equation 8 to determine the coefficients of the proposed rutting model:

- Determining the cohesion c and friction angle ϕ from the triaxial compressive strength tests.
- Determining the coefficients ε_0, ρ, β, m, and n from the RLT tests at multiple stress levels.

Figures 6 and 7 present comparisons of laboratory-measured and model-predicted accumulated, permanent strains at different stress levels for both granite aggregates and limestone aggregates. Stress state is abbreviated as "S," shown in the legend. The recorded permanent strain starts from the 15th load cycle. The root-mean-square errors (RMSEs) are calculated to evaluate the goodness of model fitting at various stress states. In general, a smaller RMSE indicates a better goodness of fitting (Gauch et al. 2003). The determined RMSE at each stress level is relatively small, which indicates that the MER model accurately captures the trend of the measured permanent deformation curves for both of the tested UGMs. Figures 6 and 7 also show the determined coefficients of the MER model, which can be used to predict the rutting behavior of the tested unbound aggregates at any stress levels and number of load repetitions.

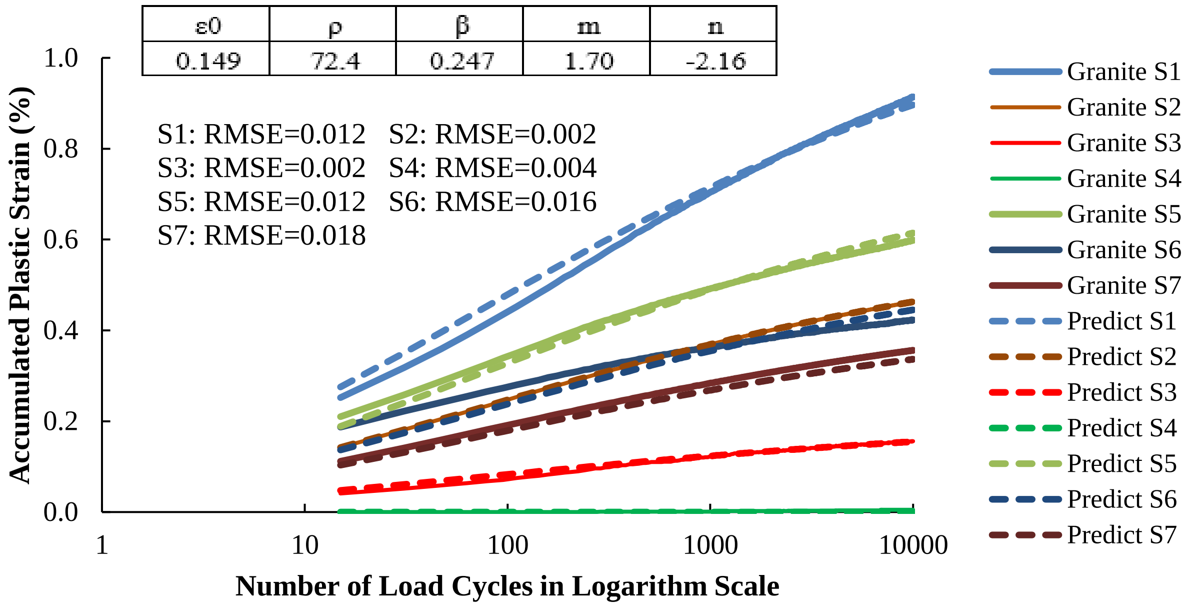

Figure 6. Comparison of Lab-Measured and Proposed Model-Predicted Permanent Deformation Curves for Granite Aggregates.

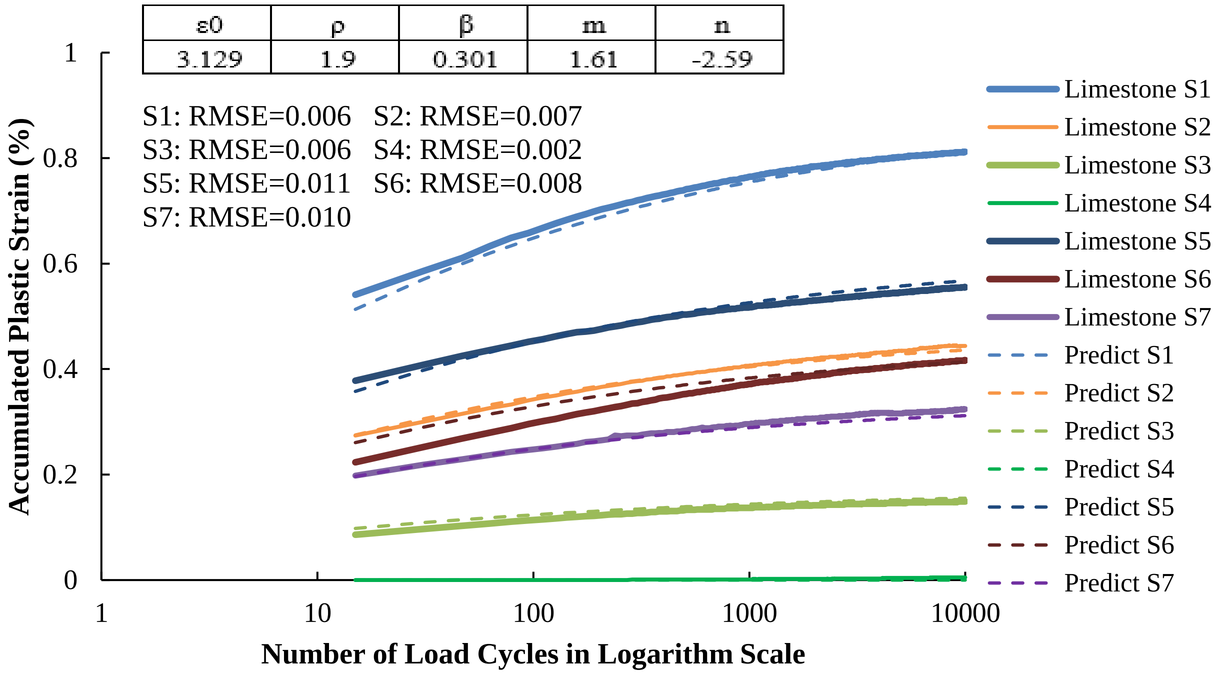

Figure 7. Comparison of Lab-Measured and Proposed Model-Predicted Permanent Deformation Curves for Limestone Aggregates.

Development of Nonlinear Finite Element Program for Flexible Pavement

In this project a nonlinear finite element program was developed to characterize the nonlinear stress-dependent and moisture-sensitive constitutive behavior of flexible base. The developed finite element program adopted the direct secant modulus approach to determine the nonlinear resilient modulus solution in each iteration. The trial vertical modulus was computed using Equation 11 in each iteration.

$$E_y^i = (1-\lambda)E_y^{i-1} + \lambda E_{ycomputed}^i \tag{11}$$

where E_y^i is the vertical modulus output from the ith iteration; E_y^{i-1} is the vertical modulus output from the (i-1)th iteration; λ is the damping factor; and $E_{ycomputed}^i$ is the vertical modulus computed from Equation 11 at the ith iteration. The convergence criteria are shown in Equations 12 and 13.

$$Error_i = \frac{\left|E_y^i - E_y^{i-1}\right|}{\left|E_y^i\right|} \le 2\% \tag{12}$$

$$Error_c = \frac{\sum_{i=1}^{n}\left(E_y^i - E_y^{i-1}\right)^2}{\sum_{i=1}^{n}\left(E_y^i\right)^2} \le 0.5\% \tag{13}$$

where $Error_i$ is the individual error for each node; $Error_c$ is the cumulative error for the entire model; and n is the number of nodes in the model. Figure 8 is the flowchart of the developed UMAT subroutine. The developed finite element program is capable of computing the stress and strain distribution of the flexible base when the flexible pavement is subjected to the traffic load (Gu, Luo, et al. 2016).

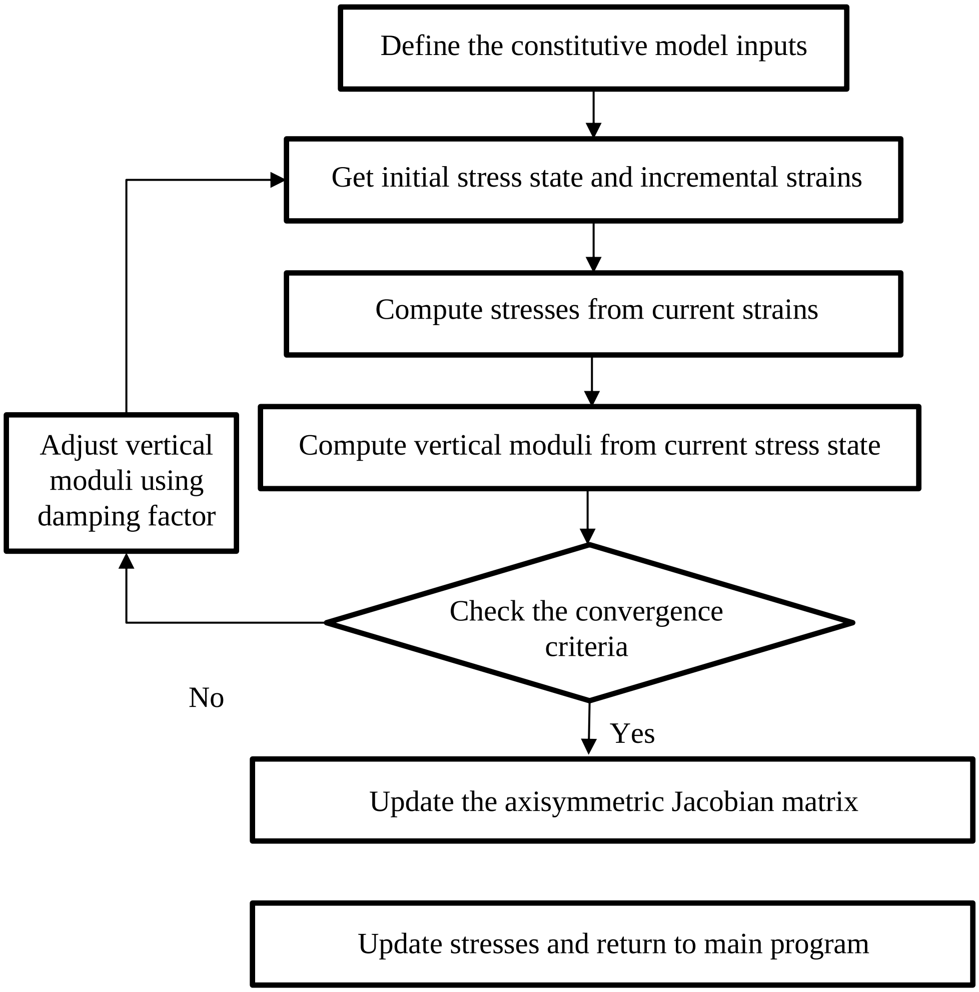
Define the constitutive model inputs
Get initial stress state and incremental strains
Compute stresses from current strains
Compute vertical moduli from current stress state
Adjust vertical moduli using damping factor
Check the convergence criteria
No
Yes
Update the axisymmetric Jacobian matrix
Update stresses and return to main program

Figure 8. Flowchart of Developed Finite Element Program.

Laboratory Characterization of Flexible Base

Test Methods

The following laboratory tests were conducted in this task:

- Tests to measure performance-related flexible base properties, including methylene blue test, aggregate imaging system (AMIS) test, PFC test, and percometer test.
- Filter paper test to measure the matric suction of unbound aggregates.
- RLT test to measure the resilient modulus and permanent deformation of anisotropic unbound aggregates.

Each test is briefly described in the following paragraphs.

Methylene Blue Test. The methylene blue test detects the clay content in the unbound aggregate mixture. The W. R. Grace methylene blue test significantly modifies the sampling and testing protocol in order to cover a wide range of soil types and to establish a direct relationship between the clay content and the MBV. This methylene blue test accommodates a reduced sample size, examines the amount of fine particles directly, and enables the detection of both non-plastic and plastic fines from soils. The fines are classified as non-plastic and plastic materials according to their different specific surface area. The Methylene Blue separates these two types of fines at the critical value of 7.00 mg/g.

As shown in Figure 9, the methylene blue test apparatus consists of a colorimeter, a timer, a 45 mL plastic tube, a 500 microliters micropipette tip, a syringe, a 0.20 micrometers size filter, an eye-dropper, a 1.4 mL small plastic tube, a portable scale, distilled water, and methylene blue solution.

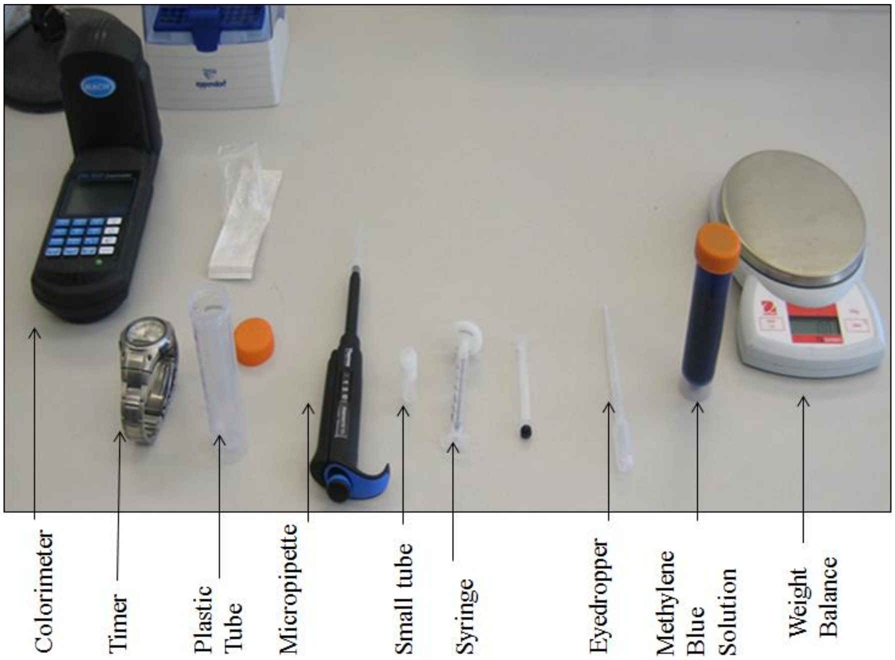

Figure 9. Configuration of Methylene Blue Test.

The modified methylene blue test method uses the fine aggregates that pass through the No. 4 sieve. The recommended initial amount of the sample is 20.00 g. The 20.00 g sample is added into 30.0 mL of calibrated methylene blue solution in a plastic tube. The mixture is shaken for 1 minute, left to stand for 3 minutes, and shaken again for 1 minute. Then, the solution is filtered through a 2.0 μm filter using a syringe. The sample passing the filter is used for the rest of the experiment. Subsequently, 130 mL of the filtered solution is taken into a plastic tube and filled with distilled water until a total of 45.00 g is collected. The newly mixed solution is placed in a small glass tube that is plugged in the colorimeter. The MBV value is determined by the colorimeter device. If the MBV reading is smaller than 7.00 mg/g, it will be considered a valid reading, and hence 20.00 g will be a valid sample size. If the MBV is higher than 7.00 mg/g, then the sample size must be cut in half to 10.00 g, and the test procedure will be repeated. A new MBV scale has been developed, ranging from 0.00 to 28.00. The MBV is calculated using Equation 14:

$$MBV_{real} = S_{correction} \times (MBV_{reading} + C_{factor}) \tag{14}$$

where $MBV_{reading}$ is the MBV reading from the colorimeter device (mg/g); MBV_{real} is the real MBV after applying two correction factors; C_{factor} is the correction factor for the concentration of the solution, and when a new methylene bottle opens, C_{factor} is calculated for each bottle (Grace, 2011) ; and $S_{correction}$ is the sample correction factor based on the size of the sample used. When the sample size used is 20.00, 10.00, and 5.00 g, $S_{correction}$ will be 1.00, 2.00, and 4.00, respectively. In other cases, the $S_{correction}$ will be recalculated based on the specified amount of sample being used (Epps et al., 2014). The total test time for one measurement is less than 10 minutes.

Aggregate Imaging System Test (AIMS). The AIMS device is a system comprised of a computer, image acquisition hardware, a high-resolution camera, microscope, aggregate tray, and lighting system. Figure 10 presents the configuration of AIMS test device. It is used to characterize the morphology of coarse aggregates, including shape, angularity and surface texture. Aggregate shape characterizes the flatness and elongation of aggregate particles. Angularity evaluates the degree of roundness of aggregate corners. Surface texture defines the roughness of aggregate surfaces. The washed coarse aggregates are separated by the ½-inch, 3/8-inch, and No. 4-size sieves. The materials retained on each sieve are placed in the aggregate tray and scanned by high-resolution camera. The distributions of angularity, shape, and surface texture indices are measured from this test.

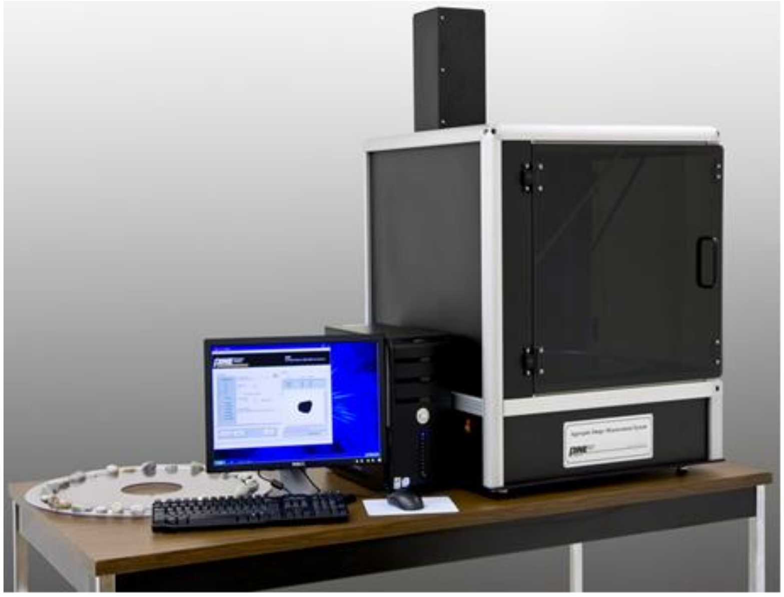

Figure 10. Configuration of Aggregate Imaging System Test Device.

In order to quantify the AIMS test results, a known statistical distribution is fitted to the distributions measured from the AIMS test. The cumulative Weibull distribution is adopted in this project, which is shown in Equation 15:

$$F(x;a,\lambda)=1-e^{-\left(x/\lambda\right)^{a}} \tag{15}$$

where $F(x;a,\lambda)$ is the cumulative probability; x is the composite angularity, shape, or surface texture indices; λ is the scale parameter; and a is the shape parameter (Montgomery and Runger 2007). The determined shape parameter a and scale parameter λ are used to quantify the AIMS test results.

Percent Fines Content Test. A Horiba laser-scattering, particle-size distribution analyzer is used to determine PFC of aggregates, which is shown in Figure 11. A viscous solution made of the particles passing through the No. 200 sieve and water flows through a beam of light. The light scattering device analyzes the dimensions of various particles in the solution and generates a particle-size distribution from the smallest to the largest particle dimension. The PFC is calculated according to Equation 16:

$$\text{Percent Fines Content } (pfc) = \frac{m_{2\mu m}}{m_{75\mu m}} \tag{16}$$

where $m_{2\mu m}$ is the mass of aggregate smaller than 2 microns, and $m_{75\mu m}$ is the mass of aggregate smaller than 75 microns.

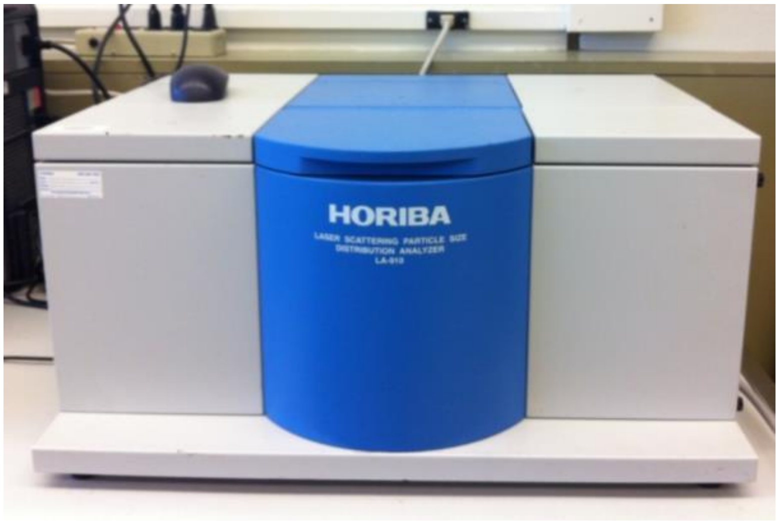

Figure 11. Configuration of Particle-Size Analyzer.

Percometer Test. The percometer test is a simple, repeatable, and quick test to measure the dielectric constant and electrical conductivity of flexible base. The frequency of the percometer is 50 kHz. Figure 12 shows the measurement of dielectric constant of flexible base using the percometer instrument. The measured dielectric constant of flexible base is directly related to the moisture content of base material.

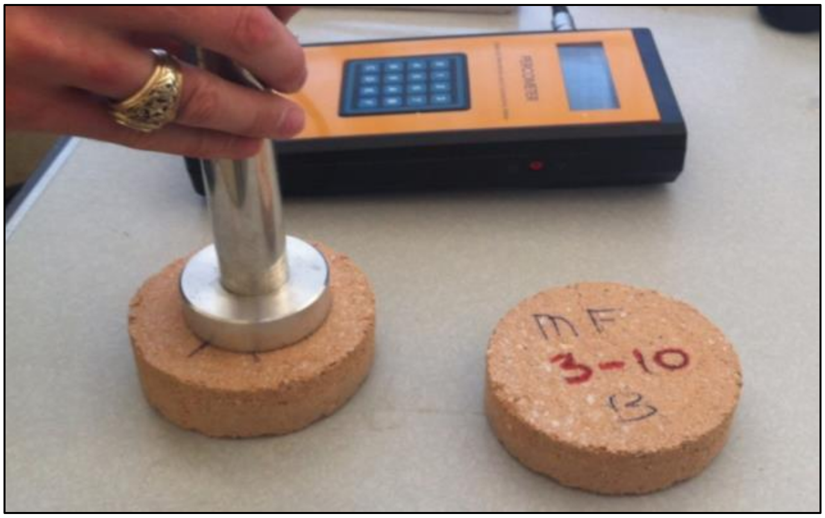

Figure 12. Measurement of Dielectric Constant of Flexible Base Using Percometer.

Filter Paper Test. The filter paper test specified in ASTM D5298 is applied to measure matric suction for unbound aggregates. The aggregates passing through the No. 4 sieve are collected and compacted at a given moisture content. Filter papers are placed in a sealed jar with the compacted unbound aggregate specimen for seven days. The increasing mass of the filter papers is subsequently measured by a highly accurate scientific scale. Finally, the matric suction of the specimen is determined from the filter paper calibration curve.

Repeated-Load Triaxial Test. The RLT test is conducted on cylindrical aggregate specimens using the triaxial chamber with a closed loop test system as shown in Figure 13. Prior to the test, the chamber is moved downward to seal the specimen; then, the pressure inside the chamber is increased until it reaches the desired constant pressure. This confining pressure is applied directly to the sample. Next, an axial load is applied to the specimen through the loading frame. The entire testing process is controlled by a computer using programs that specify the axial load and the confining pressure. During each test, the two LVDTs mounted on the middle half of the specimen are used to measure the vertical deformations of the specimen. The test data are used to determine the permanent and recoverable behavior of the granular material. The load protocol follows the standard AASHTO T 307 (AASHTO 2007).

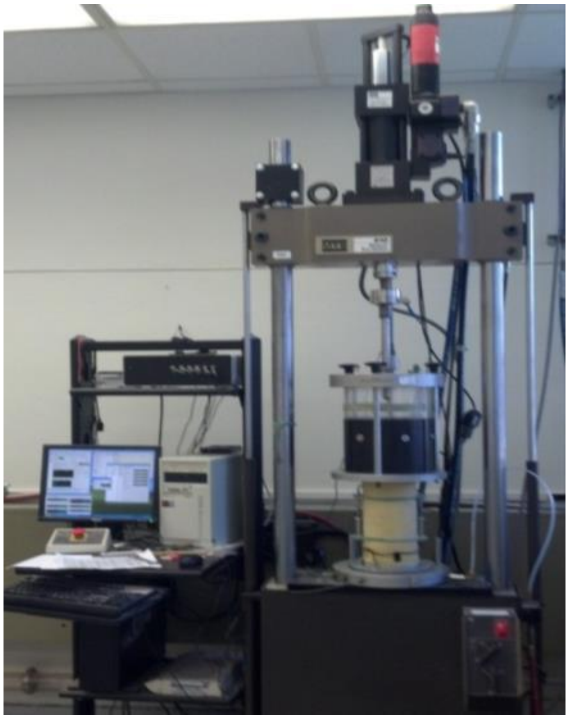

Figure 13. Configuration of RLT Test.

Materials

Base course materials used in this project were selected from five field sections in Texas, namely, State Highway (SH) 6, SH 21, SH 24, farm-to-market road (FM) 3549, and US 259. A full laboratory characterization was performed on these base course materials. Field surveys were conducted on the field sections FM 3549 and SH 21 using FWD and GPR to validate the proposed approach. Figure 14 shows the location of the identified pavement sections.

Correlation between MBV and PFC

The laboratory test program confirms that a general relationship exists between MBV and PFC, which is shown in Figure 15. This relationship presents a C-shaped curve that covers the entire methylene blue range for base course aggregate materials. The curve is divided into two zones. The MBV of 7.00 is the critical point that divides plastic and non-plastic fines. A material with MBV less than 7.00 is a relatively non-plastic soil. If the MBV is greater than 7.00, the material has high plasticity and categorized as clay mineral.

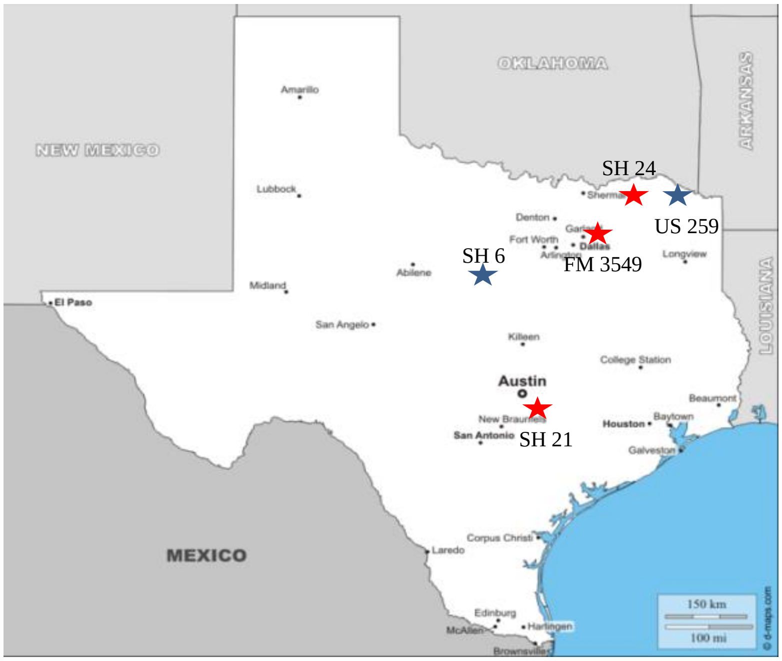
OKLAHOMA
NEW MEXICO
ARKANSAS
LOUISIANA
MEXICO
Amarillo
Lubbock
SH 24
Sherman
US 259
Denton
Garland
Fort Worth
Dallas
Arlington
SH 6
FM 3549
Longview
Midland
Abilene
El Paso
San Angelo
Killeen
College Station
Austin
Beaumont
New Braunfels
Houston
Baytown
San Antonio
SH 21
Galveston
Corpus Christi
Laredo
Edinburg
McAllen
Harlingen
Brownsville
150 km
100 mi
© d-maps.com

★: only done by lab characterization.

★: done by lab characterization and field FWD and GPR testing.

Figure 14. Location of Identified Pavement Sections.

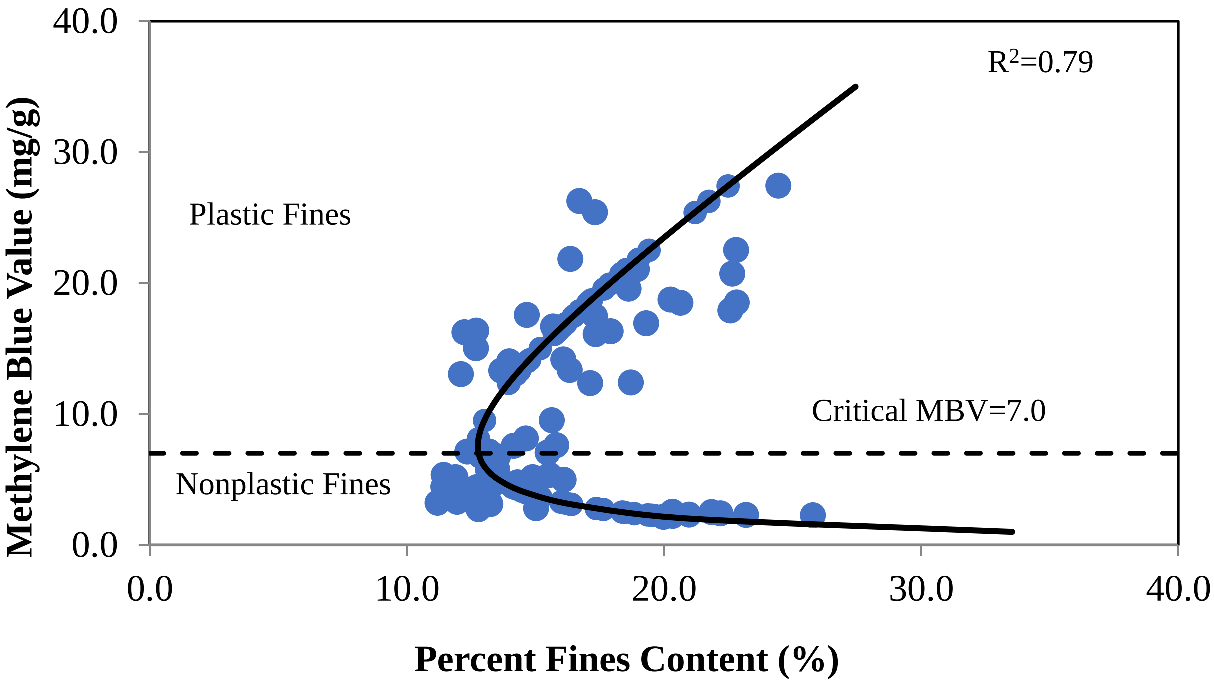

Figure 15. Correlation between MBV and PFC.

A mathematical correlation model was developed between MBV and PFC, which is shown in Equation 17.

$$PFC = \frac{a}{(MBV)^n} + m(MBV) \tag{17}$$

where PFC is the percent fines content, MBV is the methylene blue value, and *a*, *n*, and *m* are three fitting parameters that control the shape of the curve. The three fitting parameters depend on the fines content and fines composition.

Development of Soil-Water Characteristic Curve for Flexible Base

Two critical steps are involved to generate the SWCCs using the four fitting parameters method. One is to determine the four parameters using the curve-fitting method. The other step is to predict the four parameters using PFC and MBV.

The four fitting parameters a_f, b_f, c_f, and h_r shown in Equations 5 and 6 are used to find the best fitting curve through the multiple regression analysis. There are three points that are known on the SWCC curves. The first point is the maximum suction value at the zero moisture content (Point C). The second one is the saturated volumetric moisture content (Point A). The third point is the measured suction and the corresponding moisture content (Point B). Once these points are known, the analysis is ready to be executed. This analysis yields the four parameters that provide the best possible fitting curve passing through the matric suction data (Point B), which is shown in Figure 16.

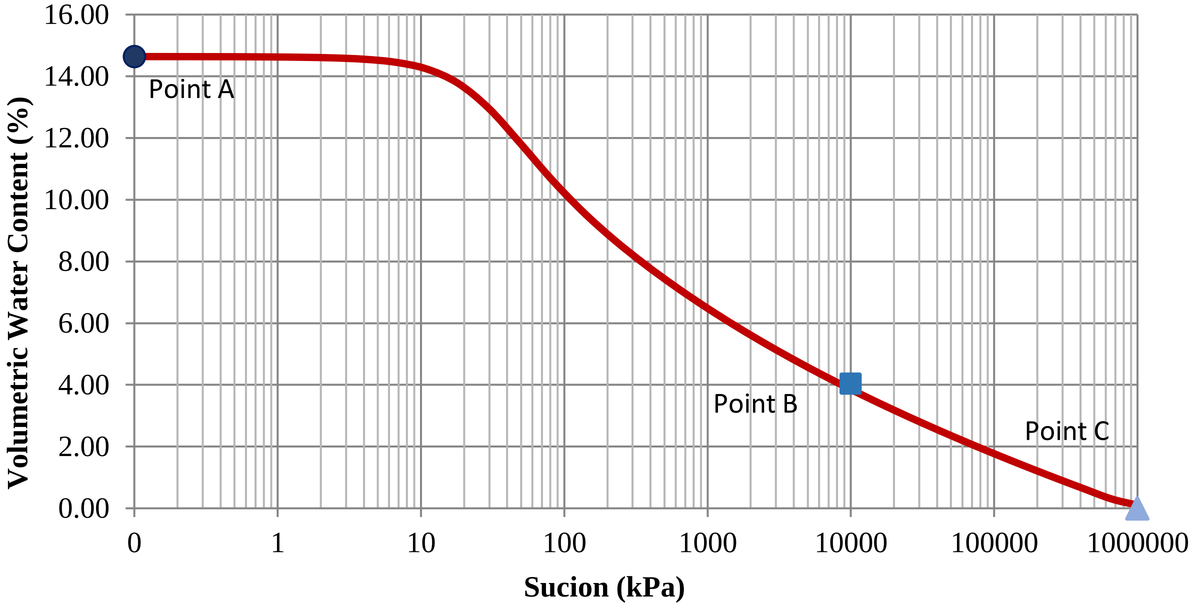

Figure 16. Illustration of Three-Point Method on Soil-Water Characteristic Curve.

A sigmoidal curve was fitted through each set of points in the graph based on the Fredlund and Xing (1994) function. In Figure 16, Point A represents the saturated volumetric water content on the SWCC, which is calculated by Equation 18. The saturated volumetric water content is correlated to the porosity of soils, which is defined as the void ratio in the saturated state.

$$\theta_{sat} = \left[1 - \frac{\gamma_d}{(G_s \gamma_w)}\right] \tag{18}$$

where θ_{sat} is saturated volumetric water content, γ_d is the maximum dry unit weight of soil, G_s is the specific gravity of soil, and γ_w is the unit weight of water. Point B represents a point that is the measured suction value at the corresponding volumetric water content. The soil suction and volumetric water content are determined from the filter paper test. Point C represents the maximum suction with zero moisture content. This particular point sets the maximum suction as 10^6 kPa when moisture content is approaching zero (Zapata, 2010). The curve fitting method aims to minimize the difference between the measured moisture Point B and the fitted moisture content. The best fitting curve for the predicted moisture content provides the four parameters in the Equations 5 and 6.

Regression analysis is performed to investigate the correlation between the determined four fitting parameters and PFC. Each fitting parameter has a unique equation to describe its relationship with PFC, which are presented in Equations 19 to 22. The PFC value significantly influences the shape of SWCC. Figure 17 shows the effect of PFC on the SWCC for the plastic materials.

$$a_f\,(psi) = 0.6384e^{0.0369\,pfc} \tag{19}$$

$$b_f = 11.748e^{-0.037\,pfc} \tag{20}$$

$$c_f = 0.126e^{0.0211\,pfc} \tag{21}$$

$$h_r\,(psi) = -0.0018\,pfc^2 + 0.5206\,pfc + 2.4305 \tag{22}$$

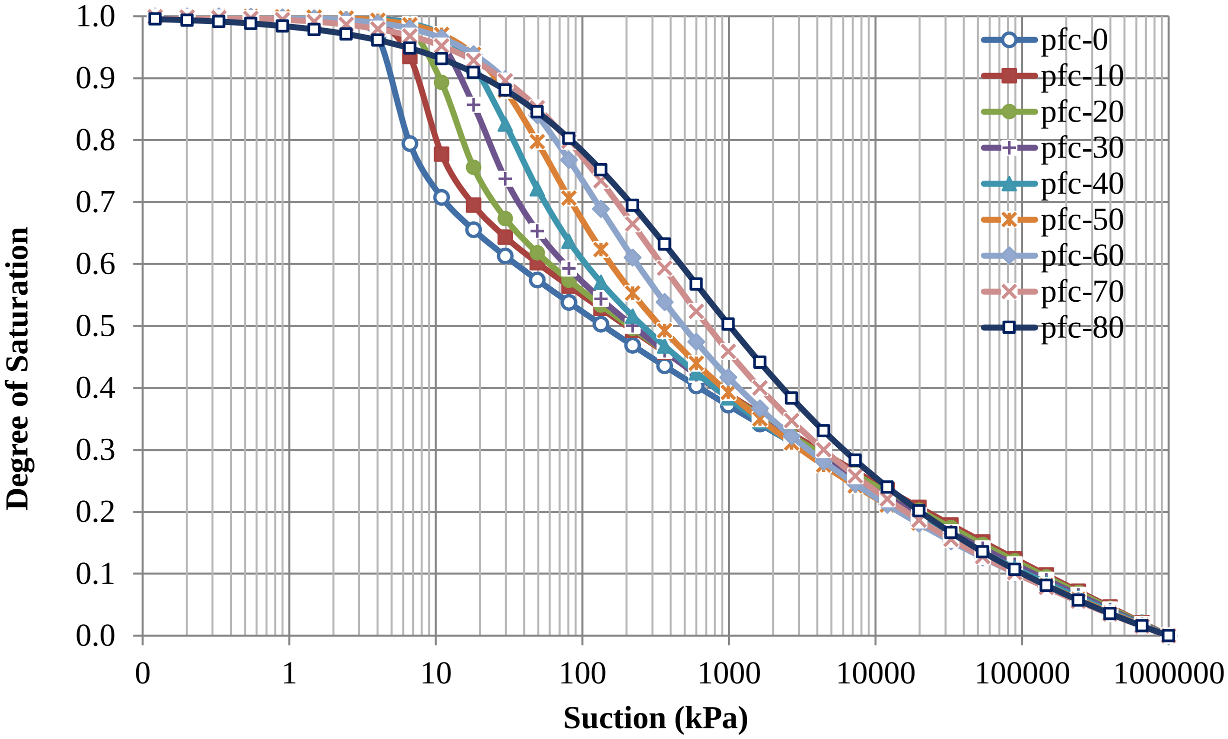

Figure 17. Effect of PFC on the Drying Soil-Water Characteristic Curves.

The accuracy of the proposed SWCCs is evaluated by comparing the predicted matric suction values and the measured matric suction obtained from the filter paper test. Figure 18 shows that the model-predicted matric suction values are in good agreement with the measured matric suction values from the filter paper test. This indicates that the developed regression model can accurately predict the SWCC of flexible base material.

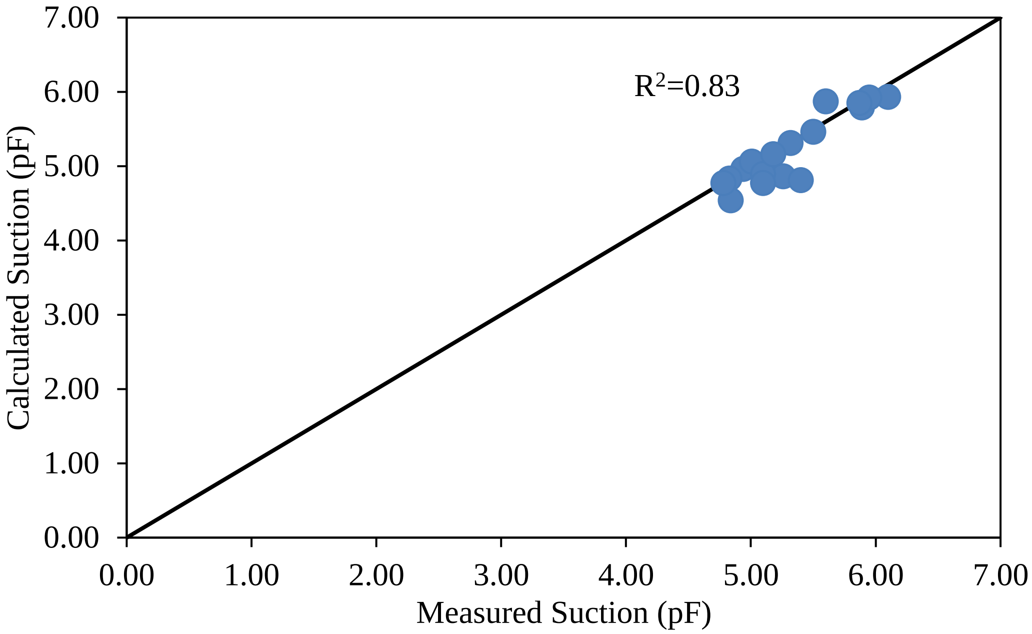

Figure 18. Comparison of Measured and Predicted Suction Values for Flexible Base.

Development of Suction Dielectric Constant Curve for Flexible Base

In this section, the dielectric constant of flexible base is used to predict the soil suction. A mathematical model is developed to generate the suction dielectric constant curve (SDCC) based on Juarez-Badilo's approach (1981). The change of the dielectric constant of flexible base within the defined boundary limits are related to the change of the soil suction. Figure 19 illustrates the concept of the SDCC model.

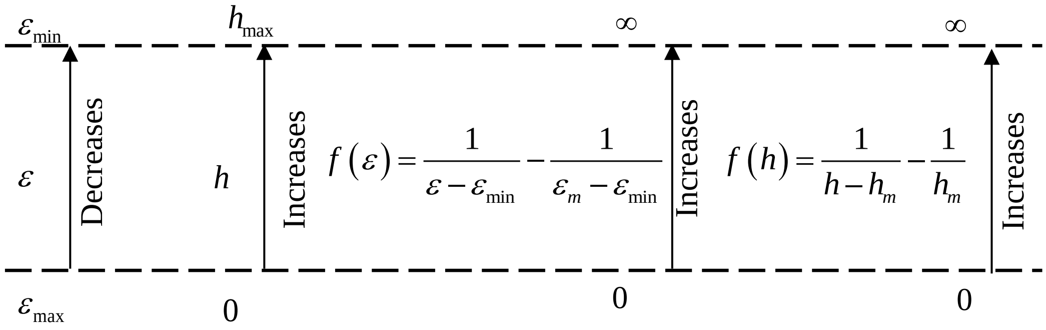
$\varepsilon_{\min}$
$h_{\max}$
∞
∞
ε
Decreases
h
Increases
$f(\varepsilon) = \frac{1}{\varepsilon - \varepsilon_{\min}} - \frac{1}{\varepsilon_m - \varepsilon_{\min}}$
Increases
$f(h) = \frac{1}{h - h_m} - \frac{1}{h_m}$
Increases
$\varepsilon_{\max}$
0
0
0

Figure 19. Concept of the SDCC Model.

The general form of the SDCC model is presented in Equation 23:

$$\varepsilon_r = \left[\frac{\varepsilon_{sat} + \varepsilon_{\min} \alpha \left[\dfrac{h}{\left(1 \times 10^6 - h\right)} \right]^{\gamma}}{1 + \alpha \left(\dfrac{h}{1 \times 10^6 - h} \right)^{\gamma}} \right] \tag{23}$$

where ε_{sat} is the saturated dielectric value, ε_r is the soil dielectric value, $\varepsilon_{\min}$ is the minimum dielectric constant, and α and γ are two fitting parameters. Figure 20 shows a typical SDCC of flexible base, which represents the relationship between matric suction and dielectric constant of flexible base.

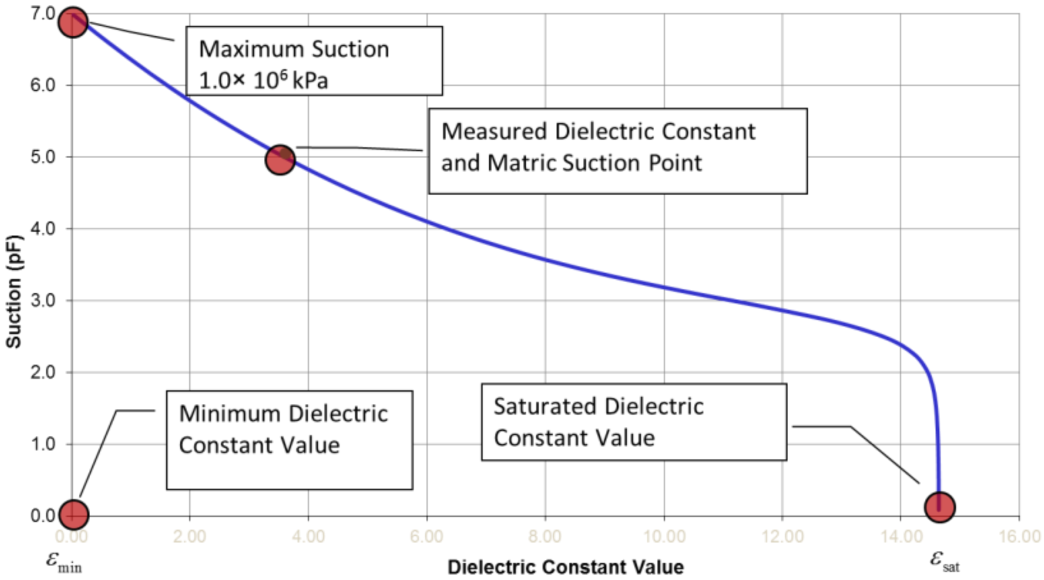

Figure 20. A Typical SDCC of Flexible Base.

Development of Mechanistic-Based Approach to Evaluate Flexible Base Construction

In this project, a mechanistic-based approach was developed to rapidly evaluate the flexible base construction using the laboratory characterization and field GPR. There are four critical steps involved in the approach, including:

- Laboratory characterization to predict the coefficients of resilient modulus model.
- Laboratory characterization to generate the SDCC.
- Field GPR measurements to determine the moisture content and matric suction of flexible base.
- Data input of the obtained resilient modulus model coefficients, moisture content, and matric suction into the nonlinear finite element program to compute the resilient modulus of in-situ flexible base.

Figure 21 presents the flowchart to predict the coefficients of resilient modulus model using the laboratory test results. The regression analysis is employed to establish the relationship between the model coefficients and the performance-related flexible base properties.

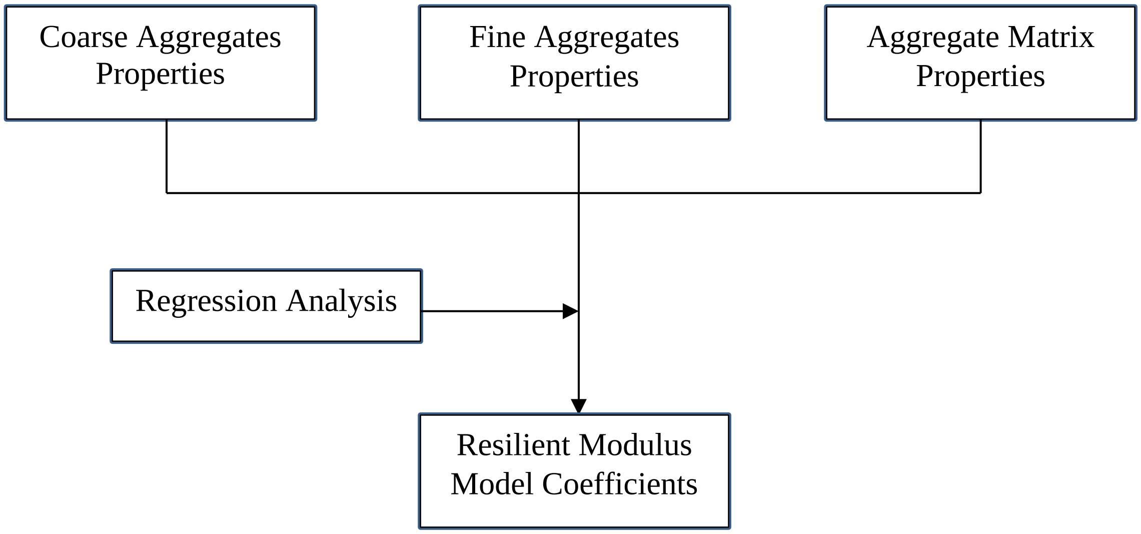
Coarse Aggregates Properties
Fine Aggregates Properties
Aggregate Matrix Properties
Regression Analysis
Resilient Modulus Model Coefficients

Figure 21. Flowchart of Prediction of Resilient Modulus Model Coefficients.

Figure 22 illustrates the process to estimate the moisture content and matric suction of the flexible base in the field. The laboratory measured MBV and PFC are used to generate the SWCC and SDCC of flexible base. The GPR survey or percometer test is used to collect the dielectric constant profile of flexible base, which is further used to determine the matric suction and moisture content of flexible base.

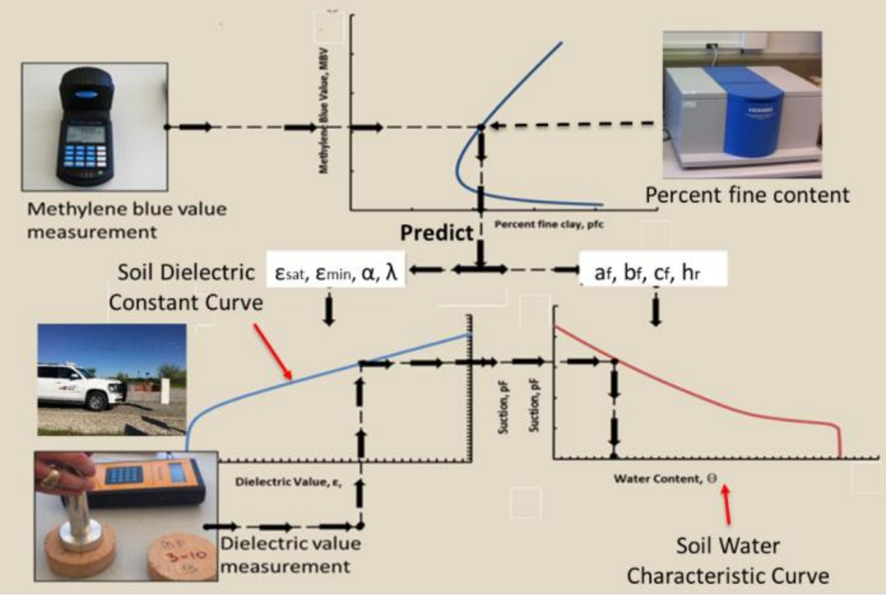
Methylene Blue Value, MBV
Percent fine content
Methylene blue value measurement
Predict
Percent fine clay, pfc
Soil Dielectric Constant Curve
$\varepsilon_{sat}, \varepsilon_{min}, \alpha, \lambda$
a_f, b_f, c_f, h_r
Suction, pF
Suction, pF
Dielectric Value, ε,
Water Content, Θ
Dielectric value measurement
Soil Water Characteristic Curve

Figure 22. Process of Estimation of Moisture Content and Matric Suction of Flexible Base in the Field.

Figure 23 describes the procedure to estimate the resilient modulus of in-situ flexible base. The determined resilient modulus coefficients, moisture content, and matric suction profile of in-situ flexible base are input into the finite element program. The developed program computes the stress distribution of flexible base when the pavement structure is subjected to the traffic load. The computed stress distribution is then input into the constitutive model of flexible base to estimate the resilient modulus of the in-situ flexible base. This approach considers the nonlinear stress-dependent and moisture-sensitive behavior of flexible base. The GPR is an efficient NDT technology used to estimate the moisture and matric suction of unbound granular material. The proposed mechanistic-based approach has been programmed into the LayerMAPP software, which is directly used to determine the resilient modulus of the in-situ flexible base based on the laboratory characterization and the dielectric constant profile from GPR test.

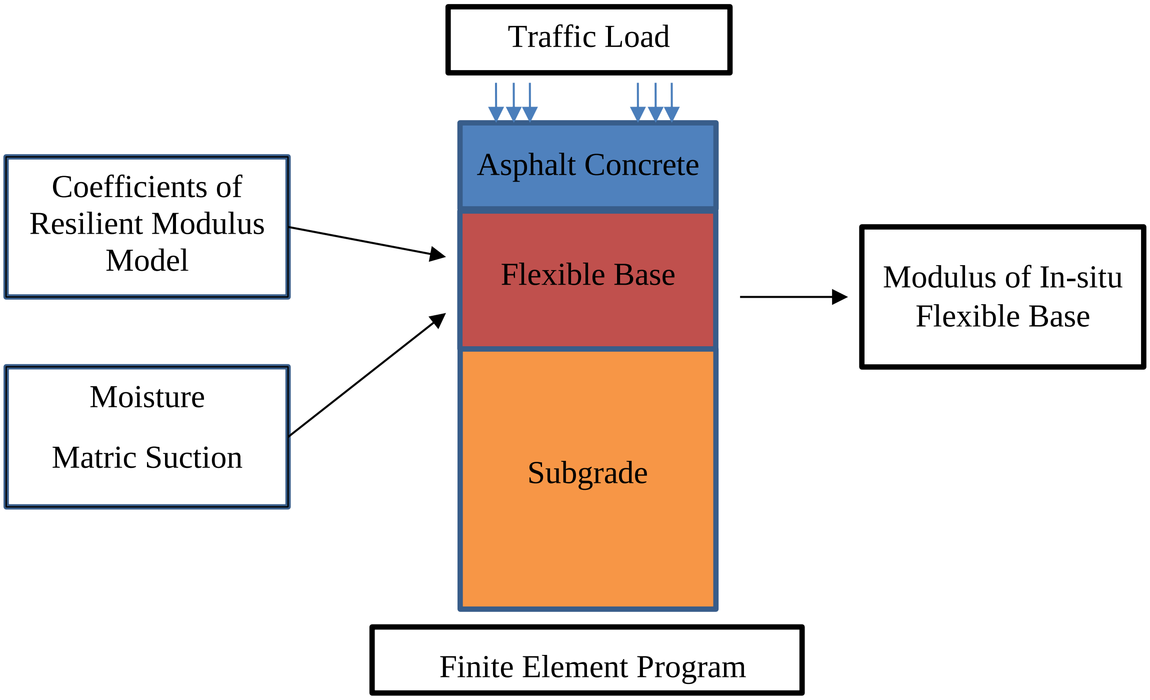
Traffic Load
Coefficients of Resilient Modulus Model
Moisture
Matric Suction
Asphalt Concrete
Flexible Base
Subgrade
Modulus of In-situ Flexible Base
Finite Element Program

Figure 23. Procedure to Estimate Resilient Modulus of In-Situ Flexible Base.

RESULTS

Estimation of Resilient Modulus of Flexible Base in the Lab

The values of k_1, k_2, and k_3 in the resilient modulus model depend on the properties of unbound aggregates. In order to predict the k values in the resilient modulus model, these performance-related base course properties are first characterized quantitatively. Multiple regression analysis is performed using the JMP software to investigate the correlation between the k values and the base course properties, including the dry density (γ_d), water content (w), MBV, PFC, aggregate gradation, angularity, shape, and texture in terms of the shape parameter a and the scale parameter λ in the Weibull distribution. Compared to PI, liquid limit, and P_{200}, these selected base course properties are much more directly related to pavement performance (Pan et al. 2006).

A stepwise multiple regression analysis is performed to detect the significant material properties of the base course for modeling k_1, k_2, and k_3. The P-value obtained from the t-test is used to identify the significant variables in the model. A P-value less than 0.05 indicates that the variable is significant at a 95 percent confidence level. Table 1 presents the results produced by the JMP software. The t-ratio is a ratio of the departure of an estimated parameter from its notional value and its standard error. A higher absolute value of the t-ratio corresponds to a smaller obtained P-value. It is shown that the dry density, shape, angularity, and texture of the aggregates and the PFC are significant variables in the prediction models. Equations 24 to 26 are the prediction models for k_1, k_2, and k_3, respectively, from the regression analysis.

$$\ln k_1 = -137.19 + 13.60\ln(\gamma_d) + 4.35\ln(\lambda_A) - 0.62\lambda_S + 1.68\ln(\lambda_T) \tag{24}$$

$$k_2 = 36.14 + 0.04 pfc - 3.81\ln\left(\lambda_A\right) - 0.22 a_S - 0.77\ln\left(\lambda_T\right) \tag{25}$$

$$k_3 = -4.39 + 0.45\ln\left(\gamma_d\right) - 0.01 pfc + 0.05 a_S + 0.15\ln\left(\lambda_T\right) \tag{26}$$

Figure 24 compares the k values predicted by Equations 24 to 26 with those predicted using simple empirical parameters, including dry unit weight, optimum water content, PI, liquid limit, and P_{200}. As can be seen from Figure 24, the R-squared values of the performance-related prediction models are much higher than those produced by simple empirical parameters. This result is because the selected material properties in this study are directly related to the performance of unbound aggregates. This fact also suggests that the proposed performance-related base course properties can accurately predict the k coefficients of the resilient modulus model. Figure 25 compares the model-predicted resilient moduli and lab-measured resilient moduli of flexible base. The model-predicted resilient moduli of flexible base shows good agreement with the laboratory measurements. This indicates that the proposed model is capable of accurately predicting the resilient modulus of flexible base in the laboratory.

Table 1. Multiple Regression Analysis of Resilient Modulus Model.

	Variables	DF	Parameter Estimate	Standard Error	t-Ratio	P-value
Prediction Model of $\ln(k_1)$	Intercept	1	-137.19	17.72	-7.74	<0.0001
	$\ln(\gamma_d)$	1	13.60	1.77	7.70	<0.0001
	$\ln(\lambda_A)$	1	4.35	1.42	3.07	0.0078
	λ_S	1	-0.62	0.17	-3.72	0.0021
	$\ln(\lambda_T)$	1	1.68	0.32	5.31	<0.0001
Prediction Model of k_2	Intercept	1	36.14	5.60	6.46	<0.0001
	pfc	1	0.04	0.01	4.87	0.0002
	$\ln(\lambda_A)$	1	-3.81	0.74	-5.17	<0.0001
	a_S	1	-0.22	0.06	-3.67	0.0023
	$\ln(\lambda_T)$	1	-0.77	0.11	6.78	<0.0001
Prediction Model of k_3	Intercept	1	-4.39	0.71	-6.16	<0.0001
	$\ln(\gamma_d)$	1	0.45	0.09	5.01	0.0002
	pfc	1	-0.01	0.001	-8.09	<0.0001
	a_S	1	0.05	0.01	5.85	<0.0001
	$\ln(\lambda_T)$	1	0.14	0.02	9.22	<0.0001

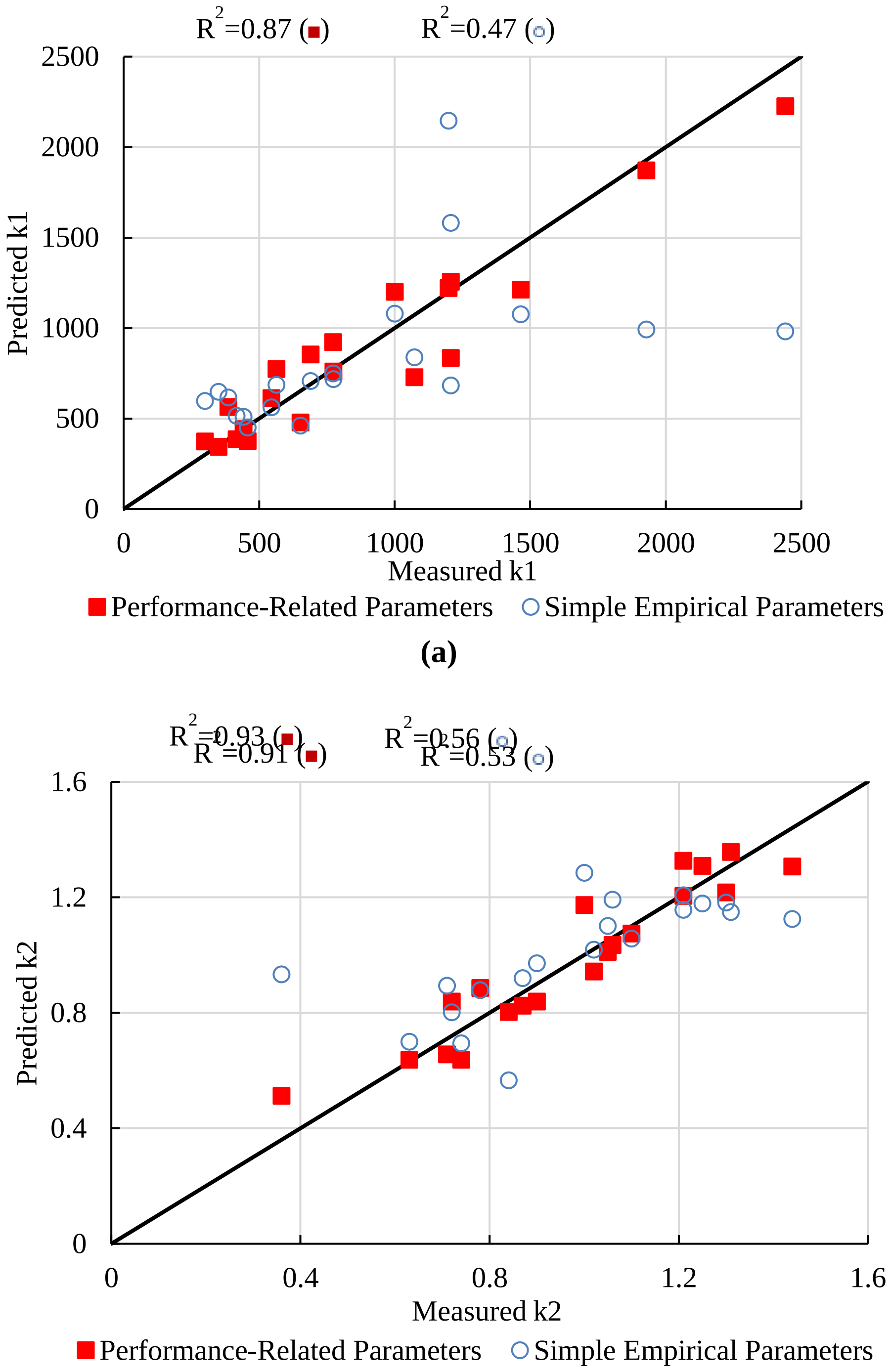

(b)

Figure 24. Comparison between Predicted K Values by Performance-Related Parameters and Simple Empirical Parameters.

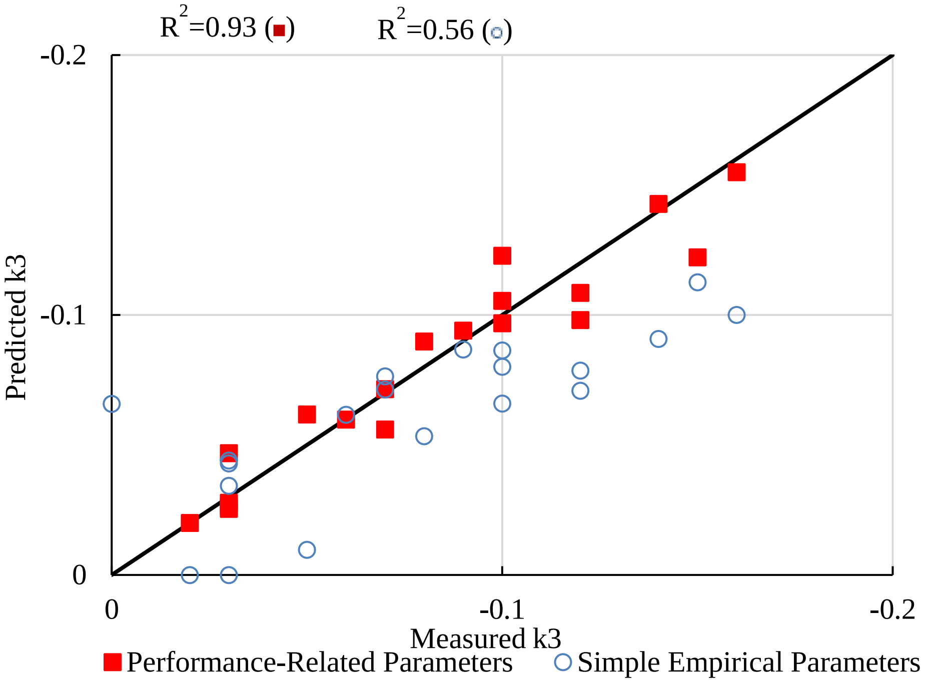

(c)

Figure 24. Comparison between Predicted K Values by Performance-Related Parameters and Simple Empirical Parameters (Continued).

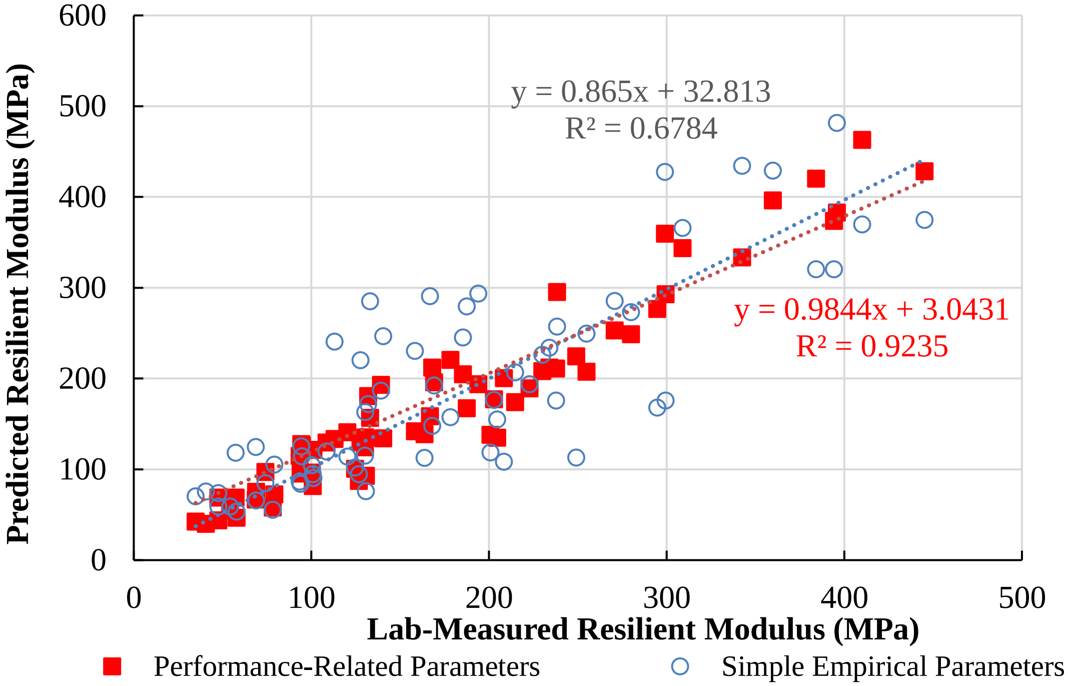

Figure 25. Comparison between Model-Predicted Resilient Modulus and Lab-Measured Resilient Modulus of Flexible Base.

Estimation of Permanent Deformation of Flexible Base in the Lab

The relations between the permanent deformation properties and performance-related base course properties were investigated to develop prediction models. A stepwise regression analysis was performed to identify the significant performance-related properties of the base course for predicting α, μ, ε_0, ρ, and β in the permanent deformation models. The analysis mixes the forward and backward stepwise regression methods. Initially, all of the variables are inputted into the model. When running the analysis, the variables are removed or entered based on the P-value threshold-stopping rule. That is, if the P-value of the variable is larger than 0.25, the variable will be removed from the model, and vice versa. Finally, the one with largest F-test value is chosen as the best regression model.

Table 2 presents the results produced by the JMP software. It is shown that maximum dry density, MBV, shape parameter of gradation, scale parameter of angularity index, shape parameter of texture, and scale parameter of texture are significantly influential variables when predicting the parameters in the VESYS model. It is also suggested that MBV, PFC, shape parameter of angularity index, shape parameter of texture, and scale parameter of texture are significantly influential variables to predict the parameters in the Tseng-Lytton Model. According to the regression analysis, Equations 27 to 31 list the prediction models for α, μ, ε_0, ρ, and β, respectively. Figure 26 compares the predicted permanent deformation parameter values as predicted by Equations 27 through 31 to the measured values listed in Table 2. A good agreement is observed between the predicted permanent deformation properties and the measured ones. This indicates that the proposed regression models can predict the permanent deformation behavior accurately.

$$\ln\alpha = 4.91 + 1.23\ln\gamma_d - 0.02MBV + 0.59a_G - 1.91\ln\lambda_A + 0.17a_T \tag{27}$$

$$\ln\mu = -54.68 + 16.89\ln\gamma_d + 0.06pfc + 3.34a_G - 7.60\ln\lambda_A - 3.72\ln\lambda_T \tag{28}$$

$$\ln\varepsilon_0 = 10.24 - 0.03MBV + 0.10pfc + 0.88a_A - 3.95\ln\lambda_T \tag{29}$$

$$\ln\rho = 6.74 + 0.02MBV + 0.04pfc - 0.85a_G + 0.03\lambda_G - 0.13a_T \tag{30}$$

$$\ln\beta = 10.17 - 2.75\ln\gamma_d - 0.05pfc - 2.00a_G - 1.61\ln\lambda_A - 0.34a_T \tag{31}$$

Table 2. Multiple Regression Analysis of Permanent Deformation Model.

	Variables	DF	Parameter Estimate	Standard Error	t-Ratio	P-value
Prediction Model of $\ln\alpha$	Intercept	1	4.9077	8.565	0.57	0.58
	$\ln\gamma_d$	1	1.2260	0.732	1.68	0.13
	MBV	1	-0.0180	0.006	-3.23	0.01
	a_G	1	0.5875	0.258	2.28	0.05
	$\ln\lambda_A$	1	-1.9066	0.629	-3.03	0.02
	a_T	1	0.1701	0.05	3.23	0.01
Prediction Model of $\ln\mu$	Intercept	1	-54.678	51.48	-1.06	0.32
	$\ln\gamma_d$	1	16.894	4.262	3.96	0.004
	pfc	1	0.0558	0.053	1.05	0.33
	a_G	1	3.3356	1.724	1.93	0.09
	$\ln\lambda_A$	1	-7.598	5.808	-1.31	0.23
	$\ln\lambda_T$	1	-3.2748	0.989	-3.77	0.006
Prediction Model of $\ln\varepsilon_0$	Intercept	1	10.238	3.728	2.75	0.02
	MBV	1	-0.0263	0.025	-1.07	0.31
	pfc	1	0.0995	0.052	1.92	0.09
	a_A	1	0.8882	0.316	2.81	0.02
	$\ln\lambda_T$	1	-3.9520	0.615	-6.42	0.0001
Prediction Model of $\ln\rho$	Intercept	1	6.7414	0.43	15.67	<0.0001
	MBV	1	0.0167	0.007	2.42	0.04
	pfc	1	0.0432	0.009	5.02	0.001
	a_G	1	-0.8545	0.346	-2.47	0.04
	λ_G	1	0.0328	0.026	1.24	0.25
	a_T	1	-0.126	0.064	-1.96	0.09
Prediction Model of $\ln\beta$	Intercept	1	10.174	16.21	0.63	0.55
	$\ln\gamma_d$	1	-2.7506	1.488	-1.85	0.10
	pfc	1	-0.0492	0.018	-2.7	0.03
	a_G	1	-2.000	0.503	-3.98	0.004
	$\ln\lambda_A$	1	1.6072	1.522	1.06	0.32
	a_T	1	-0.3403	0.095	-3.58	0.007

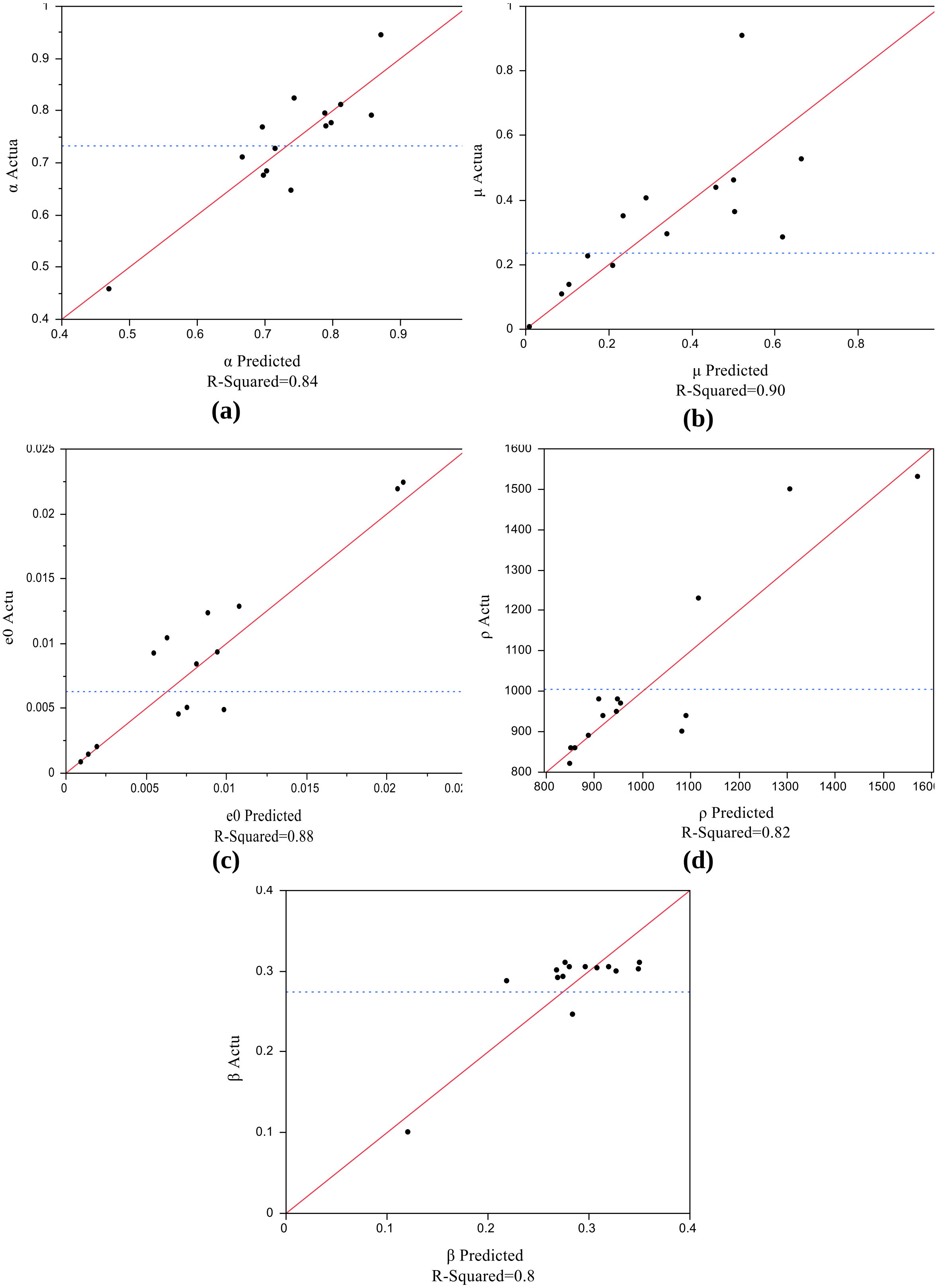

(a) **(b)**

(c) **(d)**

(e)

Figure 26. Comparison of Predicted Permanent Deformation Properties and Measured Permanent Deformation Properties.

Estimation of Moisture Density Curve of Flexible Base in the Lab

A mathematic model was developed to characterize the moisture density curve of flexible base, which is shown in Equation 32.

$$\frac{\gamma_d}{\gamma_w} = a_d\left[\operatorname{csc}h\left(\frac{\theta_w\theta_{sat}}{G_s\left(\theta_{sat}-\theta_w\right)}\right)\right]^{n_d} - b_d\left[\operatorname{csc}h\left(\frac{\theta_w\theta_{sat}}{G_s\left(\theta_{sat}-\theta_w\right)}\right)\right] \tag{32}$$

where γ_d is the dry unit weight of flexible base, γ_w is the unit weight of water, G_s is the specific gravity of aggregates, w is the gravimetric moisture content, θ_w is the volumetric water content, θ_{sat} is the saturated volumetric water content, and a_d, b_d, and n_d are three model coefficients dependent on the material properties of flexible base. To validate the proposed dry density model, the model-predicted moisture dry density curve of flexible base was compared with the laboratory measured one, which is shown in Figure 27. The model-predicted dry density curve demonstrates good agreement with the lab-measured curve. This demonstrates that the proposed dry density model is capable of predicting the relationship between the moisture content and the dry density of flexible base.

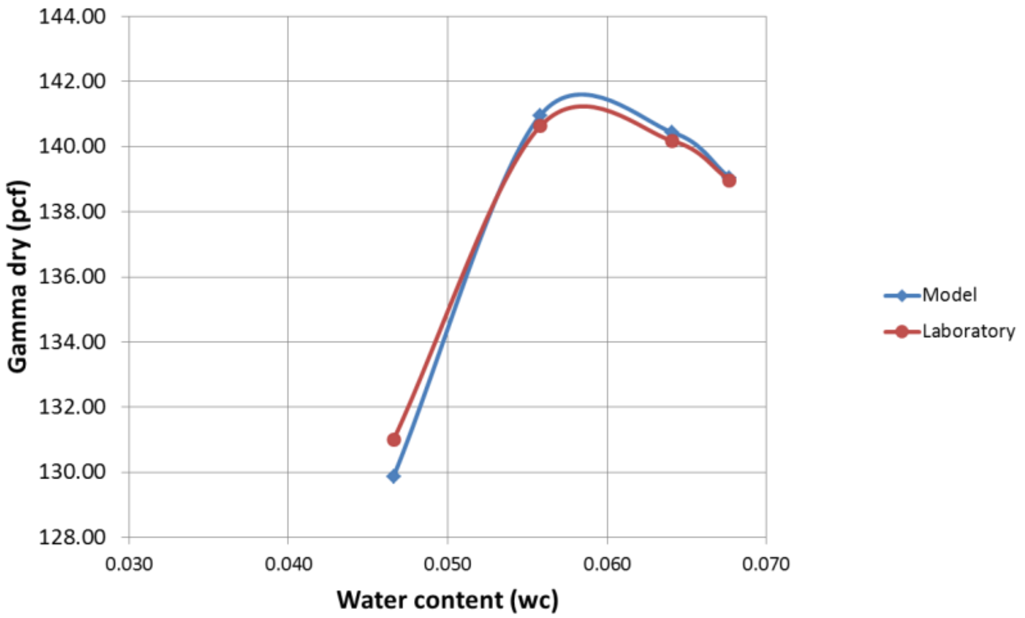

Figure 27. Comparison of Model-Predicted Dry Density and Lab-Measured Dry Density.

In order to determine the three model coefficients, a_d, b_d, and n_d, a neural network model was developed to establish the relationship among the model coefficients and the material properties of flexible base. A three-layered neural network architecture consisting of one input layer, one hidden layer and one output layer was constructed, as shown Figure 28. The input parameters are the material properties of flexible base, such as the specific gravity of aggregates, MBV, PFC, etc. The output variables are the three coefficients of the dry density model. The hidden layer is used to establish the connection between the output layer and the input layer. In this study, the transfer function used a sigmoidal functional form, which is shown in Equation 33,

$$f\left(I_i\right)=\frac{1}{1+\exp\left(-\varphi I_i\right)} \tag{33}$$

where I_i is the input quantity and φ is a positive scaling constant that controls the steepness between the two asymptotic values 0 and 1. The constructed neural network structure is programmed by the software MATLAB 2013a. The training algorithm uses the Levenberg-Marquardt back propagation method to minimize the mean squared error. The gradient descent weight function is employed as a learning algorithm to adjust the weight factors w_{ji}.

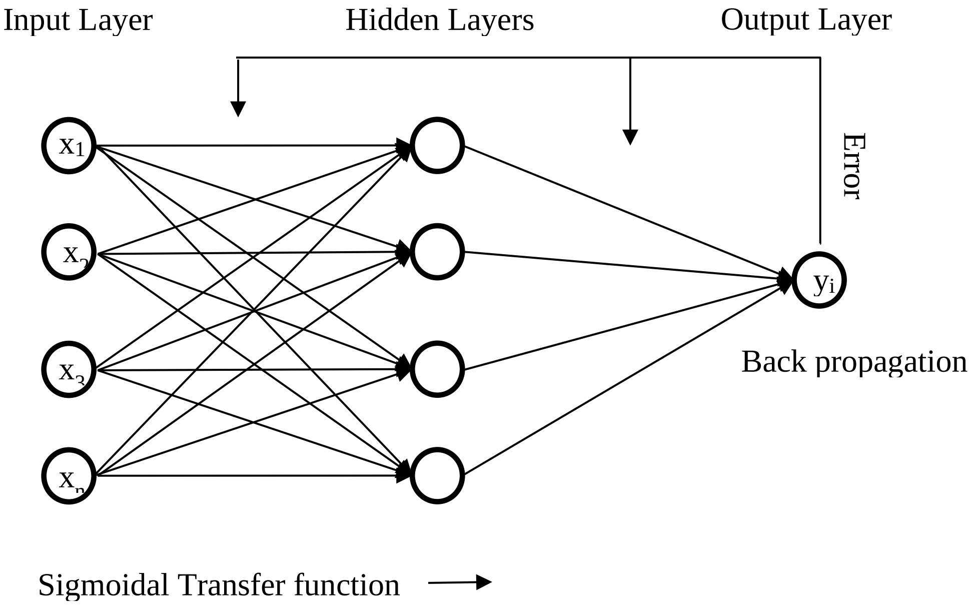

Figure 28. Illustration of Three-layered Neural Network Architecture

Figure 29 compares the neural-network-predicted, maximum dry density with the laboratory measurements. The model predictions match well with the laboratory results. This match indicates that the developed model can accurately capture the moisture density relationship of flexible base.

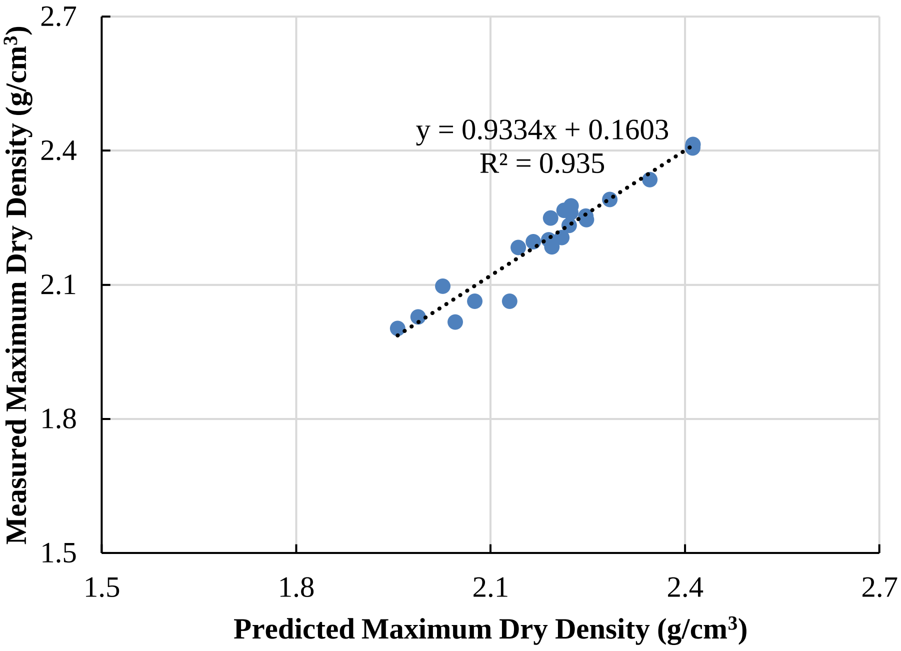

Figure 29. Comparison of Maximum Dry Density of Flexible Base between Model Predictions and Laboratory Measurements

Estimation of Resilient Modulus of Flexible Base in the Field

In this section, the mechanistic-based NDT approach is employed to evaluate the quality of flexible base in terms of the determined resilient modulus and dry density profiles. Figure 30 illustrates the procedures of implementing the mechanistic-based NDT approach for field projects. The GPR outputs are analyzed by the software Pavecheck to obtain the dielectric constant profile of flexible base. The laboratory characterization results and the dielectric constant data are input into the software LayerMAPP to estimate the resilient modulus of the in-situ flexible base. The FWD test is also conducted on the field test sections. The FWD test data is analyzed by the software Modulus 6.0 to backcalculate the resilient modulus of the in-situ flexible base. To validate the mechanistic-based NDT approach, the predicted resilient moduli of flexible base are compared to those backcalculated from the FWD test data.

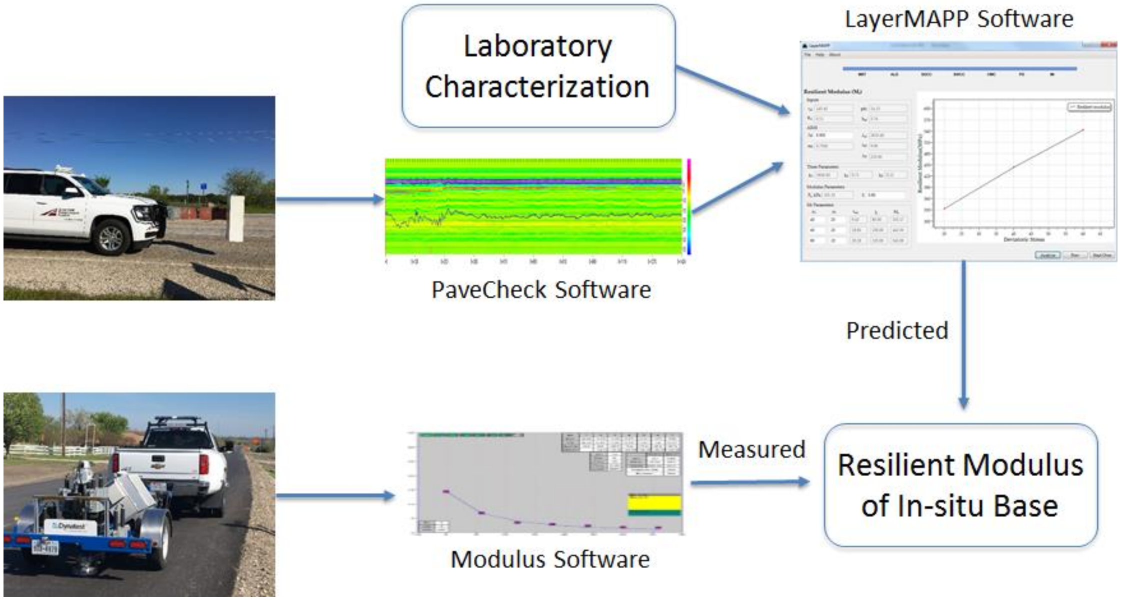
Laboratory Characterization
LayerMAPP Software
PaveCheck Software
Predicted
Measured
Resilient Modulus of In-situ Base
Modulus Software

Figure 30. Validation of Mechanistic-Based NDT Approach Using Field Project Data

Case Study: State Highway 21

Two pavement sections were identified from SH 21, which are shown in Figures 31a and 31b. The investigated length of the pavement sections are 2 miles and 4.5 miles, respectively. The two pavement sections had the same structure, which is presented in Figure 32. The pavement consisted of a 3-inch hot mix asphalt (HMA) layer, a 6-inch flexible base course, a 6-inch cement-treated subbase, and subgrade soil. The geogrid layer was placed at the interface between the flexible base and the cement-treated subbase. The only difference between the two pavement sections was that two different types of flexible base were used. Flexible base A was used for the pavement section A. Flexible base B was constructed for the pavement section B.

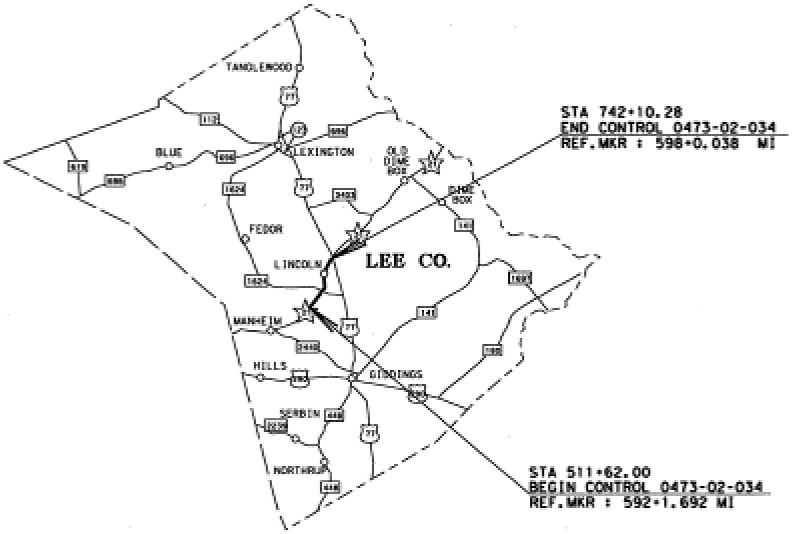
STA 742+10.28
END CONTROL 0473-02-034
REF.MKR : 598+0.038 MI
STA 511+62.00
BEGIN CONTROL 0473-02-034
REF.MKR : 592+1.692 MI
TANGLEWOOD
BLUE
LEXINGTON
OLD DIME BOX
DIME BOX
FEDOR
LINCOLN
LEE CO.
MANHEIM
HILLS
GIDDINGS
SERBIN
NORTHRUP

a. Location of Pavement Section A in SH 21

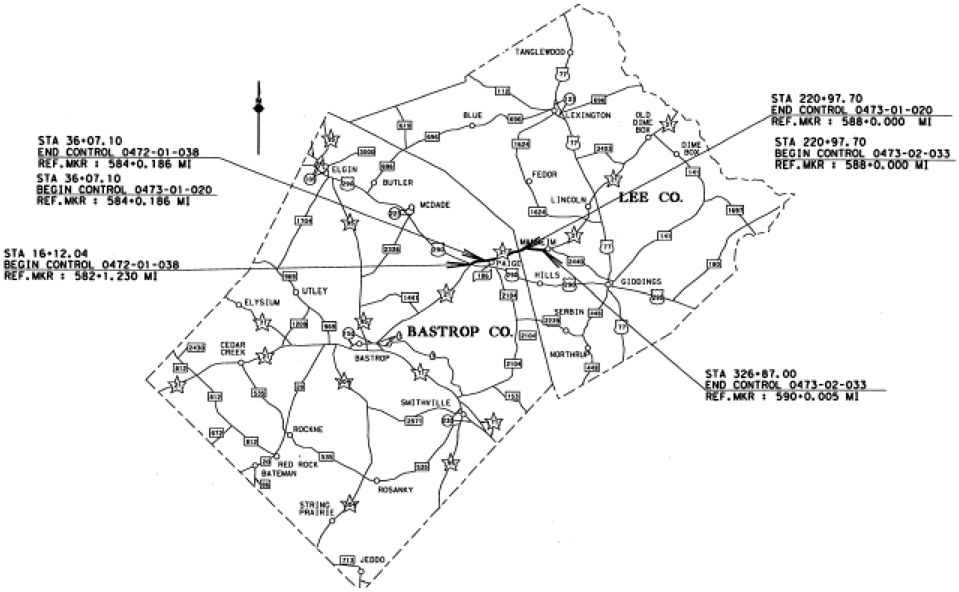
STA 36+07.10
END CONTROL 0472-01-038
REF.MKR : 584+0.186 MI
STA 36+07.10
BEGIN CONTROL 0473-01-020
REF.MKR : 584+0.186 MI
STA 16+12.04
BEGIN CONTROL 0472-01-038
REF.MKR : 582+1.230 MI
STA 220+97.70
END CONTROL 0473-01-020
REF.MKR : 588+0.000 MI
STA 220+97.70
BEGIN CONTROL 0473-02-033
REF.MKR : 588+0.000 MI
STA 326+87.00
END CONTROL 0473-02-033
REF.MKR : 590+0.005 MI
TANGLEWOOD
BLUE
LEXINGTON
OLD DIME BOX
DIME BOX
FEDOR
LINCOLN
LEE CO.
ELGIN
BUTLER
MCDADE
MANHEIM
PAIGE
HILLS
GIDDINGS
SERBIN
NORTHRUP
UTLEY
ELYSIUM
CEDAR CREEK
BASTROP CO.
BASTROP
SMITHVILLE
ROCKNE
RED ROCK
BATEMAN
ROSANKY
STRING PRAIRIE
JEDDO

b. Location of Pavement Section B in SH 21

Figure 31. Location of Two Identified Pavement Sections in SH 21.

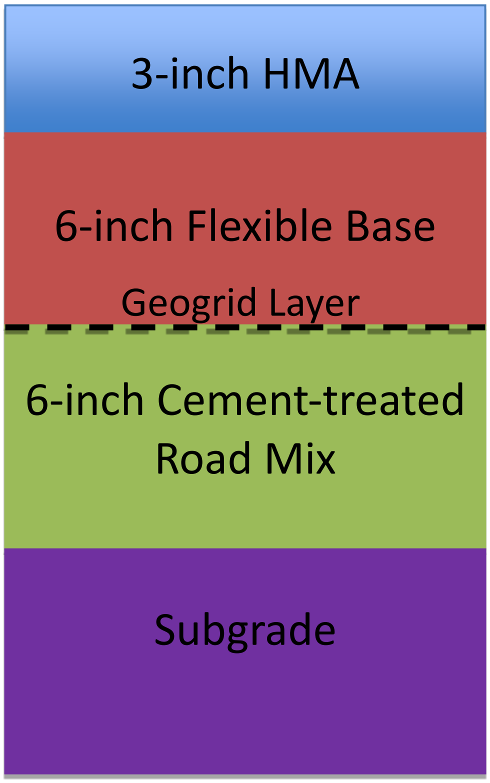
3-inch HMA
6-inch Flexible Base
Geogrid Layer
6-inch Cement-treated Road Mix
Subgrade

Figure 32. Structures of Identified Pavement Sections in SH 21.

Figure 33 shows the surface conditions of the two pavement sections. Pavement section A had severe alligator cracking damages at the wheel path of the right lane, but there was no severe damage observed in the pavement section B. It was inferred that the significant different performance of the two pavement sections was caused by the quality of flexible base materials.

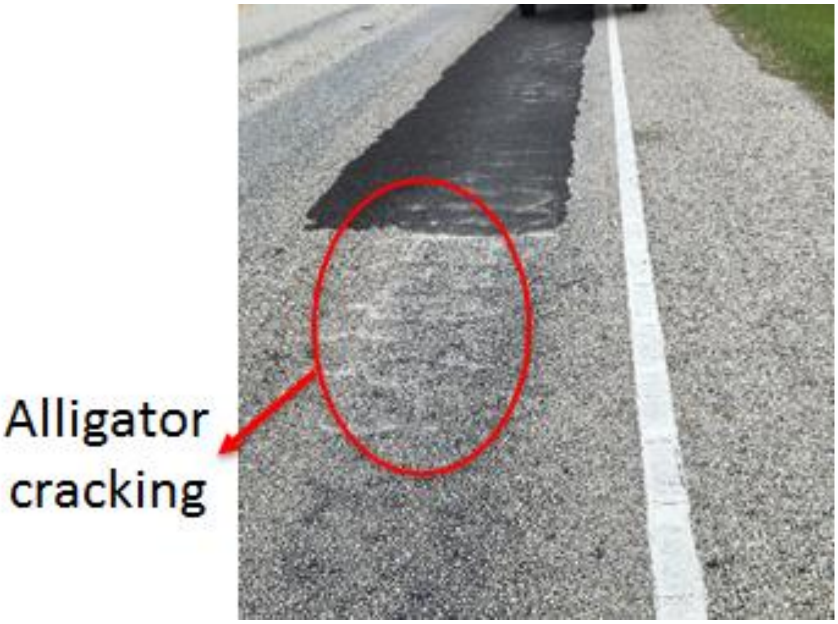

a. Surface Condition of Pavement Section A

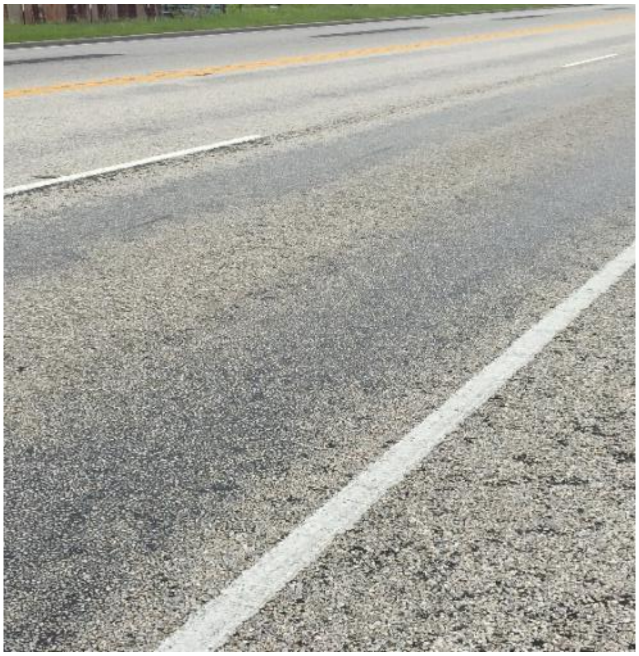

b. Surface Condition of Pavement Section B

Figure 33. Surface Conditions of Identified Pavement Sections in SH 21.

Full laboratory characterization was performed on the flexible base materials A and B. Figure 34 shows the results of MBV and PFC for the two base materials. Flexible base A had a greater MBV than flexible base B. This indicates that flexible base A was more sensitive to moisture change than flexible base B. The MBV has a threshold value 7.0. If the MBV is less than 7.0, the flexible base material has a good resistance to moisture. In this case, the MBV of flexible base B is far less than 7.0. The MBV of flexible base A fluctuated around 7.0. The MBV results suggest that flexible base B had a better quality than the flexible base A. This finding is consistent with the field condition where section A had more damage than pavement section B.

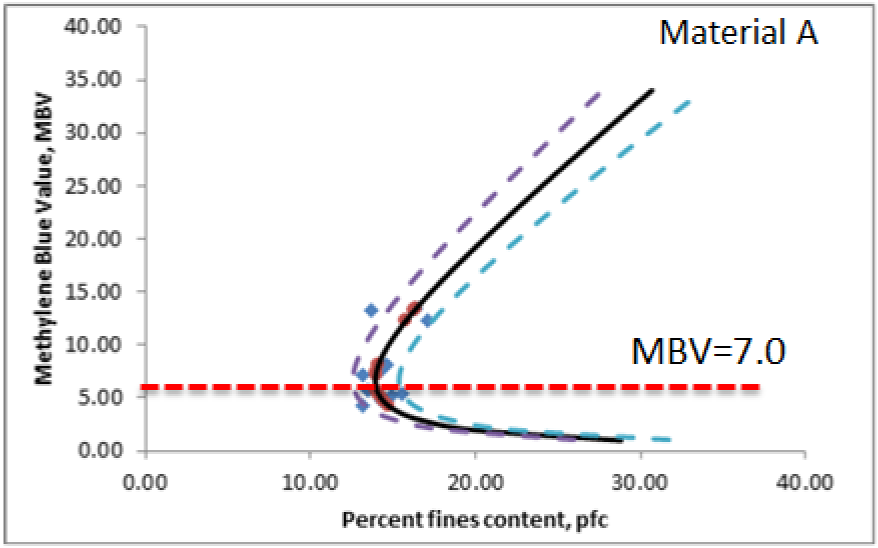

a. Results of MBV and PFC for Material A

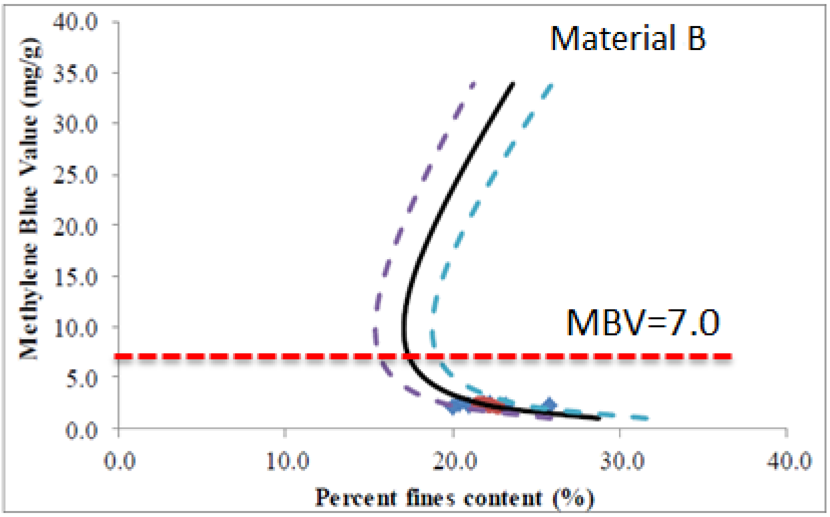

b. Results of MBV and PFC for Material B

Figure 34. Results of Laboratory Characterization for Materials A and B.

The FWD test was also performed on the two test sections. Figure 35 presents the surface deflection basins of the test sections with and without the alligator cracks when they were subjected to a 9-kip FWD load. The pavement section without the alligator cracks had smaller surface deflections than the one with the alligator cracks. This characteristic was because the alligator cracks reduced the structural properties of the asphalt concrete layer. Compared to the non-crack pavement section A, pavement section B still had smaller surface deflections. This result indicated that pavement section B had a better supporting layer than pavement section A.

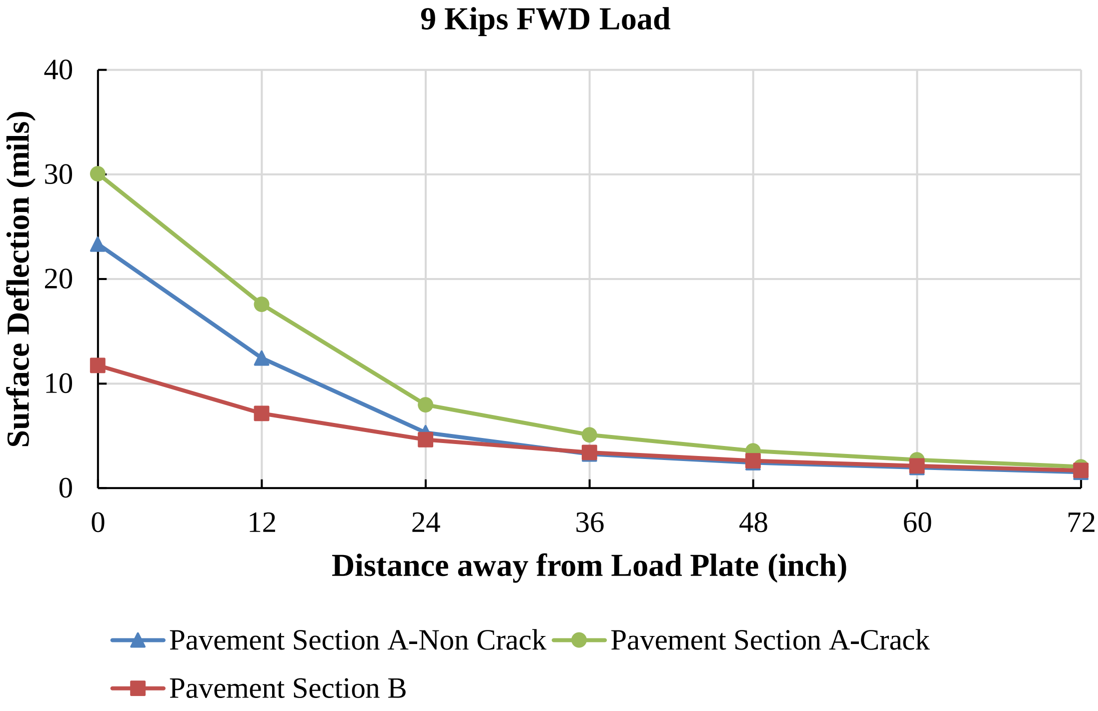

Figure 35. Surface Deflection Basin of Identified Pavement Sections.

Figure 36 compares the model-predicted resilient moduli of flexible base with those backcalculated from the FWD data. It was determined that the mechanistic-based approach predicting the resilient moduli of flexible base was in good agreement with the backcalculation results. This comparison validated that the proposed mechanistic-based approach was capable of accurately predicting the resilient modulus profile of the in-situ flexible base. Both the model predictions and FWD backcalculated results indicated that pavement section B had greater resilient moduli of flexible base than pavement section A. This finding confirmed that pavement section B had a better supporting layer than pavement section A. The finding was also consistent with the conclusion from the laboratory characterization that base material B had a better quality than base material A.

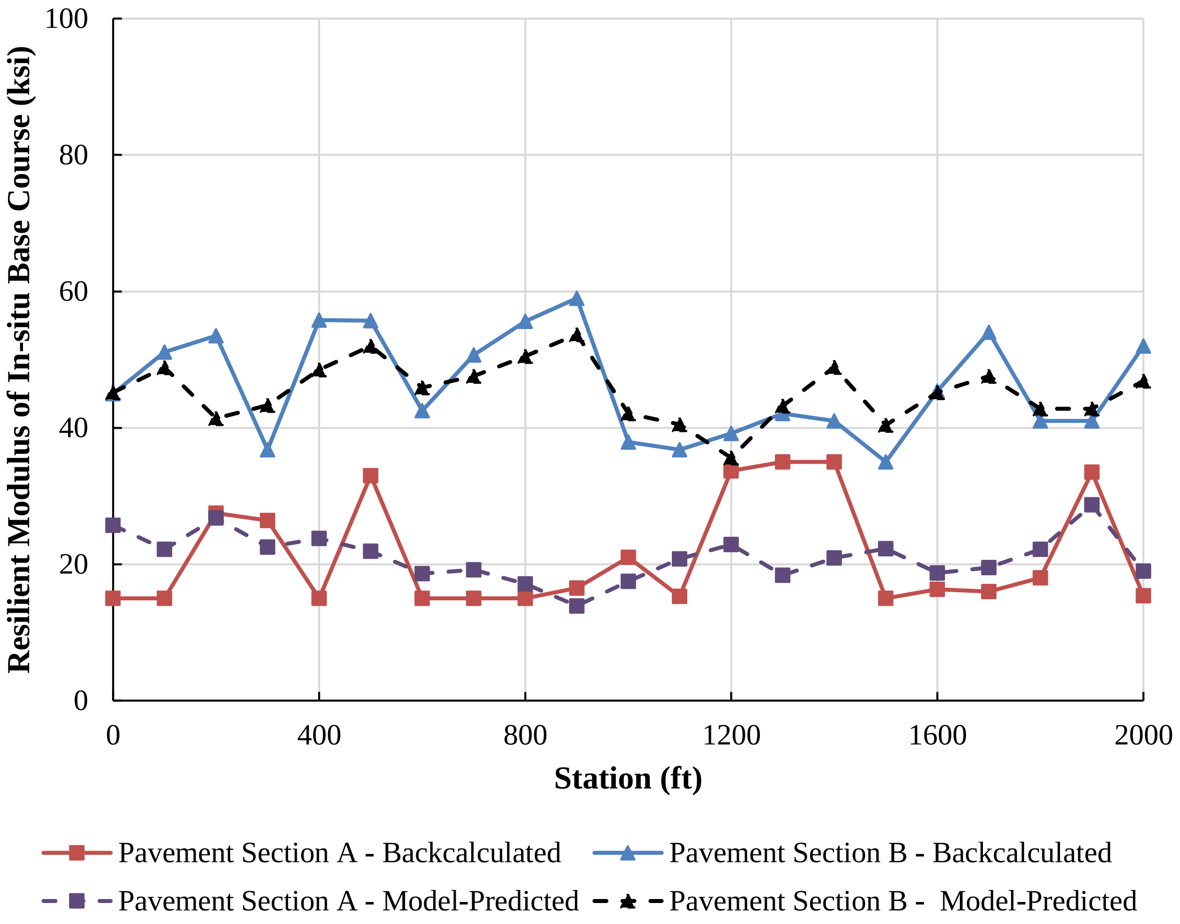

Figure 36. Comparison of Resilient Moduli of Flexible Base between Model Predictions and FWD Backcalculations.

Case Study: State Highway 24

The investigated field section SH 24 was located in Delta County, Texas, as shown in Figure 37. The data was collected using an air-coupled GPR system mounted on a van. The ambient temperature during data collection was 90°F. There was no rainfall prior to the survey. The total length of the project is 6.43 miles, including 6.19 miles of roadway and 0.24 miles of bridge. The data analyzed in this study were taken from the westbound lane of the construction site. The data was collected for a length of 4.5 miles from the beginning section of the project. The PI of flexible base was 3.2. The optimum moisture content was 6.9 percent, and the maximum dry unit weight was 137.3 lb/ft^3.

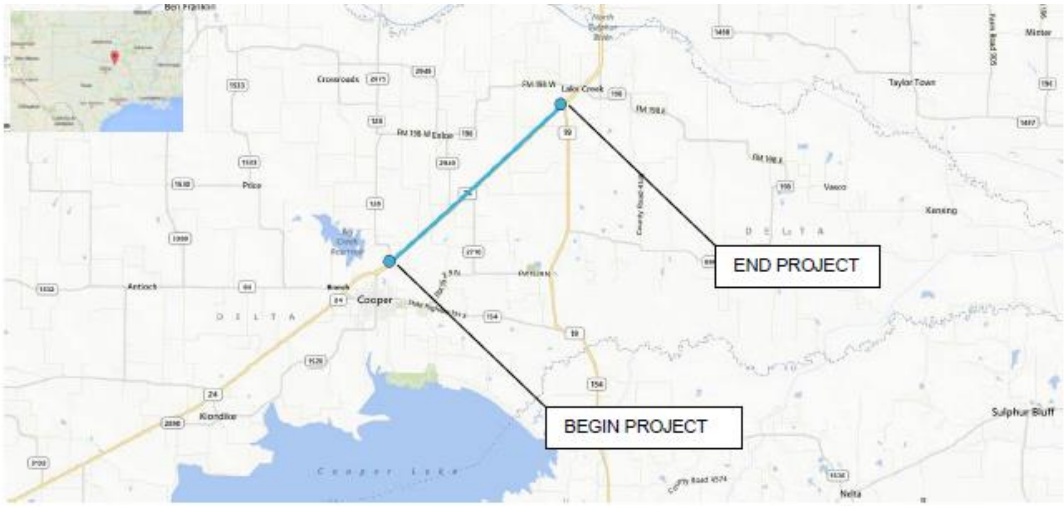

Figure 37. Location of Construction Project in SH 24.

The measured data were analyzed in the following order: (a) refine the dielectric constant profile from the radar survey using the Pavecheck software; (b) input the dielectric constant measurements to estimate the moisture content and matric suction of flexible base based on the data generated the SWCC and SDCC; and (c) input the moisture content and matric suction to LayerMAPP software to generate the dry unit weight profile and resilient modulus profile of flexible base. The relevant outputs are presented in Figures 38–41. Figure 40 shows the dry density profile of flexible base. The low-density zone and the sharp density change zone were identified as the weak spots in the construction. In this section, the weak spots were identified as the red shaded zone. Figure 41 compares the model-predicted resilient moduli of flexible base to those backcalculated from the FWD data. Generally, the model predictions agree well with the backcalculated results. These results validated the proposed mechanistic-based NDT approach again.

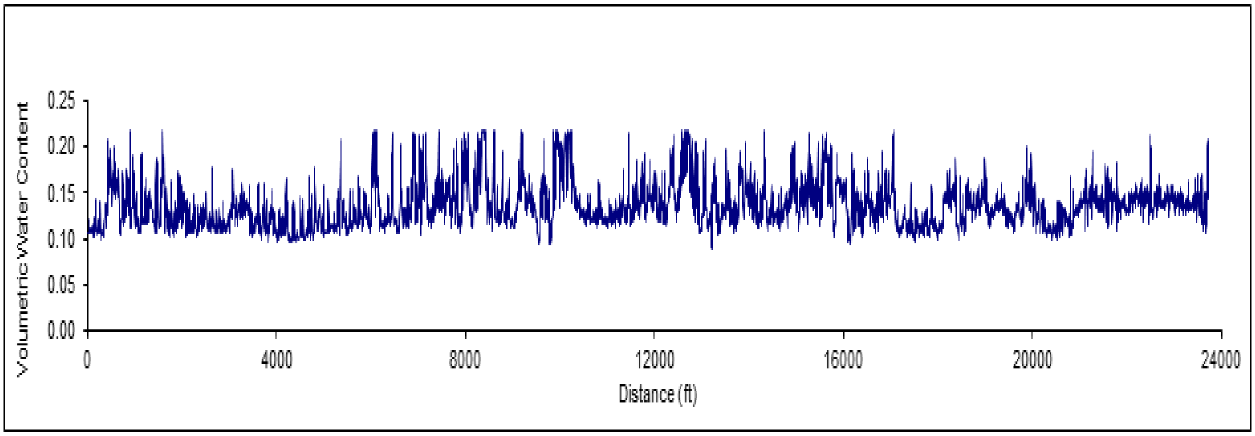

Figure 38. Volumetric Water Content Profile of Flexible Base.

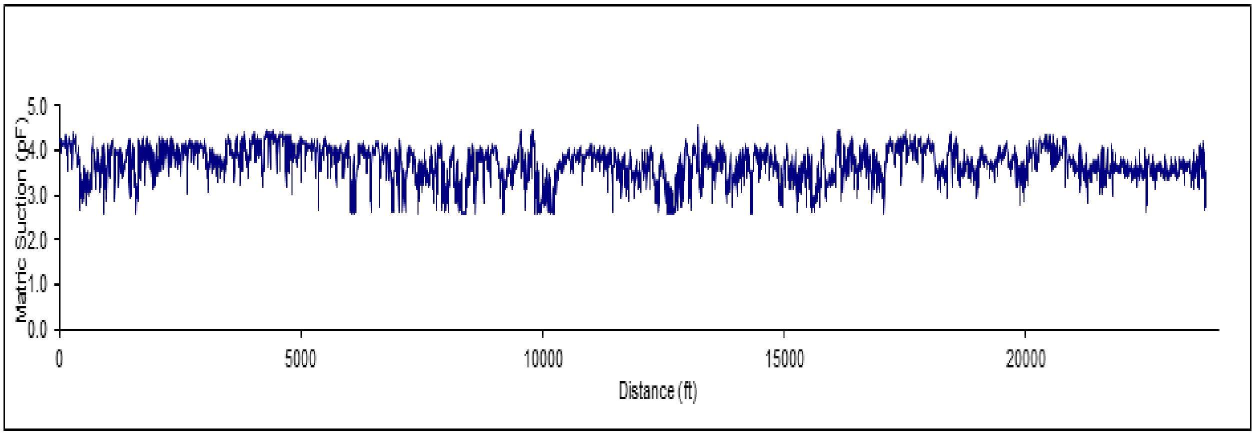

Figure 39. Matric Suction Profile of Flexible Base.

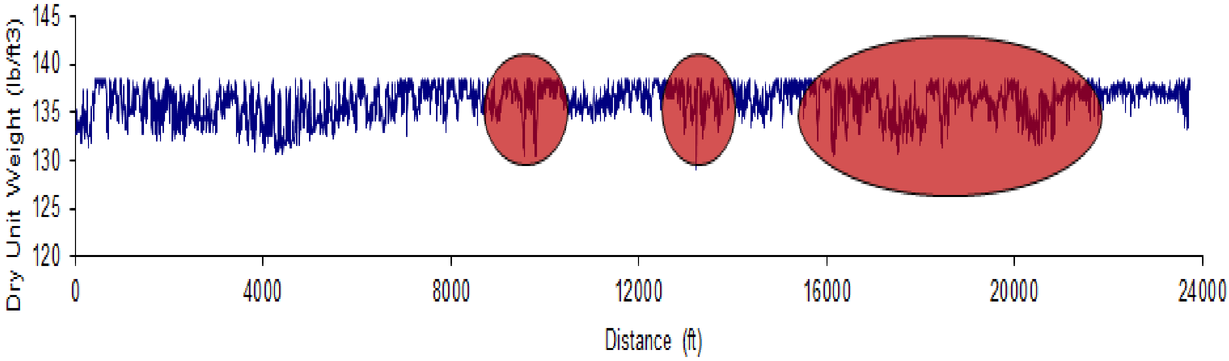

Figure 40. Dry Unit Weight Profile of Flexible Base.

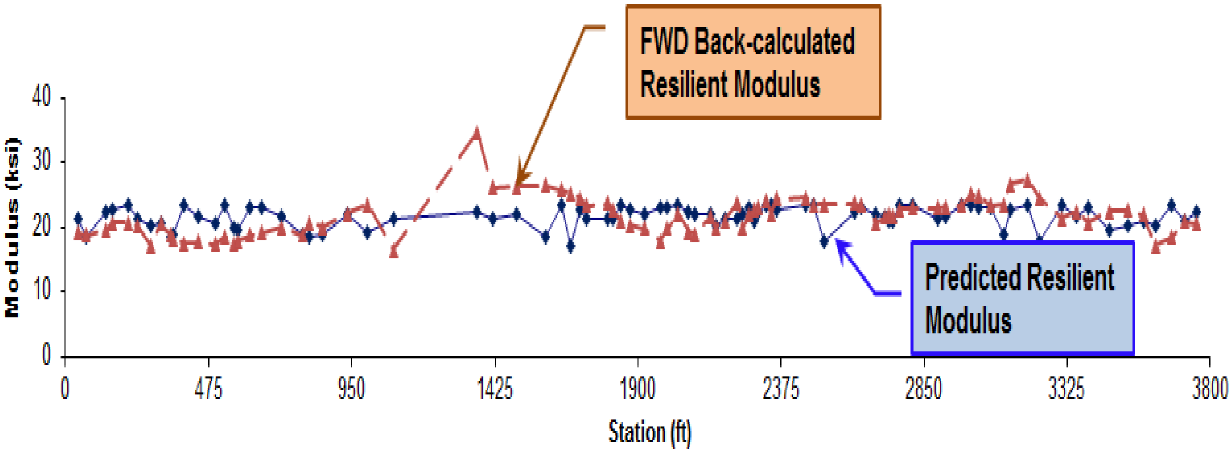

Figure 41. Resilient Modulus Profile of Flexible Base.

CONCLUSION

Conclusions

This project demonstrated proof of concept for a quick, accurate, and simple method for determining reliable values of the in-place-as-compacted base course modulus, dry density, and permanent deformation properties. The mechanistic-based models are provided to characterize the performance properties of unbound base aggregate for a variety of environmental conditions. The major contributions of this study are summarized as follows:

- A new resilient modulus model was developed to consider the stress dependence and moisture sensitivity of flexible base. The degree of saturation and the matric suction are incorporated in the model to discriminate the effect of moisture variations. The model was validated by comparing the predicted and measured resilient moduli of three selected materials with different moisture contents. Compared to the MEPDG model, the proposed model is better characterizing the moisture dependence of unbound aggregates. It was shown that the matric suction of flexible base is a key element that reflects the moisture dependence of the resilient modulus.
- A new permanent deformation model was developed to consider the stress dependence of flexible base by incorporating the two terms $\sqrt{J_2}$ and $\alpha I_1 + K$ into the Tseng-Lytton model. This modification is based on the concept of Drucker-Prager plastic yield criterion, which considers $\sqrt{J_2}$ as a softening term and $\alpha I_1 + K$ as a hardening term for flexible base.
- New prediction models were developed to predict the coefficients of the SWCC model using the MBV and the PFC of flexible base. Compared to the previous prediction model using PI and percent of fine aggregates passing sieve No. 200, the new indicators, such as MBV and PFC, are more reliable and repeatable.
- An SDCC was developed to characterize the relationship between the soil suction and the dielectric constant. The MBV and the PFC are used to estimate the coefficients of the SDCC model. The use of SDCC is efficient to establish the relation between the GPR measurements and the mechanical performance of the flexible base.
- A multiple regression analysis was performed to develop the prediction models for the coefficients of the resilient modulus model, the permanent deformation model, and the dry density model using a set of performance-related base course properties. The dry density, shape, angularity, and texture of the aggregates and the PFC were demonstrated to be significant variables in the prediction models. The proposed performance-related base course properties are more accurate, repeatable, and reliable than the simple empirical parameters. The tests needed to determine these performance-related base course properties are simpler and more efficient than the RLT test. The developed prediction models using the performance-related properties have higher R-squared values than those using the simple empirical parameters.
- A mechanistic-based approach was developed to rapidly evaluate the flexible base construction using the laboratory characterization and non-destruction test method (i.e., GPR). Four critical steps are involved in the approach: (a) laboratory characterization to predict the coefficients of resilient modulus model, (b) laboratory characterization to

generate the SDCC, (c) field GPR measurements to determine the moisture content and matric suction of flexible base, and (d) input of the obtained resilient modulus model coefficients, moisture content, and matric suction into the nonlinear finite element program to compute the resilient modulus of in-situ flexible base. The proposed mechanistic-based NDT approach was demonstrated on three field projects. The model-predicted resilient moduli of in-situ flexible base were in good agreement with those backcalculated from the FWD data. This comparison validates that the proposed mechanistic-based NDT approach is a promising tool for rapid QC and QA of the flexible base construction.

Recommendations for Future Work

This project focues on the development of the mechanistic-based NDT approach to evaluate the flexible base construction. The model has been validated by comparing the model predictions with the field test measurements. To further the technology readiness of the approach demonstrated, the following future work is needed:

- Upgrade LayerMAPP to accurately predict performance properties of base material:
    - Develop a new, internal, finite element program to take into account the cross-anisotropy nature of base material.
    - Develop a new solution for wet condition of base layer using the Thornthwaite Moisture Index and the relationship between matric suction and moisture content.
    - Extend the LayerMAPP software to predict the performance properties of stabilized material.
    - Program subroutines to make LayerMAPP software compatible with both the GPR output and the TxME Design software input.
    - Design a user-friendly interface for LayerMAPP.
- Extend mechanistic-based models to employ commercial GPR systems:
    - Identify the commercial GPR systems that are available in the United States.
    - Deploy the selected commercial GPR system on validation projects to evaluate the influence of operating frequency and system used on calibration and accuracy of mechanistic-based models.
    - Develop solutions for any bias or variations in results introduced by different GPR systems.
- Calibrate mechanistic-based models for stabilized base materials:
    - Develop a test procedure to measure the suction-water characteristic curve for stabilized material.
    - Develop a new dielectric constant-suction curve and a conductivity-lime content curve for stabilized material.
    - Perform the laboratory tests to fully characterize the material properties of stabilized material.

- Use mechanistic-based models with the laboratory test results to predict resilient modulus and permanent deformation of the stabilized base materials.
- Perform the GPR scanning on two field projects to determine the dielectric constant and conductivity of the in-situ stabilized base layers.
- Use the mechanistic-based models with the upgraded LayerMAPP to predict the performance properties and stabilizer content of stabilized base material from the field NDT.
- Select at least 30 points from along the GPR line profiles and test those points with the FWD’s load zone program to obtain reference values for resilient modulus.
- Calibrate the mechanistic-based model for stabilized materials to minimize the prediction error from the data generated on the demonstration projects.

CHAPTER 2. COMPACTION MONITORING FOR QUALITY CONTROL DURING ASPHALT MIXTURE CONSTRUCTION

BACKGROUND

Construction variability and isolated defects can be the limiting factors in a pavement's life. One technology allowing for minimal traffic disruption, increased level of testing coverage, and potential for increased pavement life is rapid quality measurement during asphalt mixture compaction and roller-based testing in order to quantify roller compaction effort applied and evaluate final in-place density.

Figure 42 illustrates the initial compaction monitoring system (CMS) concept in this project. The overall concept stayed functionally the same during the course of the project, with some modification as the research progressed.

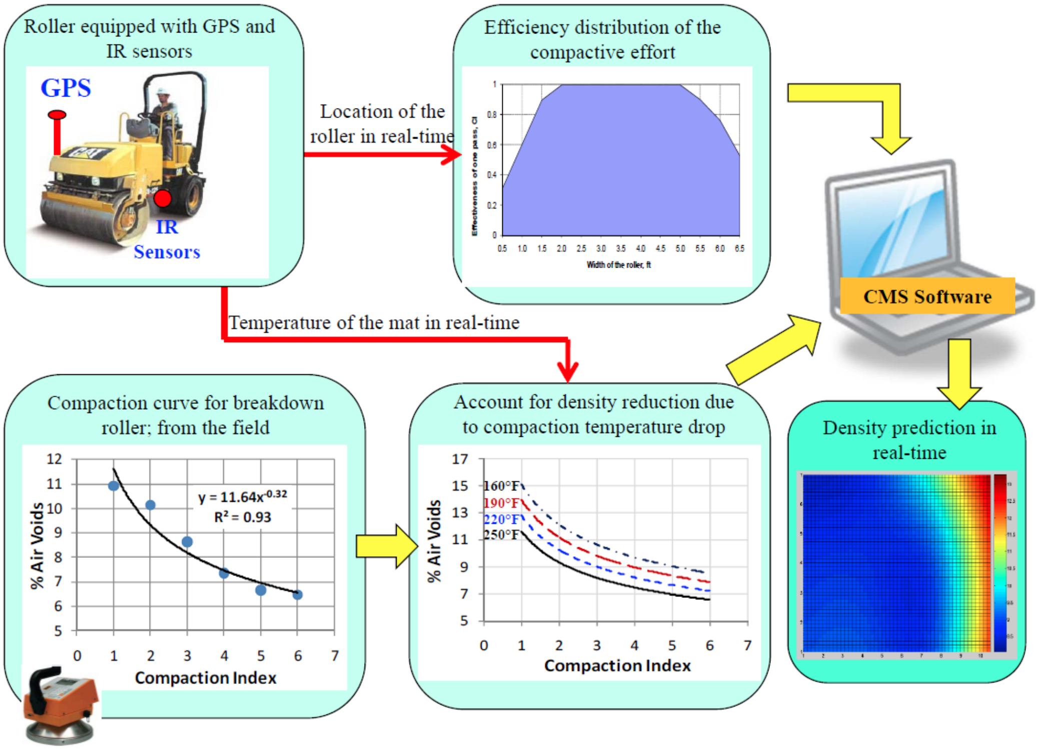
Roller equipped with GPS and IR sensors
GPS
IR
Sensors
Location of the roller in real-time
Efficiency distribution of the compactive effort
Effectiveness of one pass, Ci
Width of the roller, ft
CMS Software
Temperature of the mat in real-time
Compaction curve for breakdown roller; from the field
% Air Voids
Compaction Index
y = 11.64x^-0.32
R² = 0.93
Account for density reduction due to compaction temperature drop
160°F
190°F
220°F
250°F
% Air Voids
Compaction Index
Density prediction in real-time

Figure 42. Initial Proposed Block Diagram of CMS.

An additional effort to integrate laboratory measurements into the process was undertaken during this project. This effort took the form of a laboratory compaction index (LCI). The LCI is obtained from the laboratory compaction curve (the relationship between percent air voids and number of gyrations, or in the case of the linear kneading compactor, number of passes) to the point of reaching the prescribed air void content.

A preliminary relationship was developed between the laboratory and field compaction indices, as shown in Figure 43.

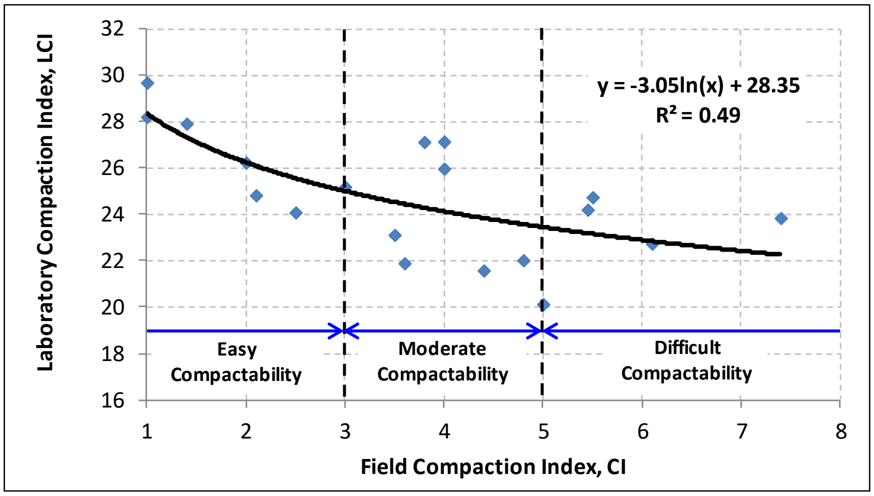

Figure 43. Lab vs. field compaction index (to 8 percent air voids).

It is obvious from Figure 43 that the correlation between laboratory and field indices was not particularly well defined when the preliminary relationship was developed. However, there does seem to be some visual indication that the lab and field may be related by some nonlinear function.

The compaction index is similar in concept to optimum moisture density in soils and considers factors such as temperature, compactor drum efficiency, and type of compaction being done (e.g., is the vibration turned on or off?). Other factors that are not currently fully implemented include subgrade support, type of energy input (e.g., type/magnitude/frequency of vibration, type/magnitude of "static" load, ground contact characteristics), lift thickness/stone skeleton characteristics, and roller pattern prediction versus roller pattern assurance.

The first CMS was based on the Windows operating system, and this device is referred to as the PC version. An additional system was developed that is based on a different type of operating system and is referred to as the PLC version. A summary of the differences between the two systems is shown in Table 3..

Table 3. Comparison of PC and PLC platforms.

Feature	PC	PLC
User Interface	Windows standard	Gauge & button pictorial HMI
Programming	C++, LabVIEW	Ladder
Index	Numerical rating	Normalized to 100%
Pass Map	Pixel address based	X-Y plot based (later bitmap)
Hardware primary voltage	12 VDC	24 VDC
Battery	Sealed lead acid (later Li-ion)	Li-ion
Display	Touchscreen	
External sensors (T, GPS, Vibrate)	Same	

PROCEDURES

Compactor Characteristics

Compactors are available in several different configurations, some of which perform the densification process differently from others. Most compactors can be operated statically (i.e., rolling but just operating with the static weight of the vehicle) or by vibration. The vibration is typically applied by using an eccentric weight arrangement inside the drum assembly, and this arrangement generally applies a vertical impact load on the mat while traveling. The effect of the impacts can sometimes be seen with the naked eye, especially at night under lights, and with infrared video during day or night. During this project, this type of vibratory compactor was the only type used. Some of the other types of compactors (excluding pneumatic types) are discussed below. These other compactor technologies shown in Figures 44-46 are documented here because some of the features of these compactors have the potential to improve overall compaction process efficiency for a wide range of mat types, in particular the thin overlay mix (TOM) type mixtures, and this potential improvement may eventually need to be factored into the CMS algorithm. With the three technologies noted below, the potential is there to reduce the negative effects of vertical impact vibration (e.g., negative effects that may even include the drum coming completely off the mat on the upward stroke of the impact cycle).

"Tangential" Compaction (Bomag)

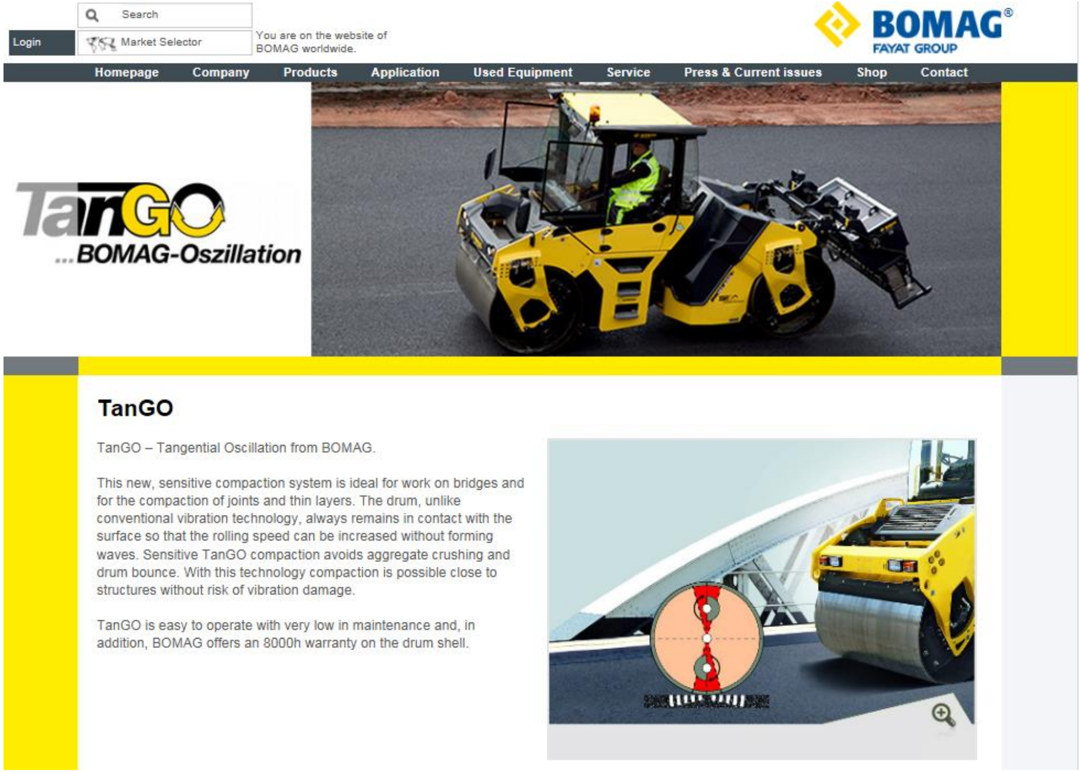

TanGO

TanGO – Tangential Oscillation from BOMAG.

This new, sensitive compaction system is ideal for work on bridges and for the compaction of joints and thin layers. The drum, unlike conventional vibration technology, always remains in contact with the surface so that the rolling speed can be increased without forming waves. Sensitive TanGO compaction avoids aggregate crushing and drum bounce. With this technology compaction is possible close to structures without risk of vibration damage.

TanGO is easy to operate with very low in maintenance and, in addition, BOMAG offers an 8000h warranty on the drum shell.

Figure 44. Bomag approach to reducing negative effects of standard vertical impact vibration (from the Bomag website).

“Oscillation” Compaction (Hamm)

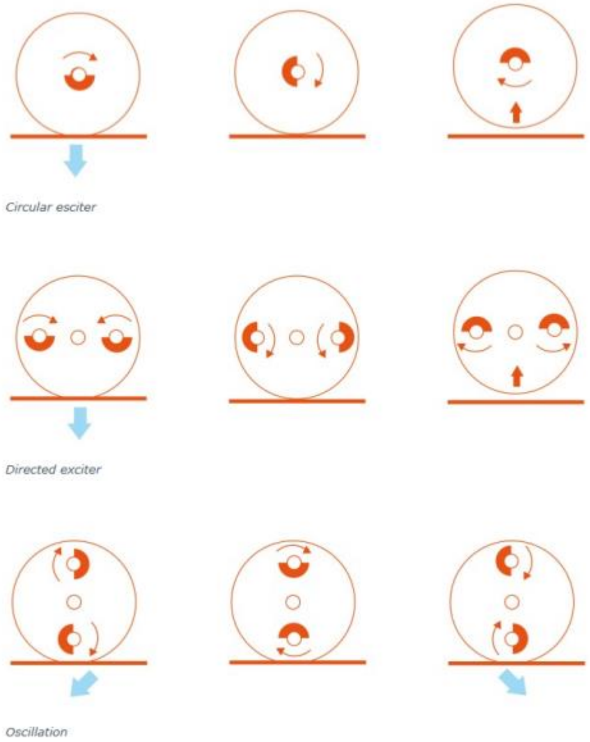

Figure 45. The Hamm oscillation approach to reducing negative effects of standard vertical impact vibration (from the Hamm AG website).

“Belt” Compaction (AMIR)

The AMIR device shown in Figure 46 is a machine originally developed in Canada (A. O. Abd El Halim, Carleton University, Ottawa). A version of this compactor has also been used in Australia. One of its purposes is to decrease roller checking, but recent versions have been used with success for all phases of compaction, and there has been recent emphasis for using it to decrease permeability of asphalt. In general, it has lower ground contact pressure and also retains heat better because of the belt system.

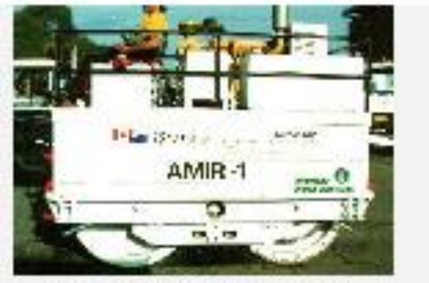

Asphalt Multi-Integrated Roller (AMIR)

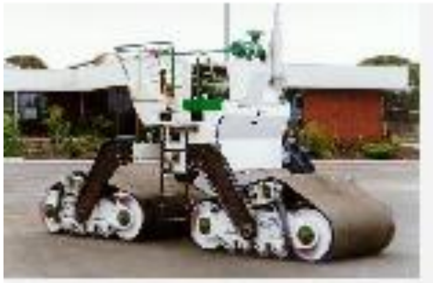

Hot Iron Process Asphalt Compaction (HIPAC)

Figure 46. Belt type rollers (from the Internet).

Steel Drum Efficiency

As noted in Figure 42, experimental observations indicated that the efficiency of the compaction across the width of the drum on the compactor was not constant. This was further investigated with linear elastic finite element (LEFM) analysis. Because the mat is not truly linear elastic, the results require some qualitative interpretation to suggest factors that may alter the LEFM analysis to compare more favorably to the experimental observations. Nonlinear analyses including slip elements, nonlinear material properties, stress-dependent material properties, dynamic loading, and heat transfer elements were beyond the scope of this phase of this project. The LEFM mesh is shown in Figure 47. The pavement was a two-layer system with a crown. Pavement material properties were typical for the conditions being modeled. The compactor drum was treated as a rigid body, and boundary conditions included an elastic (spring) foundation, rollers at the far edge of the pavement in the upper left of the figure, traction-free boundaries elsewhere, and the load of the drum. Figure 48 illustrates the deflections under the drum. These deflections are only the X component of the total deflections, and the X-axis is parallel to the line of contact of the drum (i.e., it is perpendicular to the travel direction of the roller). The blue and red areas indicate areas of maximum and minimum deflection, and in this case, they are of opposite signs. This deflection indicates that the pavement material wants to move out away from the edges of the drum along the X-axis (it also wants to move up in front and behind the drum). Somewhere (the location is dependent on boundary conditions, material properties, and structure among other factors) along the line of contact between the drum and the hot mix, there is negligible horizontal movement. The horizontal (i.e., X-axis) movement was chosen for this illustration because it is related to Poisson’s ratio and/or dilation, and discussions of stress-dependent behavior can proceed from that point. The upper right empirical distribution curve shown in Figure 42 might be explained in part by this behavior. One possible way of explaining the empirical distribution is that the material is more confined in the middle part of the drum, leading to more efficient compaction in that area, while the material at the edges of the drum is trying to get out of the way of the high shear stresses and vertical loading of the drum. This feature also explains why there may be differences at the edge of the pavement—there is basically nothing to keep the material from moving perpendicular to the rolling direction at a free edge unless it is a curbed pavement operation in which the curb stops the horizontal movement (i.e., it effectively introduces a fixed or roller boundary condition on that edge).

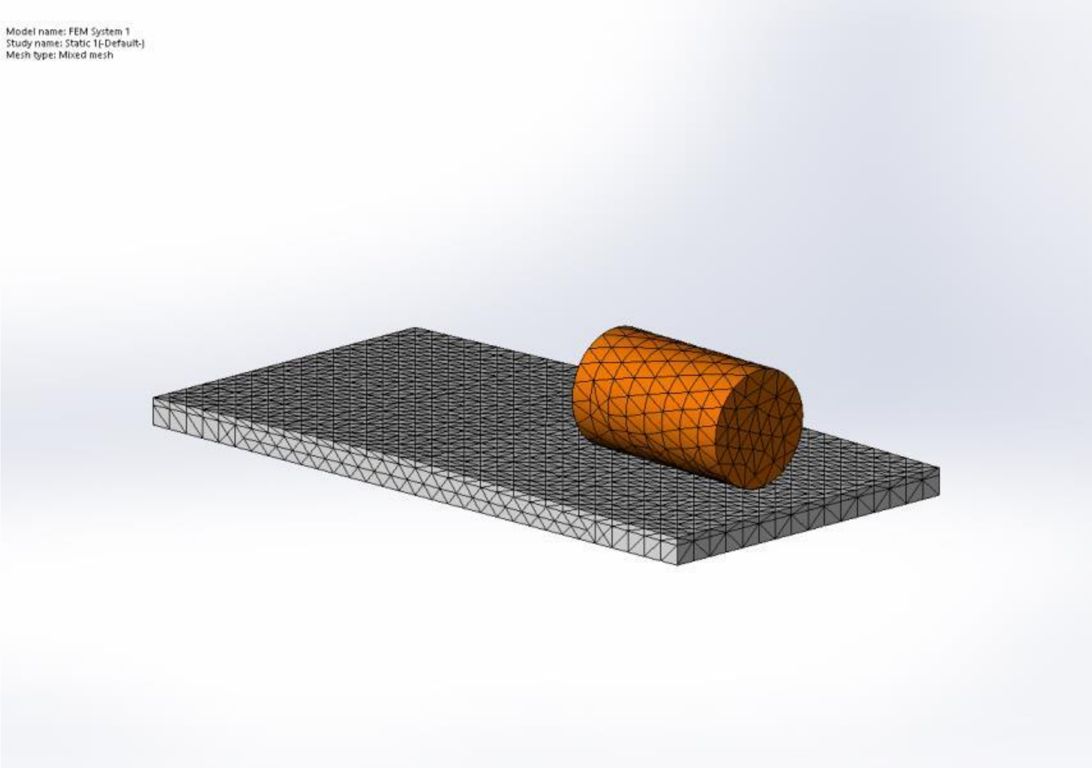

Figure 47. Finite element mesh (full-scale roller drum).

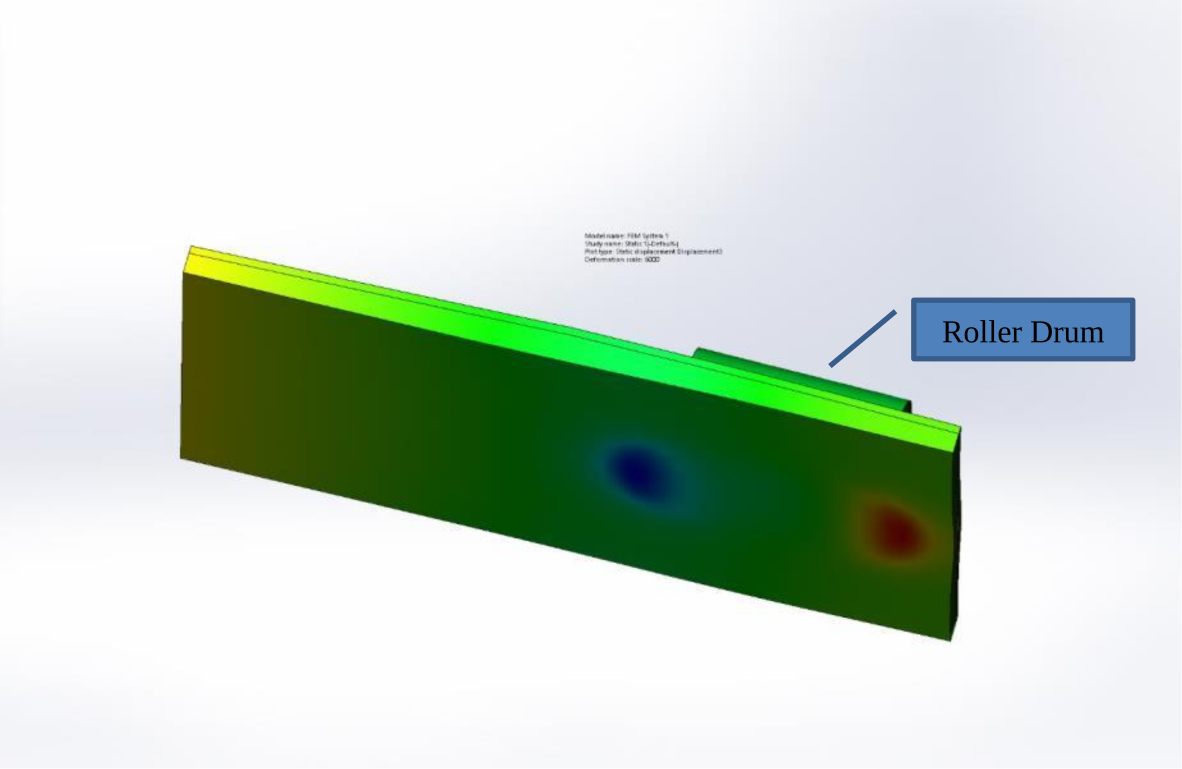
Model name: FEM System 1
Study name: Static 1(-Default-)
Plot type: Static displacement Displacement3
Roller Drum

Figure 48. Deflection results at bottom of pavement model.

“Intelligent” Compaction

Compactor manufacturers have various methods of trying to quantify how the mat progresses from plant mix to in-service pavement. A summary of the computational methods used by some of the manufacturers is given in Table 4. Note that the computations are not all the same, and acquiring data and generating the parameter is functionally proprietary with each manufacturer. Since there does not appear to be a universally accepted approach, nor a clear winner in the intelligent compaction race at this point, the CMS system does not include a stated objective of “intelligent compaction.”

Table 4. An incomplete listing of various approaches to intelligent compaction (Brandon Crockett—Sakai).

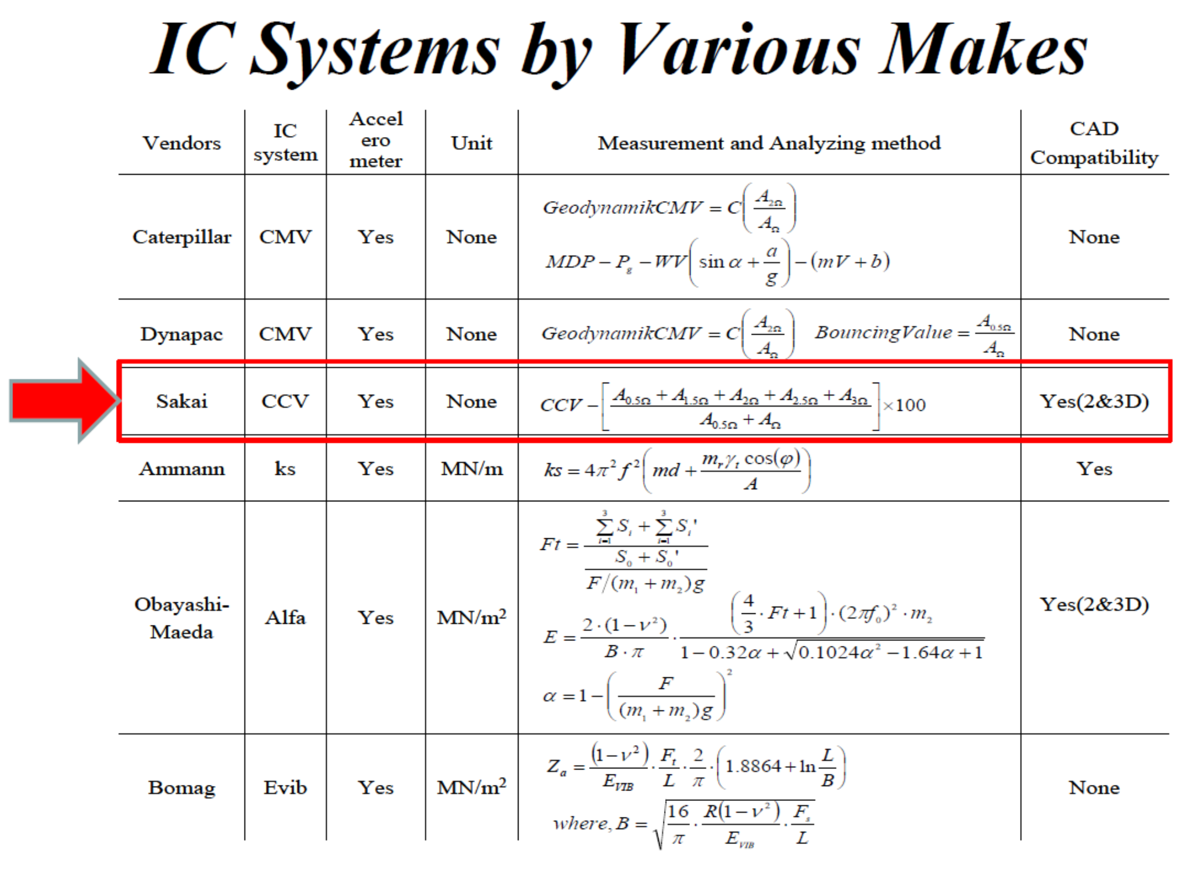

IC Systems by Various Makes

Vendors	IC system	Accel ero meter	Unit	Measurement and Analyzing method	CAD Compatibility
Caterpillar	CMV	Yes	None	$GeodynamikCMV = C\left(\frac{A_{2\Omega}}{A_{\Omega}}\right)$ $MDP - P_g - WV\left(\sin\alpha + \frac{a}{g}\right) - (mV + b)$	None
Dynapac	CMV	Yes	None	$GeodynamikCMV = C\left(\frac{A_{2\Omega}}{A_{\Omega}}\right)$ $BouncingValue = \frac{A_{0.5\Omega}}{A_{\Omega}}$	None
Sakai	CCV	Yes	None	$CCV - \left[\frac{A_{0.5\Omega} + A_{1.5\Omega} + A_{2\Omega} + A_{2.5\Omega} + A_{3\Omega}}{A_{0.5\Omega} + A_{\Omega}}\right] \times 100$	Yes(2&3D)
Ammann	ks	Yes	MN/m	$ks = 4\pi^2 f^2\left(md + \frac{m_r \gamma_t \cos(\varphi)}{A}\right)$	Yes
Obayashi-Maeda	Alfa	Yes	MN/m²	$Ft = \frac{\frac{\sum_{i=1}^{3} S_i + \sum_{i=1}^{3} S_i'}{S_0 + S_0'}}{F/(m_1 + m_2)g}$ $E = \frac{2\cdot(1-\nu^2)}{B\cdot\pi}\cdot\frac{\left(\frac{4}{3}\cdot Ft + 1\right)\cdot(2\pi f_0)^2\cdot m_2}{1 - 0.32\alpha + \sqrt{0.1024\alpha^2 - 1.64\alpha + 1}}$ $\alpha = 1 - \left(\frac{F}{(m_1 + m_2)g}\right)^2$	Yes(2&3D)
Bomag	Evib	Yes	MN/m²	$Z_a = \frac{(1-\nu^2)}{E_{VIB}}\cdot\frac{F_t}{L}\cdot\frac{2}{\pi}\cdot\left(1.8864 + \ln\frac{L}{B}\right)$ $where, B = \sqrt{\frac{16}{\pi}\cdot\frac{R(1-\nu^2)}{E_{VIB}}\cdot\frac{F_s}{L}}$	None

PC (Personal Computer/Laptop) System

The PC-based CMS consists of a Global Positioning System (GPS) unit mounted on the roller to track the location of the roller on the mat. Temperature sensors are attached to the sides of the roller to record the mat surface temperature. In addition, an accelerometer sensor is mounted on the roller to determine the mode of operation—static or vibratory. The CMS monitors the location of the roller on the mat and number of passes across the mat. Each pass is multiplied by the effectiveness factors across the roller's width (Figure 49) in order to produce the Compaction Index (CI) distribution. Such distribution is converted to colored maps in real time. The operators of the roller as well as the QC and inspection staff at the site are able to see the colored map on a screen during the compaction. The operator can use the colored maps to adjust the compaction patterns (by changing number of passes, overlapping, and overhanging) to achieve a uniform CI in order to obtain the required density uniformly across the mat. In addition, these maps can be converted to predict density distribution if the compaction curves for each compaction method are already known.

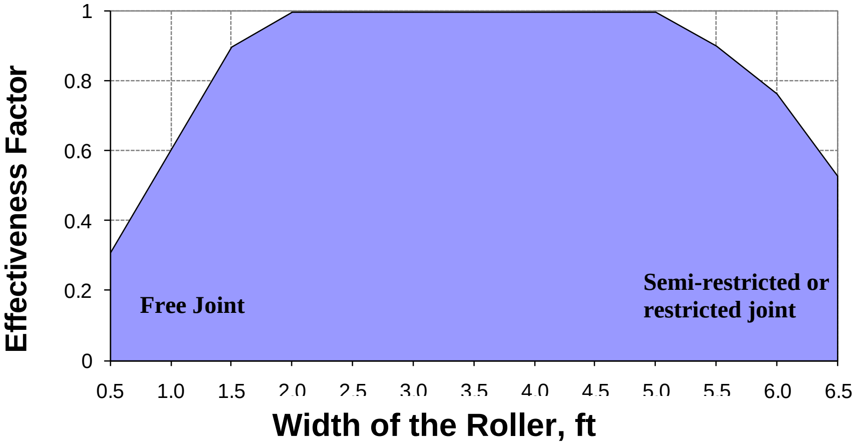

Figure 49. Efficiency distribution of the compaction effort across roller width.

The operational system is shown in Figure 50. Post-processing the CMS data produces color-coded maps showing:

- The number of roller passes on the entire mat.
- The compaction effectiveness (number of passes * effectiveness factor).
- The temperature of the mat on the first pass of the roller.

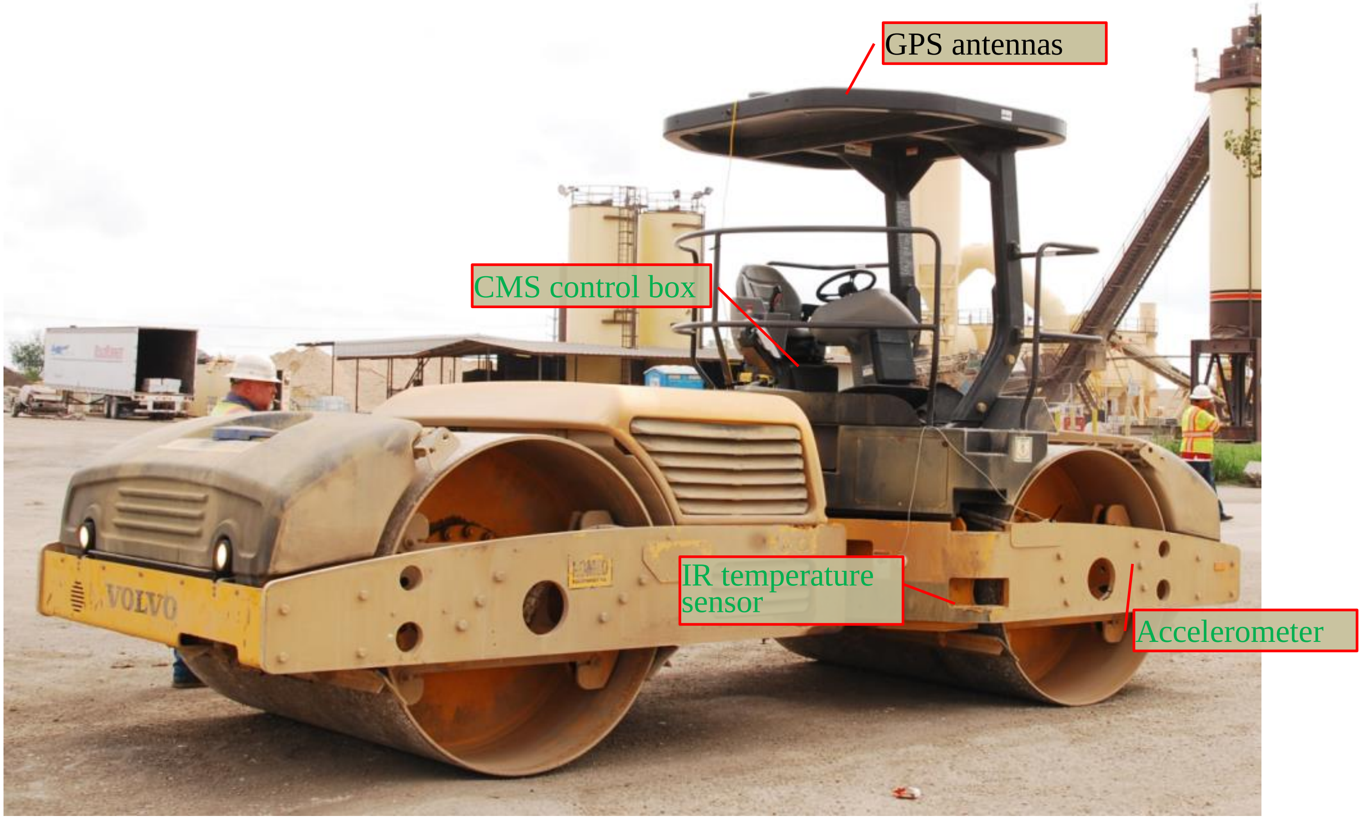

Figure 50. TTI's CMS.

System Update

From the initial version of the CMS, this project performed many hardware and software updates including:

- Hardware update:
  - Update the battery from a seal acid battery to a Lithium long life battery.
  - Update the computer from a Panasonic Toughbook to a Microsoft Surface laptop computer.
  - Add a voltage meter for real-time monitoring the battery condition.
  - Remove the internal battery of the GPS control unit.
  - Put the GPS control unit inside the package box for better integration.
  - Re-build the CMS package box and re-wire the unit for better performance.
- Software update:
  - Add a new function showing the core location on the final result.
  - Change the software toolbar buttons and remove some un-necessary buttons.
  - Refine the pavement cross-section compaction chart.
  - Show the temperature change for each compaction and the temperature drop rate for one location.

  - Add a feature showing the raw accelerometer data and fast Fourier transform (FFT) output data.
  - Change the accelerometer data-acquisition rate to 1024 Hz to improve FFT calculation.

Hardware update-1: Lithium Battery is used. The change to dual lithium batteries established a total capacity of 44 Ah for a run time of more than 10 hours. The benefits of a Lithium battery are:

- Less charge time.
- Significantly reduced weight.
- Lithium maintains their voltage throughout the entire discharge cycle.
- Charge cycle life is 10 times that of the lead-acid battery.

Hardware update-2: Laptop computer update. A Toughbook was replaced with a Surface for the following advantages:

- 12-inch Full HD touchscreen display.
- Windows 10 Pro operating system.
- Intel i7 4th Gen CPU.
- Docking station that acvepts 12 VDC directly from battery.

Figure 51 shows the old CMS system, and Figure 52 shows the new updated CMS system. The size and the weight of the package all improved.

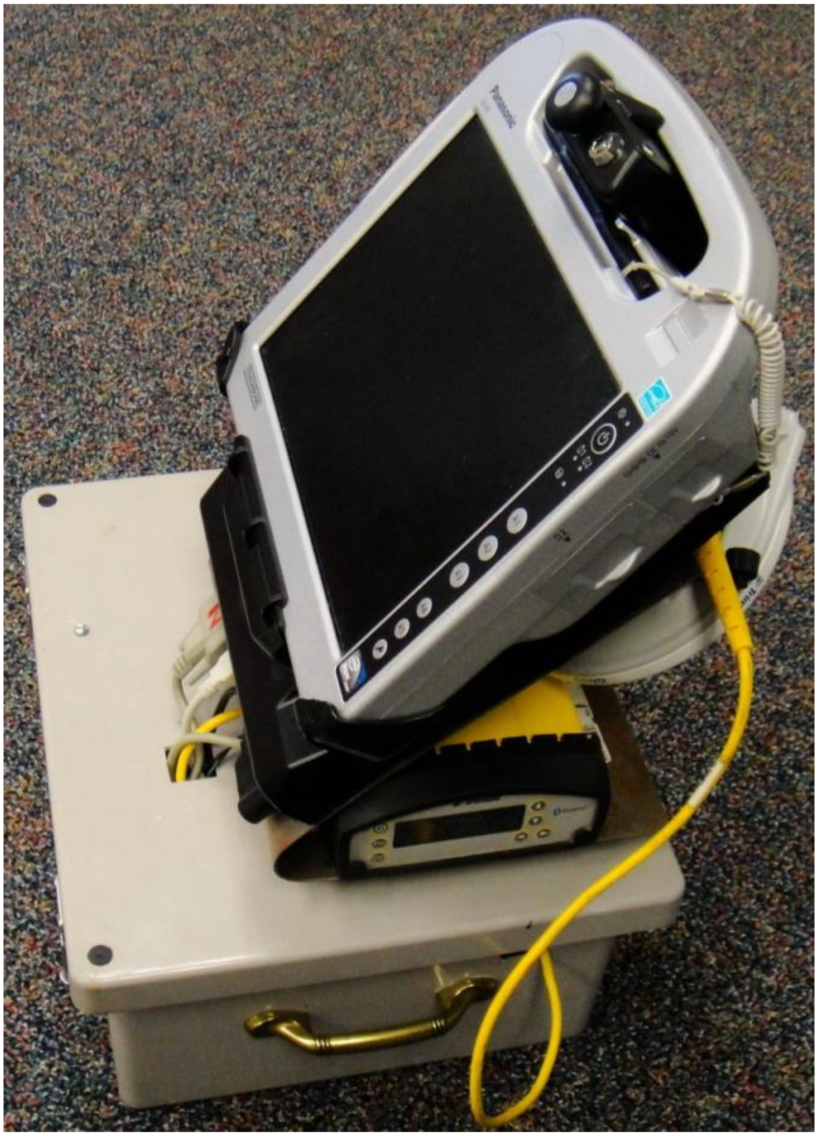

Figure 51. Original CMS.

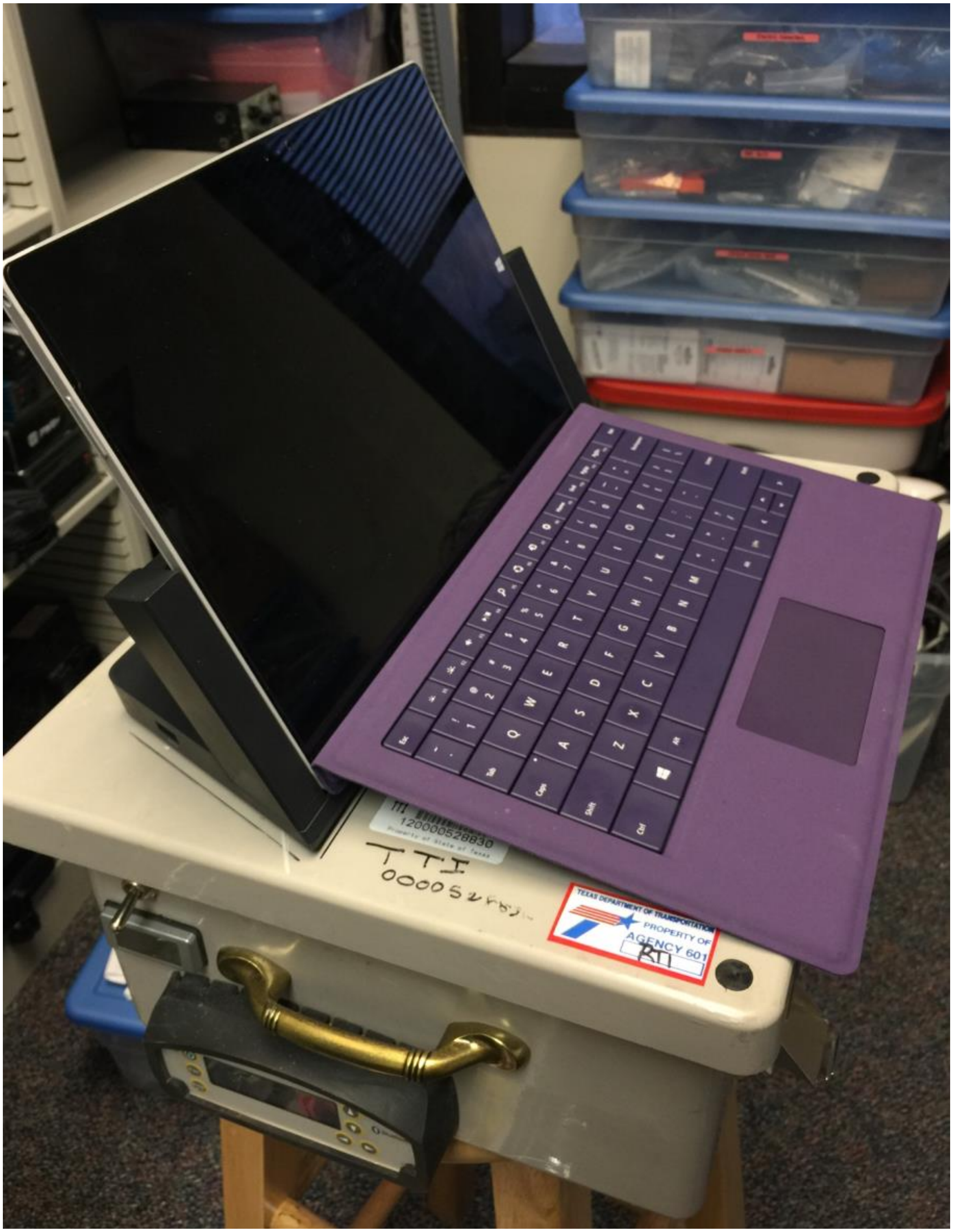

Figure 52. TTI's New CMS.

Hardware update-3: Add voltage meter. A voltage meter for real time monitoring of the battery condition was installed on the CMS. If the battery is fully charged, the initial voltage is around 13.3 V. If the voltage drops to 11.5 V, the operator needs to change the battery. Since the CMS uses two batteries in parallel, a battery can be changed without stopping data collection. Figure 53 shows the CMS control box side view with the voltage meter showing 13.2 VDC.

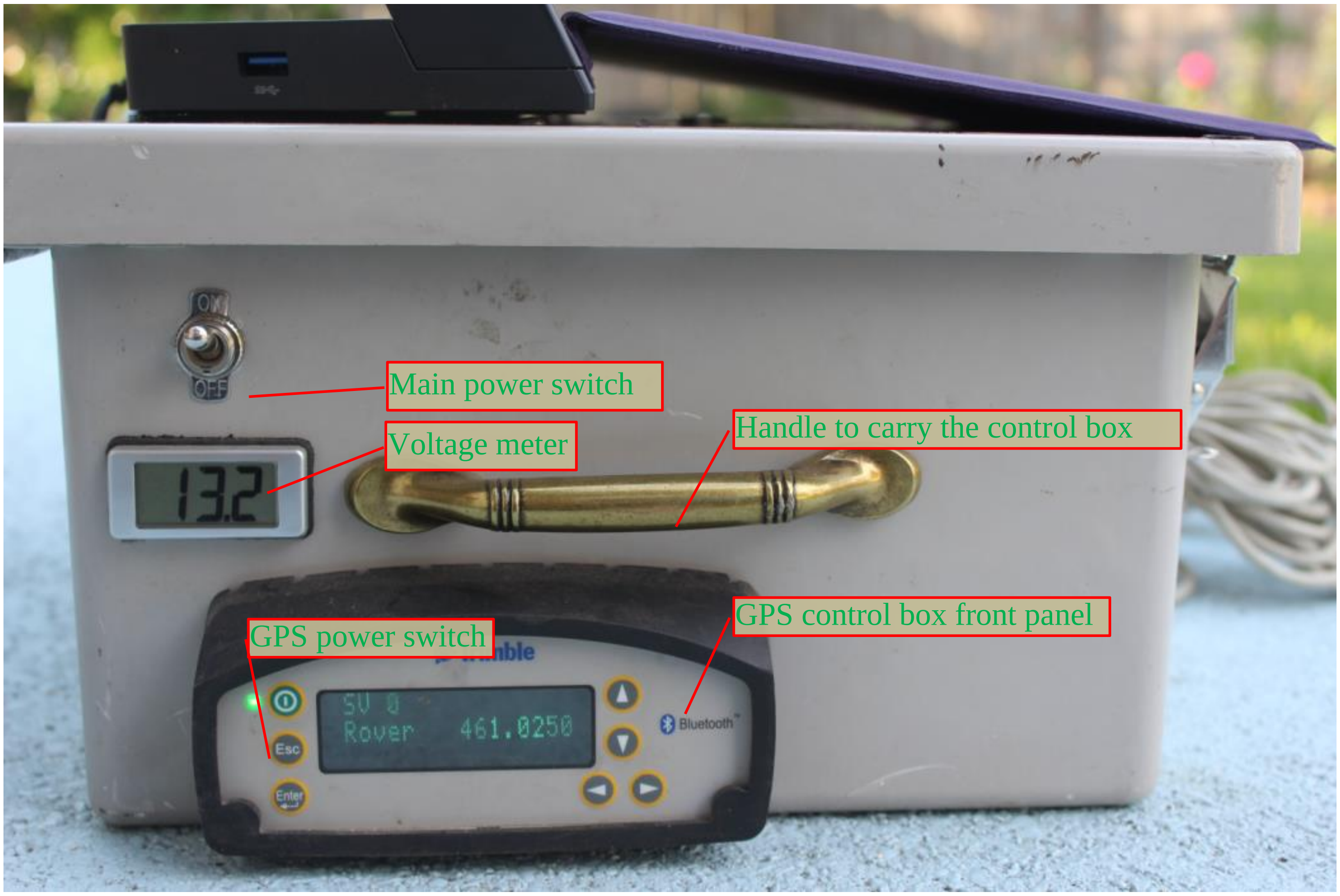
ON
OFF
Main power switch
Voltage meter
13.2
Handle to carry the control box
GPS power switch
Trimble
SV 0
Rover 461.0250
Esc
Enter
Bluetooth
GPS control box front panel

Figure 53. TTI's New CMS Control box side view.

Hardware update-4: Remove the internal battery of the GPS control unit. Inside the Trimble SPS852 GNSS control unit, there is an integrated, internal 7.2 V, 7800 ma-hr Lithium-ion battery. When a field test finishes, the main power is turned off, but the GPS unit is still on, the battery will drain. For this reason, researchers removed the internal GPS battery. This step simplifies the operation of the CMS system. When the main power switch is turned off, the entire system is powered off. Also, this makes the system's power supply more efficient, and the CMS power supply will last longer.

Hardware update-5: Install GPS control unit inside the package box for better integration. Figure 53 shows how the GPS control box is packaged into the box, but the panel still can be accessed for adjusting the GPS setting.

Hardware update-6: Re-build the CMS package box and re-wire the unit for better performance. All the cable and components are re-designed and re-wired for better performance. Figure 54 offers a final inside view of the current PC-based CMS unit, and Figure 55 is an inside view of the original unit.

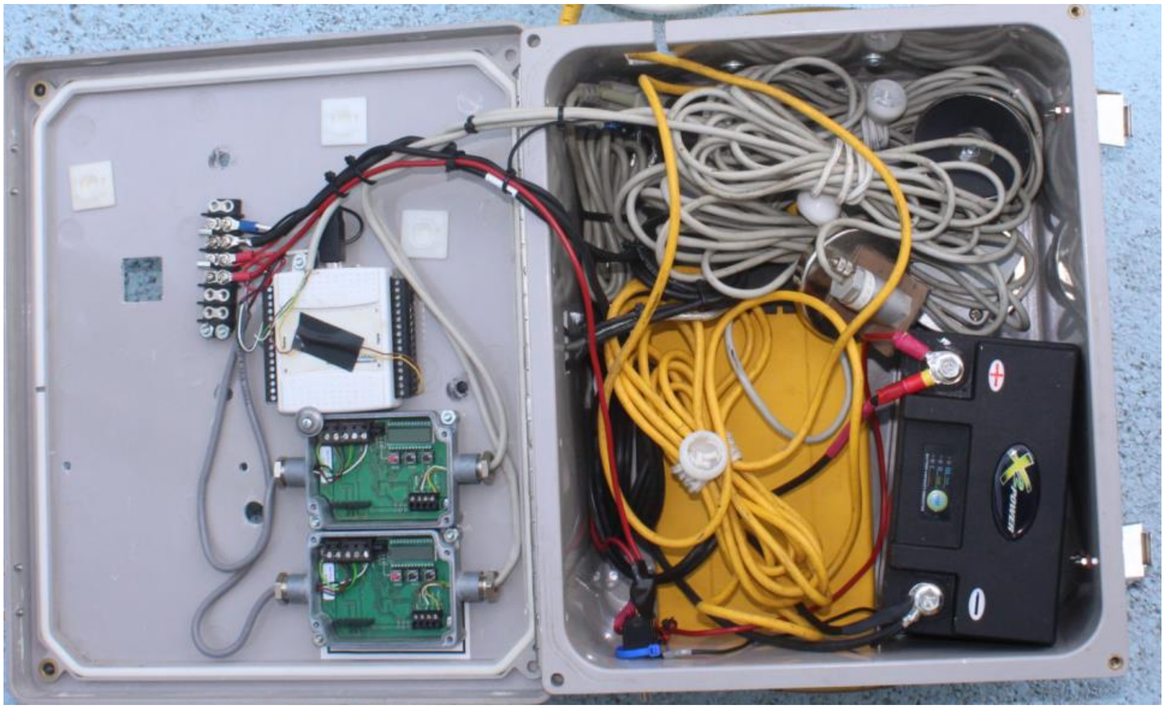

Figure 54. Updated CMS control box, inside view.

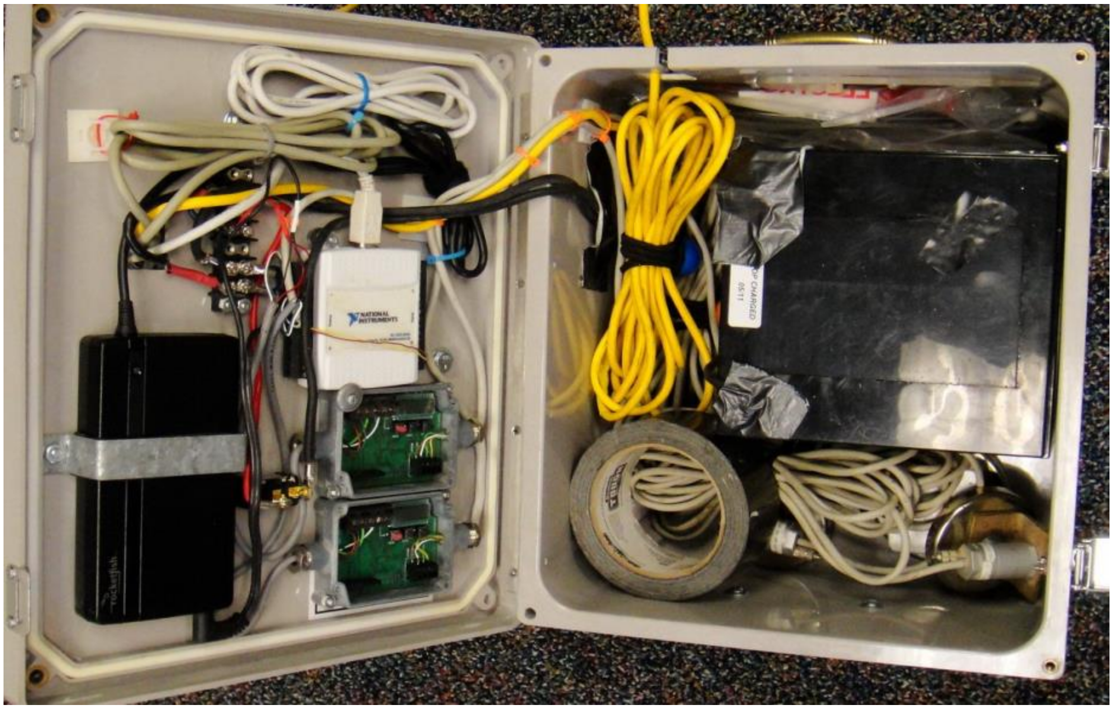

Figure 55. Old CMS control box inside view.

Field Testing

Before the field test trip, the following checklist is useful for the operator in order to make sure all the required items are available:

- Make sure the GPS antenna is inside the package in the CMS system.
- Make sure the computer is included; normally, the computer is separate from the system.
- Fully charge the battery; also bring the correct charger for the Lithium battery.
- Bring duct tape and some fastening device for installing the sensors.
- Bring a multi-meter for checking the system in case something happens.
- Bring a fully-charged extra battery in case the voltage drop too much.

At least a half hour before the paving job starts, the operator should get to the field, meet with the paving team, and make note of basic paving information such as the following:

- The paving lift thickness and paving mix design.
- The number of paving rollers and which one is the breakdown roller.
- The starting and ending paving location.
- The starting and ending paving time.
- The name and phone number of the roller operator.
- The roller model and basic information about the roller.
- The rolling pattern (Static or vibration? If vibration, variable or fixed?).
- The weather condition at the job site—wind speed, temperature.

After this, the operator should plan how to install the CMS to optimize the roller operator's station. Installation should follow the steps outlined below:

- Before installation, make sure the CMS main switch is off.
- Find a place for the CMS control box. It must be stable and secure, not on the engine compartment (because of a heat problem). Use bungee cord or duct tape to fasten the CMS securely.
- Without the laptop installed (docking station is empty), open the CMS control box, take out the two IR sensors, one accelerometer, and GPS antenna (as shown in Figure 56).
- Install the GPS antenna on the roof along the middle line of the roller. If the roller roof is plastic, use duct tape and bungee cord to secure the antenna on the top of the roof.
- Install two IR sensors on both sides of the roller (normally the triangle area on the middle of the roller). This triangle shape is used in order to leave space for the roller to make turns. Make sure the IR sensors' lens point to the ground vertically and the sensors are off the ground about 18 inches. Secure the cable.
- Install the accelerometer inside the drum buffer of the roller if there is frame that does not turn with the drum; make sure the acceleration direction is vertical with the ground. Secure the cable and leave extra cable for the roller to make turns. Figure 57 is an example of an accelerometer installed inside the buffer. In case there is no inside buffer location, the user can select a location where the accelerometer can pick up the roller's vibration.
- Put all the extra cable inside the CMS control box. Close the box and lock it up.

- Put the Microsoft Surface laptop on the docking station.
- Turn on the main power switch of the CMS system; also, turn on the computer. Turn on GPS by pressing the green power button on its control panel (Figure 53).
- Find the CMS field testing software icon on the desktop and start the software.
- Check that the GPS is working.
- Start a project by giving it a file name, and the system will then begin to collect data.
- For night paving, adjust the screen brightness low to save power.
- Check that all the cable and components are secure. Also, take a photo for documentation.
- Generally, for safety reasons, the CMS operator does not disturb the roller driver by climbing on the roller to check the data. However, when the paving job stops while waiting for the asphalt mix to delivered, the CMS operator can ask if he can access the roller to ensure that the CMS is working correctly.
- When the paving job finished, the operator can disassemble the CMS from the roller by following the process outlined below:

    1. Copy the test data to an external USB driver.
    2. Turn off the computer and remove the computer from the docking station.
    3. Turn off the CMS main switch.
    4. Remove the IR sensors and wrap the cable.
    5. Remove the accelerometer and wrap the cable.
    6. Remove the GPS antenna from the top of the roller and wrap the cable.
    7. Open the top cover of the CMS control box.
    8. Put the IR sensor, accelerometer, and GPS back into the box.
    9. Close the top cover, and disassembly is complete.

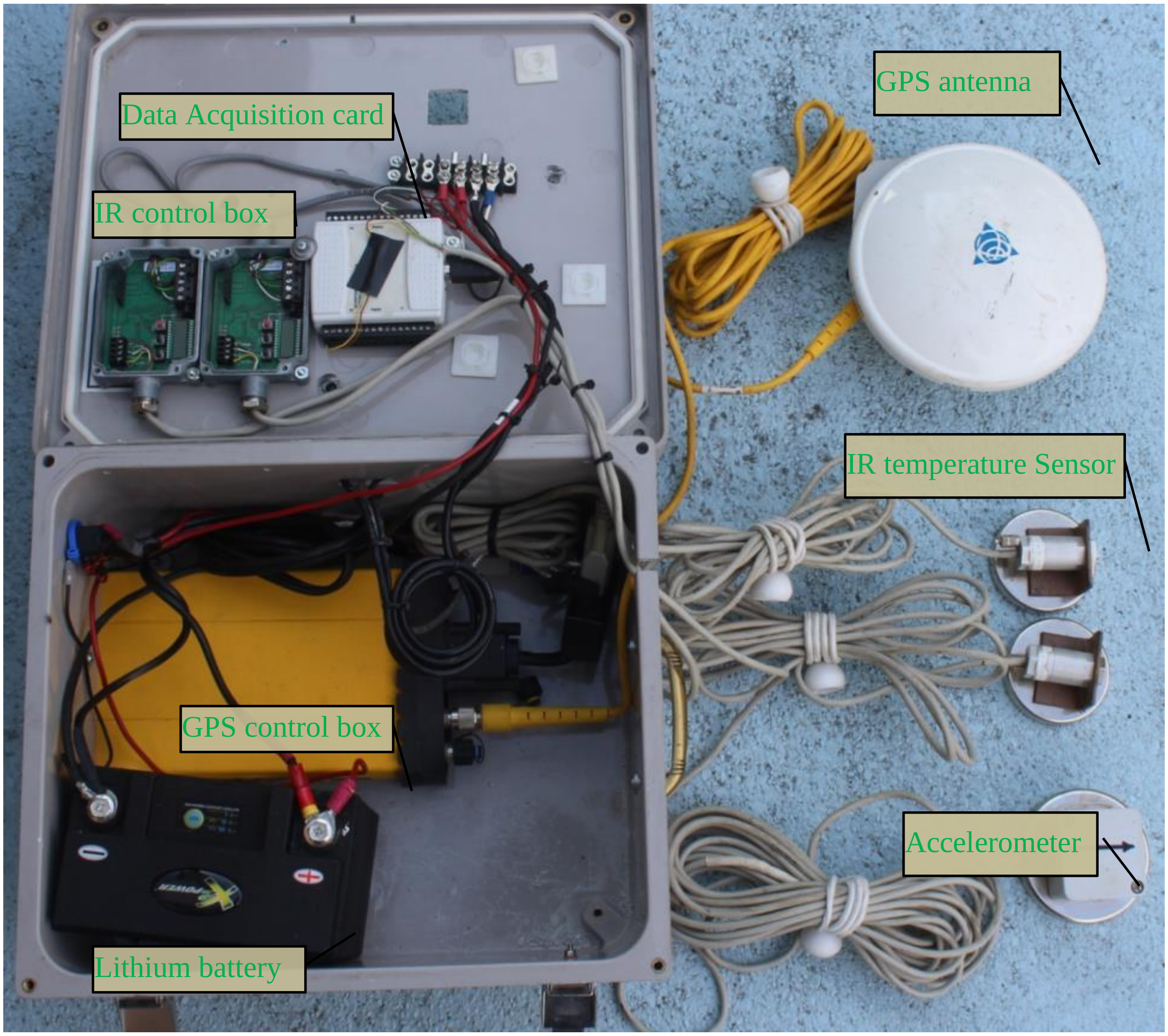
Data Acquisition card
IR control box
GPS antenna
IR temperature Sensor
GPS control box
Accelerometer
Lithium battery

Figure 56. Remove the sensors out of the CMS control box.

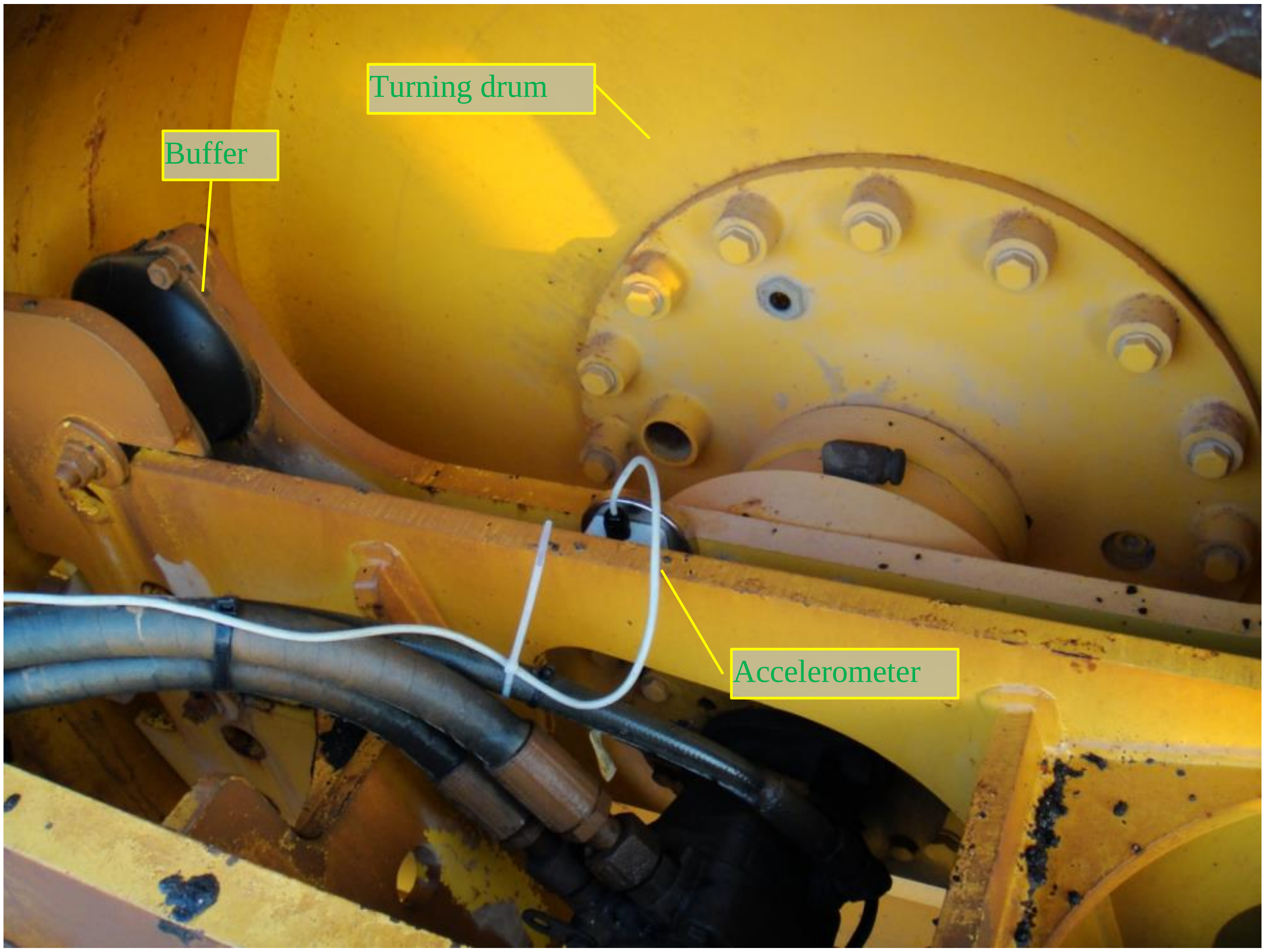

Figure 57. Accelerometer installed inside the buffer.

Data Collection with the Asphalt CMS

The intention of the designers of the CMS is that the data will eventually be collected and viewed by the roller operator. The system should take less than 10 minutes to install on any roller, and all of the sensors are attached using magnets that can be easily removed. The data-acquisition system uses a laptop computer that can withstand the harsh environment on the roller. The operator can view in real time a color-coded map showing the total mat coverage for the entire mat being compacted; also, the same data can be saved and post-processed to document the effectiveness and uniformity of the compaction process.

As the operator moves back and forth over the new mat, the GPS system accurately tracks the position of the roller, and the infrared sensors measure the mat temperatures on either side of the roller. The location and temperature information are displayed in real time for the operator to view. The number of passes and compaction-effectiveness displays are continually updated as additional passes are applied to the mat. Appendix A presents how to use the Windows-based CMS for testing.

PLC (Programmable Logic Control) System

For actual potential implementation, researchers believe a PLC system offers many advantages to stakeholders in terms of ease of use, durability, and speed of installation. This project conducted an effort to implement a PLC in the CMS and to use an HMI (Human Machine Interface) as the user interface instead of a laptop PC system. Figure 58 shows a prototype PLC system.

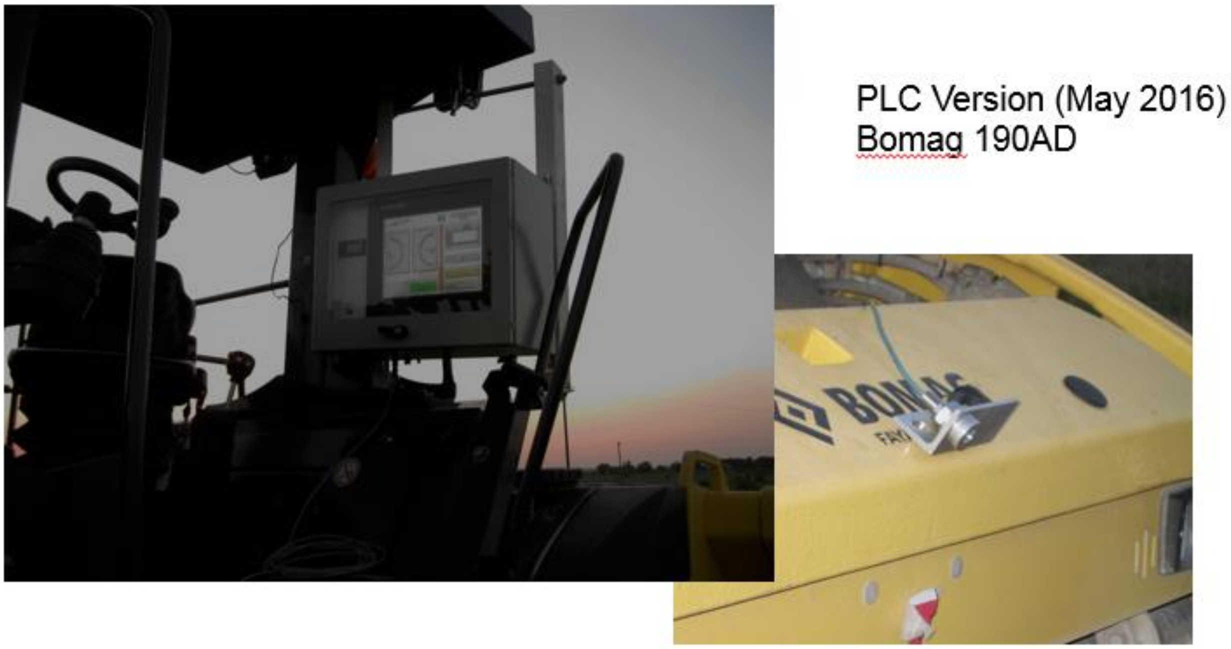

Figure 58. PLC version mounted on Bomag compactor.

The approach for the PLC system was slightly different from that of the PC system. The main focus of the PLC was to provide a simple means to incorporate the operator as a component in the loop controlling the compaction operation. The use of two primary instrument displays was selected to attain the desired focus: temperature and compaction index. These two displays are effectively real time and therefore present the data only for the current position of the roller, so their purpose is to assist with controlling the progress of the roller by adjusting speed, vibration, and position in real time. Historical progress of the rolling operation is a secondary focus of the approach. Overviews of the circuitry and software for the PLC system are illustrated in Figures 59-60. The particular Lithium-ion battery used in this system was chosen because it has a proprietary cell protection material that is claimed to be more temperature and impact stable than other Lithium-ion batteries. Lithium-ion batteries of this capacity are much lighter than sealed lead acid, but they are much more expensive and require special shipping practices, so lead times are longer.

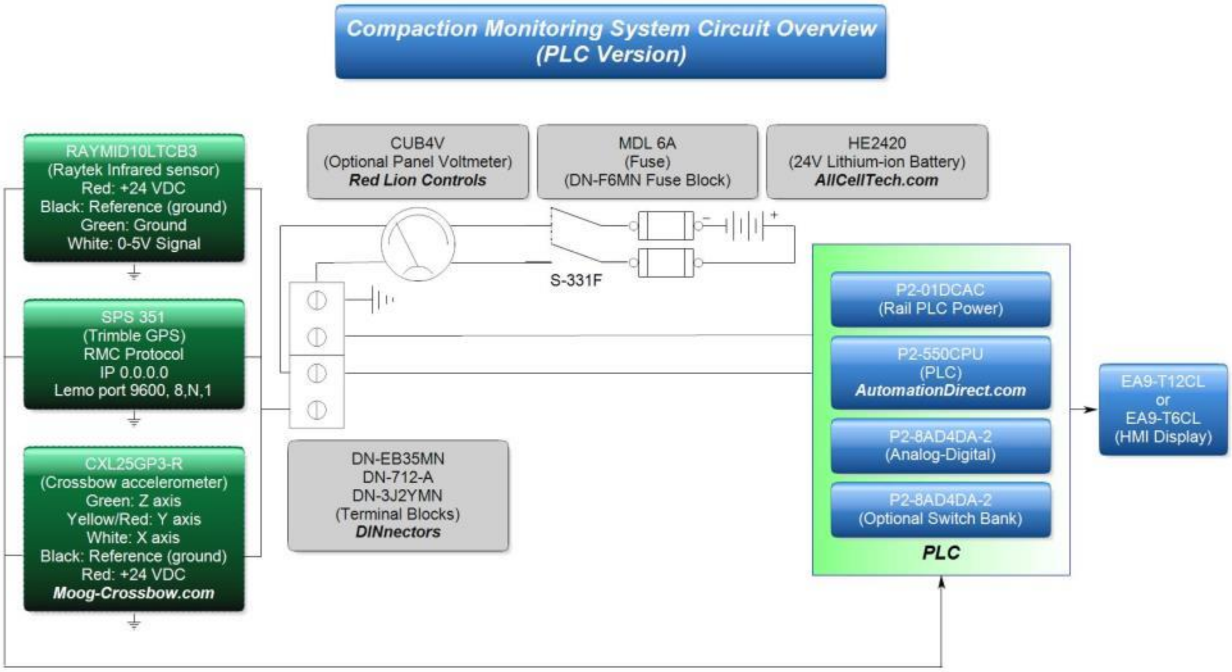
Compaction Monitoring System Circuit Overview
(PLC Version)
RAYMID10LTCB3
(Raytek Infrared sensor)
Red: +24 VDC
Black: Reference (ground)
Green: Ground
White: 0-5V Signal
SPS 351
(Trimble GPS)
RMC Protocol
IP 0.0.0.0
Lemo port 9600, 8,N,1
CXL25GP3-R
(Crossbow accelerometer)
Green: Z axis
Yellow/Red: Y axis
White: X axis
Black: Reference (ground)
Red: +24 VDC
Moog-Crossbow.com
CUB4V
(Optional Panel Voltmeter)
Red Lion Controls
MDL 6A
(Fuse)
(DN-F6MN Fuse Block)
HE2420
(24V Lithium-ion Battery)
AllCellTech.com
S-331F
DN-EB35MN
DN-712-A
DN-3J2YMN
(Terminal Blocks)
DINnectors
P2-01DCAC
(Rail PLC Power)
P2-550CPU
(PLC)
AutomationDirect.com
P2-8AD4DA-2
(Analog-Digital)
P2-8AD4DA-2
(Optional Switch Bank)
PLC
EA9-T12CL
or
EA9-T6CL
(HMI Display)

Figure 59. Basic PLC circuit (overview).

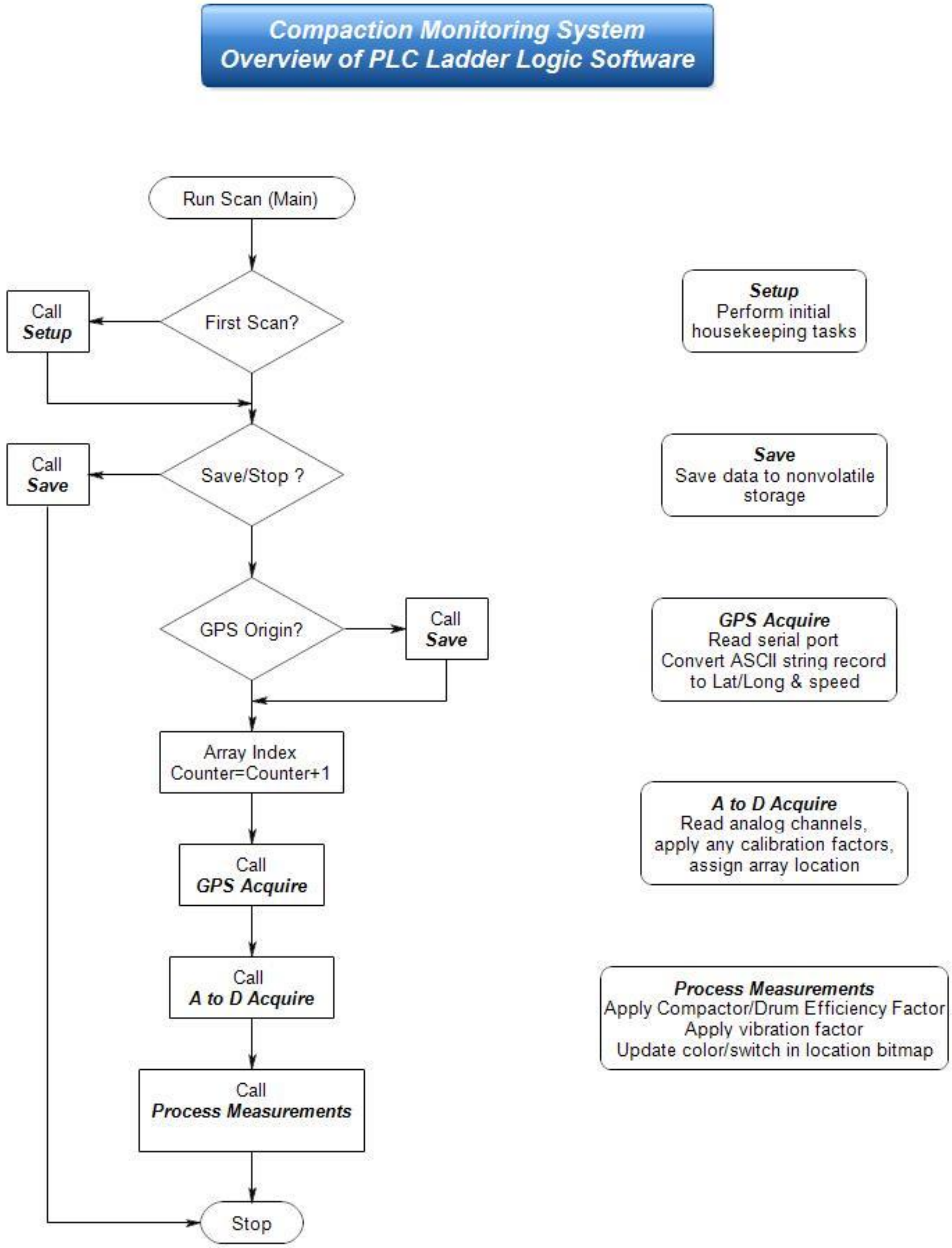
Compaction Monitoring System
Overview of PLC Ladder Logic Software
Run Scan (Main)
First Scan?
Call **Setup**
Save/Stop ?
Call **Save**
GPS Origin?
Call **Save**
Array Index Counter=Counter+1
Call **GPS Acquire**
Call **A to D Acquire**
Call **Process Measurements**
Stop
Setup Perform initial housekeeping tasks
Save Save data to nonvolatile storage
GPS Acquire Read serial port Convert ASCII string record to Lat/Long & speed
A to D Acquire Read analog channels, apply any calibration factors, assign array location
Process Measurements Apply Compactor/Drum Efficiency Factor Apply vibration factor Update color/switch in location bitmap

Figure 60. Basic software logic for PLC (overview).

RESULTS

A common assumption is that vibratory compaction makes the pavement denser. While this is generally not a particularly bad assumption, it depends somewhat on the mix, the roller, and the thickness of the mat. During this project project, a TOM mix was placed on US 183 in Austin. This is a particularly thin mat, which has several implications for the compaction process. One implication is that the mat is normally expected to cool more rapidly that a normal thickness mat and another is that the use of vibration must be carefully thought out. On this particular job, using the vibration for more of the rolling pattern than necessary actually resulted in a reduction of density, so the rolling pattern was changed to increase the static coverage versus coverage with vibration. It is unknown whether one of the other types of compactors that use a form of oscillation, or a lighter compactor, could have compacted the mat more efficiently with fewer coverages.

The PC-based CMS achieved good results in the field. The PLC system appears to be functionally capable of achieving similar success but is not ready for full field implementation.

PLC System

The first hardware version of the PLC system was designed and built as a single integrated unit (Figure 61 and Figure 62). This unit housed the battery, all of the signal conditioning, computational hardware, and HMI. The enclosure was quite bulky and very heavy since it was a heavy gauge steel enclosure with an interior panel for mounting the HMI plus another exterior door with a window in it to protect the face of the HMI.

Based on the experience with the first version of the hardware, it was decided to divide the system into two components: the HMI and the rest of the system. Figures 63-64 show the final version of the PLC hardware from this project. Figure 65 shows the final version of the PLC-based HMI interface chosen for the following reasons:

- The operator focus should be on the real-time display of temperature and index.
- The simplified display allows the use of a much smaller HMI that is easier to mount.

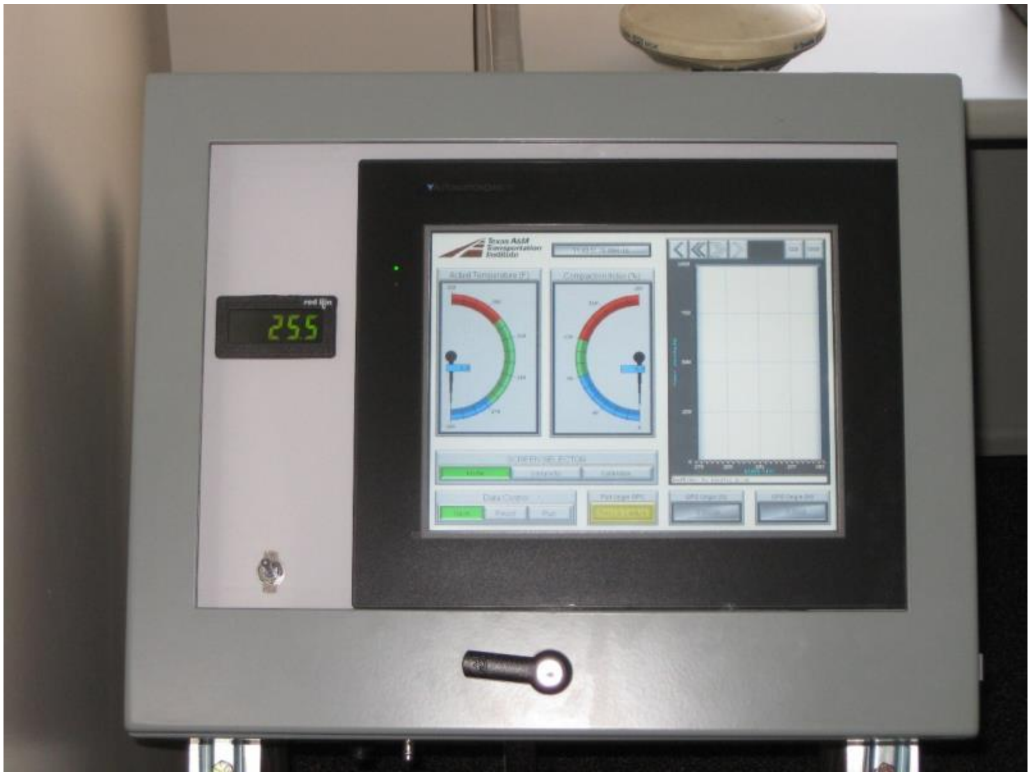

Figure 61. First version of PLC system hardware (main HMI screen shown).

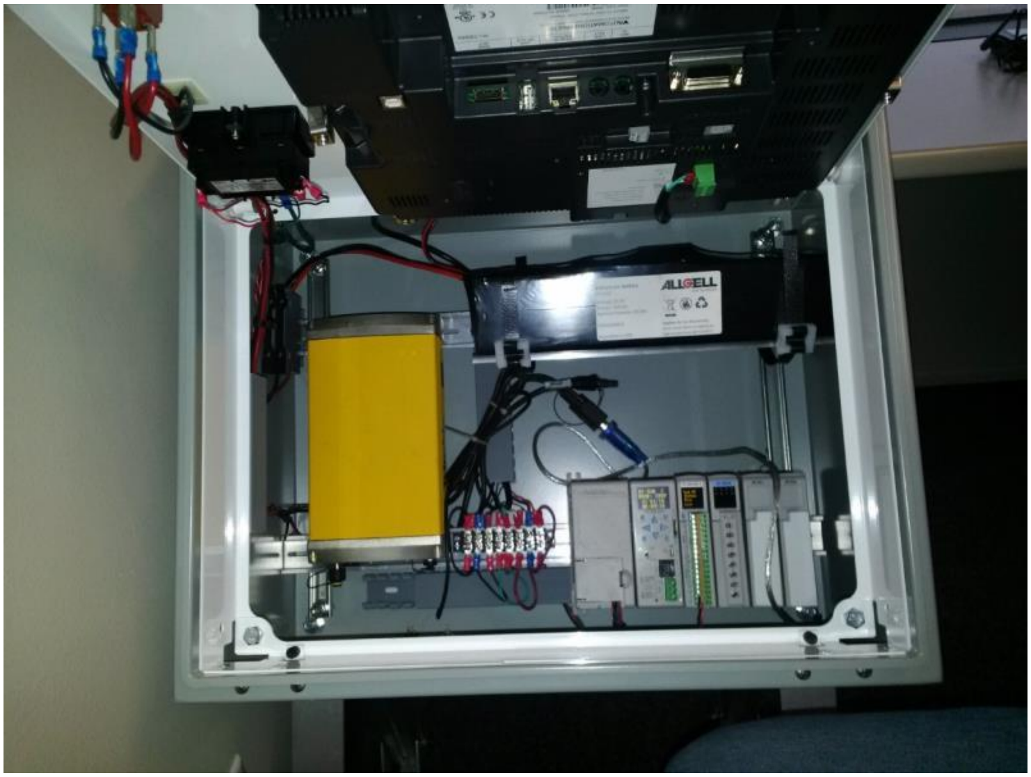

Figure 62. First version of PLC system hardware (battery, PLC, terminal strip, and GPS unit shown with HMI panel raised).

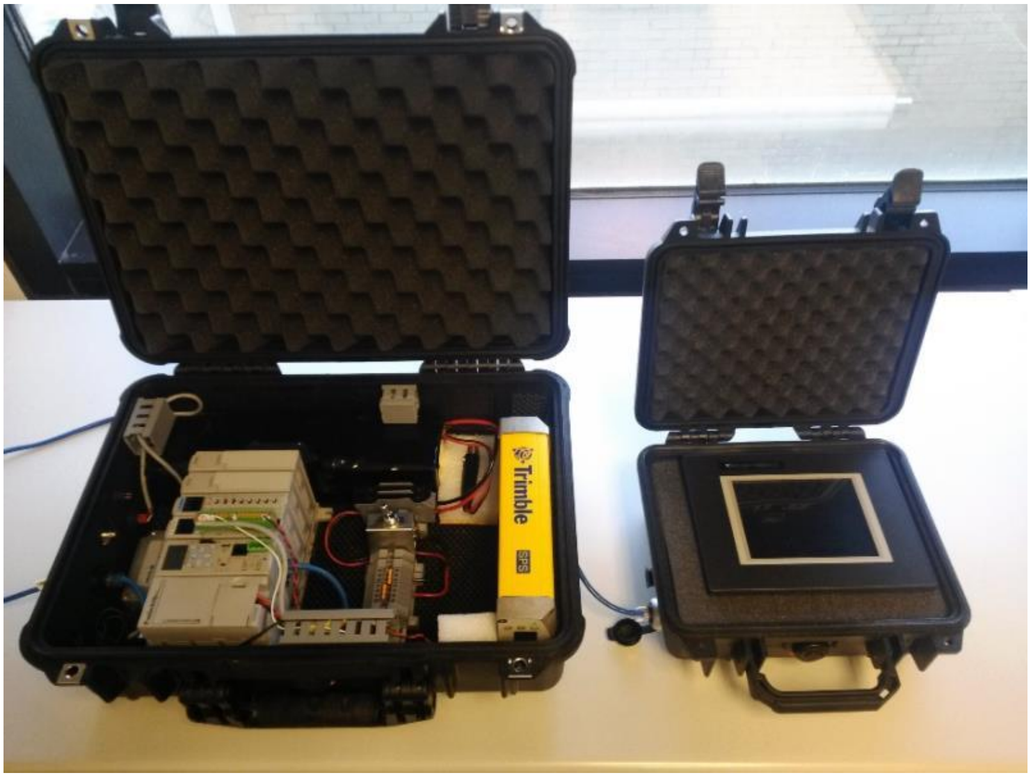

Figure 63. Final Hardware version (small nominal 6" HMI on right, PLC, battery, signal conditioning, GPS unit and on/off switch in left case).

Figure 64. Final hardware version (carry cases closed for transport).

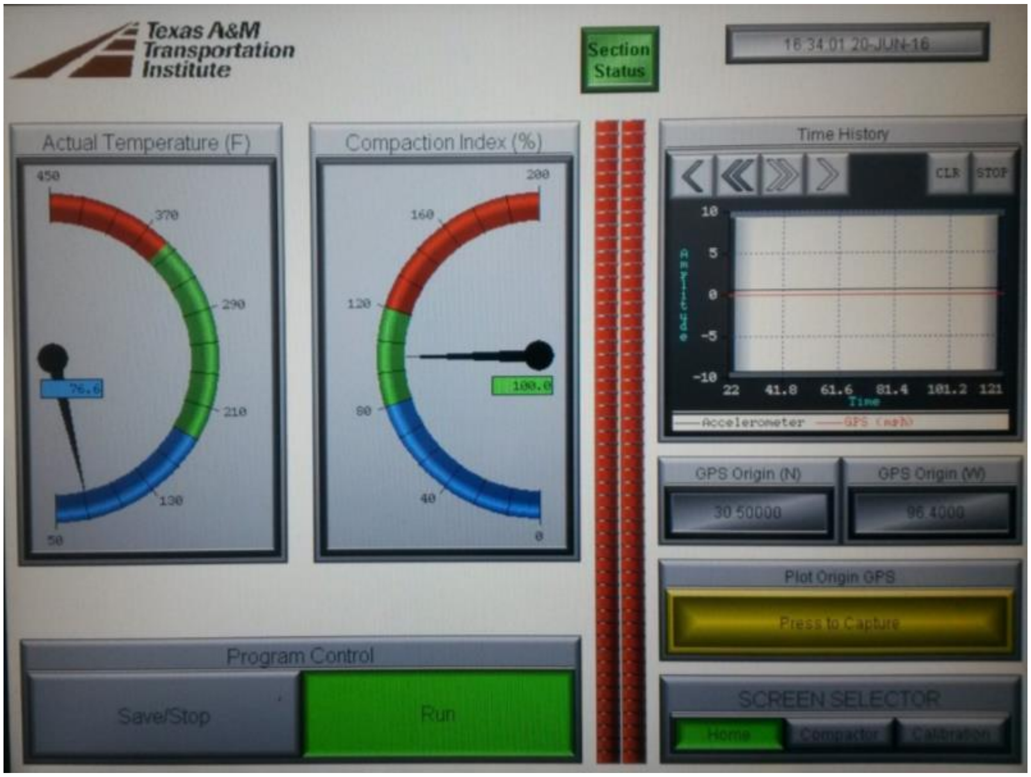
Texas A&M Transportation Institute
Section Status
16:34:01 20-JUN-16
Actual Temperature (F)
450
370
290
210
130
50
76.6
Compaction Index (%)
200
160
120
80
40
0
100.0
Time History
CLR
STOP
10
5
0
-5
-10
Amplitude
22
41.8
61.6
81.4
101.2
121
Time
Accelerometer
GPS (mph)
GPS Origin (N)
30.50000
GPS Origin (W)
96.4000
Plot Origin GPS
Press to Capture
Program Control
Save/Stop
Run
SCREEN SELECTOR
Home
Compactor
Calibration

Figure 65. Second version of HMI main screen (with section status bars and time history plot of vibration and travel speed).

Guide to PLC Version 3 Software

Figure 66 through Figure 69 illustrate the screens for PLC operation. They are in general order of decreasing frequency of usage, and the **Home** screen (Figure 66) is the screen that should be on the operator's display for virtually all of the roller operating time. By manipulating the roller's position and speed such that the needle on the temperature display remains essentially horizontal (i.e., in the green) and the needle on the compaction index display increases into the green, the desired pavement quality should be attained. In summary, the operator should do whatever it takes to keep the needles generally pointed at each other. This approach should allow the operator to concentrate on operating the compactor while only using the CMS for rapid verification that the process is proceeding according to plan. This practice keeps the focus of the operator on the pavement instead of on understanding and sorting out what message the CMS is trying to convey.

Each of the four screens in the CMS software has a selection bar along the left side that allows switching from one screen to the next. The ***Run/Stop/Save*** button is only available on the **Home** screen. The software is not used to turn off the CMS; an external toggle switch is used for turning the system off. A ***Section Start*** button is available on the **Home** screen. This button allows for manually resetting the starting location (i.e., the "origin") of the historical data to the current position of the roller. Typical usage of the button would be pressing it to capture the starting GPS coordinates of a test section (e.g., the edge of pavement at the start of the hot mix laydown for an 800 ft–1000 ft test section). It is not necessary to continually press the position

Capture button during operation. It is only used for restarting the position of the historical displays as desired and can also be used to break up the data file into smaller chunks while operating.

The **Section History** screen, Figure 67 is meant to display the status of various parameters from the GPS origin to the current time/position. The upper plot on the screen displays the accelerometer response, the GPS speed, the compaction index, and the temperature over time since the program was started or since the starting position capture button was pressed, whichever is later. The lower portion of the screen is under development, comprising a bitmap representation of a two-dimensional array of values of the compaction index assigned by converting GPS coordinates to array indices and storing the value of CI for the coordinate pair in that array element location.

The **Compactor** screen, Figure 68, depicts where items related to the compactor can be entered. In use, the intent is to fill out this information once per job. However, there are features here that still have loose ends. For example, without a prior database and unlimited storage space for that database, or without video recognition of the pavement edge, it is virtually impossible for this software to automatically tell whether the roller is at one edge or in the middle of the mat. Thus, while provision is made for addressing the roller’s proximity to the edge of the mat by manually pressing the appropriate button, it is not anticipated that the operator would be changing this value all the time, so the usual practice would be to leave it on the most representative location button for the section. The other parameters on the screen are self-explanatory. However, at present, there is still a limitation associated with the method of accounting for vibration versus no vibration and a penalty for not being in the proper mode. The ***rolling pattern deviation factor*** is meant to handle this by reducing the compactor efficiency (e.g., the 75 percent figure shown would reduce the middle of the drum efficiency from 1.0 to 0.75). However, there is currently no accurate method in the software of handling, for example, the case in which the rolling pattern is planned for three coverages: two static, and one vibrating. In this case, if the operator vibrates for two coverages and does one static (i.e., the opposite of what is planned), a single rolling pattern deviation factor might not give a picture of what happened that would be as accurate as desired.

The final calibration screen, Figure 69, is where data related to the laboratory correlations and the two graphs on the bottom left of Figure 42 come into play. In use, the intent is again to enter data on this screen only once per job before roller operations start. Some of the variables on this screen are retained in nonvolatile memory and therefore do not need reentry from job to job unless differences in the situation call for it.

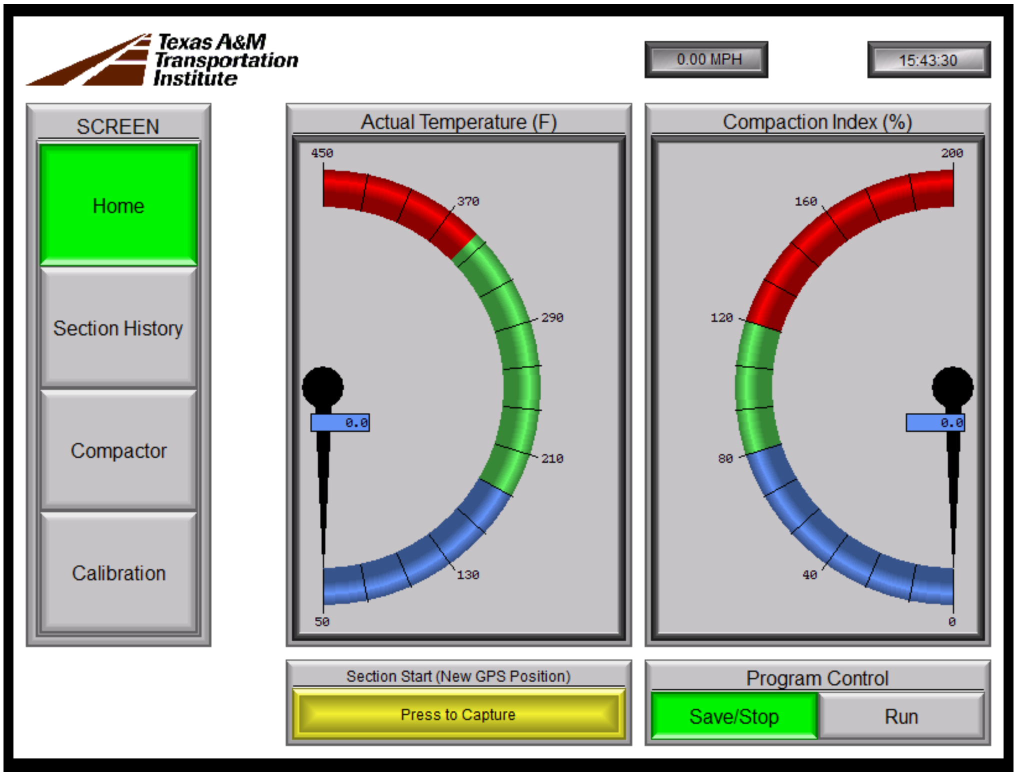
Texas A&M Transportation Institute
0.00 MPH
15:43:30
SCREEN
Home
Section History
Compactor
Calibration
Actual Temperature (F)
450
370
290
210
130
50
0.0
Compaction Index (%)
200
160
120
80
40
0
0.0
Section Start (New GPS Position)
Press to Capture
Program Control
Save/Stop
Run

Figure 66. Version 3 (final) of HMI main (Home) screen (optimized for 6-inch HMI).

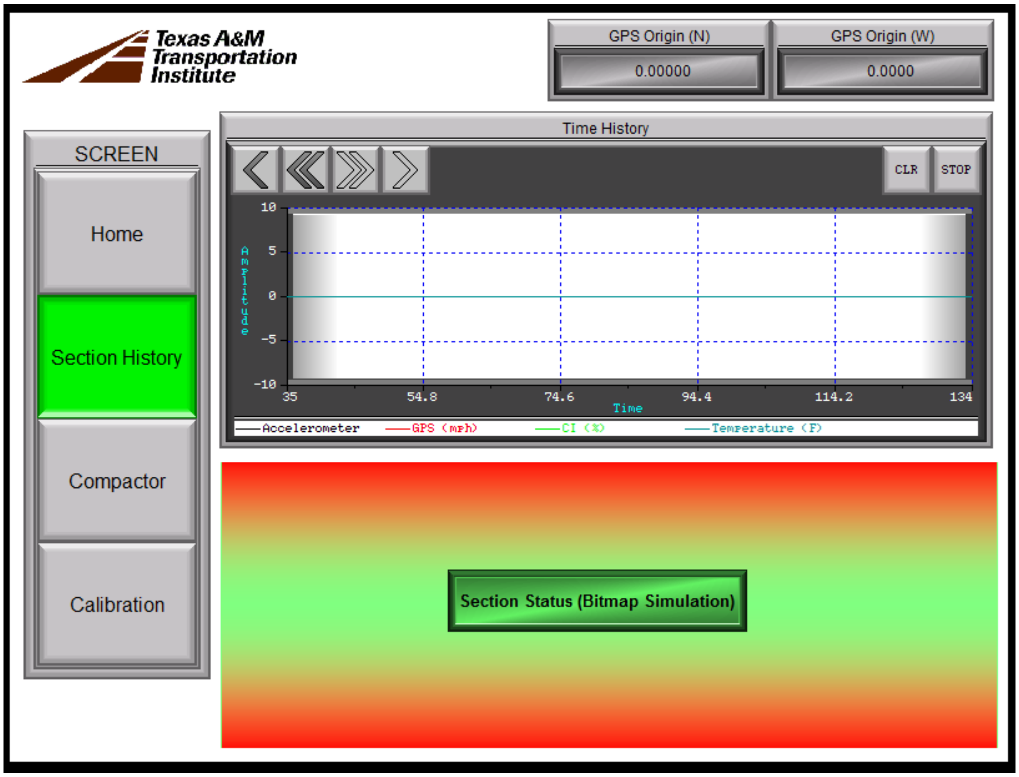
Texas A&M Transportation Institute
GPS Origin (N)
0.00000
GPS Origin (W)
0.0000
SCREEN
Home
Section History
Compactor
Calibration
Time History
CLR
STOP
10
5
0
-5
-10
Amplitude
35
54.8
74.6
94.4
114.2
134
Time
Accelerometer
GPS (mph)
CI (%)
Temperature (F)
Section Status (Bitmap Simulation)

Figure 67. Version 3 time history screen.

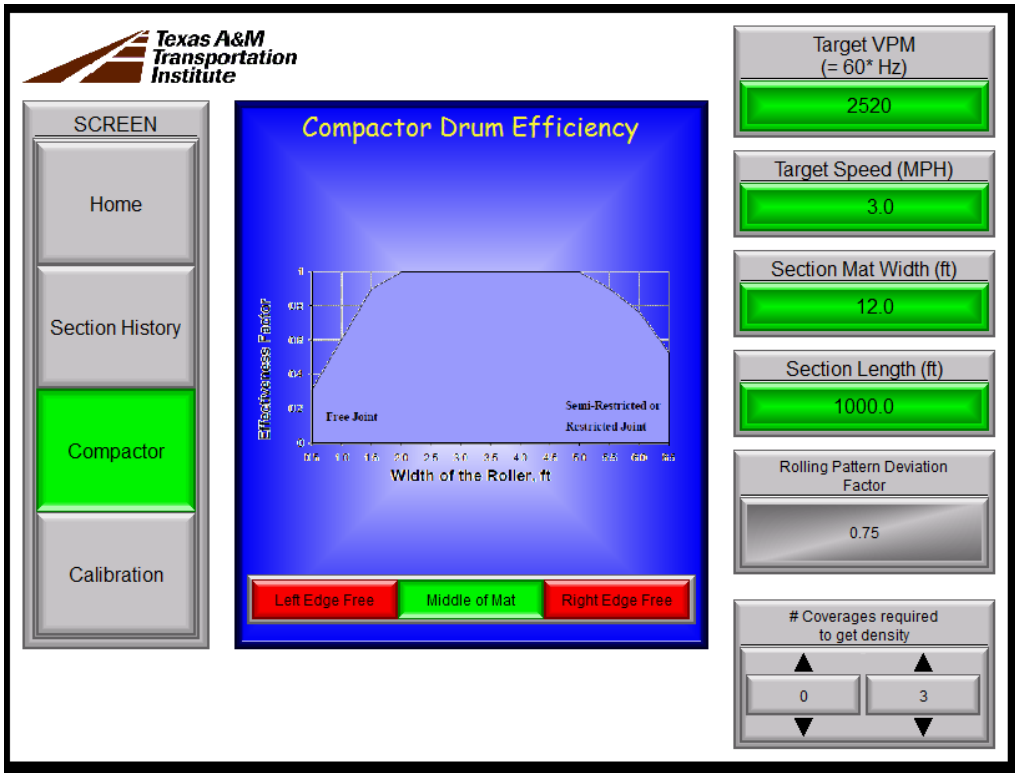
Texas A&M Transportation Institute
SCREEN
Home
Section History
Compactor
Calibration
Compactor Drum Efficiency
Effectiveness Factor
1
0.8
0.6
0.4
0.2
0
Free Joint
Semi-Restricted or Restricted Joint
0.5
1.0
1.5
2.0
2.5
3.0
3.5
4.0
4.5
5.0
5.5
6.0
6.5
Width of the Roller, ft
Left Edge Free
Middle of Mat
Right Edge Free

Target VPM (= 60* Hz): 2520

Target Speed (MPH): 3.0

Section Mat Width (ft): 12.0

Section Length (ft): 1000.0

Rolling Pattern Deviation Factor: 0.75

Coverages required to get density: 0 3

Figure 68. Version 3 compactor-related setup screen.

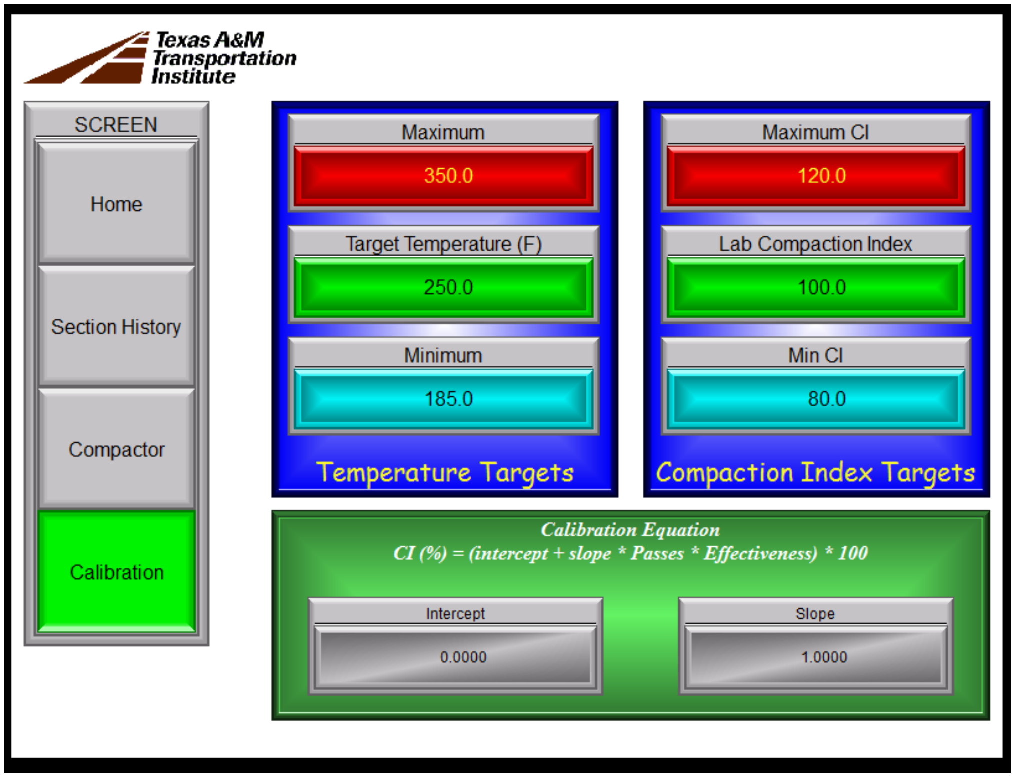
Texas A&M Transportation Institute
SCREEN
Home
Section History
Compactor
Calibration
Temperature Targets
Compaction Index Targets

Maximum: 350.0

Target Temperature (F): 250.0

Minimum: 185.0

Maximum CI: 120.0

Lab Compaction Index: 100.0

Min CI: 80.0

Calibration Equation

*CI (%) = (intercept + slope * Passes * Effectiveness) * 100*

Intercept: 0.0000

Slope: 1.0000

Figure 69. Version 3 setup screen for entering targets and prediction equation parameters.

Field Experiments to Demonstrate CMS with PC System

The researchers deployed the PC-based CMS on field projects to demonstrate the compaction monitoring system for real-time operator feedback. Projects that were selected for this study were the following:

- US 183 in the Austin District.
- US 90 in the Beaumont District.

Description of Asphalt Mixes and Field Projects

For each project, field compaction information was recorded, such as number of roller passes, location of each pass, and mat temperature. In addition, plant mix and field cores from each project were collected in order to conduct laboratory tests for further analysis. Table 5. summarizes the information on asphalt mixes used in the field projects.

The US 183 project is located in Travis County, and the entire distance of the project is about 2.2 miles, as shown in Figure 70. US 183 is a four-lane undivided highway. The TOM-F (9.5 mm nominal maximum size) mix was placed on top of an applied seal coat, and the lift thickness was 0.75 inches. Dual Bomag 190 breakdown rollers were used to compact the mat.

The US 90 project is an undivided seven-lane highway (including the center turning lane). The project is located in Liberty, TX, and the entire distance of the project is about 2.6 miles, as seen in Figure 71.. The Superpave D (9.5 mm nominal maximum size) mix with a thickness of 1.5 inches was laid after milling the existing surface layer. A HAMM HD 120 breakdown roller was used to compact the entire mat with a 12 feet mat width.

As shown in Figure 72, the PC-based CMS system was mounted onto the compaction roller to form the final assembled system used to record the compaction data. A GPS unit was mounted on the top of the roller to track the location of the roller on the mat. An accelerometer sensor was attached on the roller to determine the mode of operation. Further, temperature sensors were attached to the sides of the roller to read the temperature of the mat surface.

Figure 73 shows an example of the compaction data collected from US 183 during compaction from the start station of the project to 5,200 ft. The compaction data clearly present compaction patterns and effort of the roller compactor: the green section indicates three roller passes, while the pink section shows five times.

Table 5. Information on asphalt mixes used in this study.

Project ID	Mix Type	Date of Testing	Binder Type	Optimum AC (%)	Lift Thickness (inch)
US 183	TOM-F	May 2016	PG76-22	7.2	0.75
US 90	Superpave D	June 2016	PG70-22	5.2	1.50

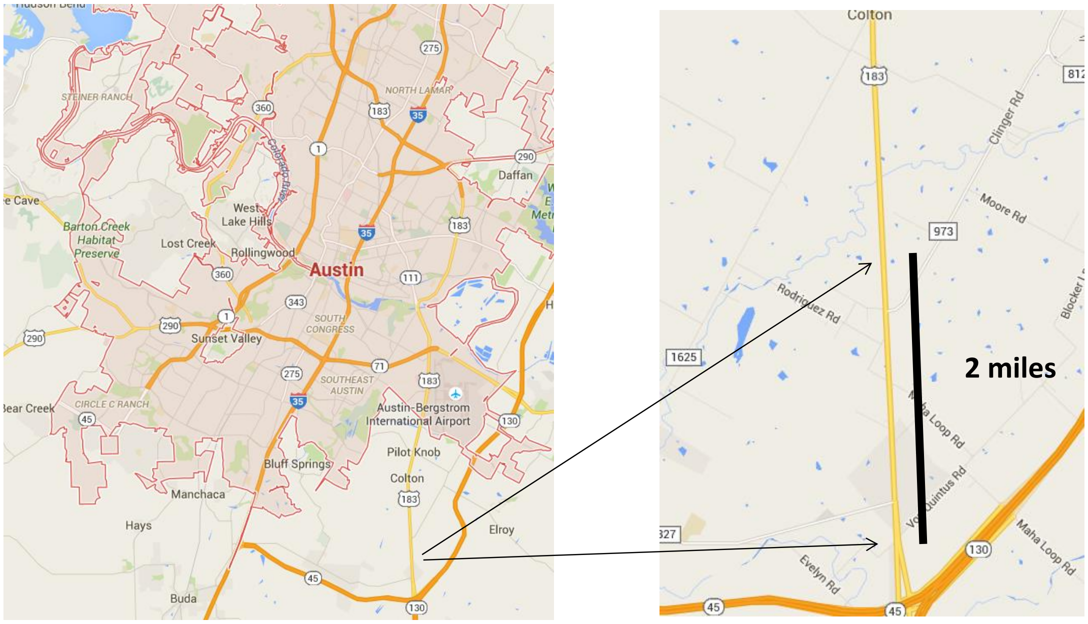
Austin
North Lamar
Daffan
West Lake Hills
Barton Creek Habitat Preserve
Lost Creek
Rollingwood
South Congress
Sunset Valley
Southeast Austin
Circle C Ranch
Austin-Bergstrom International Airport
Pilot Knob
Bluff Springs
Manchaca
Colton
Hays
Elroy
Buda
Steiner Ranch
Bear Creek
Colton
Rodriguez Rd
Clinger Rd
Moore Rd
Maha Loop Rd
Quintus Rd
Evelyn Rd
2 miles
183
973
1625
130
45

Figure 70. US 183 field project location.

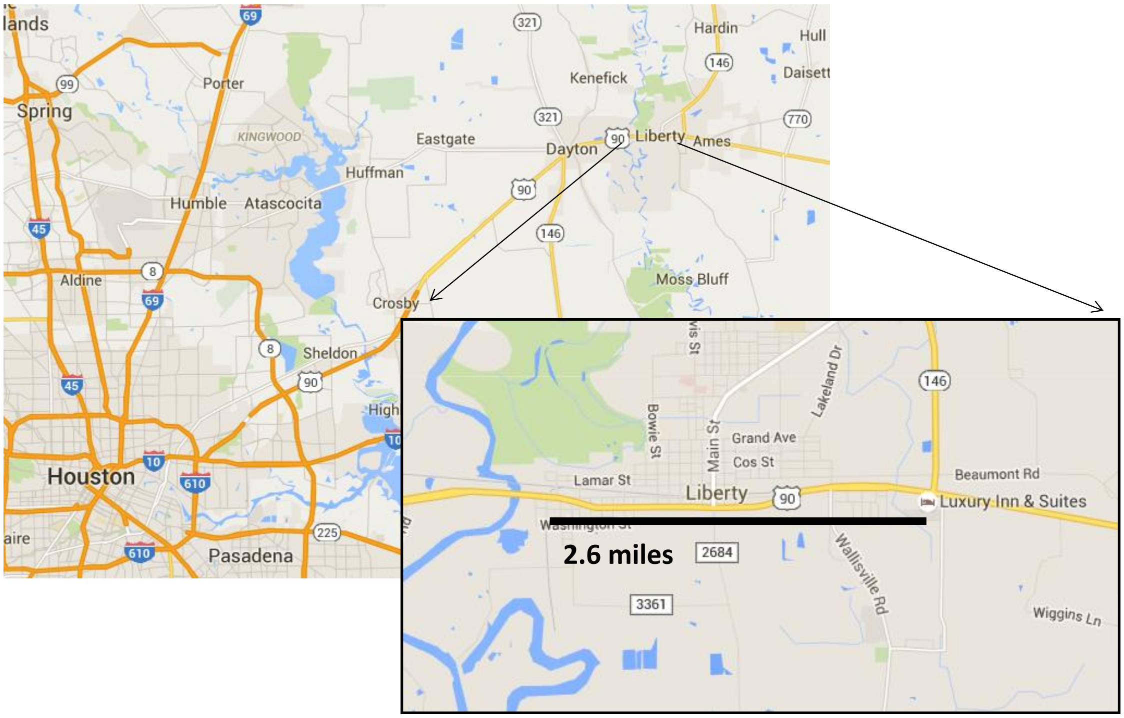
Spring
Porter
Kingwood
Eastgate
Kenefick
Hardin
Hull
Daisetta
Dayton
Liberty
Ames
Huffman
Humble
Atascocita
Aldine
Moss Bluff
Crosby
Sheldon
Houston
Pasadena
Bowie St
Main St
Grand Ave
Cos St
Lakeland Dr
Lamar St
Liberty
Beaumont Rd
Luxury Inn & Suites
Wallisville Rd
Wiggins Ln
2.6 miles
90
146
2684
3361

Figure 71. US 90 field project location.

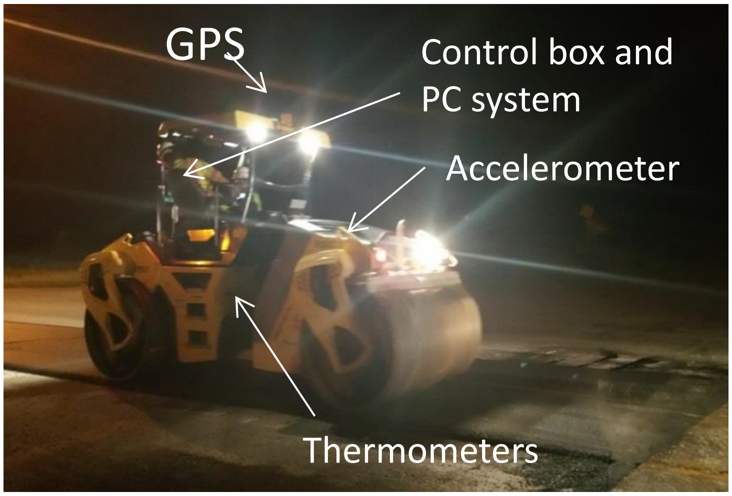
GPS
Control box and PC system
Accelerometer
Thermometers

Figure 72. Assembled PC-based CMS system onto compaction roller.

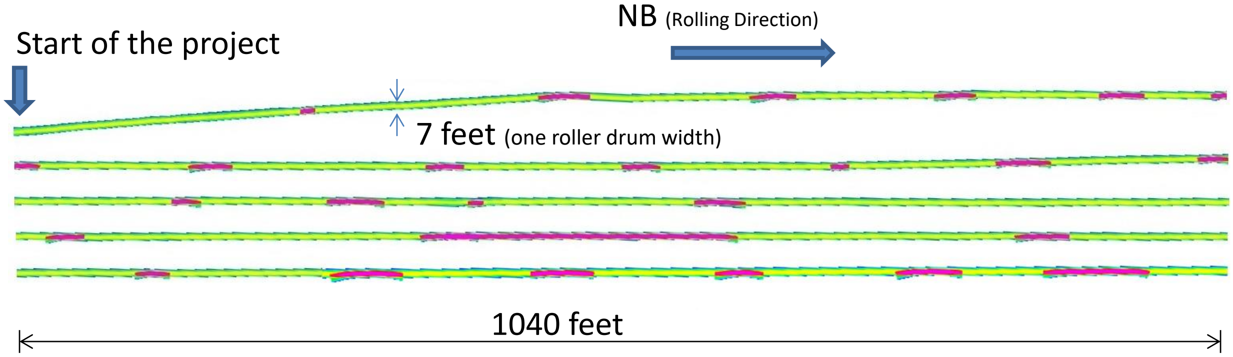
Start of the project
NB (Rolling Direction)
7 feet (one roller drum width)
1040 feet

Figure 73. Compaction efforts.

Field Cores

A number of field cores were collected from each filed project. Most field cores were randomly obtained from different locations (i.e., near the edge and middle of the mat), and some cores were extracted from different locations across the mat, as shown in Figure 74. In addition, the GPS coordinate of each core's location was recorded to calculate the compaction index for those locations which were subjected to a different number of passes. The field cores were brought back to the lab and their air voids were measured. The detailed information on field cores, GPS coordinates, compaction index, number of passes, temperatures, and air voids of field projects is summarized in Table 6. and Table 7..

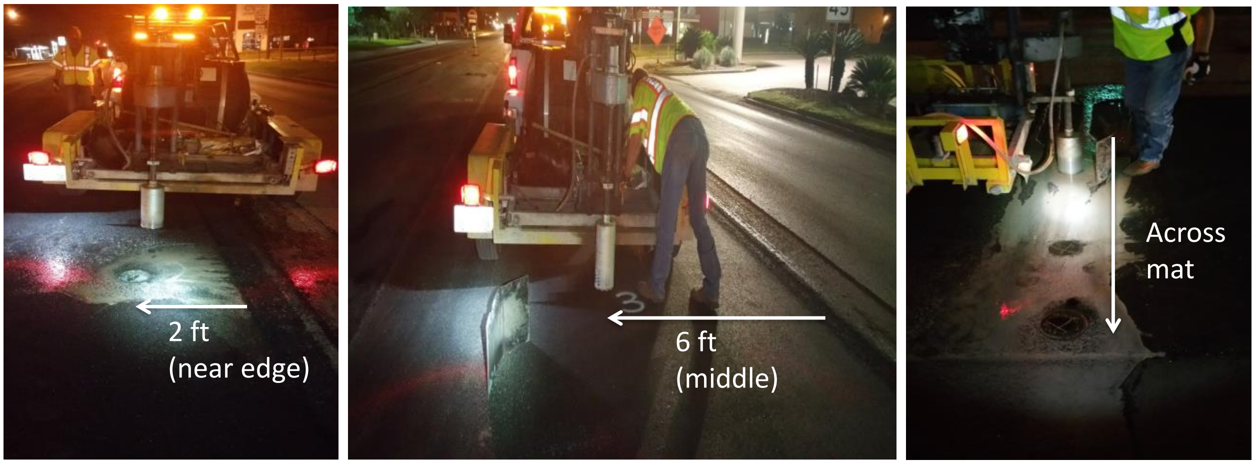

Figure 74. Extraction of field cores at different locations in the mat.

Table 6. US 183 field cores' locations, their compaction index, and air voids.

	Core ID	Latitude	Longitude	Level (ft)	Compaction Index	Number of passes	Temperature (°F)	Air Voids (%)
Section 1	#1	30.0940085	97.69388267	626.3	2.96	3	241	6.3
	#2	30.09422217	97.69389967	624.3	4.14	5	263	5.5
	#3	30.09465767	97.69393	624.7	4.94	5	252	4.7
	#4	30.09470717	97.69393467	625.7	4.94	5	257	4.2
	#5	30.09518967	97.693973	624.7	2.96	3	235	7.3
	#6	30.0954545	97.693982	623.7	2.96	3	246	14.9
	#7	30.095681	97.69399983	622.7	2.96	3	234	10.8
	#8	30.09539717	97.6939885	624.0	1.68	3	248	14.7
	#9	30.09566567	97.69400333	622.4	2.2	3	235	15.8
	#10	30.096224	97.6940365	624.3	0.39	2	231	17.1
	#11	30.09635083	97.6940345	621.1	2.96	3	168	14.5
	#12	30.096383	97.69403683	619.8	2.96	3	218	13.8
	#13	30.09645533	97.6940375	622.7	2.96	3	234	17.4
Section 2	#1	30.10956217	97.694803	600.7	0.99	1	222	10.5
	#2	30.108956.83	97.69478983	594.1	0.72	3	256	9.9
	#3	30.108805	97.69478	593.1	2.48	5	264	8.5
	#4	30.1051885	97.694541	560.7	2.62	3	246	9.7
	#5	30.102976	97.694425	575.4	2.49	3	272	8.5
	#6	30.10288467	97.694419	583.0	4.08	5	278	10.1
	#7	30.1001655	97.69426767	573.1	0.97	1	199	9.6
	#8	30.098958	97.69417817	601.3	N/A	N/A	N/A	12.2
	#9	30.09720483	97.69410033	615.1	3.03	5	277	7.3
	#10	30.09514017	97.6939835	626.3	2.93	3	234	15.6

Table 7. US 90 field cores' locations, their compaction index, and air voids.

	Core ID	Latitude	Longitude	Level (ft)	Compaction Index	Number of passes	Temperature (°F)	Air Voids (%)
Section 1	#1	30.0579575	94.78653067	14.76	6.75	8	253	3.0
	#2	30.0579625	94.78649033	15.75	5.79	7	250	4.7
	#3	30.0579835	94.78643733	15.42	5.24	8	265	3.5
	#4	30.05808883	94.78601417	16.08	6.29	12	260	3.6
	#5	30.0581385	94.78583267	17.06	3.18	4	252	4.6
	#6	30.05822767	94.78521867	16.4	6.64	7	235	3.8
	#7	30.05834933	94.78435933	24.61	2.51	4	239	7.1
	#8	30.05835117	94.78431633	23.29	2.82	3	232	6.9
	#9	30.0583835	94.7839925	24.61	2.95	4	252	6.4
	#10	30.058436	94.78366643	24.93	9.87	11	234	4.0
Section 2	#1	30.05663017	94.7922985	8.2	4.14	8	253	6.5
	#2	30.05661417	94.79413383	8.9	4.39	5	255	5.8
	#3-1	30.05661067	94.79662083	10.5	2.01	4	281	N/A
	#3-2	30.05662317	94.79661967	11.2	1.38	2	258	7.4
	#4	30.056624	94.7971035	18.4	3.14	4	260	6.3
	#5	30.05666833	94.8005315	22.3	1.98	2	257	9.0
	#6	30.05664967	94.8022755	20.3	1.98	2	218	9.3
	#7	30.0566205	94.803916	23	1.98	2	208	10.9
	#8	30.05660067	94.80486983	20.7	N/A	N/A	N/A	7.1
	#9	30.05655183	94.80797583	18	N/A	N/A	N/A	5.8
	#10	30.05657017	94.808603	23.6	N/A	N/A	N/A	7.3
Section 3	#1-1	30.05657483	94.79987167	17.7	0.13	1	237	11.1
	#1-2	30.05657683	94.799872	17.4	0.45	1	237	7.7
	#1-3	30.0565885	94.79987267	12.8	3.81	4	261	7.8
	#1-4	30.05660017	94.79987657	10.8	3.65	7	262	5.6
	#2	30.0566025	94.799238	7.9	4.36	5	271	9.9
	#3-1	30.0565695	94.79783483	7.9	4.52	6	260	6.5
	#3-2	30.056577	94.79783517	10.2	4.38	5	260	7.9
	#3-3	30.05658383	94.79783583	10.5	2.32	3	260	8.7
	#4	30.05655167	94.79749483	16.4	4.09	5	256	7.4
	#5	30.05654033	94.79385267	9.2	3.33	4	260	8.3
	#6	30.05652983	94.7936035	13.5	2.45	4	255	8.5
	#7	30.0565535	94.7929125	6.2	3.87	6	249	8.0
	#8	30.05714633	94.78855233	9.2	5.88	6	247	7.8
	#9	30.05798833	94.7862975	13.5	3.33	4	252	5.4
	#10	30.05831967	94.78444583	23.3	4.09	5	272	8.5

Compaction Curves

A compaction curve for each field section was developed by relating field cores' air voids to the compaction index, which is defined as the summation of the number of roller passes multiplied by an effectiveness factor corresponding to each pass. The effectiveness factor used in this study is shown in Figure 49. The compaction index values in Table 6 and Table 7 were finally provided by the PC-based CMS system as the outcome. Compaction curves showing the relationship between the percent air voids and compaction index for each field section are presented in Figure 75 and Figure 76. Although not all sections show very good correlations, the concept of the compaction index would be still useful to obtain or predict uniform density distribution in the mat. It’s possible that the correlations could be improved by considering more factors (e.g., sublayer types, compaction modes, and joint conditions) in the future.

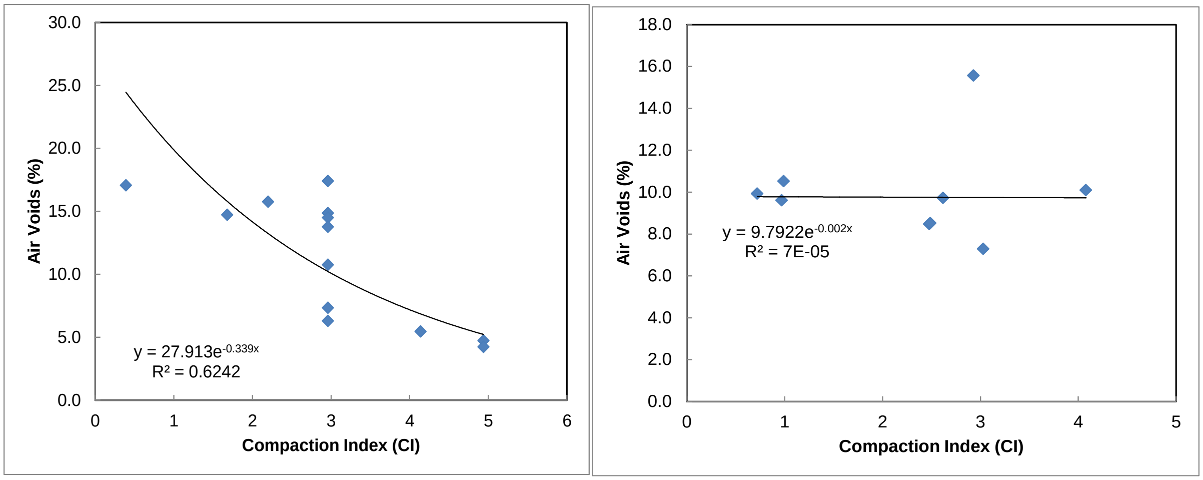

(a) Section 1 of US 183 (b) Section 2 of US 183

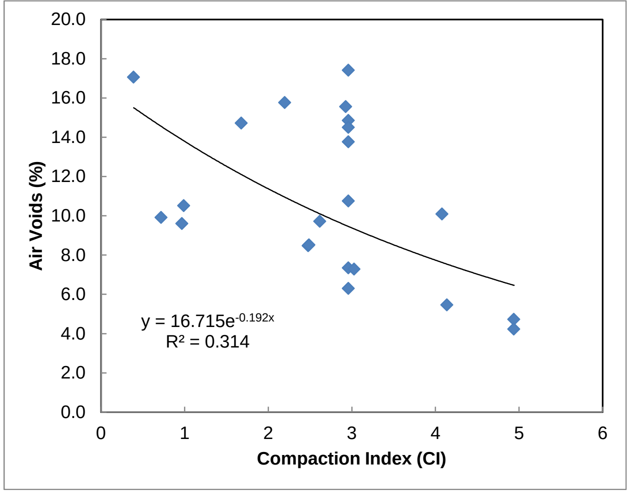

(c) all sections (1 & 2) of US 183

Figure 75. Compaction curves of US 183 field project.

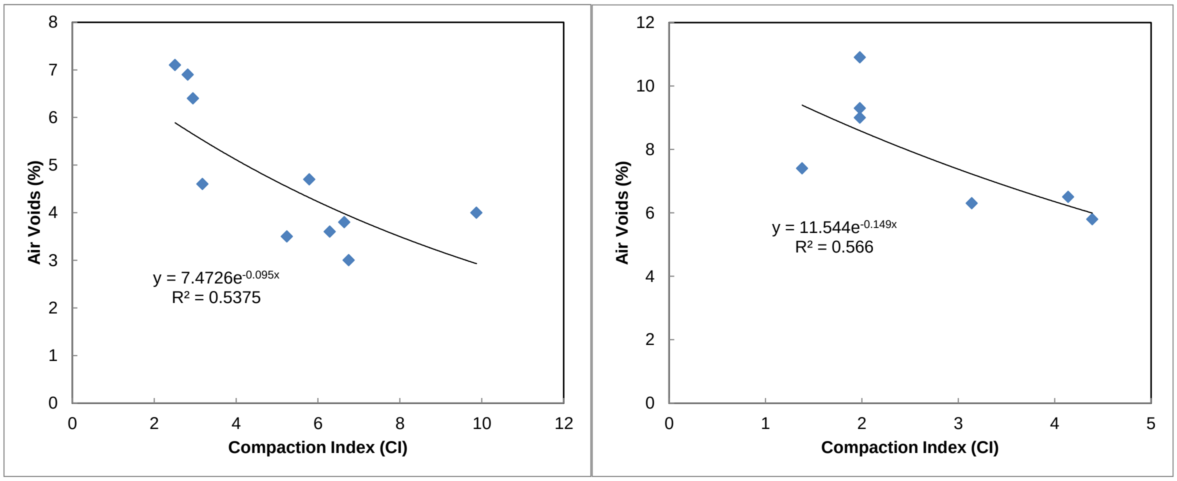

(a) Section 1 of US 90 (b) Section 2 of US 90

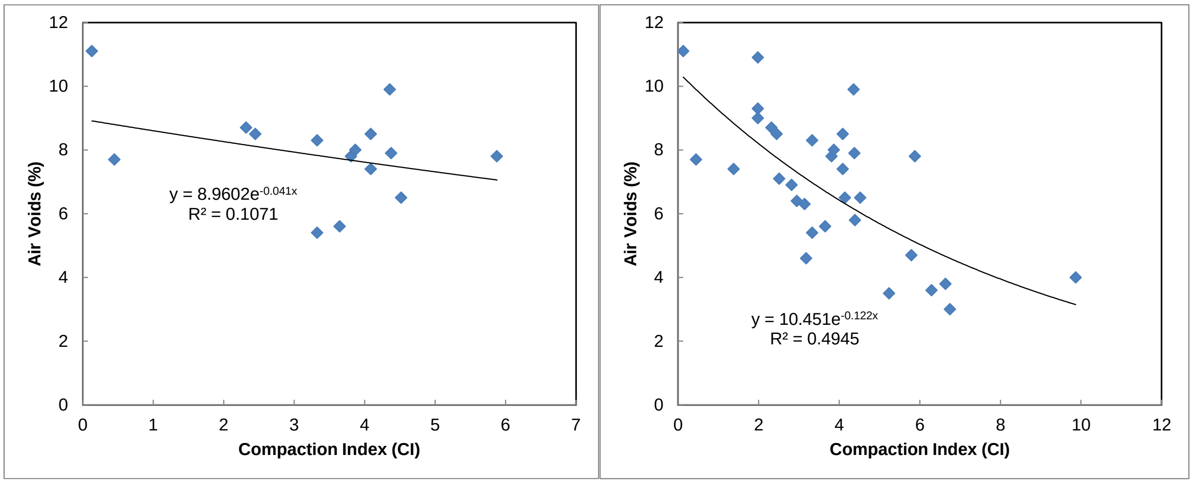

(c) Section 3 of US 90 (d) all sections (1, 2, & 3) of US 90

Figure 76. Compaction curves of US 90 field project.

Relationship between Laboratory Compaction and Field Compaction

Plant mixes were sampled at the field project sites during the construction. Plant mixes were brought back to the TTI McNew Lab and reheated to fabricate specimens. To estimate the required compaction effort in the field, a number of samples with a wide range of air void levels were molded using a Superpave gyratory compactor. Each sample was fabricated in a diameter of 150 mm and a height of 62 mm. The number of gyrations of each sample was also recorded during compacting. Two different compaction temperatures were considered based on the asphalt binder type of each mix. Figure 77 shows the results of air voids measured over the number of gyrations in the logarithmic scale. The ratio of the air void of 8 percent to the number of gyrations in the logarithmic scale was calculated. Next, the relationship between the ratio obtained and the compaction index at an air void level of 8 percent was developed for each field project, as shown in Figure 78. This correlation can provide the potential to estimate the compaction effort required in the field. Conducting more field and laboratory tests is recommended for better prediction and analysis since limited data were used to develop the relationship.

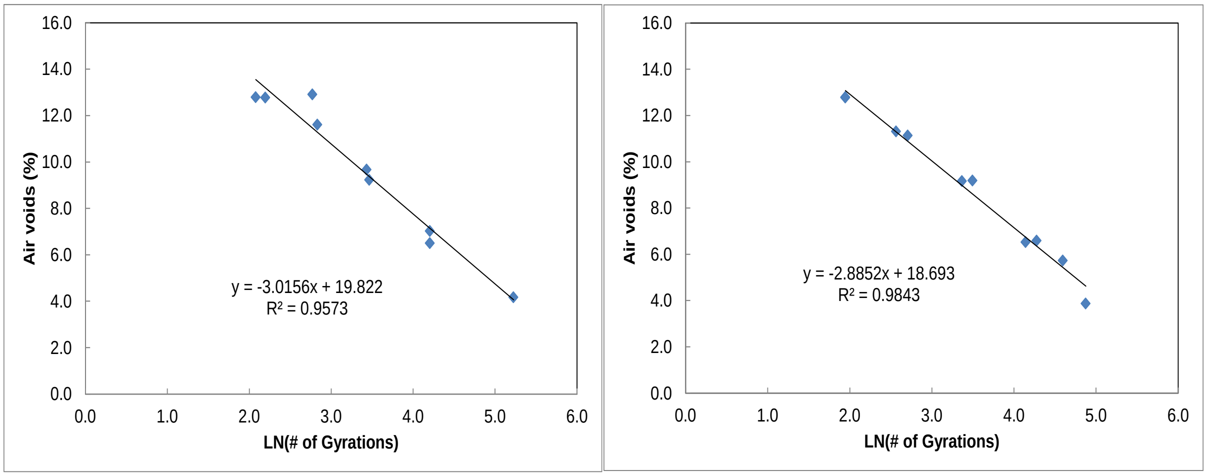

(a) TOM-F at 250 °F (b) TOM-F at 275 °F

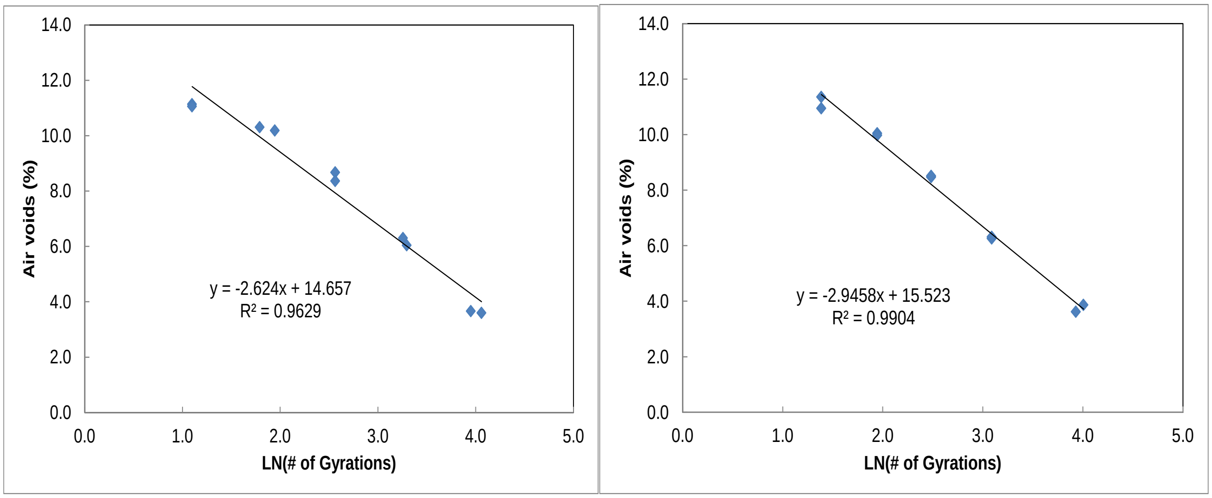

(c) Superpave D at 250 °F (d) Superpave D at 275 °F

Figure 77. Relationship between air voids and number of gyrations in semi-log scale for each project.

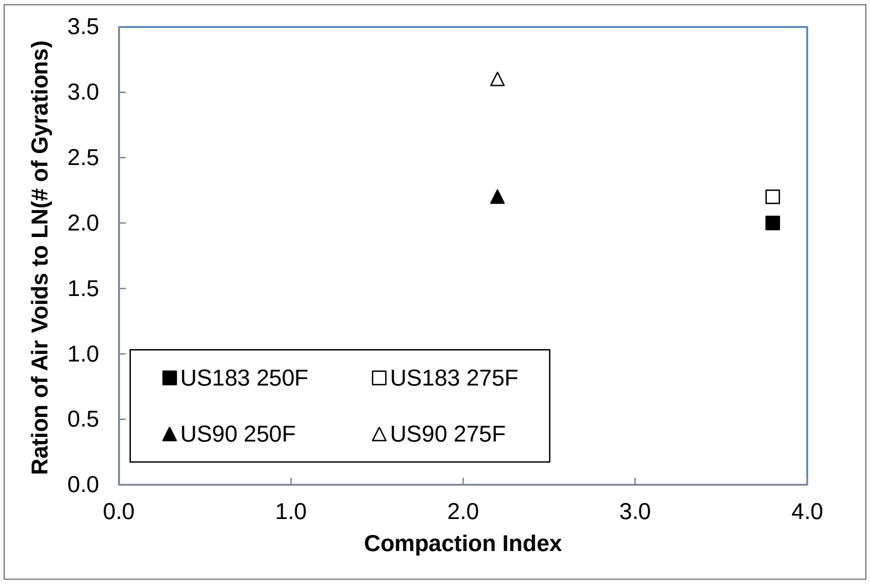

Figure 78. Relationship between laboratory compaction and field compaction at 8 percent air voids for different mixes

Multifactor ANOVA—Air Voids

A multifactor analysis of variance for air voids was conducted. This analysis constructed various tests and graphs to determine which factors have a statistically significant effect on air voids. The analysis also tested for significant interactions among the factors, given sufficient data. The F-tests in the ANOVA table allows identification of the significant factors. For each significant factor, the Multiple Range Tests indicate which means are significantly different from others. In Figure 79, an illustration of the spread of the data categorized by the project factor is presented. There was more spread in the data on US 183, and there were more high air void observations than on US 90. While the top size of the aggregate was effectively the same on both jobs, the gradation curves were slightly different, and the target layer thickness was quite different, with the target being only 0.75 inches for US 183 and double that value for US 90. This difference could easily explain the difference in the distribution on the scatterplot.

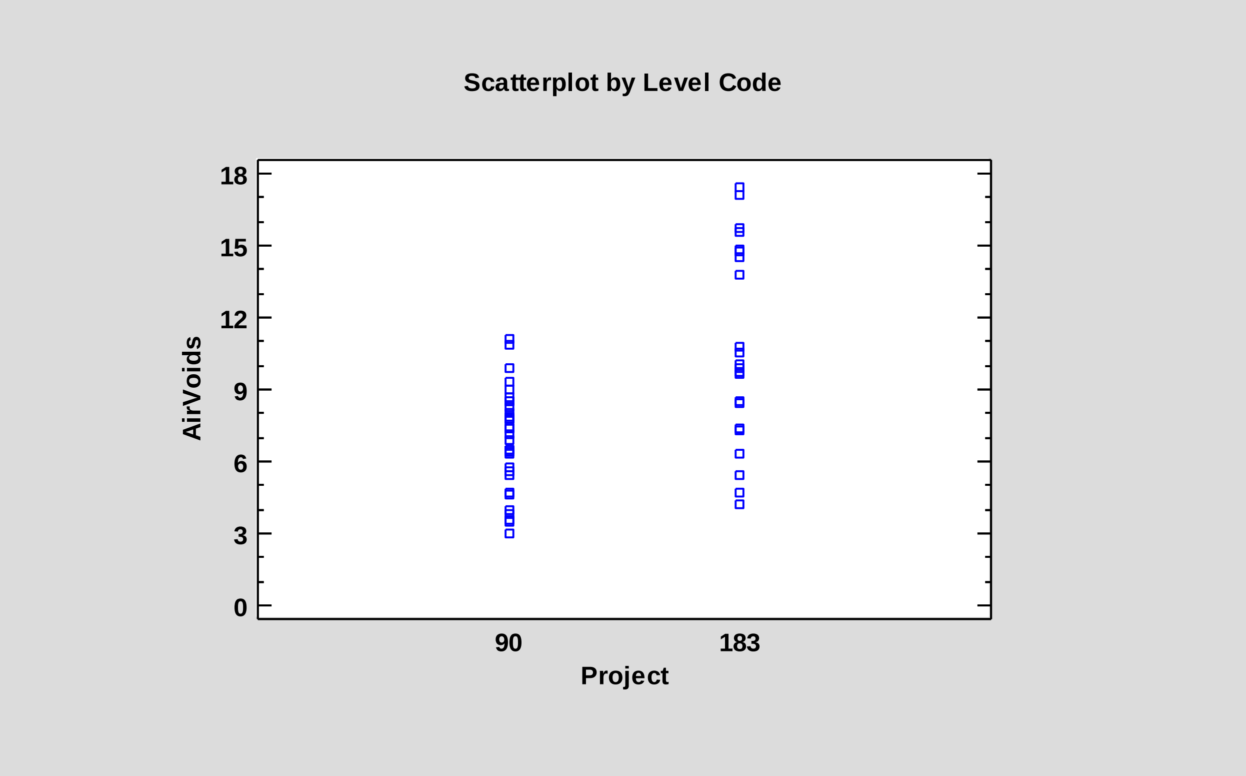

Figure 79. ANOVA Project factor summary.

The ANOVA table (Table 8.) decomposes the variability of air voids into contributions due to various factors. Since Type III sums of squares were used, the contribution of each factor is measured having removed the effects of all other factors. The P-values test the statistical significance of each of the factors. Since three P-values are less than 0.05, these factors have a statistically significant effect on air voids at the 95.0 percent confidence level.

Table 8. Analysis of Variance for Air Voids—Type III Sums of Squares.

Source	*Sum of Squares*	*Df*	*Mean Square*	*F-Ratio*	*P-value*
COVARIATES					
Compaction	97.6045	1	97.6045	14.88	0.0003
Temperature	36.85	1	36.85	5.62	0.0217
MAIN EFFECTS					
A:Project	72.1696	1	72.1696	11.00	0.0017
RESIDUAL	328.047	50	6.56093		
TOTAL (CORRECTED)	682.147	53			

All F-ratios are based on the residual mean square error.

Table 9 shows the mean air voids for each level of the factors. Table 9 also shows the standard error of each mean, which is a measure of its sampling variability. The rightmost two columns show 95.0 percent confidence intervals for each of the means, which are illustrated in Figure 80.

Table 9. Table of Least Squares Means for Air Voids with 95.0 percent Confidence Intervals.

Level	*Count*	*Mean*	*Std. Error*	*Lower Limit*	*Upper Limit*
GRAND MEAN	54	8.72165			
Project					
90	32	7.46773	0.465187	6.53338	8.40209
183	22	9.97557	0.567697	8.83532	11.1158

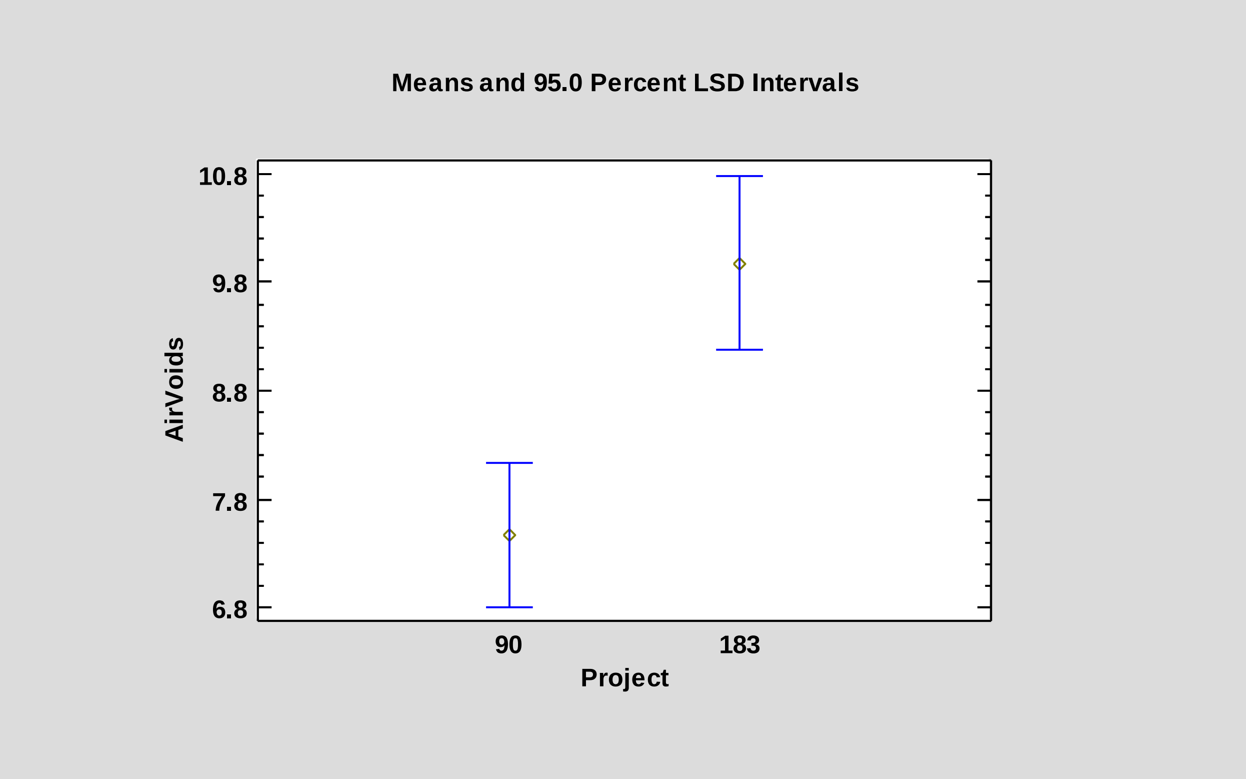

Figure 80. Means and interval plot for air voids by project.

Table 10 applies a multiple comparison procedure to determine which means are significantly different from which others. The bottom part of the table shows the estimated difference between each pair of means. This pair shows a statistically significant difference at the 95.0 percent confidence level. Homogenous groups are identified using columns of Xs. Within each column, the levels containing Xs form a group of means within which there are no statistically significant differences. The method used to discriminate among the means is Fisher's least significant difference (LSD) procedure. With this method, there is a 5.0 percent risk of calling each pair of means significantly different when the actual difference equals zero.

Table 10. Multiple Range Tests for Air Voids by Project (Method: 95.0 percent LSD).

Project	*Count*	*LS Mean*	*LS Sigma*	*Homogeneous Groups*
90	32	7.46773	0.465187	X
183	22	9.97557	0.567697	X

Contrast	*Sig.*	*Difference*	*+/- Limits*
90 - 183	*	-2.50784	1.51876

* denotes a statistically significant difference.

Multiple Regression—Air Voids

Table 11. shows the results of fitting a multiple linear regression model to describe the relationship between air voids and three independent variables. In Table 3, the project (US highway number) was used in the analysis. In this regression analysis, CC was used as an independent variable, but it performs much the same function in this analysis as "project" did in the earlier ANOVA since there was only one aggregate gradation used at each of the projects.

Table 11. Regression Analysis.

Parameter	*Estimate*	*Standard Error*	*T Statistic*	*P-value*
CONSTANT	27.3618	4.44364	6.15752	0.0000
Compaction	-0.816229	0.211622	-3.85702	0.0003
Temperature	-0.0438419	0.0184992	-2.36993	0.0217
CC	-1.31991	0.397971	-3.31661	0.0017

Analysis of Variance

Source	*Sum of Squares*	*Df*	*Mean Square*	*F-Ratio*	*P-value*
Model	354.1	3	118.033	17.99	0.0000
Residual	328.047	50	6.56093		
Total (Corr.)	682.147	53			

R-squared = 51.9097 percent
R-squared (adjusted for d.f.) = 49.0243 percent
Standard Error of Est. = 2.56143
Mean absolute error = 2.00008
Durbin-Watson statistic = 1.49364 (P=0.0163)
Lag 1 residual autocorrelation = 0.214203

The equation of the fitted model is as follows:

AirVoids = 27.3618 - 0.816229*Compaction - 0.0438419*Temperature - 1.31991*CC.

Since the P-value in the ANOVA table is less than 0.05, there is a statistically significant relationship between the variables at the 95.0 percent confidence level.

Figure 81 shows the observed versus predicted air voids from the model. The R-squared statistic indicates that the model as fitted explains 51.9097 percent of the variability in AirVoids. The adjusted R-squared statistic is 49.0243 percent. Figures 82-84 show residual plots. The Durbin-Watson (DW) statistic tests the residuals to determine if there is any significant correlation based on the order in which they occur in the data file. Since the P-value is less than 0.05, there is an indication of possible serial correlation at the 95.0 percent confidence level. This result will be covered later in this section when discussing unusual residuals. In determining whether the model can be simplified, notice that the highest P-value on the independent variables is 0.0217, which belongs to temperature. Since the P-value is less than 0.05, that term (in addition to the others) is statistically significant at the 95.0 percent confidence level. Consequently, one probably does not want to remove any variables from the model.

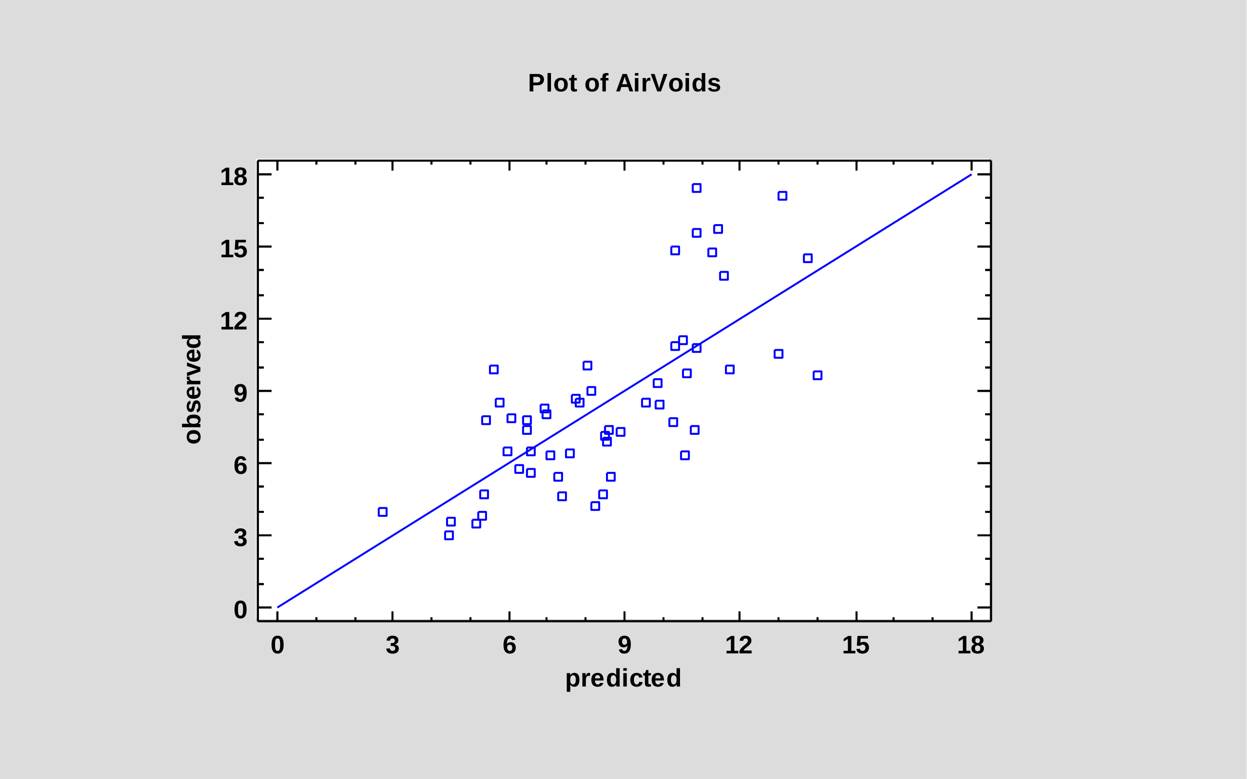

Figure 81. Model Predictions of air voids versus observed values.

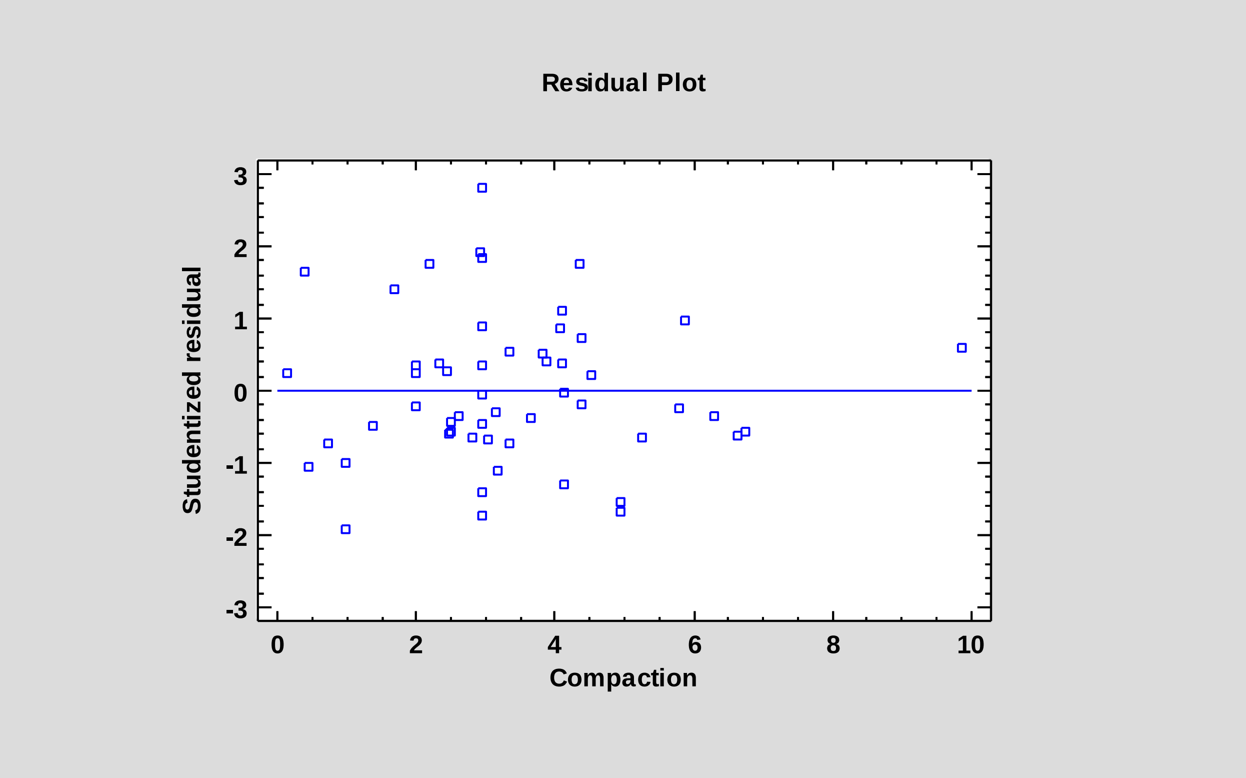

Figure 82. Residual plot by compaction (random scatter is desirable).

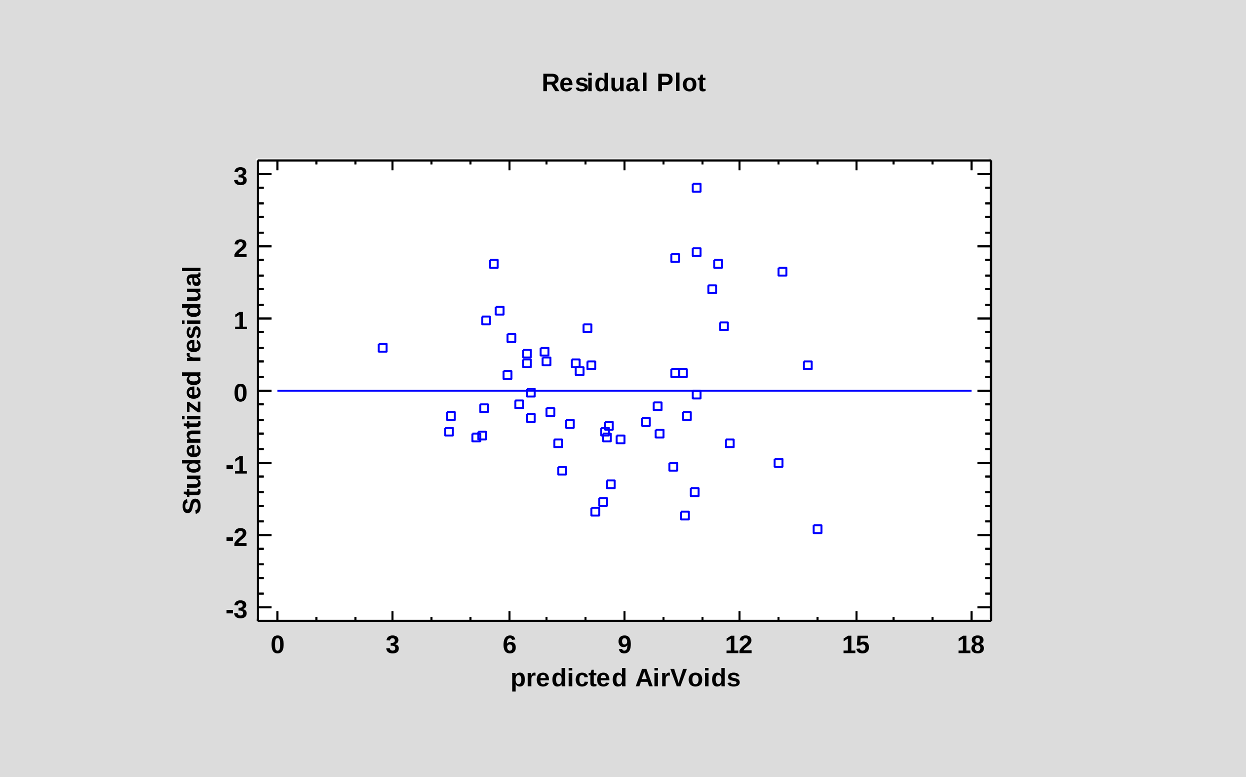

Figure 83. Residual plot by air voids (random scatter is desirable).

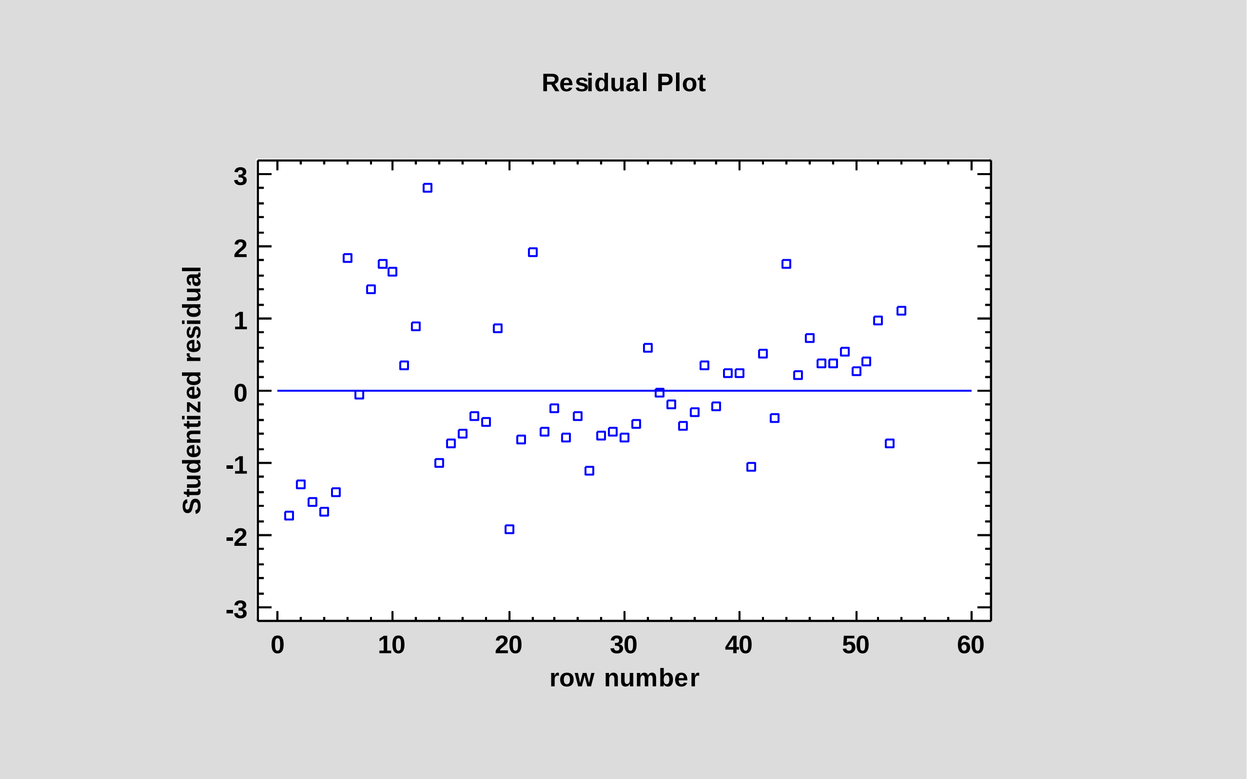

Figure 84. Residual plot by data row (see text for discussion).

The table of unusual residuals (Table 12) lists all observations that have studentized residuals greater than 2 in absolute value. Studentized residuals measure how many standard deviations each observed value of AirVoids deviates from a model fitted using all of the data except that observation. In this case, there is one studentized residual greater than 2, but none greater than 3.

Table 12. Unusual Residuals

		Predicted		*Studentized*
Row	*Y*	*Y*	*Residual*	*Residual*
13	17.41	10.859	6.55099	2.80

In Figure 84, it appears that there is some pattern to the residuals, and the unusual residual noted in Table 12 is fairly obvious. The row numbers for US 183 are 1 through 22, and the remainder of the row numbers are for US 90. Therefore, all of the residuals that are greater than zero and below row 22 are from US 183, and most of those are on the second night of paving. If that subset of the residuals is discarded from the plot, a linear pattern can be imagined in the residuals that slopes upward from left to right. This is probably the source of the concerns from the DW statistic mentioned earlier. It indicates that there may be another linear variable which has not been identified and incorporated into the model. The temperature used in the model is the first pass temperature. The difference between the first and last pass temperature may be an important variable that should be evaluated along with exploring other potential parameters.

Table 13 of influential data points lists all observations that have leverage values greater than three times that of an average data point or that have an unusually large value of DFITS. Leverage is a statistic that measures how influential each observation is in determining the coefficients of the estimated model. DFITS is a statistic that measures how much the estimated coefficients would change if each observation were removed from the data set. In this case, an average data point would have a leverage value equal to 0.0740741. There are two data points with more than three times the average leverage, but none with more than five times. There are two data points with unusually large values of DFITS. Note that all except one of the influential points came from the US 183 data.

Table 13. Influential Points

		Mahalanobis	
Row	*Leverage*	*Distance*	*DFITS*
11	0.331179	24.7676	0.248869
13	0.04921	1.71023	0.636096
20	0.142355	7.65005	-0.776725
32	0.32045	23.5401	0.416538

Average leverage of single data point = 0.0740741

Table 13 shows there are influential and unusual data points included in the analysis. The regression fit may improve if those data records are removed from the set. It was also found that there might be another factor that, if identified and included in the analysis, may improve the quality of the fit. It is also worth noting that the ANOVA and the regression analyses undertaken here are linear models. Since no obvious nonlinear pattern is seen in Figure 83, there is not a compelling reason to use nonlinear functional forms for the regression analysis. However, it should also be noted that the same figure might illustrate a small amount of divergence in the plot from left to right. This may be an indication of higher variability at higher air voids, which is not entirely unexpected since precise control of density on a thin mat at high voids is difficult at best.

CONCLUSION

The CMSs (PC and PLC systems) were developed in this project for proof of concept. The systems utilize the GPS technology with several sensors to provide real-time operator feedback, pertaining to the number of roller passes, location of each pass, operation mode, and mat temperature. The PC-based CMS was deployed in field projects to monitor the field compaction during construction. The CMS can be used to provide the consistent rolling sequence and compaction effectiveness of the mat. The proof of concept work showed the CMS can relate to eventual compacted density; however some additional variables requiring consideration may exist, and consideration of a linear or nonlinear approach to relating the CMS to density needs further study. Future work should be extended to enhance the capabilities of the systems and to improve the concept of the compaction index by considering more factors. Based on the research presented in this project, the following recommendations are made.

Recommendations

- The PLC version is ready for limited field testing and should be used in Phase II work.
- In addition to acquiring more data for prediction and analysis algorithms, other improvements should be explored, such as:

    - Communication between units, particularly when using multiple compactor echelon formations. This communication is envisioned to be a wireless LAN-type operation or a cloud-hosted wireless cellular type application.
    - New GPS units should be evaluated. The GPS units currently used for the CMS are quite capable units, but they are large and are becoming dated. Next to the battery, they are the largest/heaviest component of the system. Newer units may be smaller, lighter, and still have the desired position accuracy/resolution. Suitable new units may also be lower cost.
    - Miniaturization options should be evaluated. There are several small computer board products on the market that are typically used for building projects such as robots. Some of these products may be applicable to the CMS. However, durability and start-up costs in terms of the programming environment are factors that must be carefully evaluated.

- More field and laboratory tests are needed for better density prediction and analysis improvement.

CHAPTER 3. QUALITY ASSURANCE OF ASPHALT MIXTURE CONSTRUCTION USING GROUND-PENETRATING RADAR

BACKGROUND

Current Quality Assurance Methods

Long-term asphalt mixture performance is largely governed by compaction quality during construction (Vivar and Haddock 2006). Reducing the air voids seals the layer against moisture and oxidation and enhances structural integrity. In typical asphalt mixture construction, measuring mat density is a critical QA tool. The most common mat density measurement methods are nondestructive density gauge testing and measuring the bulk density of field cores (Choubane et al. 1998). Both of these methods are spot measurements, which exposes both the agency and contractor to significant risk due to the low level of test coverage.

Risk to the agency (consumer risk) occurs as follows. The agency accepts or rejects a whole day's production based on the results of a few random locations. In the end, the actual compaction variability on a project is unknown. In one case, the agency would accept this day's production based on the spot measurements, while the actual project has significant areas of under-compaction (a statistical Type II error). Since the life of a pavement is often governed by the worst-performing locations, the agency mistakenly accepts construction with limited life.

On the other hand, risk to the contractor (producer risk) occurs when the random spot locations coincide with localized under-compacted areas. In this case, the contractor receives a penalty for the day's production despite the fact that the large majority of the construction was acceptable (a statistical Type I error). Figure 85 illustrates the concept of Type I and II errors in acceptance testing.

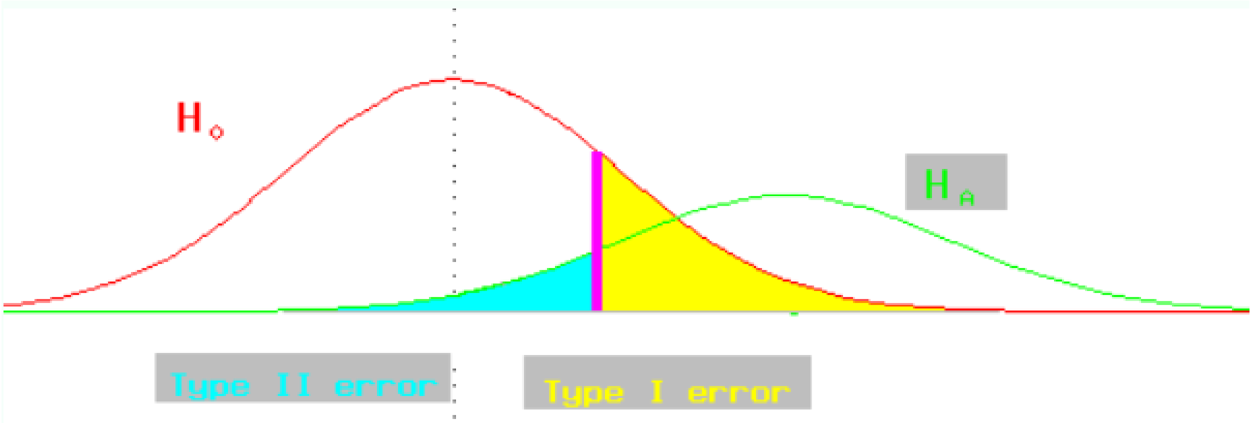

Figure 85. Illustration of Type I and II Errors in Acceptance Testing.

Another limitation of coring and density gauge testing is that the methods are often considered impractical for thin lift pavements. The lift can be too thin to feasibly extract, trim, and reliably measure the density. Nuclear and non-nuclear gauges are not recommended either because the probing depth of such devices is greater than the lift thickness of these treatments. Even thin lift gauges are not suitable for thicknesses less than 1.75 in. (44 mm), because the area of influence will include the underlying layer (Williams 2008).

Ground-Penetrating Radar

One promising technology for rapid, continuous QA of in-field density is GPR. This technology has shown significant promise is several past research studies (Sebesta and Scullion, 2002; Wilson and Sebesta, 2015; Popik, Maser, and Holzschuher 2009; Maser 2014; Maser and Carmichael 2015; Stroup-Gardiner and Brown 2000). GPR works by sending discrete pulses of electromagnetic waves into the pavement and capturing the reflections as the signal moves through the different layers. The amplitude of radar reflections and the time delay between reflections are used to calculate layer dielectrics. Dielectrics for various materials are shown in Figure 86. Within a given pavement layer, as the dielectric approaches 1.0, the air void content is assumed to be increasing. General surface dielectric values for HMA are between 4 and 6, depending on the aggregate type, asphalt content, and gradation. Very high dielectric values often indicate moisture on the surface.

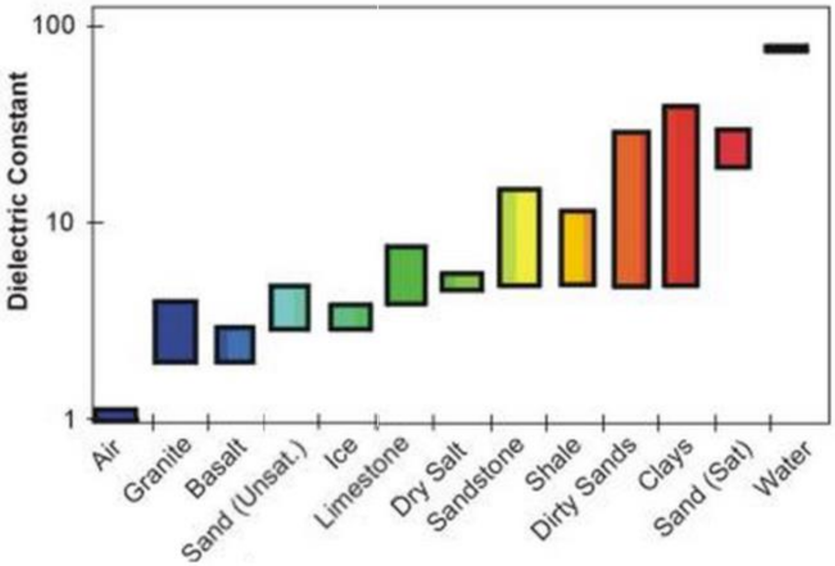

Figure 86. Materials and associated dielectric constants (U.S. Environmental Protecton Agency n.d.).

Lower frequency radar can penetrate deep into the pavement, while higher frequency radar (2 GHz and greater) will measure shallower depths at a higher resolution. A high-frequency radar, therefore, could have good resolution for typical HMA overlays less than 2 inches thick. Another advantage with a smaller, high-frequency antenna is that the unit is more portable, and easier to deploy for quick, nondestructive field measurements. The greatest benefit of the system, however, is the ability to collect continuous measurements rapidly.

To correlate the GPR to density, the operator needs to first generate a calibration curve. This is performed by first making spot measurements with the radar in several locations and then coring the same locations and measuring the air voids in the lab. With this correlation established, the GPR surface dielectric results can be immediately converted to air voids. This calibration currently needs to be performed on a project-by-project basis since the surface dielectric is affected by the specific mix design (aggregate type, asphalt content, and gradation).

Despite the promise of GPR as a QA technique, the technology has yet to move beyond research and into practice. There are still important questions to answer before adoption in the industry can happen:

- How precise and reproducible are the data from different GPR antennas?
- What are the correct procedures for establishing calibration curves between surface dielectric and core density?
- How sensitive is the surface dielectric to normal variation of HMA production?
- Are the hardware and software robust and user-friendly?

PROCEDURES

Precision and Reproducibility Analysis

The research team identified, sampled, and fabricated test slabs for precision testing using a TOM and a Type C (TY C) mix. The research team fabricated three slabs with each mix at different densities to meet the minimum of six materials required for development of precision estimates.

The research team developed and set up a system to precisely align the GPR test system repeatedly over the same spot of the asphalt mixture slabs to minimize variability from system positioning. Four different GPR antennas were used in the analysis. With each antenna and test slab, researchers collected measurements as follows to represent different expected test conditions:

- Constant on: 10 tests evenly spaced over a 1-hour period to represent the time frame for conducting a typical field survey.
- Hard reset: 10 tests after hard reset with at least 1 hour of system shut down, to represent shutting down the system and returning to the survey site for additional testing at a later time.

Researchers collected at least 1,000 scans in the time mode for each test. In reducing each data file, staff reported the dielectric from each test with two different approaches to represent the minimum and maximum number of scans that may be suitable for averaging depending on the forward travel speed of the radar system when used in the field:

- Average five scans starting with scan number 200.
- Average 500 scans starting with scan number 200.

With the data reduced, researchers analyzed the data as follows:

- Used a paired t-test to evaluate if the average dielectric from five scans is equivalent to the average value from 500 scans.
- Used processing methods of ASTM E691 to develop repeatability and reproducibility estimates for the measured dielectric values.

Figure 87 shows the general test arrangement. The antennas were operated at a distance of 11.5 in. from the asphalt surface to the bottom of the antenna. The antennas were leveled within ±0.0° on the transverse axis and within ±0.5° on the longitudinal axis. An alignment method was used to position each antenna at the same location over each test slab within ±0.15 in. The ambient environment during testing was 22 ±2°C.

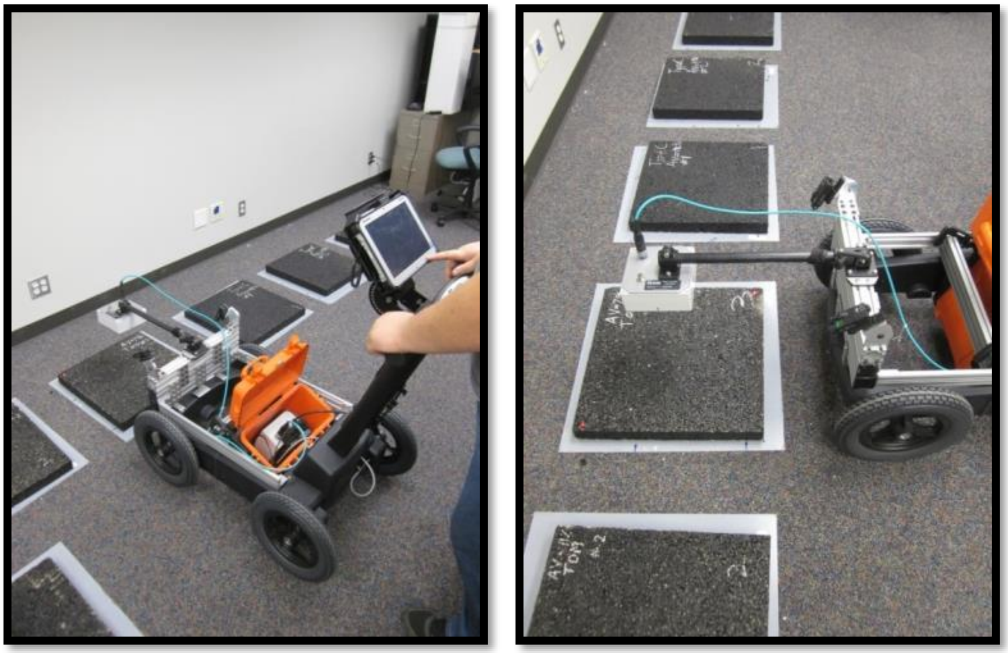

Figure 87. Test Arrangement for Precision of Radar System.

The research team also investigated the impact of layer thickness on the GPR measurements. The research team used the precision data to perform an analytical study on the impact of how GPR reproducibility may impact calibration needs.

Calibration Procedures between GPR Data and In-Field Density

The surface dielectric of compacted HMA depends not only on in-place density, but also on the specific asphalt mixture properties (asphalt content, aggregate type, and aggregate bin percentages). To account for these factors, the surface dielectric measurements from the GPR must be calibrated for each mixture type. However, if this calibration curve is inaccurate, the subsequent density predictions will also be incorrect.

The researchers evaluated the procedures for developing calibration curves at the Texas A&M Riverside Campus, and again evaluated the reproducibility of each GPR channel. They considered the effect of measurement location accuracy and sample size.

The researchers measured 1000 feet with three channels and, using an algorithm in the GPR software, selected 10 spot locations with low, moderate, and high surface dielectric values. Centered at each location, the surface dielectric was measured with each antenna in two methods: first, with a spot reading in time mode, and then along a 24-inch line path with the position of 12 inches corresponding to the center of the spot. In this manner, the surface dielectric could be computed on the exact location, on the location with a 6-inch moving average, and at a location +/- 6 and 12 inches from the spot. To ensure the GPR antennas were positioned accurately, a laser system was mounted onto the system and aligned directly under each antenna (Figure 88). After GPR measurements, 6-inch-diameter cores were taken centered on the location and in some cases offset by 6 inches. The measurement and core-sampling configuration is illustrated in Figure 89.

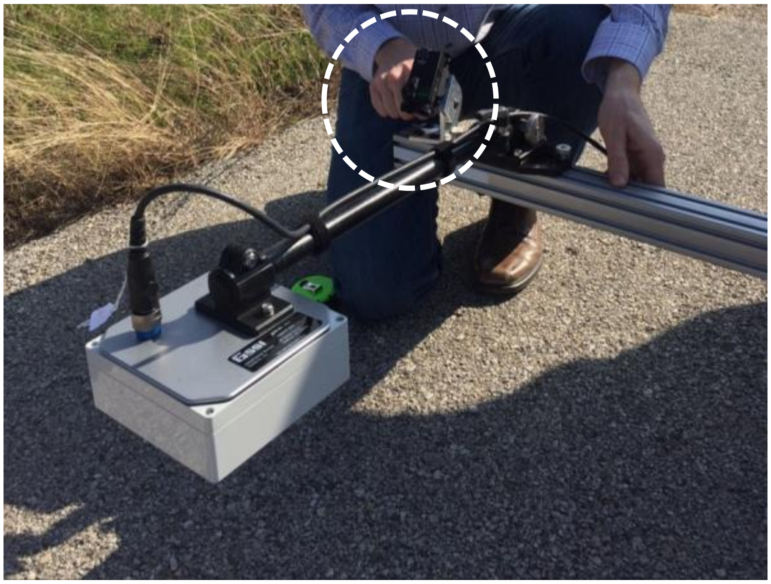

Figure 88. Laser-Alignment System.

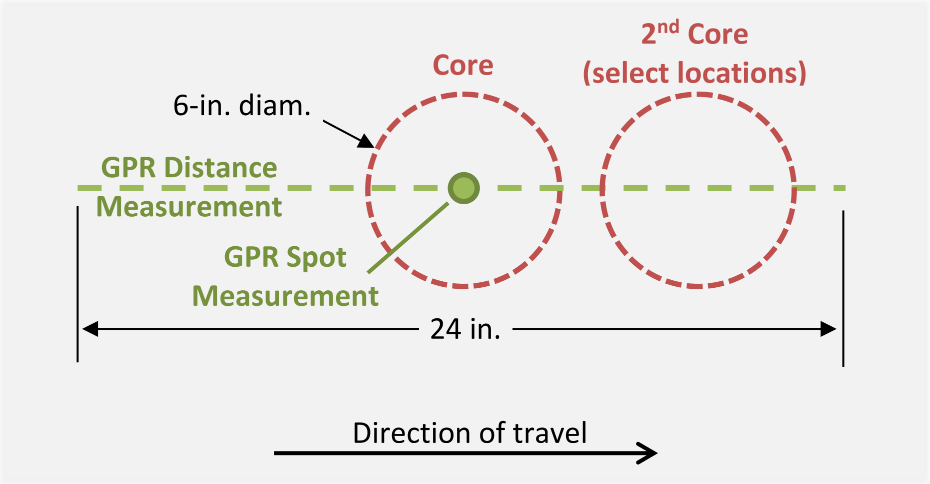
2nd Core
(select locations)
Core
6-in. diam.
GPR Distance
Measurement
GPR Spot
Measurement
24 in.
Direction of travel

Figure 89. Measurement Layout.

The bulk density of each core was measured by three methods: first, the full intact core; second, the core reduced to a 4-inch diameter at the spot location; and third, the 4-inch core trimmed to a thickness of 1 inch.

Calibration curves were identified for each of these scenarios and with each antenna, and the calibration coefficients were compared statistically.

To consider the impact of the measurement location accuracy on the calibration curve, researchers performed a Monte Carlo-like simulation to simulate random 0-, 6- and 12-inch offsets of surface dielectric measurement from the core locations. The calibration curves from 30 random scenarios were plotted as the potential window of error.

To consider the impact of sample size on the calibration curve, the researchers again randomly sampled five and seven samples to create calibration curves. Each of these curves was plotted and the potential window of error illustrated.

Field Implementation

The GPR system was deployed on two construction projects in the 2016 paving season: the first was a TOM-F job on US 183 in the Austin District, and the second was a Superpave Ty-D on US 90 in Liberty in the Beaumont District.

The US 183 project is located in Travis County, and the entire distance of the project is about 2.2 miles, as shown in Figure 90. The project is a rural, four-lane undivided highway. A TOM-F (9.5 mm nominal maximum size) mix was placed on top of an existing seal coat, and the lift thickness was 0.75 inches. Dual Bomag 190 breakdown rollers were used to compact the mat.

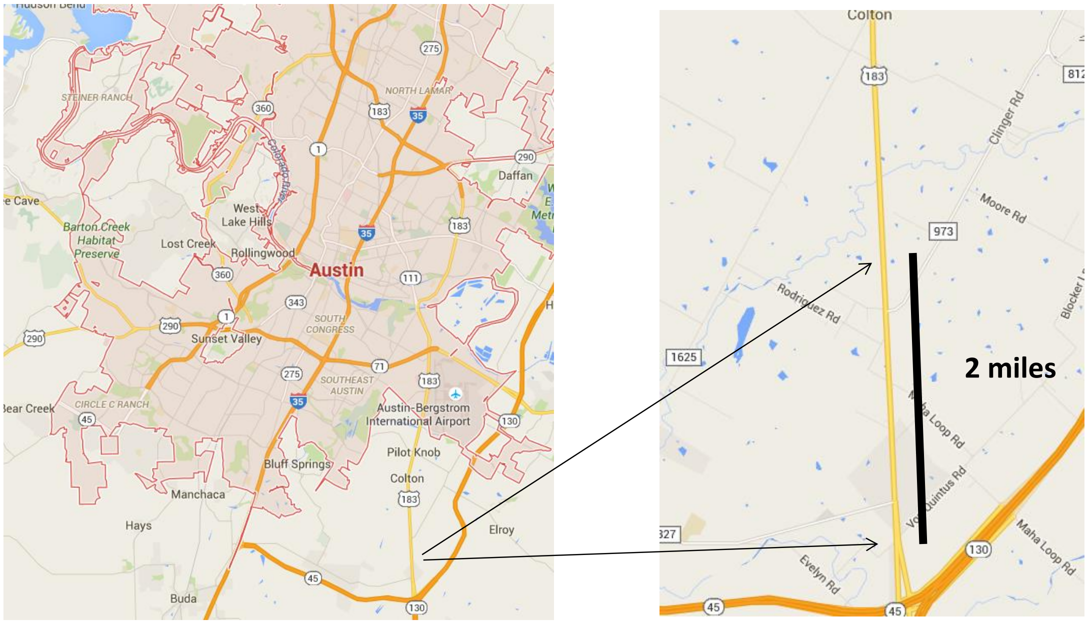
Austin
Steiner Ranch
North Lamar
Daffan
West Lake Hills
Barton Creek Habitat Preserve
Lost Creek
Rollingwood
South Congress
Sunset Valley
Southeast Austin
Circle C Ranch
Austin-Bergstrom International Airport
Pilot Knob
Bluff Springs
Colton
Manchaca
Hays
Elroy
Buda
Bear Creek
Colton
Clinger Rd
Moore Rd
Rodriguez Rd
Maha Loop Rd
Evelyn Rd
2 miles

Figure 90. US 183 Project Location.

The US 90 project is located in Liberty, and the entire distance of the project is about 2.6 miles, as seen in Figure 91. This roadway is an undivided seven-lane highway, including the center turn lane. A Superpave D (9.5 mm nominal maximum size) mix with a thickness of 1.5 inches was laid after milling the existing HMA layer. The subsurface pavement was heavily distressed, jointed concrete. A HAMM HD 120 breakdown roller was used to compact the entire mat with a 12 feet mat width.

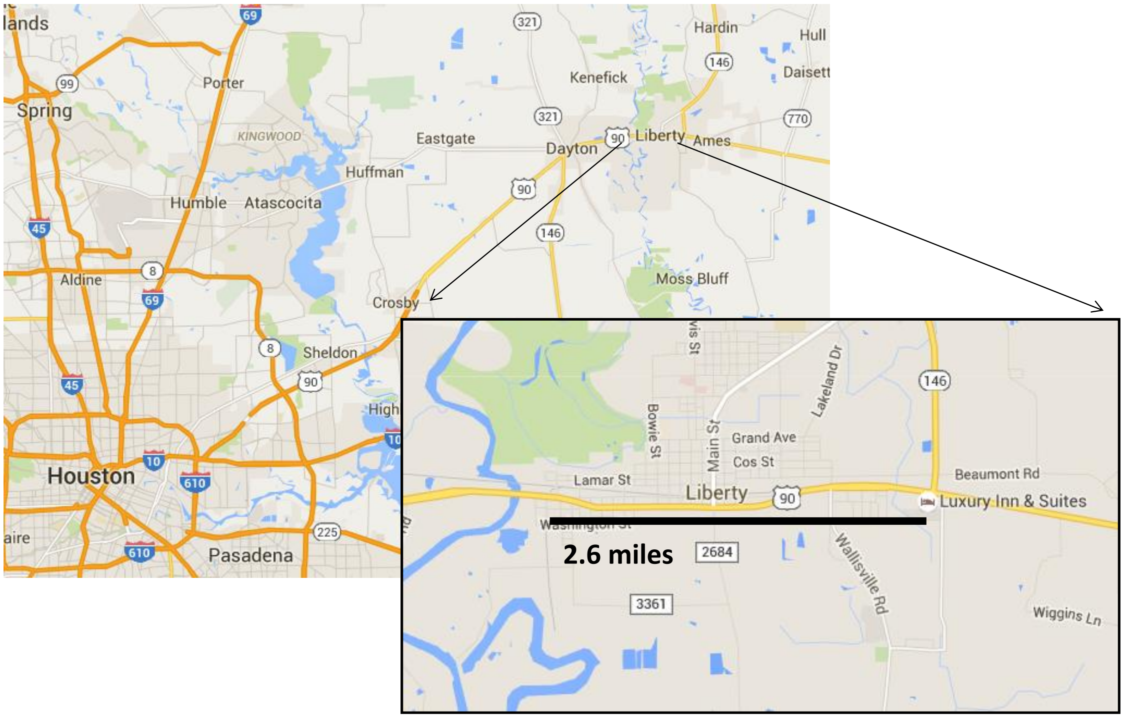
lands
Spring
Porter
Kingwood
Humble
Atascocita
Huffman
Eastgate
Dayton
Liberty
Ames
Kenefick
Hardin
Hull
Daisett
Moss Bluff
Aldine
Crosby
Sheldon
Houston
Pasadena
aire
High
Bowie St
Main St
Grand Ave
Cos St
Lamar St
Lakeland Dr
Beaumont Rd
Luxury Inn & Suites
Washington St
Wallisville Rd
Wiggins Ln
2.6 miles
2684
3361
146
90

Figure 91. US 90 Field Project Location.

Table 14 summarizes details for each mixture type used in the field projects.

Table 14. Project and Asphalt Mixture Details.

Project ID	Mix Type	Binder Type	Optimum AC (%)	Aggregate Type	Theo. Max SG	Thickness (in.)
US 183	TOM-F	PG76-22	7.2	Sandstone (Delta Mtls)	2.376	0.75
US 90	SP Ty-D	PG70-22	5.2	Quartzite (Jones Mill) Limestone (Medina)	2.443	1.50

TTI researchers performed density testing on each project for three days of paving (Figure 92). On the first day, they established a 1000-ft test section and measured the surface dielectric with the three-channel GPR system over the centerline and both wheel patches. The core-location software identified 10 spot locations with low, moderate, and high surface dielectric values. At each location, the researchers made spot measurements with the GPR system by collecting in time mode and moving the antenna +/- 6 in. over the core location. In-place density was then measured using a nuclear density gauge, and then a 6-inch core was sampled. These readings were intended to serve as a density calibration curve for the remainder of the project.

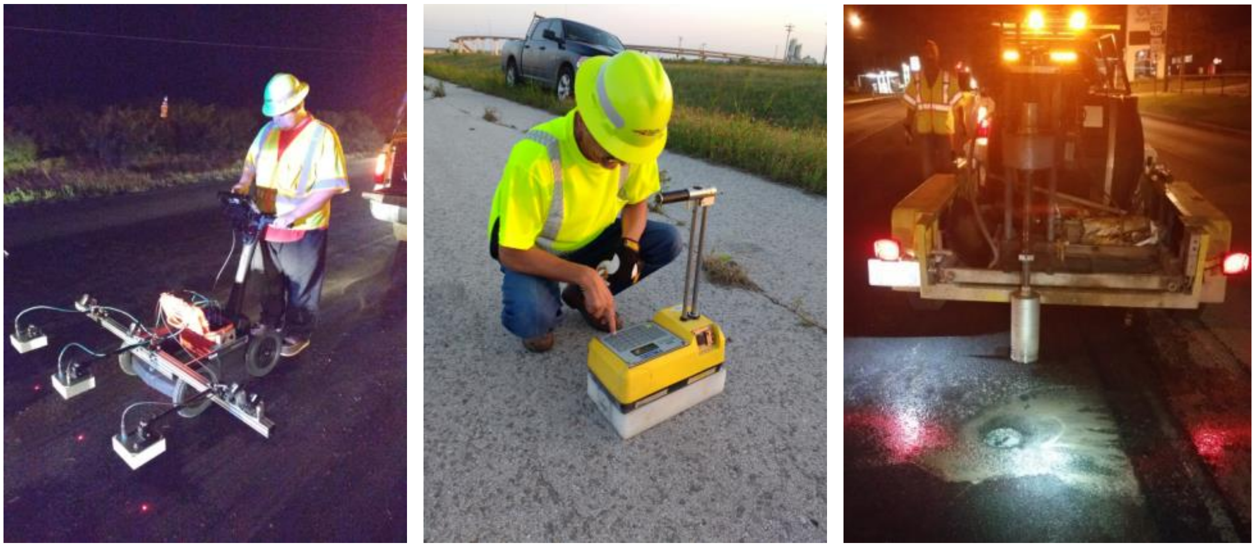

(a) **(b)** **(c)**

Figure 92. Testing and Sampling: (a) Surface Dielectric, (b) Nuclear Density, (c) Cores for Bulk Density

On the second and third days, the researchers measured surface dielectric over both wheel paths and the centerline for a large portion of the project (between 6000 and 8000 ft per day of testing). Ten locations were randomly selected within the first 6000 ft of paving (Figure 93). Surface dielectric and nuclear density gauge readings were made at each location followed by coring. The air voids of the field cores were measured in the lab.

Loose mixture was sampled on all three days of paving, and TxDOT and contractor QC/QA data were collected.

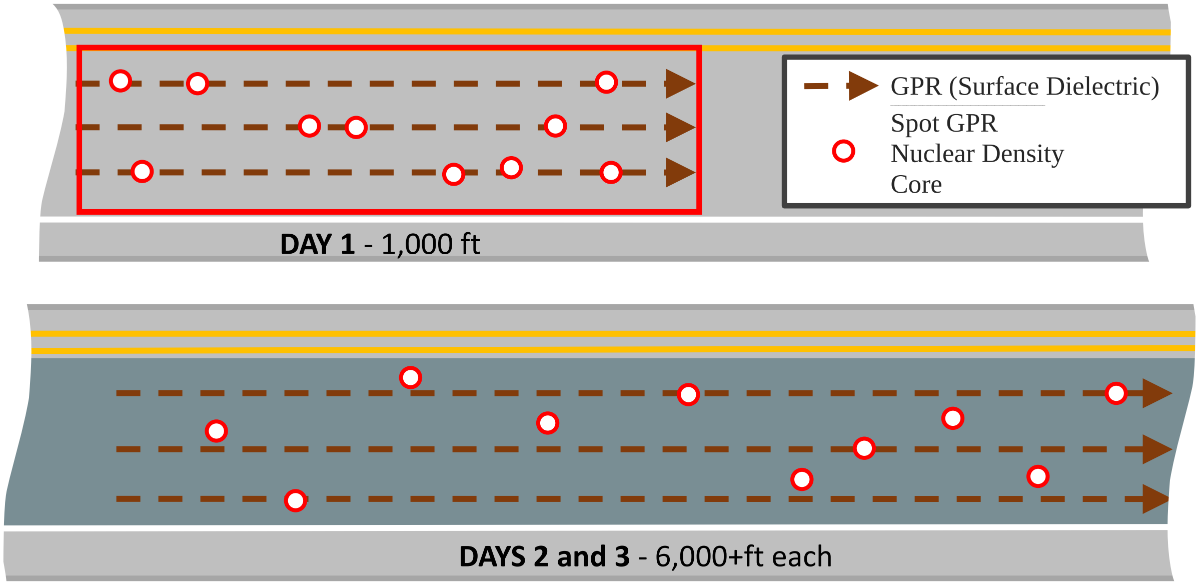
GPR (Surface Dielectric)
Spot GPR
Nuclear Density
Core
DAY 1 - 1,000 ft
DAYS 2 and 3 - 6,000+ft each

Figure 93. Test Section Layout.

Using the Day 1 results, a surface dielectric calibration curve was determined. This calibration was then applied to the subsequent days of paving to predict the continuous density in and between the wheel paths. Calibration curves were also identified for Days 2 and 3 and the correlation results were compared to the Day 1 correlations.

RESULTS

Precision and Reproducibility Analysis

Table 15 presents the paired t-test results. Using a 5 percent level of significance, the results show:

- For a given antenna and test condition, only Antenna 7A resulted in computed dielectrics that differed according to how many scans were averaged.
- For all antennas pooled within a test condition, the number of scans averaged did not influence the computed dielectric for the constant on condition. For all antennas pooled with the hard reset test condition, the number of scans averaged did produce statistically different results.

- For all antennas and test conditions pooled, the number of scans averaged did produce statistically different results.

Further investigation of these data in Table 15 revealed that, if Antenna 7A is omitted, the computed dielectric value is not impacted by whether five scans or 500 scans are averaged to report the test result.

Table 15. Paired t-test Results for Computing Dielectric with either 5 or 500 Scans.

Test Condition	Antenna	Slab	xbar 5	xbar 500	Difference	p value (1 antenna)	p value (test condition) (all antenna,	p value (all)
Constant On	8	1	6.4234	6.4199	-0.0035	0.768	0.242	0.016
		2	5.9556	5.9566	0.0010			
		3	6.0472	6.0351	-0.0121			
		4	4.9851	4.9915	0.0064			
		5	5.1274	5.1380	0.0106			
		6	4.3705	4.3742	0.0037			
	7a	1	6.6090	6.5835	-0.0256	0.032		
		2	6.1173	6.1236	0.0062			
		3	6.0623	6.0097	-0.0526			
		4	5.0410	4.9865	-0.0544			
		5	4.9896	4.9740	-0.0156			
		6	4.3537	4.3293	-0.0244			
	7b	1	6.3070	6.3156	0.0085	0.228		
		2	6.1051	6.1221	0.0170			
		3	5.9476	5.9537	0.0061			
		4	5.0333	5.0351	0.0018			
		5	5.0276	5.0150	-0.0126			
		6	4.3401	4.3554	0.0153			
	3	1	6.4114	6.4017	-0.0097	0.573		
		2	6.0403	6.0550	0.0147			
		3	6.0007	6.0068	0.0062			
		4	5.0652	5.0671	0.0018			
		5	5.0983	5.0937	-0.0046			
		6	4.4239	4.4281	0.0042			
Hard Reset	8	1	6.4647	6.4516	-0.0131	0.592	0.010	
		2	6.0623	6.0507	-0.0116			
		3	6.0257	6.0419	0.0162			
		4	5.0198	5.0119	-0.0079			
		5	5.1043	5.0969	-0.0074			
		6	4.4048	4.4121	0.0073			
	7a	1	6.6744	6.6540	-0.0203	0.002		
		2	6.2088	6.1817	-0.0270			
		3	6.1864	6.1654	-0.0210			
		4	5.0333	5.0173	-0.0160			
		5	5.0733	5.0630	-0.0104			
		6	4.3804	4.3714	-0.0091			
	7b	1	6.4687	6.4785	0.0098	0.582		
		2	6.0827	6.0837	0.0010			
		3	6.0523	6.0539	0.0016			
		4	5.0509	5.0316	-0.0194			
		5	5.0724	5.0731	0.0007			
		6	4.3783	4.3701	-0.0082			
	3	1	6.4769	6.4605	-0.0164	0.464		
		2	6.0756	6.0592	-0.0164			
		3	6.0400	6.0308	-0.0092			
		4	4.9890	5.0022	0.0132			
		5	5.0529	5.0562	0.0032			
		6	4.3664	4.3685	0.0022			

Due to the observed potential influence of the number of scans averaged, TTI developed precision statistics both by averaging five scans, and by averaging 500 scans. Table 16 presents the summary data from computing the dielectric value for each test by averaging five scans. Table 17 presents the summary data from computing the dielectric value for each test by averaging 500 scans.

Table 16. Precision Summary Data using a 5-Scan Average to Measure Dielectric.

Test Condition	Slab	Antenna	xbar (from 10 tests)	s	d	h	k	xbarbar	s xbar	s repeat	sL2	s repro	Repeatability limit	Reproducibility Limt
Constant On	1	8	6.423	0.047	-0.014	-0.114	0.852	6.438	0.126	0.055	0.015	0.136	0.15	0.38
		7a	6.609	0.078	0.171	1.364	1.407							
		7b	6.307	0.027	-0.131	-1.040	0.489							
		3	6.411	0.057	-0.026	-0.210	1.028							
	2	8	5.956	0.033	-0.099	-1.335	0.480	6.055	0.074	0.069	0.005	0.099	0.19	0.28
		7a	6.117	0.117	0.063	0.846	1.685							
		7b	6.105	0.039	0.051	0.681	0.558							
		3	6.040	0.055	-0.014	-0.193	0.787							
	3	8	6.047	0.048	0.033	0.634	0.605	6.014	0.052	0.079	0.002	0.091	0.22	0.26
		7a	6.062	0.120	0.048	0.925	1.518							
		7b	5.948	0.059	-0.067	-1.293	0.752							
		3	6.001	0.069	-0.014	-0.266	0.874							
	4	8	4.985	0.055	-0.046	-1.371	1.067	5.031	0.034	0.051	0.001	0.059	0.14	0.17
		7a	5.041	0.076	0.010	0.293	1.492							
		7b	5.033	0.033	0.002	0.063	0.646							
		3	5.065	0.024	0.034	1.015	0.467							
	5	8	5.127	0.031	0.067	1.053	0.640	5.061	0.063	0.048	0.004	0.078	0.14	0.22
		7a	4.990	0.075	-0.071	-1.124	1.552							
		7b	5.028	0.039	-0.033	-0.523	0.813							
		3	5.098	0.035	0.038	0.594	0.722							
	6	8	4.370	0.031	-0.002	-0.042	0.630	4.372	0.037	0.049	0.001	0.060	0.14	0.17
		7a	4.354	0.088	-0.018	-0.500	1.776							
		7b	4.340	0.026	-0.032	-0.869	0.525							
		3	4.424	0.021	0.052	1.412	0.417							
Hard Reset	1	8	6.465	0.051	-0.056	-0.552	1.038	6.521	0.102	0.049	0.010	0.112	0.14	0.31
		7a	6.674	0.054	0.153	1.498	1.110							
		7b	6.469	0.035	-0.052	-0.513	0.724							
		3	6.477	0.053	-0.044	-0.433	1.080							
	2	8	6.062	0.029	-0.045	-0.661	0.657	6.107	0.068	0.045	0.004	0.080	0.13	0.22
		7a	6.209	0.056	0.101	1.488	1.248							
		7b	6.083	0.046	-0.025	-0.362	1.038							
		3	6.076	0.043	-0.032	-0.466	0.966							
	3	8	6.026	0.060	-0.050	-0.678	1.012	6.076	0.074	0.059	0.005	0.093	0.17	0.26
		7a	6.186	0.056	0.110	1.484	0.941							
		7b	6.052	0.054	-0.024	-0.320	0.920							
		3	6.040	0.066	-0.036	-0.486	1.116							
	4	8	5.020	0.047	-0.003	-0.132	1.135	5.023	0.026	0.042	0.001	0.047	0.12	0.13
		7a	5.033	0.033	0.010	0.385	0.790							
		7b	5.051	0.032	0.028	1.057	0.770							
		3	4.989	0.051	-0.034	-1.310	1.222							
	5	8	5.104	0.030	0.029	1.344	0.675	5.076	0.021	0.044	0.000	0.047	0.12	0.13
		7a	5.073	0.067	-0.002	-0.113	1.518							
		7b	5.072	0.024	-0.003	-0.156	0.546							
		3	5.053	0.043	-0.023	-1.075	0.971							
	6	8	4.405	0.036	0.022	1.385	0.895	4.382	0.016	0.040	0.000	0.041	0.11	0.12
		7a	4.380	0.059	-0.002	-0.127	1.479							
		7b	4.378	0.024	-0.004	-0.260	0.604							
		3	4.366	0.032	-0.016	-0.998	0.804							

Table 17. Precision Summary Data using a 500-Scan Average to Measure Dielectric.

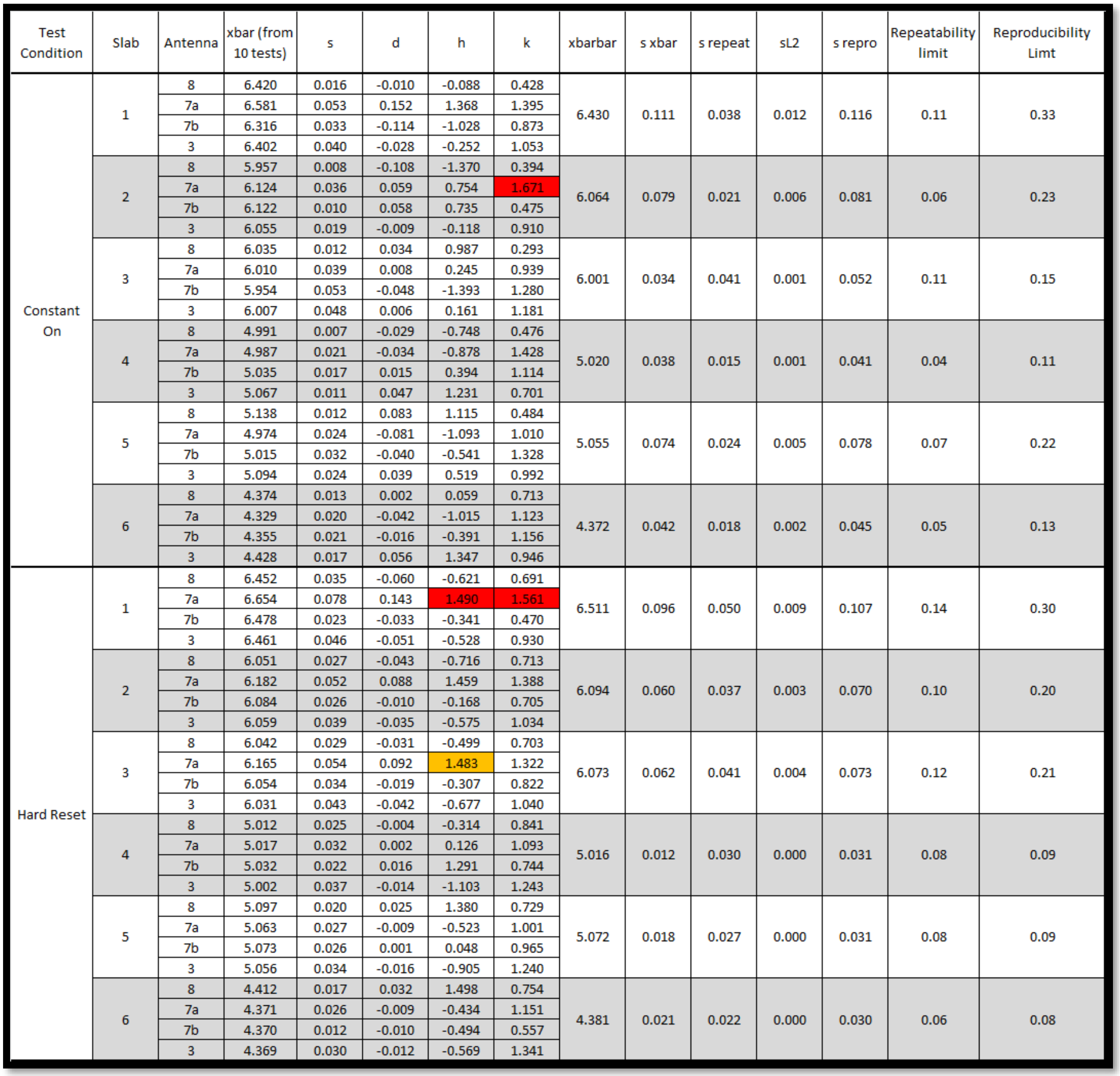

Test Condition	Slab	Antenna	xbar (from 10 tests)	s	d	h	k	xbarbar	s xbar	s repeat	sL2	s repro	Repeatability limit	Reproducibility Limt
Constant On	1	8	6.420	0.016	-0.010	-0.088	0.428	6.430	0.111	0.038	0.012	0.116	0.11	0.33
		7a	6.581	0.053	0.152	1.368	1.395							
		7b	6.316	0.033	-0.114	-1.028	0.873							
		3	6.402	0.040	-0.028	-0.252	1.053							
	2	8	5.957	0.008	-0.108	-1.370	0.394	6.064	0.079	0.021	0.006	0.081	0.06	0.23
		7a	6.124	0.036	0.059	0.754	1.671							
		7b	6.122	0.010	0.058	0.735	0.475							
		3	6.055	0.019	-0.009	-0.118	0.910							
	3	8	6.035	0.012	0.034	0.987	0.293	6.001	0.034	0.041	0.001	0.052	0.11	0.15
		7a	6.010	0.039	0.008	0.245	0.939							
		7b	5.954	0.053	-0.048	-1.393	1.280							
		3	6.007	0.048	0.006	0.161	1.181							
	4	8	4.991	0.007	-0.029	-0.748	0.476	5.020	0.038	0.015	0.001	0.041	0.04	0.11
		7a	4.987	0.021	-0.034	-0.878	1.428							
		7b	5.035	0.017	0.015	0.394	1.114							
		3	5.067	0.011	0.047	1.231	0.701							
	5	8	5.138	0.012	0.083	1.115	0.484	5.055	0.074	0.024	0.005	0.078	0.07	0.22
		7a	4.974	0.024	-0.081	-1.093	1.010							
		7b	5.015	0.032	-0.040	-0.541	1.328							
		3	5.094	0.024	0.039	0.519	0.992							
	6	8	4.374	0.013	0.002	0.059	0.713	4.372	0.042	0.018	0.002	0.045	0.05	0.13
		7a	4.329	0.020	-0.042	-1.015	1.123							
		7b	4.355	0.021	-0.016	-0.391	1.156							
		3	4.428	0.017	0.056	1.347	0.946							
Hard Reset	1	8	6.452	0.035	-0.060	-0.621	0.691	6.511	0.096	0.050	0.009	0.107	0.14	0.30
		7a	6.654	0.078	0.143	1.490	1.561							
		7b	6.478	0.023	-0.033	-0.341	0.470							
		3	6.461	0.046	-0.051	-0.528	0.930							
	2	8	6.051	0.027	-0.043	-0.716	0.713	6.094	0.060	0.037	0.003	0.070	0.10	0.20
		7a	6.182	0.052	0.088	1.459	1.388							
		7b	6.084	0.026	-0.010	-0.168	0.705							
		3	6.059	0.039	-0.035	-0.575	1.034							
	3	8	6.042	0.029	-0.031	-0.499	0.703	6.073	0.062	0.041	0.004	0.073	0.12	0.21
		7a	6.165	0.054	0.092	1.483	1.322							
		7b	6.054	0.034	-0.019	-0.307	0.822							
		3	6.031	0.043	-0.042	-0.677	1.040							
	4	8	5.012	0.025	-0.004	-0.314	0.841	5.016	0.012	0.030	0.000	0.031	0.08	0.09
		7a	5.017	0.032	0.002	0.126	1.093							
		7b	5.032	0.022	0.016	1.291	0.744							
		3	5.002	0.037	-0.014	-1.103	1.243							
	5	8	5.097	0.020	0.025	1.380	0.729	5.072	0.018	0.027	0.000	0.031	0.08	0.09
		7a	5.063	0.027	-0.009	-0.523	1.001							
		7b	5.073	0.026	0.001	0.048	0.965							
		3	5.056	0.034	-0.016	-0.905	1.240							
	6	8	4.412	0.017	0.032	1.498	0.754	4.381	0.021	0.022	0.000	0.030	0.06	0.08
		7a	4.371	0.026	-0.009	-0.434	1.151							
		7b	4.370	0.012	-0.010	-0.494	0.557							
		3	4.369	0.030	-0.012	-0.569	1.341							

The results in Table 16 and Table 17 show that:

- The dielectric values included in the precision tests ranged from 4.4 to 6.4.
- Within that range of dielectric values:
  - The repeatability limit averages 0.15 when using five scans to generate a measurement, and the repeatability limit averages 0.09 when using 500 scans to generate a measurement.

  - The reproducibility limit averages 0.22 when using five scans to generate a measurement, and the reproducibility limit averages 0.18 when using 500 scans to generate a measurement.

- With some test conditions and data processing methods, the precision limit may increase as the actual material dielectric constant increases, as Figure 94 illustrates. This situation of increased variability with increasing values is common with many tests and not a cause for concern.

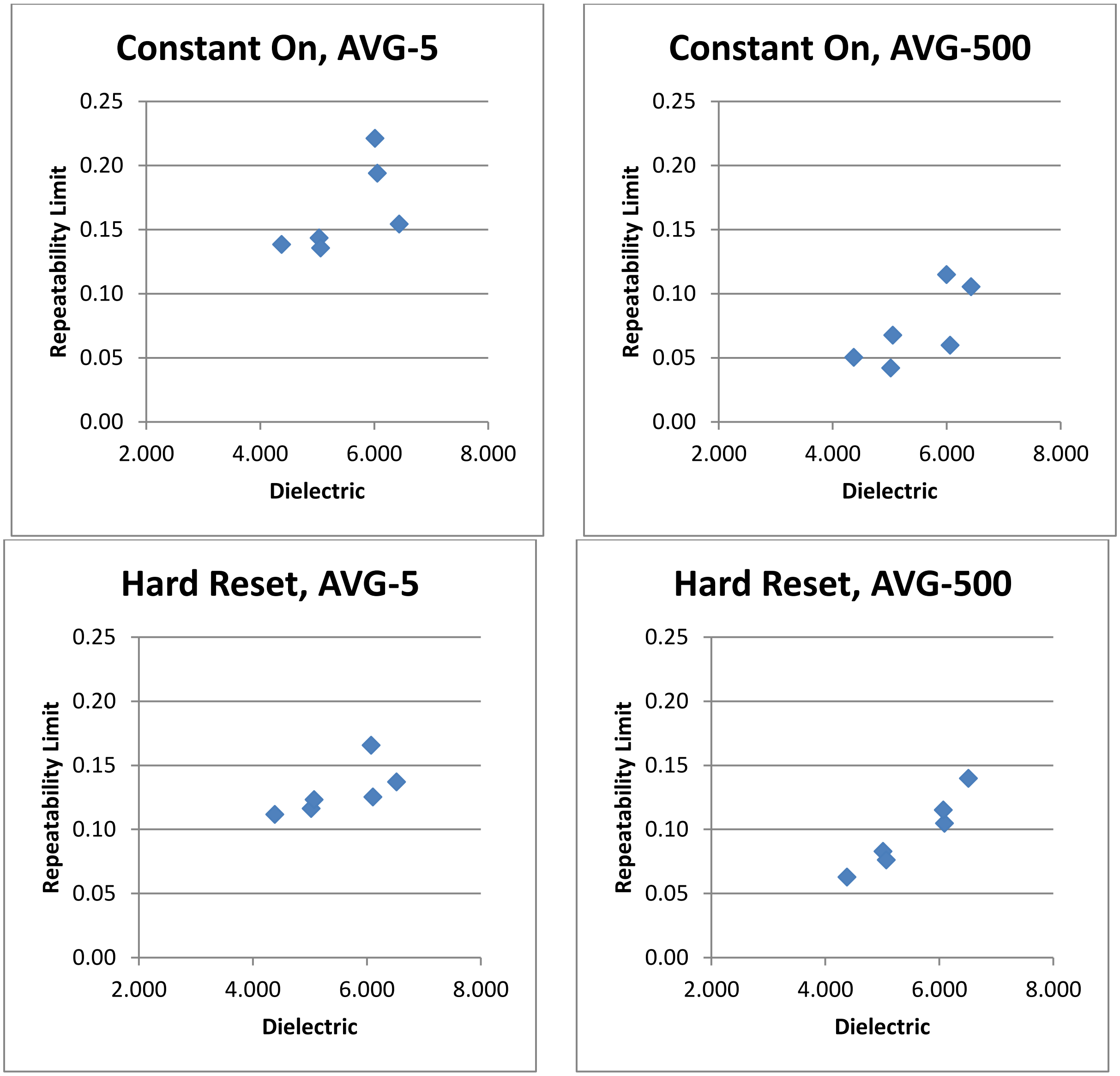

Figure 94. Potential Relationship between Precision Limit and Material Dielectric.

- The consistency statistics, *h* and *k*, suggest issues may exist with Antenna 7A. In review of the data with lab staff, no data collection, tabulation, reduction, or reporting errors were discovered with this antenna. Specific observations in consistency for this antenna include:

- With the hard reset test condition and materials 1–3, which were the same mixture type only at different compacted densities, the between-lab consistency statistic *h* for Antenna 7A was positive, while *h* for all other antennas in the hard reset test condition and materials 1–3 was negative. In this test condition and with that particular asphalt mixture type, the data suggest Antenna 7A systematically measured higher dielectric values than all the other antennas. Figure 95 illustrates the *h* statistics.
- Regardless of test condition, all high within-lab consistency *k* values occurred with Antenna 7A. This situation indicates that particular antenna has imprecision as compared to the other antenna. The data particularly show this problem in the constant on test condition when only five scans were averaged to measure the dielectric constant. Figure 96 illustrates the *k* statistics.

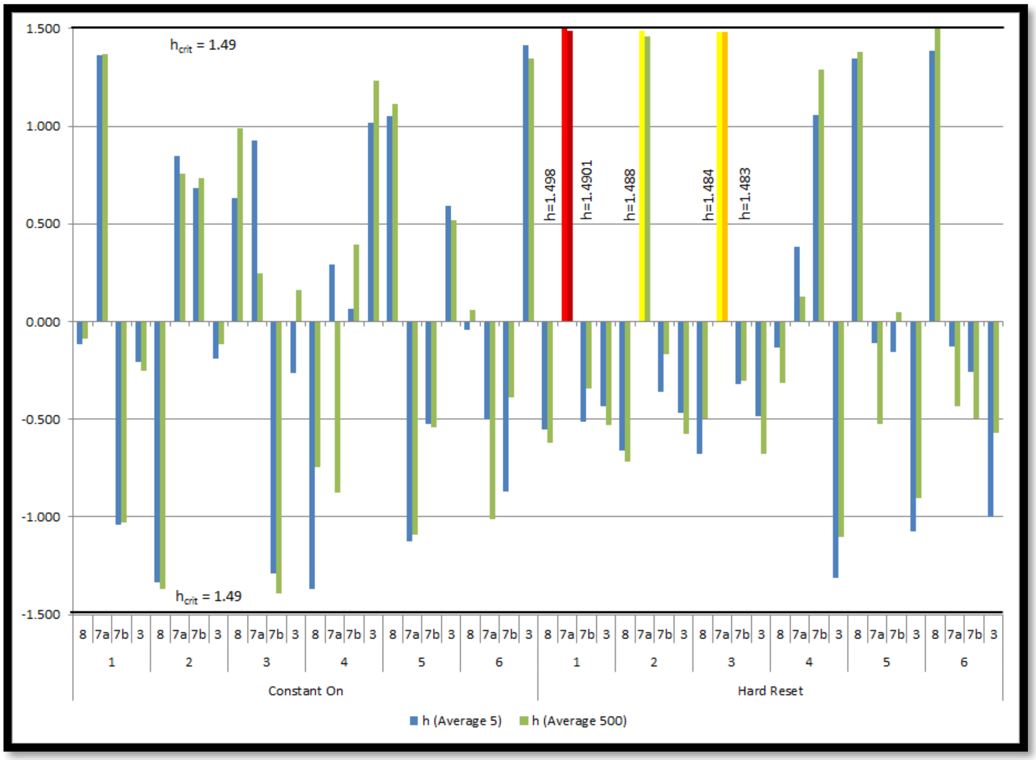

Figure 95. Between-Lab Consistency h for Precision Test.

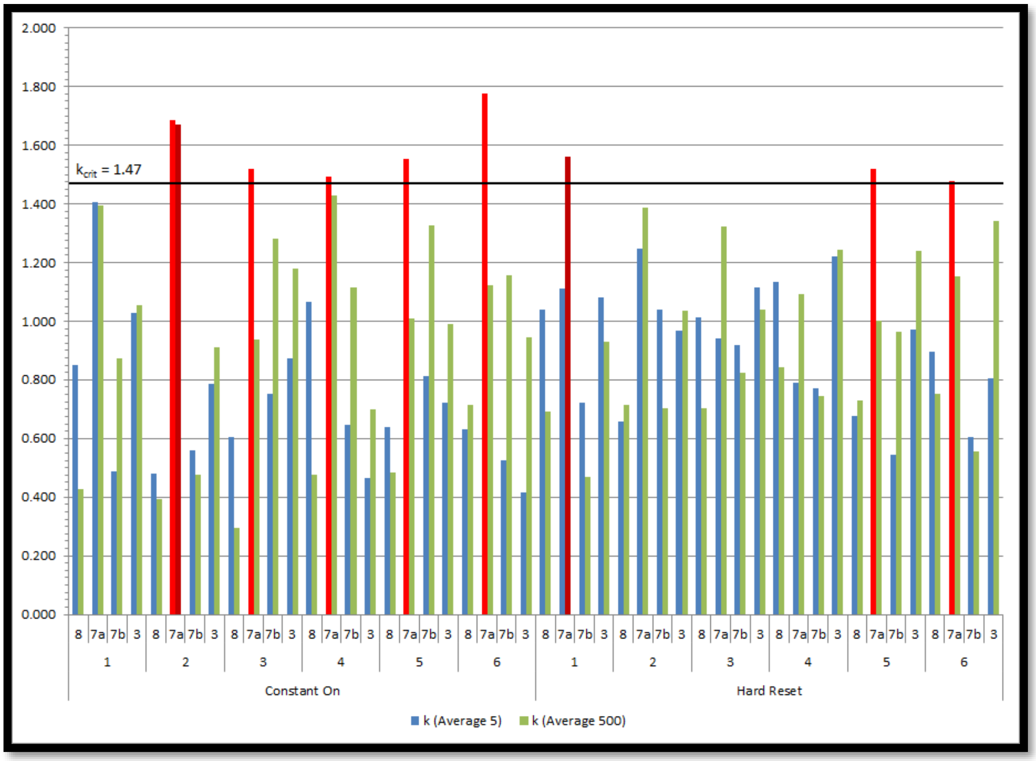

Figure 96. Within-Lab Consistency k for Precision Test.

Further analysis of data from Antenna 7A show two possible sources of problems:

- In some data files, the measured dielectric at the beginning of a scan starts at an elevated value and then decreases to a stable mean plus noise, as Figure 97 illustrates.
- Antenna 7A appears to possibly exhibit more random noise than other antennas, as Figure 98 illustrates.

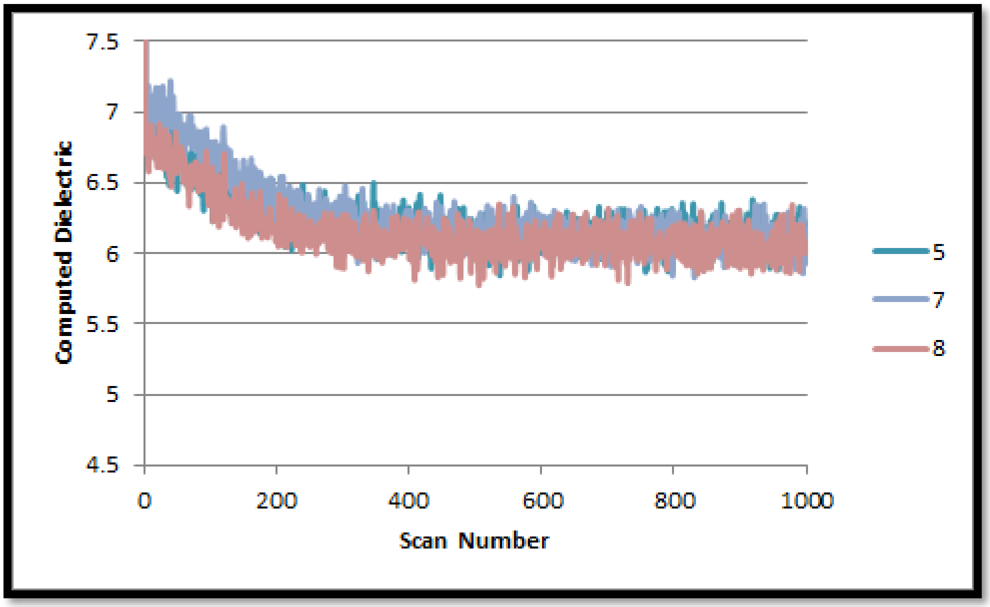

Figure 97. Example Unstable initial Readings with Antenna 7A.
Note: Slab 2, Constant On Test Condition—Data Collection runs 5, 7, and 8 illustrated.

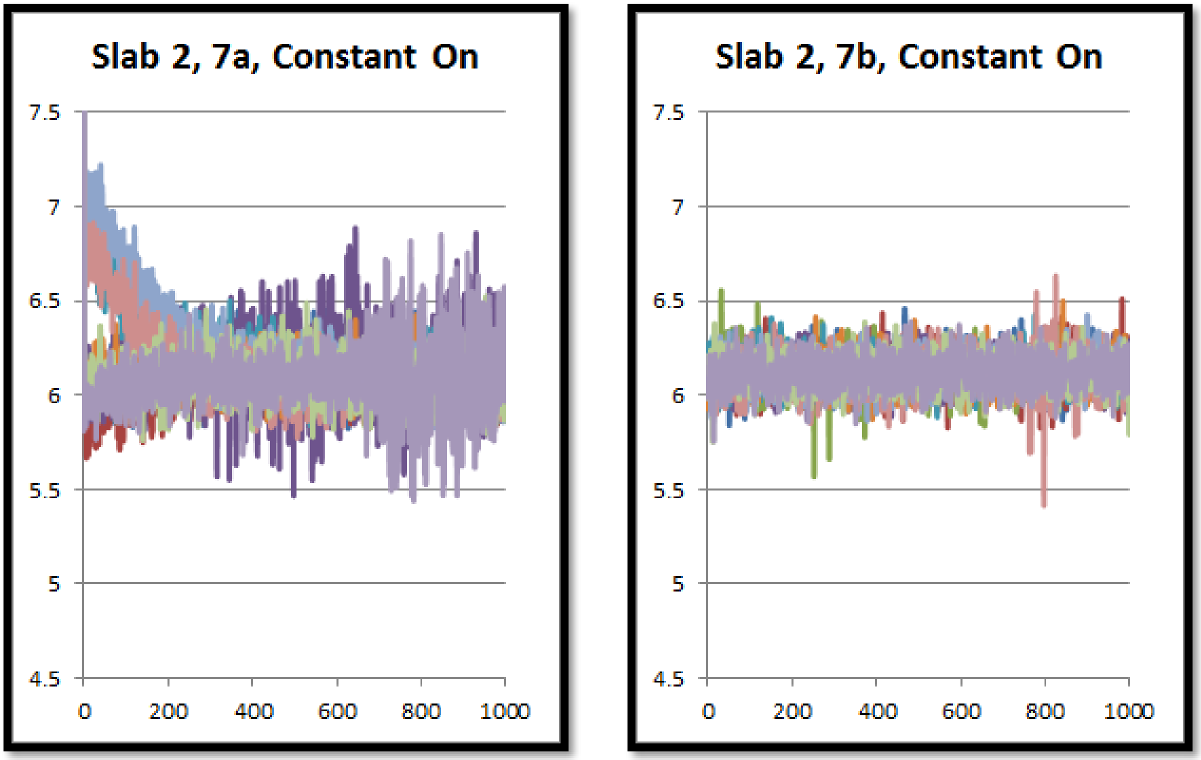

Figure 98. Random Noise from Antenna 7A appears larger than other Antennas.
Note: Antenna 7A example on left, Antennal 7B example on right.

Figure 99 shows that the GPR system can test down to a surface layer thickness of about .75 in. without interference from the layer below. This thickness should prove suitable for all but the thinnest of overlays currently in use within TxDOT.

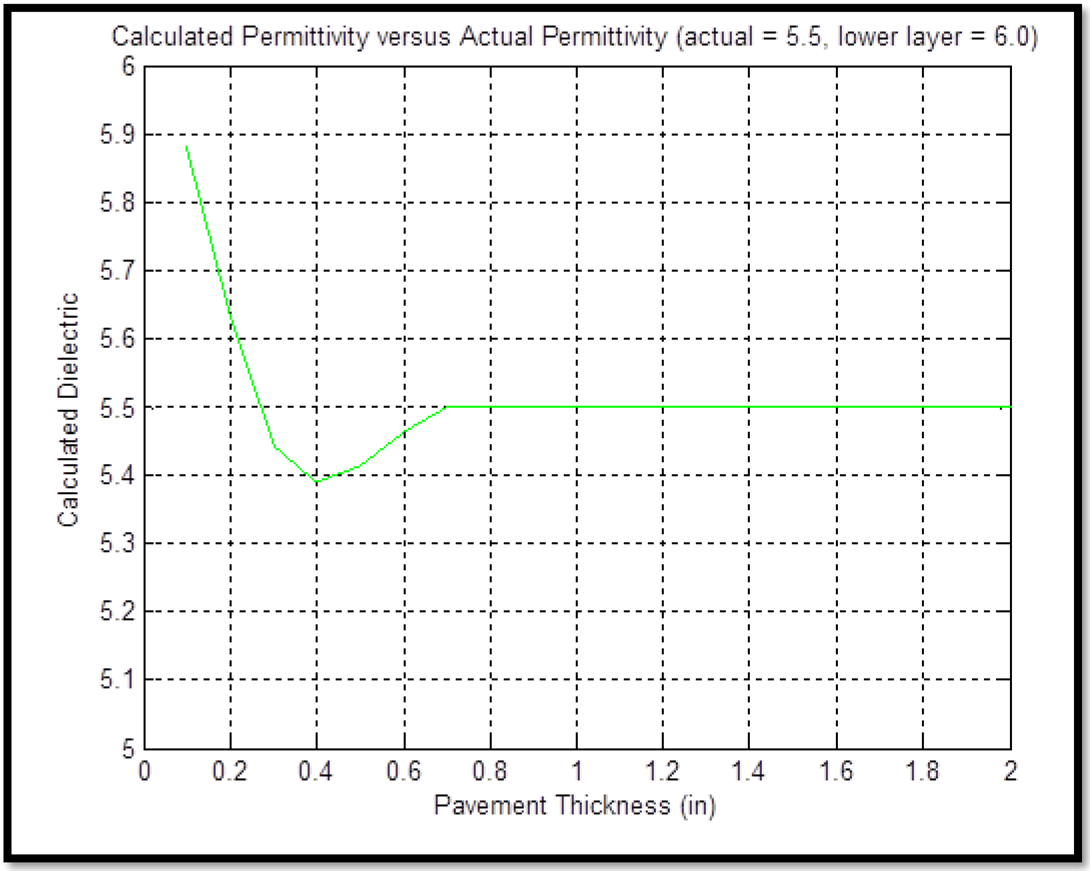

Figure 99. Influence of Surface Layer Thickness on Calculated Surface Layer Dielectric.

Figure 100 through Figure 102 show examples of how, in the worst-case scenario, the reproducibility limit would impact calibrations. The reproducibility limit only impacts the intercept of the calibration equation. Although particularly Figure 100 suggests that the curves differ, statistical tests show that the 95 percent confidence intervals for the slope coefficients significantly overlap and are not statistically different.

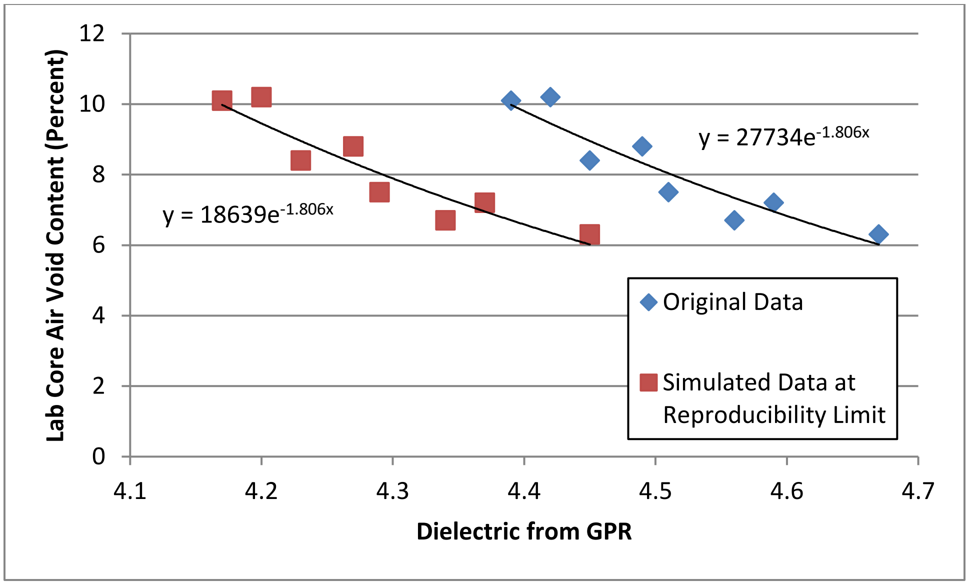

Figure 100. Example Calibration Data from SP 12.5, 1.5 inch Lift.

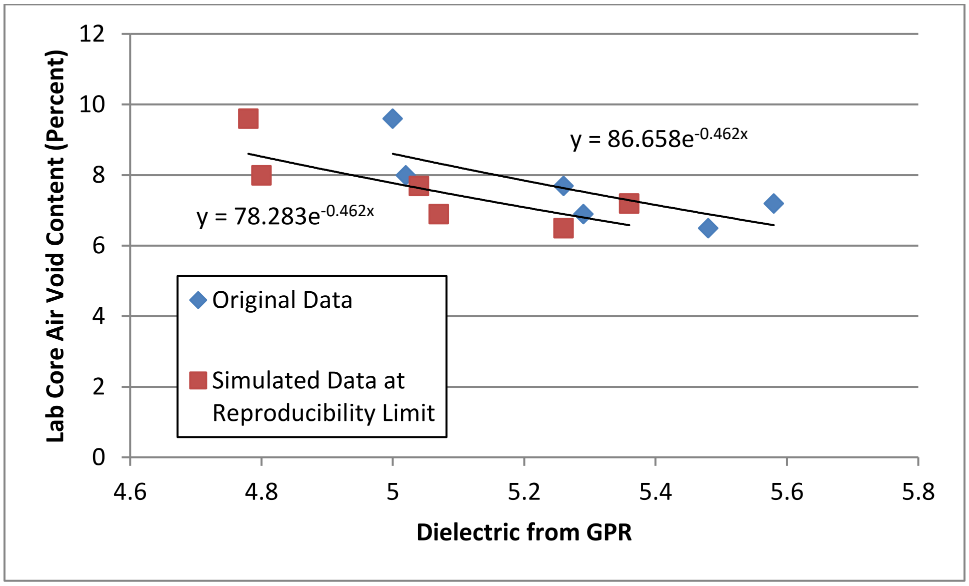

Figure 101. Example Calibration Data from SP 12.5, 2 inch Lift.

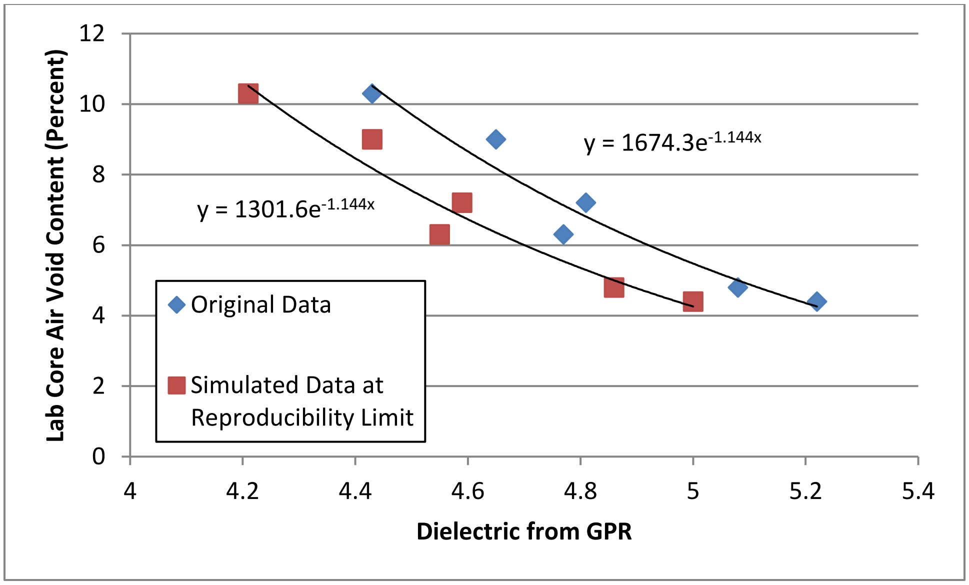

Figure 102. Example Calibration Data from SP 6.33, 1 inch Lift.

Although the simulated calibration curves suggest it may be possible to use one set of calibration factors to air voids for all antennas when the GPR is used as a multi-channel system, single factor analysis of variance tests (ANOVA) on the precision data sets show that the different GPR antennas did produce significantly different mean dielectric values for a given asphalt mixture slab. Table 18 and Table 19 illustrate this finding, where the tabulated *F* value exceeding the *F crit* value indicates that the means are not statistically equivalent across all antennas. This suggests each antenna may require a unique calibration to density.

Table 18. ANOVA Output for Slab 3, Constant On, Average of 500 Scans.

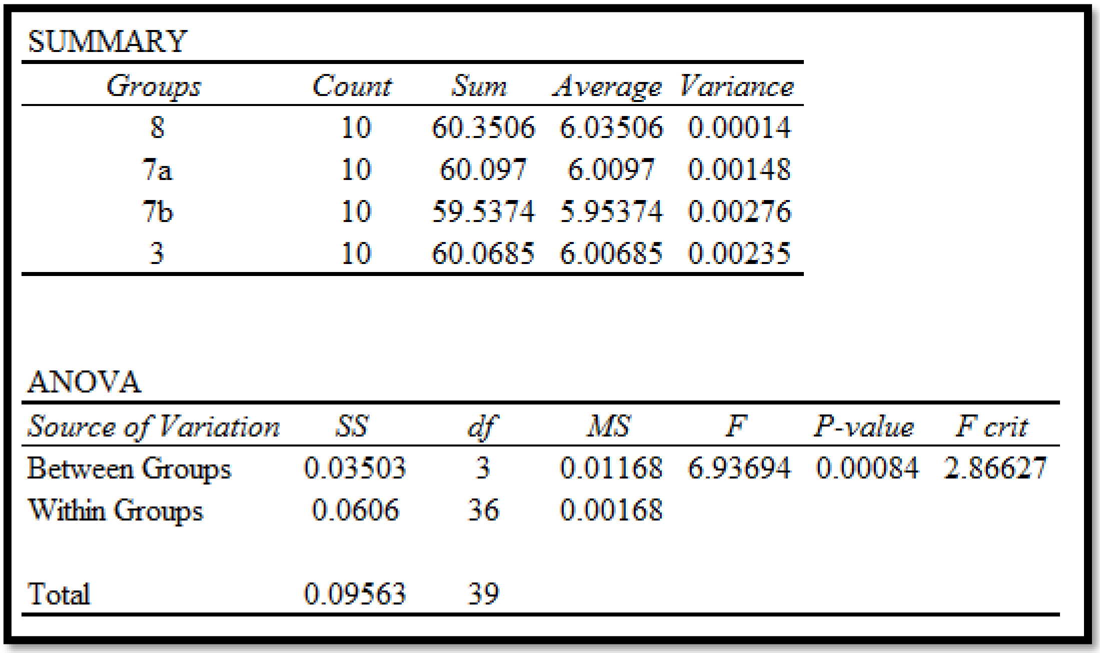

SUMMARY

Groups	*Count*	*Sum*	*Average*	*Variance*
8	10	60.3506	6.03506	0.00014
7a	10	60.097	6.0097	0.00148
7b	10	59.5374	5.95374	0.00276
3	10	60.0685	6.00685	0.00235

ANOVA

Source of Variation	*SS*	*df*	*MS*	*F*	*P-value*	*F crit*
Between Groups	0.03503	3	0.01168	6.93694	0.00084	2.86627
Within Groups	0.0606	36	0.00168			
Total	0.09563	39				

Table 19. ANOVA Output for Slab 5, Constant On, Average of 500 Scans.

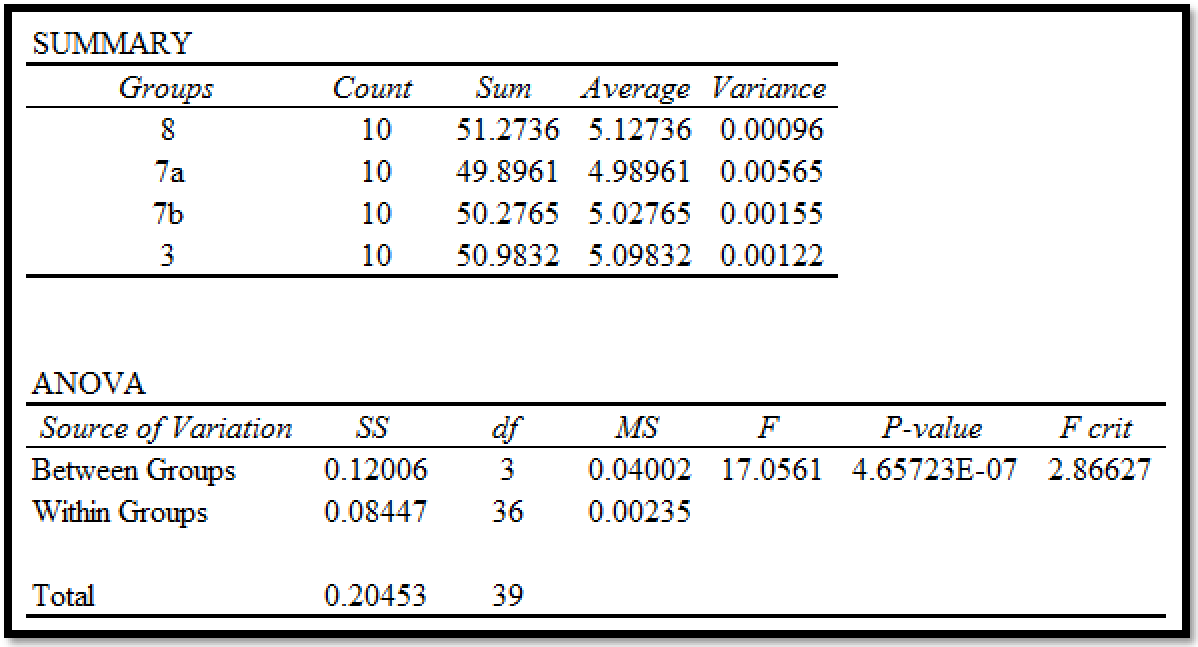

SUMMARY

Groups	*Count*	*Sum*	*Average*	*Variance*
8	10	51.2736	5.12736	0.00096
7a	10	49.8961	4.98961	0.00565
7b	10	50.2765	5.02765	0.00155
3	10	50.9832	5.09832	0.00122

ANOVA

Source of Variation	*SS*	*df*	*MS*	*F*	*P-value*	*F crit*
Between Groups	0.12006	3	0.04002	17.0561	4.65723E-07	2.86627
Within Groups	0.08447	36	0.00235			
Total	0.20453	39				

Calibration Procedures between GPR Data and In-Field Density

The core voids ranged from 6.5 to 14.9 percent and the surface dielectric values ranged from roughly 5.0 to 6.5.

Table 20 compares the R^2 values obtained by correlating core voids to the different GPR measurement methods. R^2 values were lowest when measuring surface dielectric with a single spot measurement (0.77) and were highest for the 6-inch moving-average method (0.88). In subsequent testing, the researchers decided to measure the surface dielectric within a +/- 6-inch area while collecting in the time mode.

Table 20. Comparison of GPR Measurement Methods.

Antenna	**Calibration R^2 by GPR Measurement Method**			
	Spot	12-inch avg.	6-inch avg.	24-inch avg.
#3	0.79	0.90	0.89	0.87
#4	0.77	0.85	0.87	0.88
#7	0.75	0.85	0.85	0.83
Average	0.77	0.87	**0.88**	0.86

Figure 103 shows the surface dielectric results for each antenna at each location. Practically speaking, the results from each antenna are very similar, but through paired t-tests, the differences between Antenna 3 and 4, and between 4 and 7, are statistically significant (*P-value*s of 0.007, and 0.027, respectively), while antennas 3 and 7 are not statistically different (0.549). This suggests that each antenna requires a unique calibration procedure.

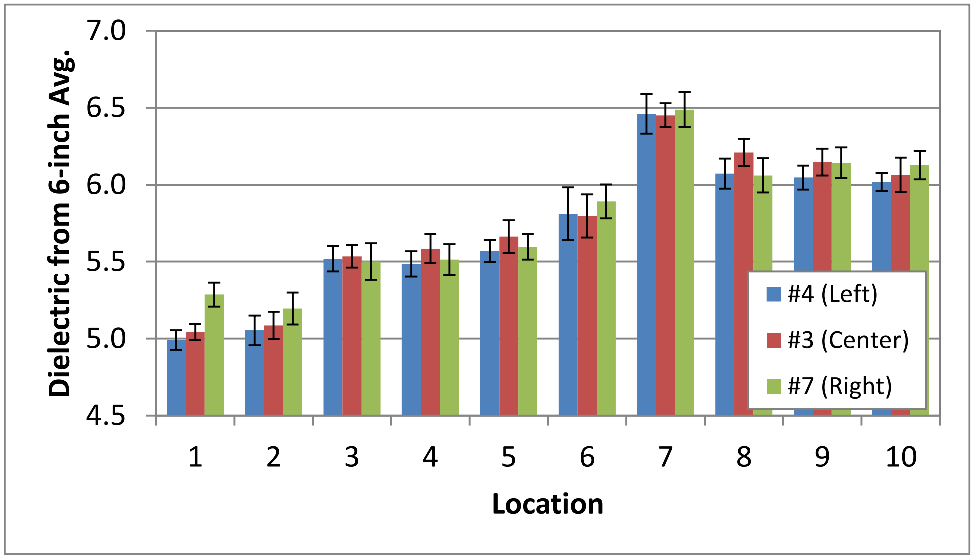

Figure 103. Surface Dielectric Results for each Antenna.

The overall comparison of surface dielectric to core voids is shown in Figure 104. The correlation coefficients would be used for further density testing with the GPR system.

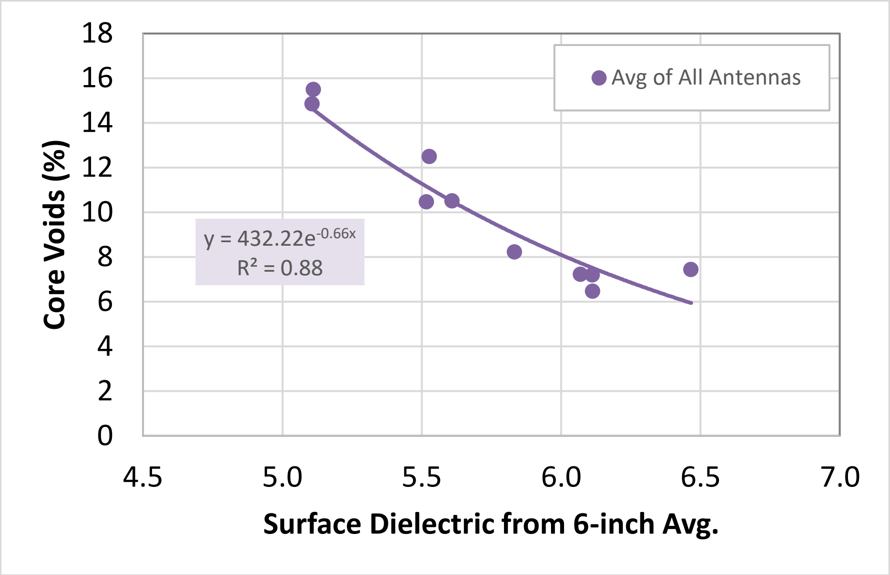

Figure 104. Dielectric-Voids Calibration Curve from Riverside Test Section.

The error that could be expected in the calibration curve by varying the core locations is illustrated in Figure 105. The most significant error occurs at the higher voids (lower dielectric) locations. Figure 106 shows the error that may occur by sampling fewer cores (six versus 10). The result here shows a total error of about 1 percent voids along most of the curve, with again the greatest chance for error at the lower end of dielectrics.

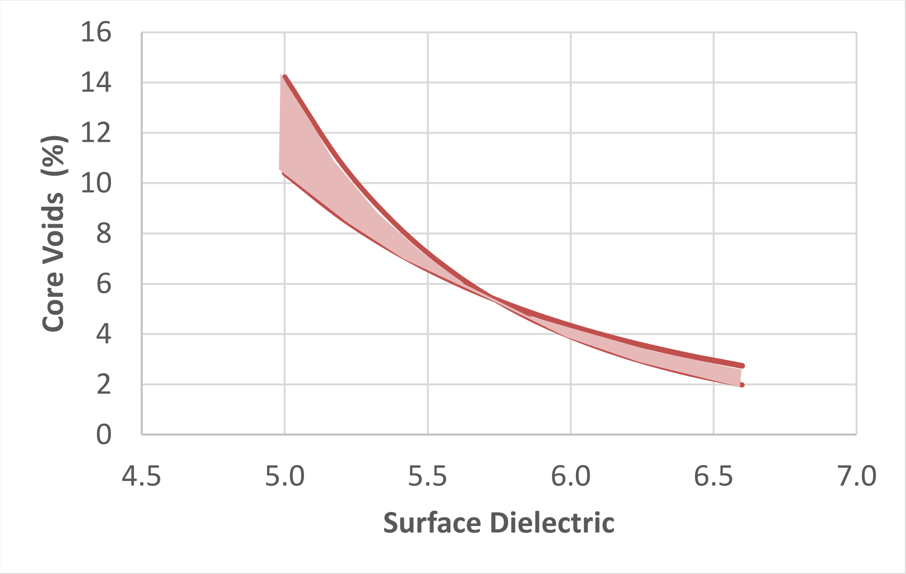

Figure 105. Calibration Curve Error—Core Location within 24 in.

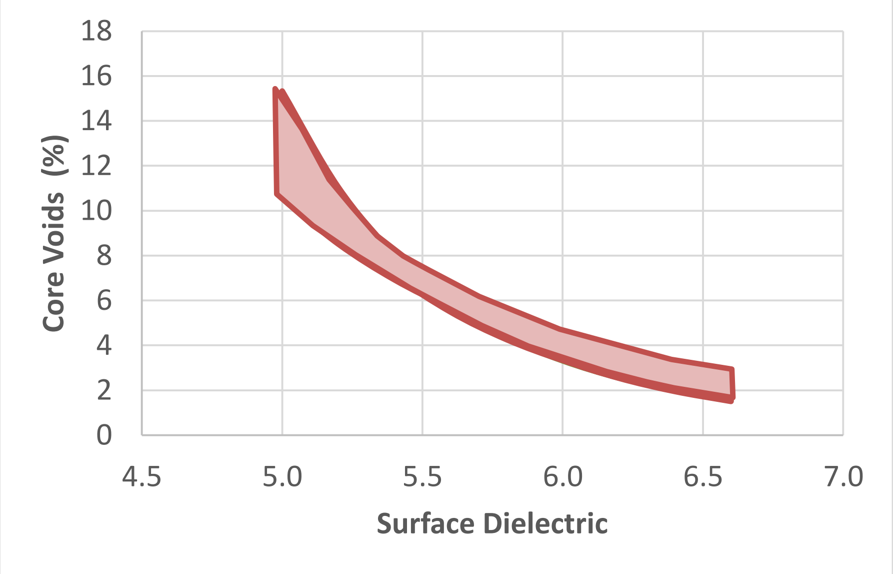

Figure 106. Calibration Curve Error—Smaller Sample Size (six cores vs. 10).

Field Implementation

US 183—TOM-F

Figure 107 and Figure 108 show the correlations of the nuclear density gauge and the GPR system to core voids. Both tests had very strong correlations, with R^2 values ranging from 0.75 to 0.97. The strongest correlations were from Day 1 construction, where cores' locations from high- and low-density locations were specifically identified. For other days, the locations were chosen randomly, reducing the data spread, and naturally lowering the R^2 values.

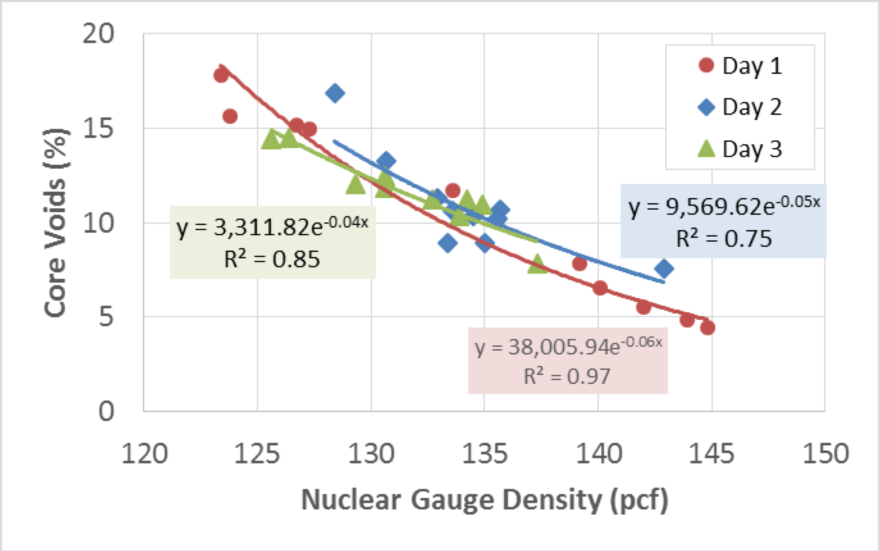

Figure 107. Correlation of Nuclear Gauge Density to Core Voids—US 183-TOM-F.

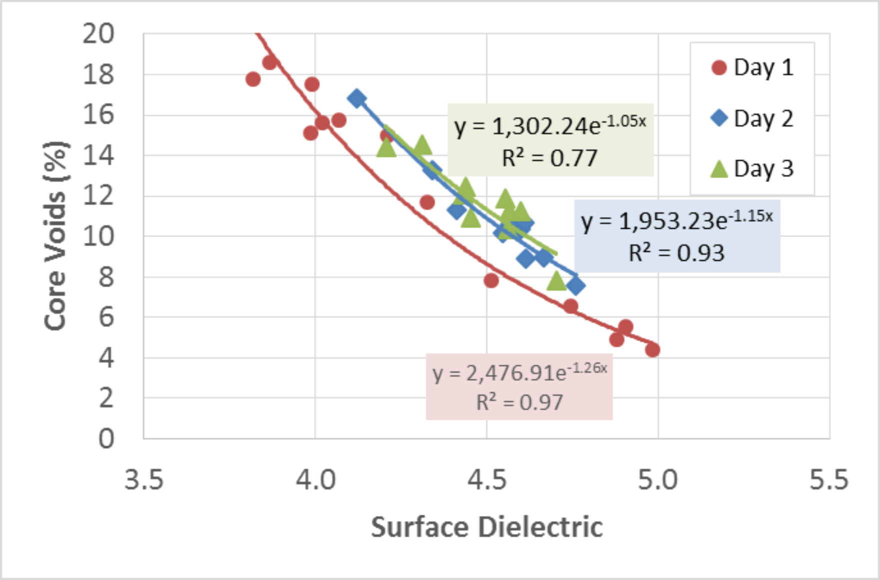

Figure 108. Correlation of Surface Dielectric to Core Voids—US 183-TOM-F.

Table 21 summarizes the HMA lab results by the agency and contractor. The asphalt content was 7.3 percent on Day 1 and then dropped slightly to 7.2 for Day 2 and 3. The rice also decreased after Day 1, which is unusual (all things being the same, when the asphalt content is lowered, the rice-specific gravity increases). The change in rice does support the change in the shift in the dielectric-voids curve. The nuclear density test was less prone to this change in the HMA.

Table 21. HMA Properties from Agency and Contractor Lab Testing—US 183-TOM-F.

HMA Properties		Day 1	Day 2	Day 3
Asphalt Content (%)		7.3	7.2	7.2
Rice Specific Gravity		2.363	2.356	2.357
Percent Passing (%)	1/2"	100.0	100.0	100.0
	3/8"	100.0	99.8	100.0
	#4	84.8	83.4	83.7
	#8	46.3	45.1	45.1
	#16	27.1	26.7	26.9
	#30	18.1	18.1	18.3
	#50	13.6	13.7	13.9
	#200	7.2	7.4	7.4

Figure 109 shows an example of the density distribution for Day 2 production. Table 22 shows the predicted voids on the test section on Day 1 and most of the production for Day 2 and Day 3. These values were predicted using the correlations in Figure 108. The predicted voids vary depending on which calibration curve is used. Using the Day 1 calibration, the average voids are between 8.1 and 8.7 percent, but using the Day 2 and Day 3 calibrations, the average voids increase to over 10 percent. This highlights a concern that the calibration on different days of production could vary significantly and may not be reliable with regular variations in HMA production. While the percent passing, marginal, and rejected are also shown in the table, the density criteria are meant for normal dense-graded mixtures, not TOM-F. The criteria should be adjusted to accommodate this newer mixture type.

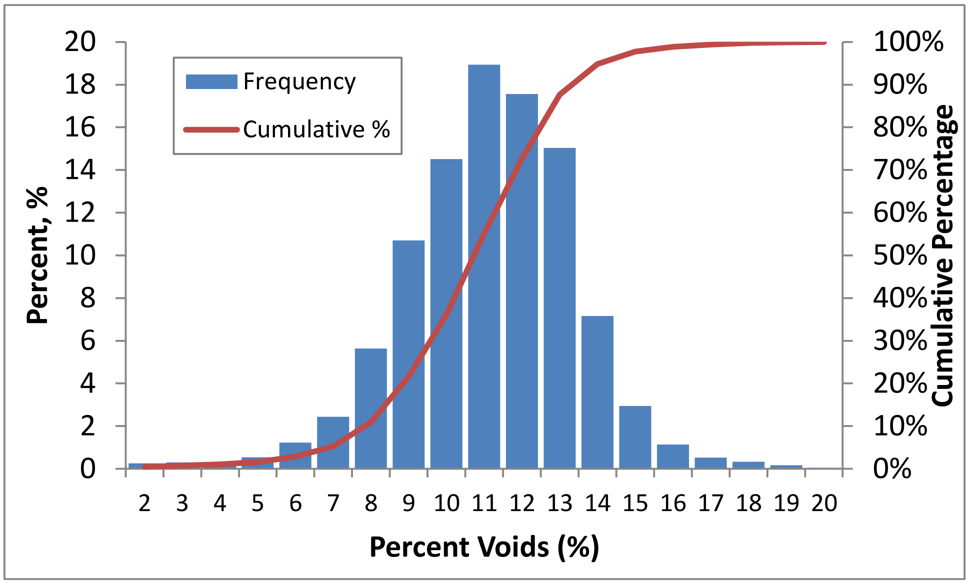

(Day 2 with Day 2 calibration)

Figure 109. Density Distribution Results—US 183-TOM-F.

Table 22. Density Results—US 183-TOM.

Production Day[1]	Calibration Data	Predicted Voids, %		Percent Passing,[2,3] %	Percent Marginal,[4] %	Percent Reject,[5] %
		Average	St. Dev.			
1	Day 1	8.1	4.7	38.4	25.2	36.4
2	Day 1	8.1	1.9	53.9	31.0	15.1
	Day 2	10.7	2.3	13.9	19.8	66.3
3	Day 1	8.6	1.8	51.2	29.2	19.6
	Day 3	11.7	2.0	4.0	13.5	82.4

1—Day 1 = 1,000 ft. Day 2 and 3 = ~8,000 ft.
2—Criteria are for performance dense-graded mixtures, not TOM.
3—Voids ≥ 4.7 and < 8.6%.
4—Voids < 4.7 and ≥ 2.7% (majority) or ≥ 8.6 and < 10%.
5—Voids < 2.6% (majority) or ≥ 10%.

Figure 110 presents the correlation from surface dielectric to the water flow time. This correlation is particularly important since the flow time test is used for quality acceptance on TOM projects. The R^2 value was 0.89 on Day 1 and 0.92 on Day 2. Applying these correlations to the three days of production, the average predicted flow times are shown in Table 23, along with the distribution of predicted passing and failed locations. The predicted average flow time ranged between 21 and 53 minutes, which, though acceptable, is higher than recommended for TOM. The typical TOM Type C mix is susceptible to over compaction, so a flow time greater than 4 minutes is discouraged. For TOM Type F, this upper-limit suggestion may not be necessary. Using the 2-minute minimum criteria, 93 percent of the Day 1 test section passed the flow test, and for Days 2 and 3, essentially the entire project passed the flow test.

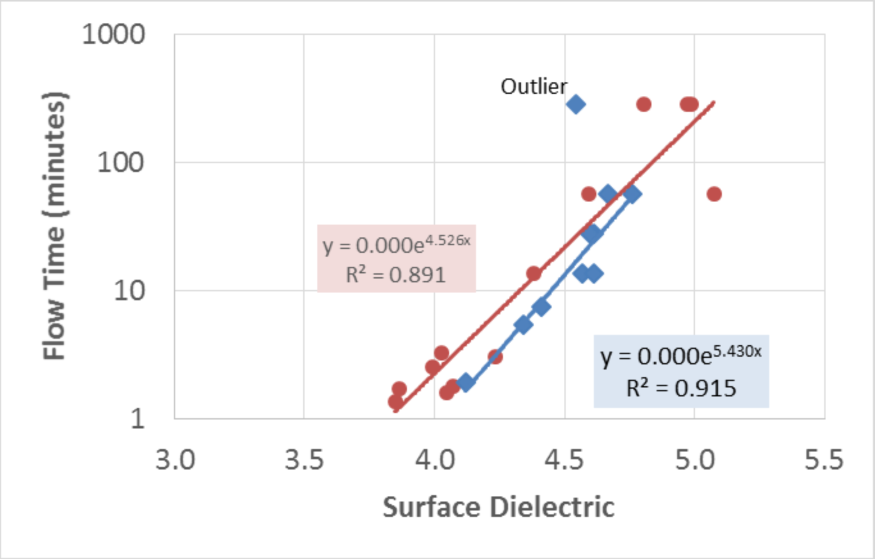

Figure 110. Correlation of Surface Dielectric to Flow Time—US 183-TOM-F.

Table 23. Flow Time Results—US 183-TOM

Production Day[1]	Calibration Data	Predicted Flow Time, min		Percent Passing,[2] %	Percent Failed,[3] %
		Average	St. Dev.		
1	Day 1	53.6	14.8	93.0	7.0
2	Day 1	27.9	3.1	100.0	0.0
	Day 2	29.6	4.1	99.7	0.3
3	Day 1	21.8	2.2	100.0	0.0

1—Day 1 = 1,000 ft. Day 2 and 3 = ~8,000 ft.
2—Flow time ≥ 2 minutes.
3—Flow time < 2 minutes.

US 90—Ty D

Figure 111 and Figure 112 show the correlation results on US 90 for the nuclear density gauge and the GPR to core voids. The correlations on this project (R^2 values from 0.03 to 0.88) were not as strong as the correlations on US 183. The data on Day 3 especially represented a narrow range of core voids, which naturally lowers the R^2 value. The lower R^2 values may also be related to the lift thickness of this project. Another concern is that the calibration curve coefficients for surface dielectric have some inconsistencies from day to day. The first day's curve, in particular, has a very different slope at lower surface dielectric values, which would greatly over-predict the core voids in low-density regions. There is uncertainty whether this curve is correct for Day 1 production, or if the locations sampled did not consider a wide-enough range of densities.

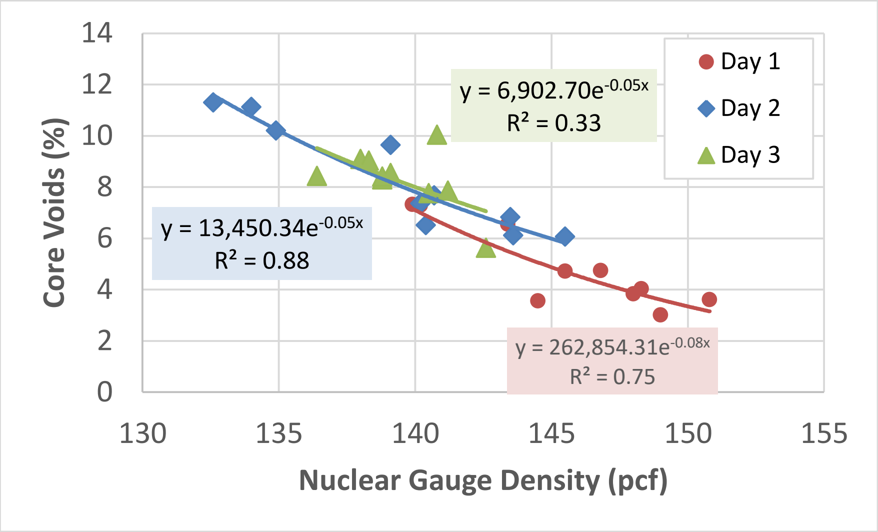

Figure 111. Correlation of Nuclear Gauge Density to Core Voids—US 90-Ty D.

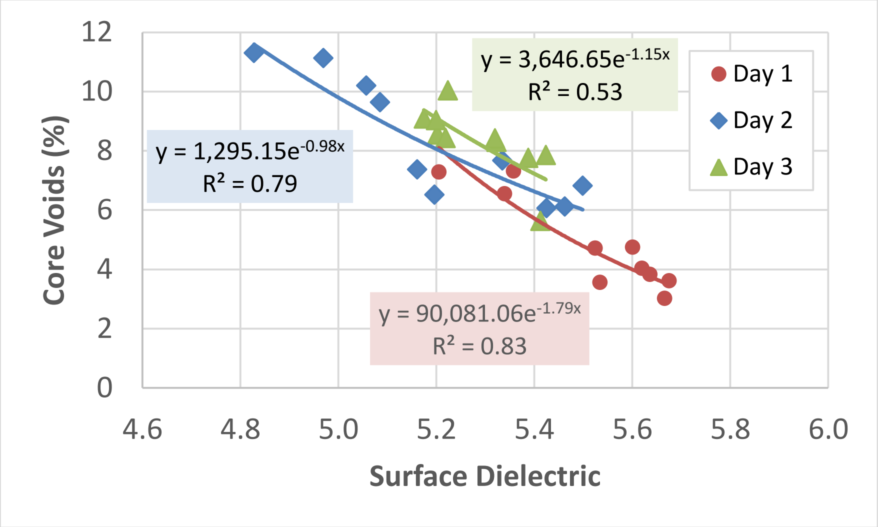

Figure 112. Correlation of Surface Dielectric to Core Voids—US 90-Ty D.

Table 24 summarizes the HMA lab results by the agency and contractor. The most notable difference is the drop in asphalt content from 5.4 percent on Day 1 and 2 to 5.2 percent on Day 3. These data coincide with the observed upward shift in the dielectric-voids curve on Day 3. The nuclear density test was less prone to this change in the HMA.

Table 24. HMA Properties from Agency and Contractor Lab Testing-US 90-Ty D.

HMA Properties		Day 1	Day 2	Day 3
Asphalt Content (%)		5.4	5.4	5.2
Rice Specific Gravity		2.443	2.447	2.465
Percent Passing (%)	3/4"	100.0	100.0	100.0
	1/2"	100.0	100.0	100.0
	3/8"	94.2	95.0	94.1
	#4	62.1	60.7	62.2
	#8	37.0	37.5	39.0
	#16	26.4	27.5	28.1
	#30	21.7	22.9	23.0
	#50	15.5	16.9	16.7
	#200	4.1	4.6	4.3

Figure 113 is an example distribution of the predicted voids on Day 2. Table 25 shows the voids for all three days of production. Depending on which calibration data are used, the average predicted voids ranged from 5.7 to 7.2 percent. The Day 2 and Day 3 calibrations predicted slightly higher voids than the Day 1 calibration (less than 1 percent different). The percent passing, percent marginal, and percent rejection are also shown in the table. The percent rejected was 4 percent or lower except for Day 2 production using the Day 1 calibration. The percent passing and percent marginal are more affected by the exact calibration data used. In most cases, the rejected areas were over-, not under-compacted.

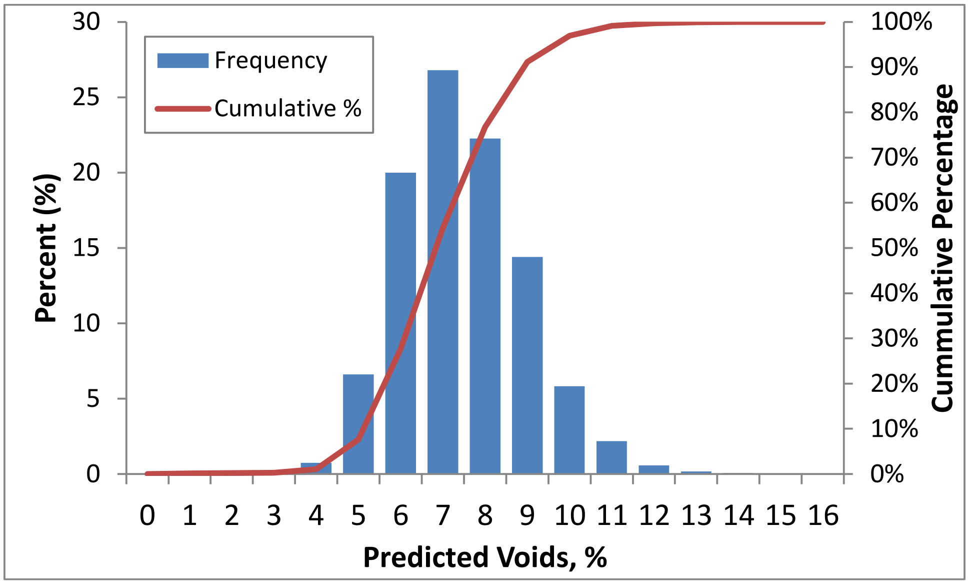

(Day 2 with Day 2 calibration)

Figure 113. Density Distribution Results—US 90-Ty D.

Table 25. Density Results—US 90-Ty D.

Production Day[1]	Calibration Data	Predicted Voids, %		Percent Passing,[2] %	Percent Marginal,[3] %	Percent Reject,[4] %
		Average	St. Dev.			
1	Day 1	5.8	1.4	79.1	19.4	1.5
2	Day 1	6.7	2.7	56.3	30.7	12.9
	Day 2	7.0	1.5	81.5	14.8	3.7
3	Day 1	5.7	4.7	61.7	34.2	4.1
	Day 3	7.2	1.9	81.4	14.7	4.0

1—Day 1 = 1,000 ft. Day 2 and 3 = ~6,500 ft.
2—Voids ≥ 4.7 and < 8.6%.
3—Voids < 4.7 and ≥ 2.7% (majority) or ≥ 8.6 and < 10%.
4—Voids < 2.6% (majority) or ≥ 10%.

CONCLUSION

Precision and Reproducibility Analysis

This precision analysis shows:

- In practice, averaging five scans or 500 scans to report the dielectric value does not greatly influence the mean reported surface dielectric constant.
- Increasing the number of scans averaged did improve the precision.

- For materials with dielectrics ranging between 4.4 and 6.4, the dielectric constant measured with GPR should be repeatable within 0.15 or better and reproducible within 0.22 or better.
- Antenna 7A should be investigated, as the data suggest that antenna may have imprecision and stability problems.

Due to the varying potential test conditions and averaging techniques that field conditions may require, Table 26 through Table 29 presents the summary precision statistics.

Table 26. GPR Precision Statistics for Constant on Condition Averaging 5 scans.

Average Dielectric	S xbar	S_r	S_R	*r*	*R*
4.37	0.037	0.049	0.060	0.14	0.17
5.03	0.034	0.051	0.059	0.14	0.17
5.06	0.06	0.048	0.078	0.14	0.22
6.01	0.05	0.079	0.091	0.22	0.26
6.06	0.074	0.069	0.099	0.19	0.28
6.44	0.13	0.055	0.14	0.15	0.38

Table 27. GPR Precision Statistics for Hard Reset Condition Averaging 5 scans.

Average Dielectric	S xbar	S_r	S_R	*r*	*R*
4.38	0.016	0.040	0.041	0.11	0.12
5.02	0.026	0.042	0.047	0.12	0.13
5.08	0.021	0.044	0.047	0.12	0.13
6.08	0.074	0.059	0.093	0.17	0.26
6.11	0.068	0.045	0.080	0.13	0.22
6.52	0.102	0.049	0.11	0.14	0.31

Table 28. GPR Precision Statistics for Constant on Condition Averaging 500 scans.

Average Dielectric	S xbar	S_r	S_R	*r*	*R*
4.37	0.0442	0.018	0.045	0.05	0.13
5.02	0.038	0.015	0.041	0.04	0.11
5.06	0.074	0.024	0.078	0.07	0.22
6.00	0.034	0.041	0.052	0.11	0.15
6.06	0.079	0.021	0.081	0.06	0.23
6.43	0.11	0.038	0.116	0.11	0.33

Table 29. GPR Precision Statistics for Hard Reset Condition Averaging 500 scans.

Average Dielectric	S xbar	S_r	S_R	r	R
4.38	0.021	0.022	0.030	0.06	0.08
5.02	0.012	0.030	0.031	0.08	0.09
5.07	0.018	0.027	0.031	0.08	0.09
6.07	0.062	0.041	0.073	0.12	0.21
6.09	0.060	0.037	0.070	0.10	0.20
6.51	0.096	0.050	0.107	0.14	0.30

Conclusions from Study of 3-Channel Reproducibility

In future work to improve the technology readiness of GPR for asphalt mixture QC, calibration data should be collected on air voids for each GPR channel. The results should be evaluated to determine the implication on predicted density for the scenarios of using a single calibration curve versus using channel-specific calibration curves. The stability of the calibrations through several days of production paving requires further investigation.

Calibration Procedures between GPR Data and In-Field Density

Researchers evaluated the possible error with different antennas in the field, different core locations, different dielectric measurement methods, and different sample sizes. The data showed statistically that each antenna requires a unique calibration (although practically speaking this may not be necessary). Researchers also recommend collecting calibration data with laser-aligned antennas, where cores should incorporate the exact location measured with the GPR. The core center should be within 2 inches of the measurement.

Field Implementation

The GPR system was deployed for three days on two overlay projects and demonstrated proof of concept for the GPR system to measure asphalt mixture density with near-full coverage. For the US 183-Tom-F project, the correlations between surface dielectric and core voids was very good, between 0.77 and 0.97. The correlation was not as strong for the US 90 project (0.53 to 0.83), which is due, in large part, to the narrower range of sampled data. The correlations on both projects shifted from one day to the next with variations in the HMA properties. Changes in the rice-specific gravity were the clearest indicator of changes in the correlation.

The air voids from the US 183-TOM-F project were much higher than observed on typical dense-graded designs; therefore, the density pass/fail criteria were not appropriate. Correlations with the water flow test did indicate acceptable performance for 99 percent of Day 2 and Day 3 production.

Construction on the US 90-Ty D project, for all three days, had 80 percent passing density requirements, between 14 and 20 percent with marginal density, and 1 to 4 percent with rejected density. In this case, the rejected areas were over-compacted. Using different calibration curves resulted in very different distributions of passing, marginal, and rejected construction.

Based on these results, the researchers recommend further investigation on the impact of HMA variability on GPR results. At this point, it seems that using a single calibration curve for several days of production could lead to unacceptable errors in density estimations as the job mix formula changes. It may be possible to adjust the correlation equation based on variations in the rice gravity or asphalt content.

CHAPTER 4. EFFECTIVENESS OF CONCRETE CURING COMPOUNDS

BACKGROUND

Durability of concrete is one of the most important factors in rigid pavement construction. Thus, curing should be evaluated with respect to the production of durable concrete since the evaporation of surface moisture from a concrete pavement can lead to some distresses, such as plastic shrinkage cracking, spalling and more critically delamination. Use of a curing compound is applied in the field in order to facilitate the hydration process of the surface concrete as well as mitigate moisture loss to decrease these issues. Presently, the current curing membrane assessment procedure is often dictated by ASTM C 156, "Standard Test Method of Water Retention by Concrete Curing Materials," in which the quality of curing compound as well as the curing practice to deploy a given compound are considered to be independent of each other. Therefore, a new curing membrane protocol is needed to evaluate the quality of curing in this regard. Such an assessment should be applicable under a range of weather conditions (e.g., temperature and relative humidity) as well as contain curing compound quality and application rates ideally accountable within a single index representing the effectiveness of the curing process.

A series of laboratory and field tests were conducted to develop a database of the main factors involved with the determination of curing effectiveness as well as validate the relationships that make up the evaluation protocol. Effectiveness Index (EI) and dielectric constant (DC) measurements at the concrete surface were used in developing the proof of concept. EI is obtained in accordance with concrete maturity concepts by considering relative humidity and temperature of concrete surface simultaneously. In addition, the DC measurement of a concrete is a rapid means to extend the application of EI to all areas of the concrete paving since it shows good sensitivity to free moisture content. To measure DC in the field, a GPR was investigated. TTI researchers used a percometer to measure the DC at the surface of concrete and fitted the DC measurements to a modified Weibull distribution function for the purposes of determining the rate of change in the DC measurement over time. It was found that this rate was useful for assessing the moisture retention capability of a given curing practice. Test results show that moisture loss and surface abrasion resistance have significant correlation with EI. A higher EI is associated with a lower moisture loss and higher surface abrasion resistance. Consequently, the type of curing compound, application rate, and ambient climatic conditions affect these types of test results.

The main goal of this research is to show the viability of the concept that concrete curing compound effectiveness can be assessed under both field and laboratory conditions through a previously established protocol described later in this report. The protocol requires establishment of a laboratory reference curve(s) that cover the range of potential of evaporations (PE) and EIs expected under field conditions. Part of the protocol involves the calibration of a field relationship between the EI and a term later described as beta. The final outcome of the protocol is the use of both of these curves to determine the appropriate rate of application of a given curing compound. To this end, curing compound effectiveness is assessed by the use of GPR and the ATEK Concrete Maturity Meter (ACMM) device—key technologies applicable for either field or laboratory measurement and an integral part of the protocol. The tasks associated with this research involve both laboratory and field curing compound effectiveness evaluation, establishing a relationship between them, and proving the viability of a protocol to evaluate curing compound effectiveness.

PROCEDURE

Laboratory Testing and Data Collection Program

The experimental study in the laboratory consists of several parts. First, a curing compound was selected and tested under different situations in order to evaluate the efficiency of curing compounds. Then, curing compounds' performances were evaluated by comparing curing quality in each condition. The ambient conditions such as relative humidity and temperature measurements were used to determine this evaluation. Moreover, moisture loss and abrasion resistance tests were conducted at the surface of concrete specimens to verify the utility in terms of the moisture retention capability of a given curing compound.

The investigation consisted of two parts. The first part, carried out in the laboratory, examined the effectiveness of curing by testing a single curing compound. Four levels of wind speed and application rate were used yielding sixteen different mixture combinations to test for moisture loss, abrasion resistance, EI, and DC.

Sample Preparation

The binder used in this research was an ASTM C 150 Type I Portland cement. Mixture proportions are presented in Table 30. A single w/c was used in this study. According to ASTM C 305, an electrical mechanical mixer was used to prepare a consistent mortar.

In this project, two different molds were used for various tests. The first one was a cylindrical mold with 12-in diameter and 3-in height to measure relative humidity, moisture loss and surface abrasion. Another one was a cylindrical mold with 6-in diameter and 2-in height for measuring dielectric constant.

Table 30. Mixture designs.

W/C	Unit Weight (lb/ft^3)		
	Water	Cement	Sand
0.40	15.38	38.45	105.75

In order to evaluate curing compound effectiveness, four different application rates were used to assess their sensitivity to changing climate conditions. It is noteworthy that to simulate field conditions, four wind conditions were represented in the laboratory. Summary of design variables are shown in the Table 31. The ranges of application rates used were 100, 140, 200, and 240 ft^2/gal with four wind levels—0, 5, 10, and 15 mph. The ambient environment conditions were represented by the PE rate calculated in following equation:

$$PE = (70^{2.5} - (\frac{RH}{100} \times T^{2.5}) \times (1 + 0.4 \times WV) \times 0.000001$$

where:

PE = potential of evaporation rate, lbs./ft^2/hr.

RH = the relative humidity of ambient conditions, %.

T = the temperature of ambient conditions, ˚F.

WV = the wind velocity of ambient conditions, mph.

Table 31. Levels of the design variables.

Variable	Level 4	Level 3	Level 2	Level 1
Application Rate of compound, ft^2/gal	100	140	200	240
Wind speed, mph	15	10	5	0

Curing Compounds to Be Tested

Testing of curing compounds is the most comprehensive in the industry and has been conducted with two primary objectives: (1) to establish and prove superior performance and (2) to ensure a close and consistent correlation between laboratory and field results. These compounds minimize or eliminate plastic shrinkage cracking in freshly placed concrete, and produces highly durable surfaces for pavements, bridge decks and precast elements.

- SINAK-Lithium Cure™ is lithium-based concrete curing treatment that protects against flooring failure due to moisture and alkalinity emanating from the concrete. The lithium silicate reaction with the hydrating cement produces additional gel products near the concrete surface. As the curing process continues to develop, the added gel products fill the channels that allow water to escape from the concrete surface. By preserving more moisture at and near the concrete surface, it reduces the buildup of surface tension that is responsible for plastic shrinkage cracks.
- W. R. Meadows 1300-CLEAR is a water-emulsion and wax-based concrete curing compound that provides a premium-grade that optimizes water retention. 1300-CLEAR appears white in color when wet, but dries clear.
- W. R. Meadows 1600-WHITE (City White) is a water-based and white-pigmented concrete curing compound. When properly applied, 1600-WHITE forms a premium-grade membrane, which optimizes water retention. The white pigment reflects the sun’s rays to help keep the concrete surface cooler and prevent excessive heat buildup.
- DAYTON DSSCC is a water-based, resin, liquid membrane forming curing compound for freshly finished concrete. White Resin Cure is formulated to comply with Federal VOC content limits. White Resin Cure forms a vapor sealing membrane that retains more than 95 percent of the reactive moisture for three or more days.

Moisture Retention Test

The moisture retention test measures the moisture loss of a concrete specimen within a given period using a high-sensitivity scale. This test carried is out in accordance with standard test, ASTM C 156, which is thought to be related to the capability of a curing compound to hold water. This procedure is practically only applicable to laboratory conditions since the temperature and relative is held constant where a chamber is used to keep temperature in 32 ± 1ºC and relative humidity in 50 ± 5 percent. To incorporate effects of wind, an industrial fan is used to create multi-wind speeds. The specimens' weight is recorded every couple of hours for 72 hours. The moisture loss is defined relative to the total specimen weight.

Concrete Surface Abrasion Resistance Test

An important characteristic of a concrete pavement is its abrasion resistance. In order to test the curing compound effects on strength, the top few inches of the concrete surface is tested. Therefore, a test on the surface concrete is useful to represent the influences of curing compounds on strength. Surface abrasion is evaluated by measuring the abraded weight loss and is based on ASTM C944.

In this procedure, a cutter rotates at 200 rpm for 10 minutes. During this test, a constant force of 22 lbs. is applied on the test specimen. A concrete specimen is weighed both before and after the test in order to determine the difference in weight loss. By dividing the weight loss of the concrete by the initial weight of the specimen, the abrasion resistance index is calculated.

For conducting abrasion resistance test, a 12-in diameter concrete cylinder is used that is also tested for relative humidity. It is noted that if the resistance to abrasion of the concrete surface increases so does the strength of concrete increase. Thus, a low weight loss in the abrasion test indicates a concrete with better mechanical characteristics.

EI Concepts

In this research, quality of a given curing compound should be evaluated. This assessment is based on the measured relative humidity (RH) and temperature within the concrete maturity concept. These data were obtained by an ACMM system. A detailed view of an ACMM system is shown in Figure 114. This device can measure temperature data pertinent to the RH under different environmental conditions. Therefore, three sensors are used with one to record the ambient RH, and the other two the RH values inside each of the two chambers (one being the filtered and the other sealed). These chambers are contained within the support base, which is placed on top of the hardening concrete, as shown in Figure 115. The filtered chamber is covered by a fine screen mesh to support a layer of mortar in which to support a curing medium such as a curing compound. The RH sensors are of the chilled mirror hygrometer type, also referred to as an optical condensation hygrometer, which is the most accurate, reliable, and fundamental hygrometer commercially available.

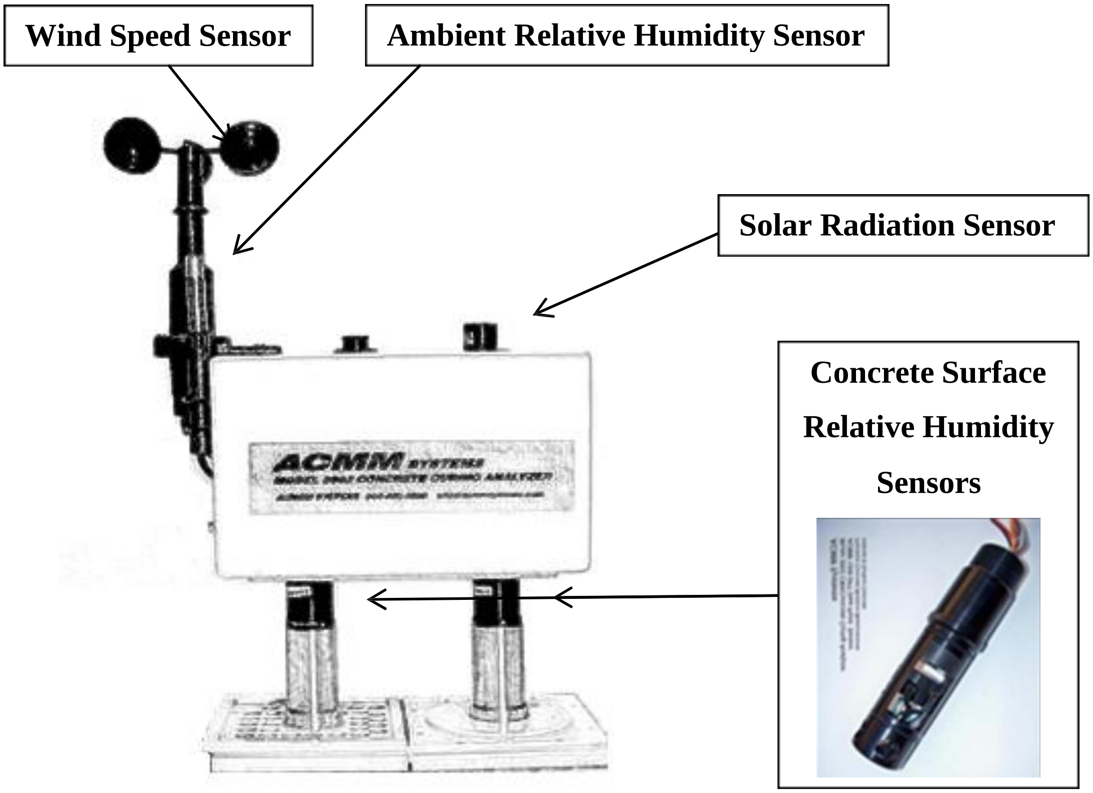
Wind Speed Sensor
Ambient Relative Humidity Sensor
Solar Radiation Sensor
Concrete Surface Relative Humidity Sensors
ACMM SYSTEMS
MODEL 3042 CONCRETE CURING ANALYZER

Figure 114. The ACMM system.

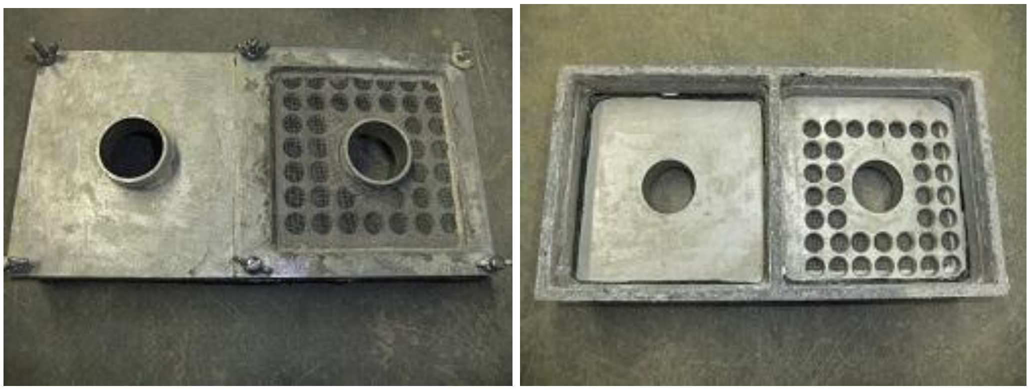

Figure 115. Top and bottom view of the curing plate.

The two chambers are utilized to measure the dew point and dry bulb temperatures (which is used to calculate the RH) of sealed and filtered conditions by the sensors that make up the ACMM system. The process of recording data starts when a mesh on the filtered side is covered with a thin layer of mortar and curing compounds are applied; and then the sensors of the ACMM system are inserted into the two housing holes on each side of the plate to measure RH related temperature. In order to isolate the sensor in each chamber, they seal in the housing holes in the chamber with an O-ring. To assess the effectiveness of a compound, the comparison between perfect curing conditions (as represented inside the sealed chamber) and curing conditions with a compound in place (as represented inside the filtered chamber) are carried out. So, the sealed the filtered conditions are provided for this purpose, respectively. The moisture-based concrete maturity is a parameter that indicates how far curing has progressed based on its relationship between temperature, age, and strength gain.

Accordingly, the temperature only based maturity is conventionally an index dependent on time and the concrete temperature. However, the temperature-based maturity model is not an efficient indicator of the curing effectiveness; therefore, a moisture-modified maturity function is utilized. A modification factor is considered for numerical computation of the effects of moisture on the equivalent concrete curing time. Based upon former observations, concrete needs to remain at a certain level of RH for curing in order to hydrate. Generally, the RH needs to be above 80 percent for hydration to take place.

Although, it is noteworthy that that concrete strength grows over time at a slow pace, a moisture modification factor was developed by adjusting the coefficients in the model as:

$$\beta_H = [1 + (a - aH)^b]^{-1}$$

where:

β_H = the moisture modification factor.

H = the RH of concrete.

a = adjusted coefficient, changing from 7.5 to 5.

b = adjusted coefficient, changing from 4 to 1.

This modification factor is used to modify the maturity index as shown in Equation 2:

$$M_H = \beta_H . \sum_0^t (T - T_0) . \Delta t = \frac{\sum_0^t (T - T_0) . \Delta t}{1 + (5 - 5H)}$$

where:

M_H = the moisture-modified maturity at age t of concrete.

T = the average concrete temperature, °C, during time interval Δt.

To = datum temperature (usually taken to be -10°C).

t = elapsed time (hours or days).

Δt = time interval (hours or days).

In this project, to evaluate effectiveness of curing compounds, EI is introduced as an index based on the adjusted maturity model. The values of EI calculated for a 72-hour period on a given curing compounds as shown below:

$$EI = \frac{t_f - t_a}{t_s - t_a}$$

where:

t_f = the equivalent age of concrete under the filtered side curing condition.

t_s = the equivalent age of concrete under the sealed side curing condition.

t_a = the equivalent age of concrete under the ambient curing condition.

Use of NDT Method

One purpose of curing is to hold surface moisture for hydration. Consequently, the amount of the free water at the concrete surface could be an index to assess effectiveness of a given curing compounds. It was already discovered by researchers that the dielectric constant is directly related to the free moisture content and the degree of hydration of concrete. Thus, a relationship between the dielectric constant and the capability of curing compounds to maintain free moisture at concrete surface could be a reliable index to evaluate this effectiveness. The dielectric constant or permittivity is measured by a percometer as shown in Figure 116. The device has two segments: a probe that used to measure the dielectric constant, and the body of the device. The specifications of the percometer are listed in Table 32. Permittivity is measured by the change in the electrical capacity of the electrode (probe) due to the influence of the measured material at a frequency of 40–50 MHz.

Figure 116. The Adek^{TM} Percometer and the probe.

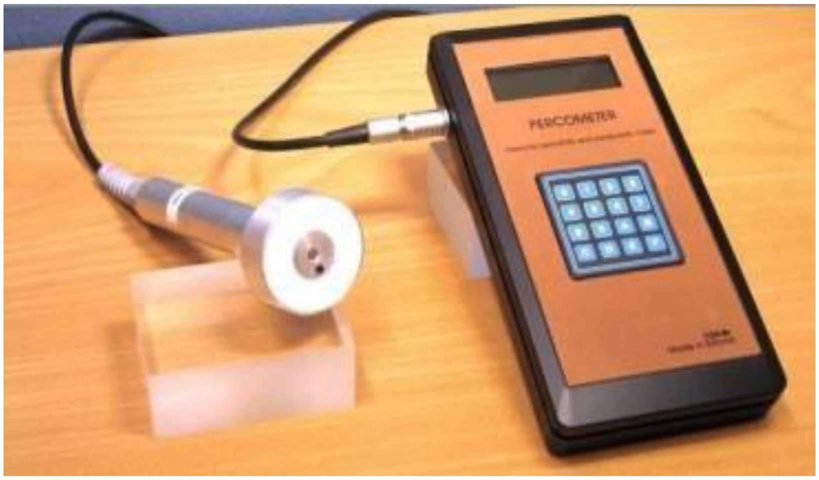

Table 32. Specifications for the Percometer.

Probe type	Measuring range Dielectric constant (ε_r)	Electrical conductivity, $\pm\mu S\ /\ m$	Temperature, °C	Accuracy of ε_r measuring	Recommended Application
Surface Probe	1 ~ 32	0 ~ 2000	-40 ~ +80	± 0.1+1%	Laboratory use, Tube Suction Test

The dielectric constant is potentially another way to assess curing compound effectiveness over a broad area since the results from the ACMM are for a specific location. The dielectric constant is measured on 6-in diameter specimens in the laboratory. A special set of chambers are placed on the surface of the bare concrete keeping this area clear of curing compound as shown in Figure 117. The chamber is sealed on to the concrete surface.

Again, a screen mesh is provided as support for the curing compound. A thin layer of mortar is placed on this cap in order to retain curing compounds sprayed on it. The dielectric constant (DC) of concrete can be obtained by removing the cap and inserting the probe into the chamber to access the bare concrete. This setup provides a direct way to measure the dielectric constant of the affected concrete immediately below the curing compound without damaging the curing compound membrane applied at the surface of concrete.

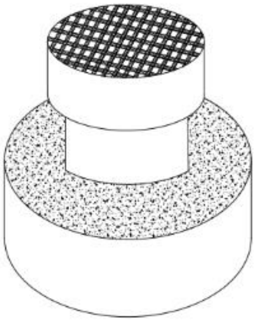

Figure 117. Dielectric constant measurement setup.

Microscopic Analysis (Thin Sections)

Another way to assess the quality of curing is by analysis of thin-section samples taken from the surface of the concrete (Figure 118). This analysis allows for the assessment of the effects of curing in terms of the microstructure of the concrete. The thin sections were 20-micron-thick pieces of concrete bonded to a glass slide commonly using fluorescent dyed epoxy.

Control Sample (No Cure)

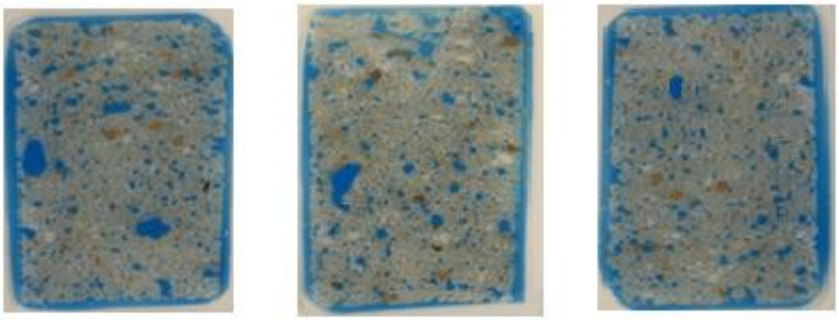

City White – 200 ft2/gal

City White – 140 ft2/gal

City White – 100 ft2/gal

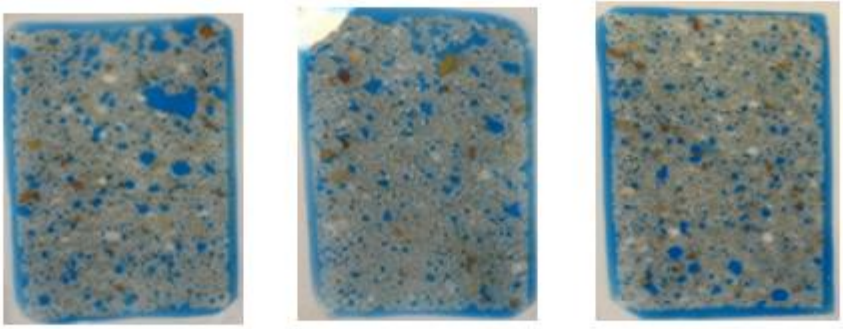

Lithium – 200 ft2/gal

Lithium – 140 ft2/gal

Lithium – 100 ft2/gal

Figure 118. Fluorescent epoxy impregnated thin sections prepared from concrete specimens.

The two types of voids that were observed are:

- **Capillary Void Percent**. Capillary voids are irregularly shaped and very small, less than 5 µm on the lapped surface of the slice examined. They represent space originally filled by mixing water, remain after the hydration of the cement gels, and are an integral part of the paste. Although they contain air at the time of examination, they are not considered part of the air void system. Percentage is based on total areas observed.
- **Total Void Percent.** Total voids observed consisted of entrapped air voids and voids created due to bleeding action that are larger than the capillaries but less than 1 mm on the lapped surface of the slice examined and have internal surfaces that indicate they

were formed by air bubbles or pockets. They may be spherical or irregularly shaped. Bleed channels are likely created during the bleeding process and tend to be reduced as the quality of curing improves. Percentage is based on total areas observed.

The specimens shown in Figure 118 are limited in scope but were taken from the batch of concrete mixes that were produced with two different curing compounds, Lithium and City White, at three different application rates. Six sets of samples were paired for comparison of curing conditions. For each sample cured at 32˚C temperature and 50 percent RH. The percentage of total voids in each sample was then compared among the methods of curing.

Shrinkage Test

The shortening of concrete slabs can be caused by temperature decreases or moisture loss. These two causes are also related to curling and warping of slabs, respectively. After hardening, concrete begins to shrink as water not consumed by cement hydration leaves the system. This is known as drying shrinkage.

The shrinkage characteristics of a concrete mixture can be determined by ASTM C 157. This test method determines the change in length on drying of mortar bars containing cement that has been cured with curing compounds. The lengths and weights at 1, 3, 7, 14, 21, and 28-day age were recorded. Concrete mixtures were prepared in the laboratory and tested for their resistance to shrinkage cracking to evaluate:

- The effectiveness of the shrinkage test apparatuses used.
- The shrinkage characteristics of typical concretes used in pavement slab.
- The effects of adding curing compound on shrinkage rate.

Field Testing and Data Collection Program

Investigation Approach

The field investigation was similar to the approach for the laboratory investigation. After the concrete pavement surface was finished, the top portion of the curing plate was placed on the concrete surface with a thin mortar layer on the filtered side of the plate, as shown in Figure 119. This portion of the curing plate was later put back and fixed on the base of the plate after application of the curing compound to create a bare spot on the pavement surface corresponding to the position of the curing plate. The operation of the ACMM system occurs over the rectangular bare concrete area which was covered by the curing plate that the supported ACMM system during data collection.

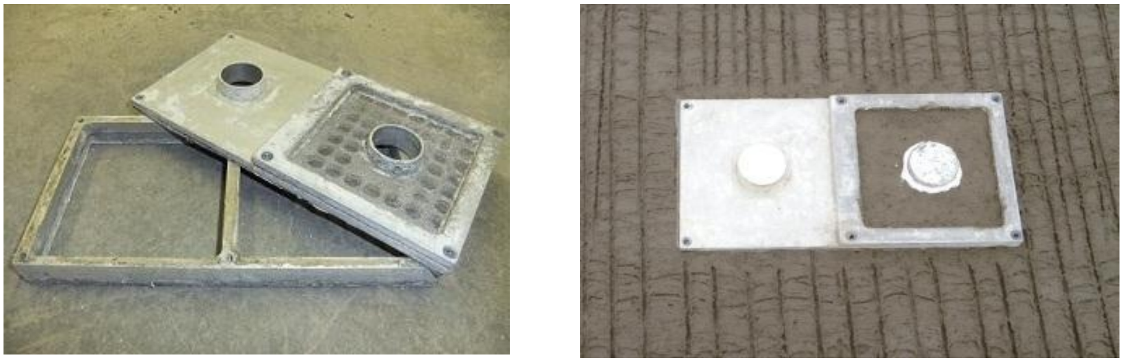

Figure 119. Curing plate Components and setup on a pavement surface.

Under field conditions, DC measurements provide a means to extend the curing compound effectiveness evaluation by the ACMM system over a wider area of paving rather than at a single position where the ACMM system is placed. After curing compounds were applied, the ACMM system was placed at the base location of the curing plate, as shown in Figure 120. The ACMM system as previously noted, records the ambient temperature, moisture and wind conditions. The top portion of the cylindrical mold was taken off the base portion when making DC measurements and was inserted back into the base tightly once the measurements were taken to prevent exceptional drying of the surface.

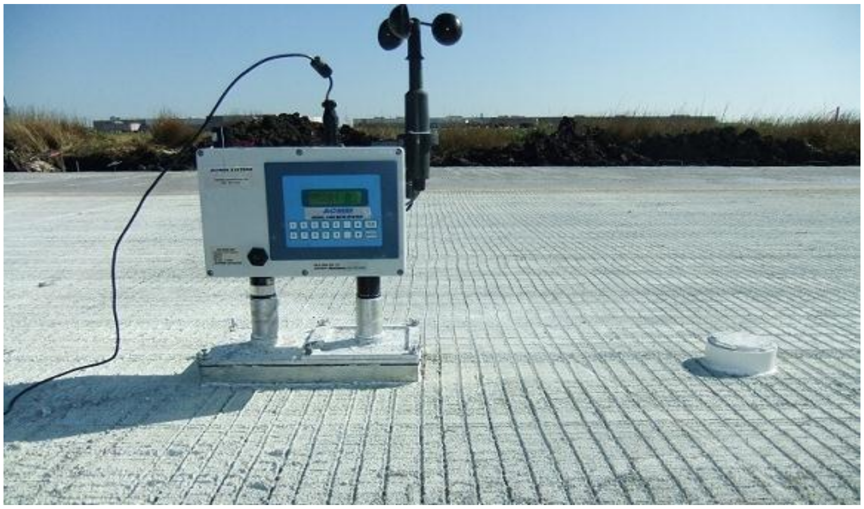

Figure 120. Setups of the ACMM system and the mold for DC measuring.

A field investigation was conducted on two continuously reinforced concrete (CRCP) paving projects in Victoria, TX—one on US 59 (John Stockbauer Dr.) and the other on Ball Airport Rd. The protocol described later includes the use of the ACMM system in the field and two devices to measure the DC, the percometer previously described and the GPR cart which uses an air-launched antenna, so the trends from this type of GPR data could be compared with those from the laboratory data to examine further the utility of the laboratory derived relationships and evaluate them in terms of the field findings.

GPR

The DC measurement in field investigation was conducted in a series of test sections established during placement of concrete. As shown in Figure 121, the system is equipped with of a 2.5 GHz air-coupled antenna in the front of the specially designed cart and a portable computer embedded near the cart handle for data collection. The system can calculate the DC for the surface concrete instantly and spatially by pushing the cart over the pavement surface. This configuration allows for a comprehensive evaluation of the conditions over the entire concrete slab to be finished within a short period of time. The DC measurements are recorded every 1/3 in. as long as the wheels are rolling. Results collected at such small increment area of great value for this research since the variability of the data can be very large at a greater incremental distance.

Prior to the data collection, the antenna was always calibrated with air and a metal plate to ensure the best data quality. To maintain good data repeatability, as shown in Figure 121, the wheels on one side of the cart were pushed align with the longitudinal joint made at the centerline of the concrete pavement.

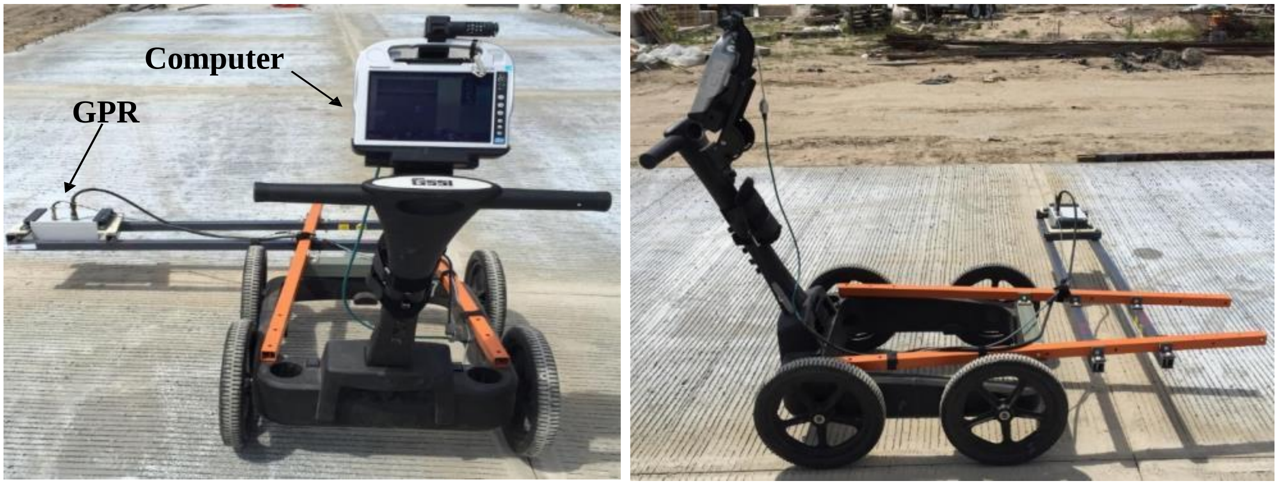

Figure 121. GRP used for concrete EI Measurement.

RESULTS

The main text contains all the results and data related to W. R. Meadow (City White 1600). Appendix B and C present fesults for other curing compounds.

Curing Effectiveness Lab Test Data Trends

Moisture Loss Trends

Laboratory testing was conducted to evaluate the effectiveness of a given curing compound with respect to moisture retention. The duration of this test was 72 hours recording weight loss over time; and dividing by original weight of specimen, the percentage of weight loss was measured. The moisture retention measured by high-sensitivity scale with 0.1 gram of resolution. The environment chamber is controlled at a fixed temperature (32 ± 1ºC) and RH (50 ± 5 percent). The weight loss percentage of mixtures with four different rates of application and four wind speed levels are shown in Figure 122 to Figure 125.

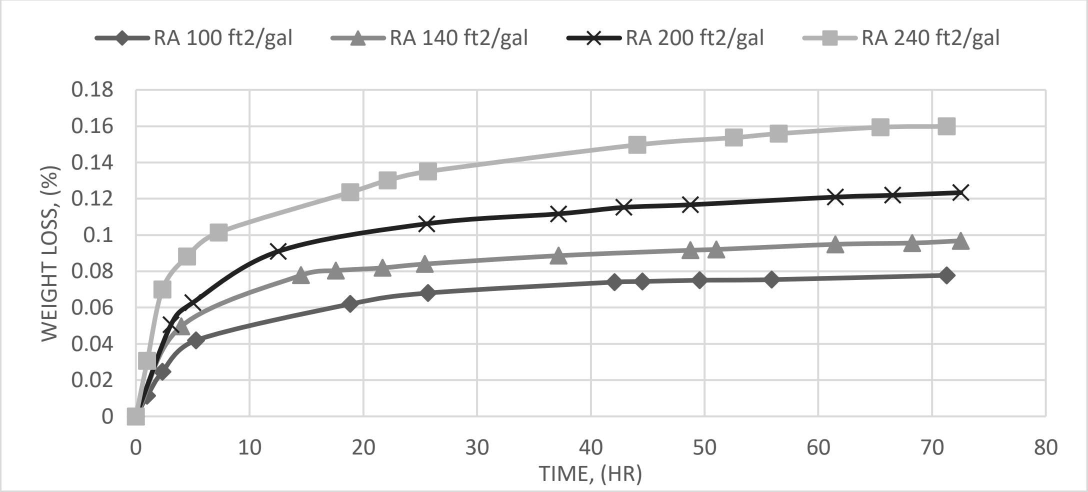

Figure 122. Weight Loss—Wind Speed 0 mph.

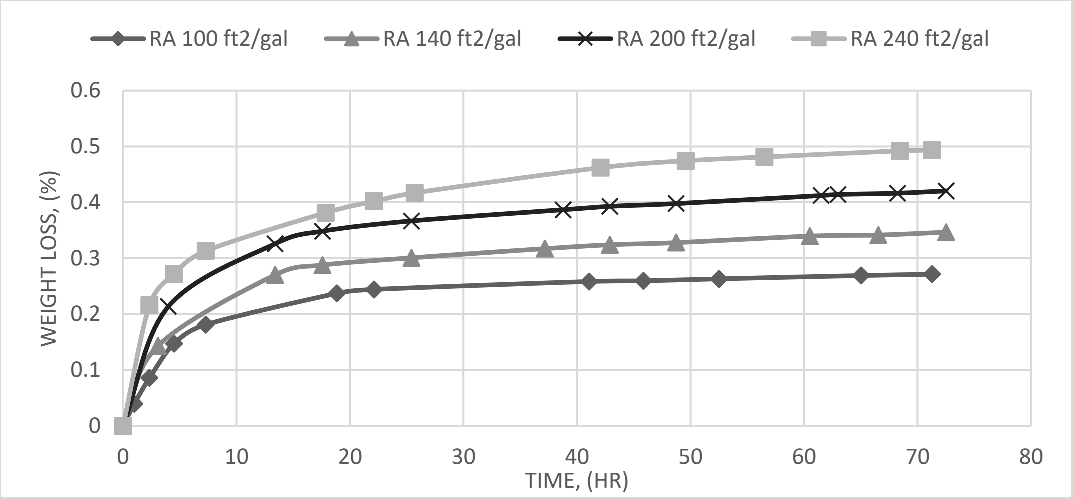

Figure 123. Weight Loss—Wind Speed 5 mph.

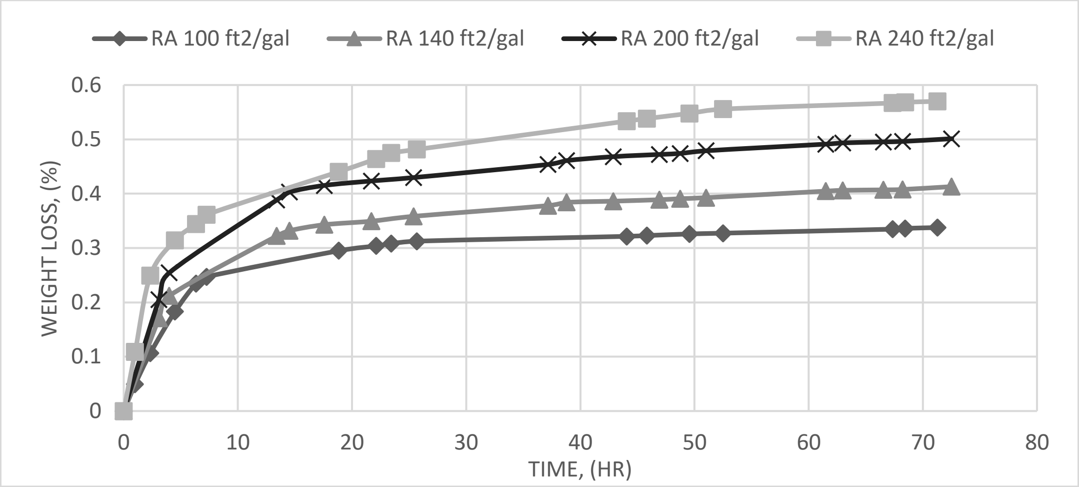

Figure 124. Weight Loss—Wind Speed 10 mph.

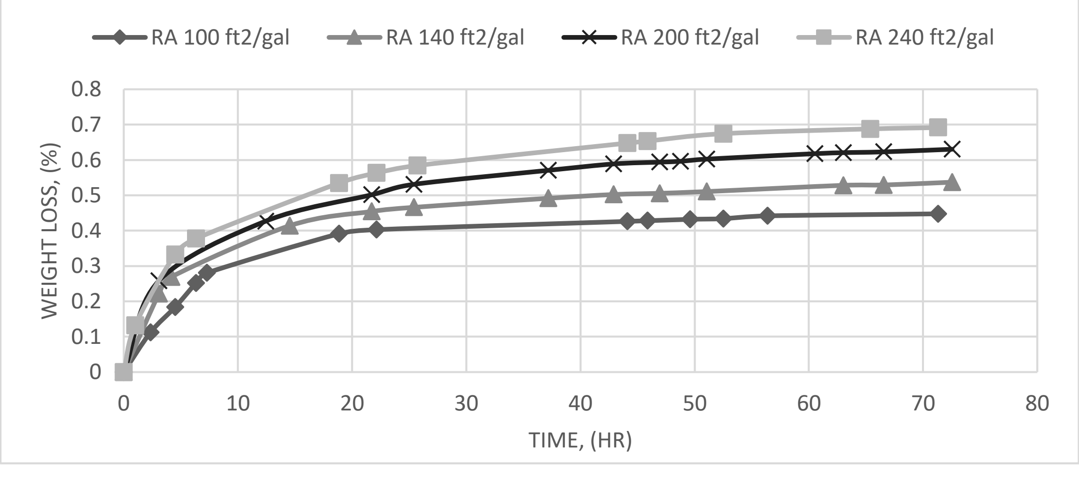

Figure 125. Weight Loss—Wind Speed 15 mph.

Abrasion Resistance Trends

The concrete surface abrasion resistance was obtained by measuring the weight loss of the concrete abraded by a rotating cutter. A 12-in diameter concrete cylinder was also used for measuring RH after 72 hours. The weight loss percentage from the abrasion resistance testing of the mixtures with four different application rates and four wind speed levels are shown in Figure 126 to Figure 129.

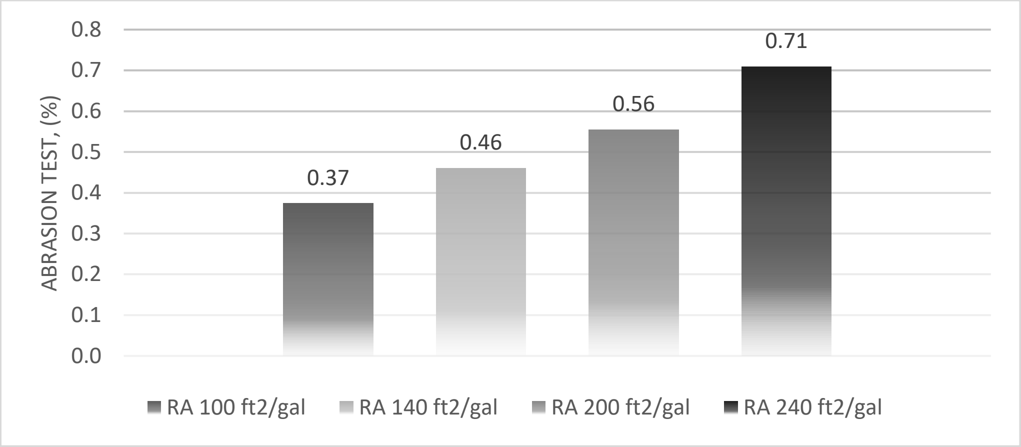

Figure 126. Weight Loss in Abrasion Resistance test—Wind Speed 0 mph.

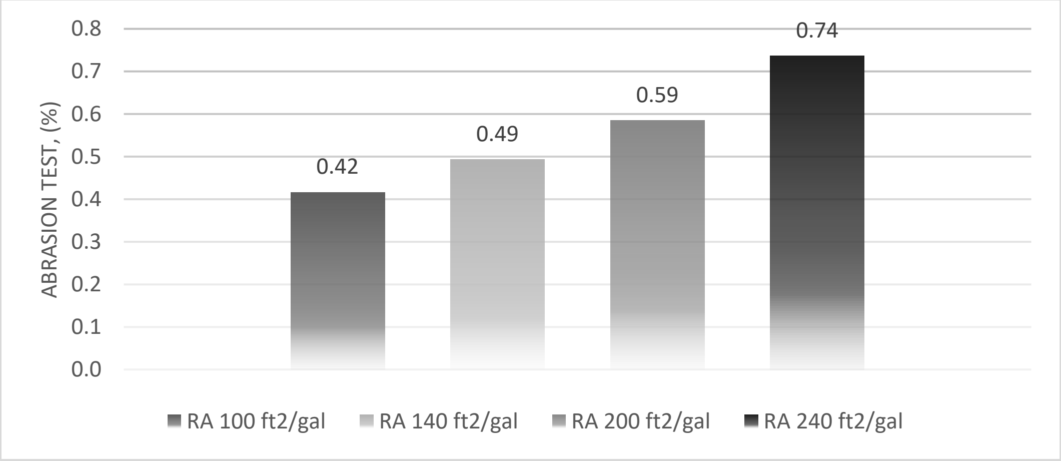

Figure 127. Weight Loss in Abrasion Resistance test—Wind Speed 5 mph.

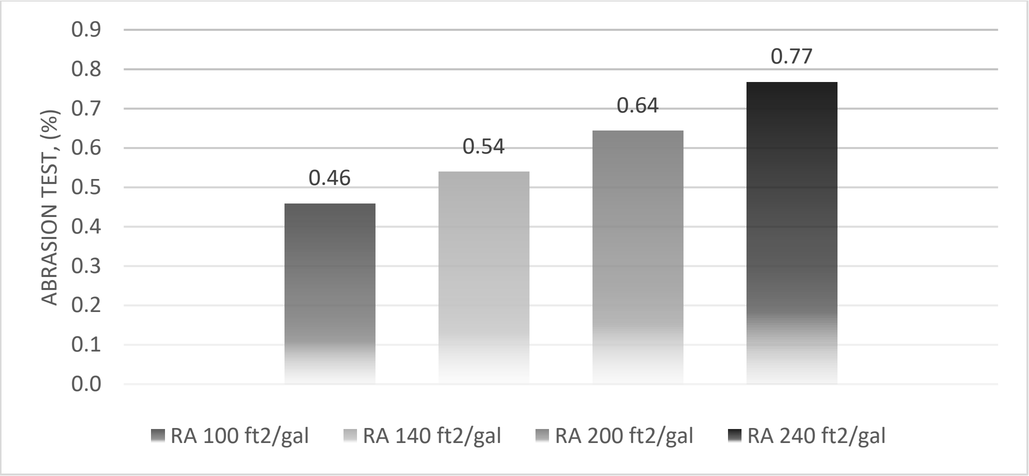

Figure 128. Weight Loss in Abrasion Resistance test—Wind Speed 10 mph.

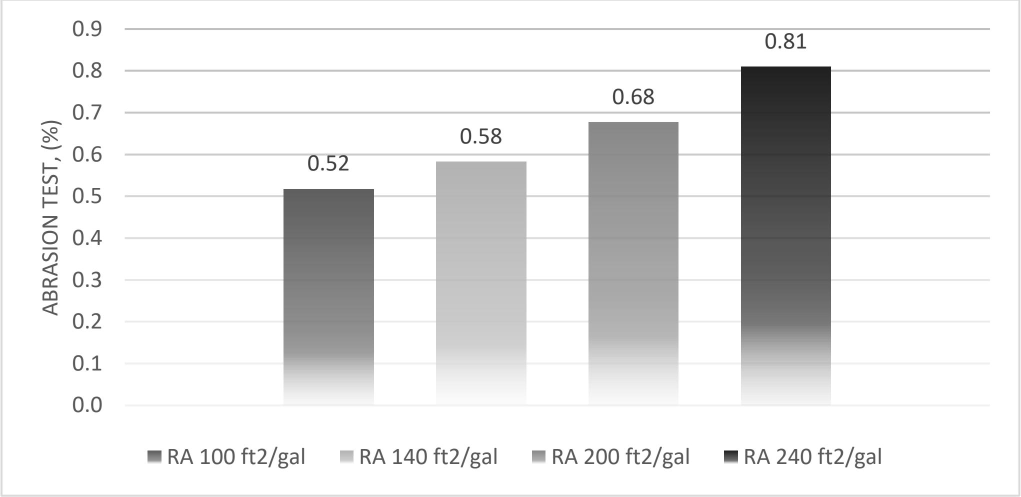

Figure 129. Weight Loss in Abrasion Resistance test—Wind Speed 15 mph.

EI Trends

EI measurements of mixtures with four different application rates and four wind speed levels are shown in Figure 130 to Figure 133. The calculated EI values were compared against moisture weight loss and abrasion results to verify its efficacy as an evaluation index.

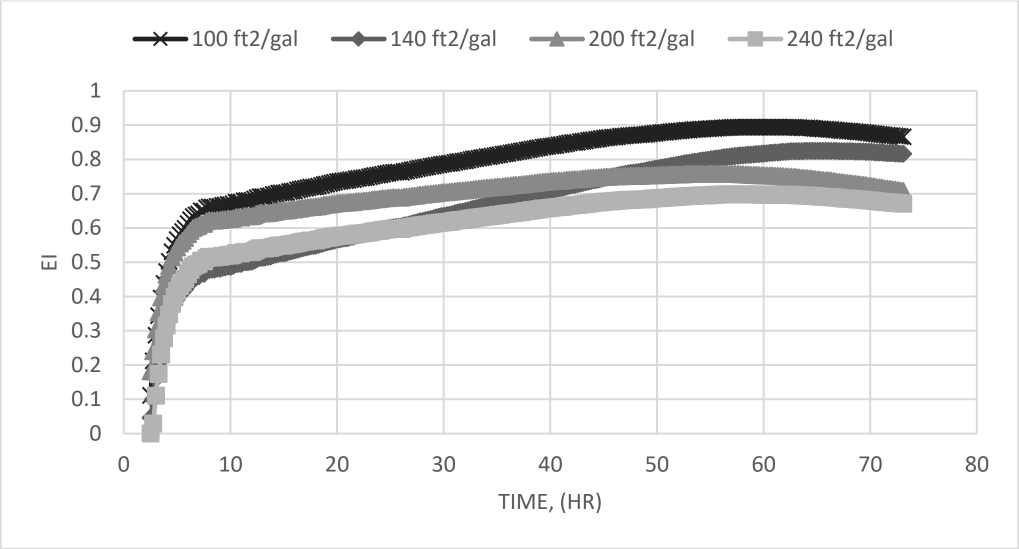

Figure 130. EI measurement—Wind Speed 0 mph.

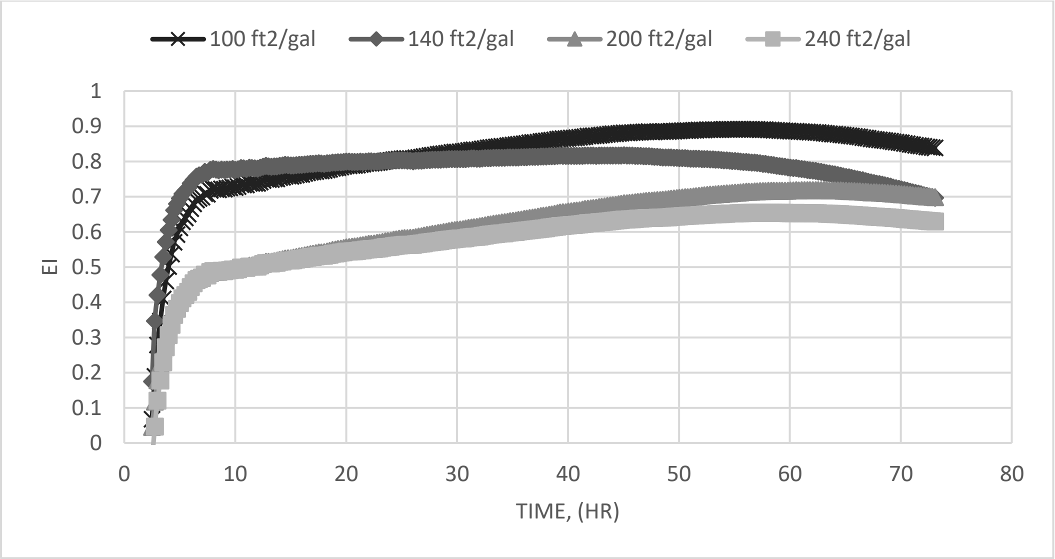

Figure 131. EI measurement—Wind Speed 5 mph.

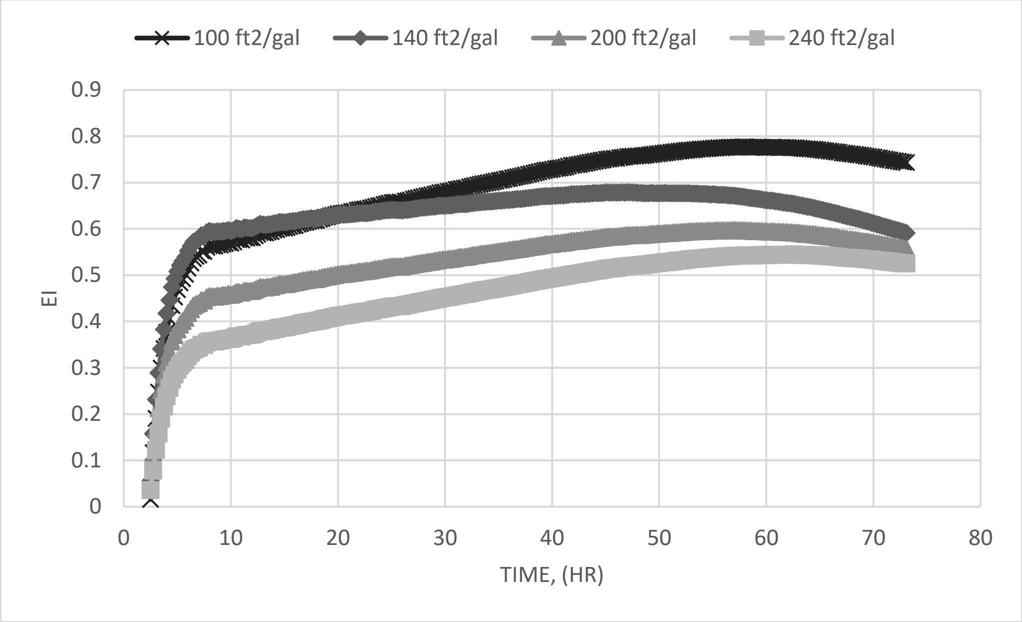

Figure 132. EI measurement—Wind Speed 10 mph.

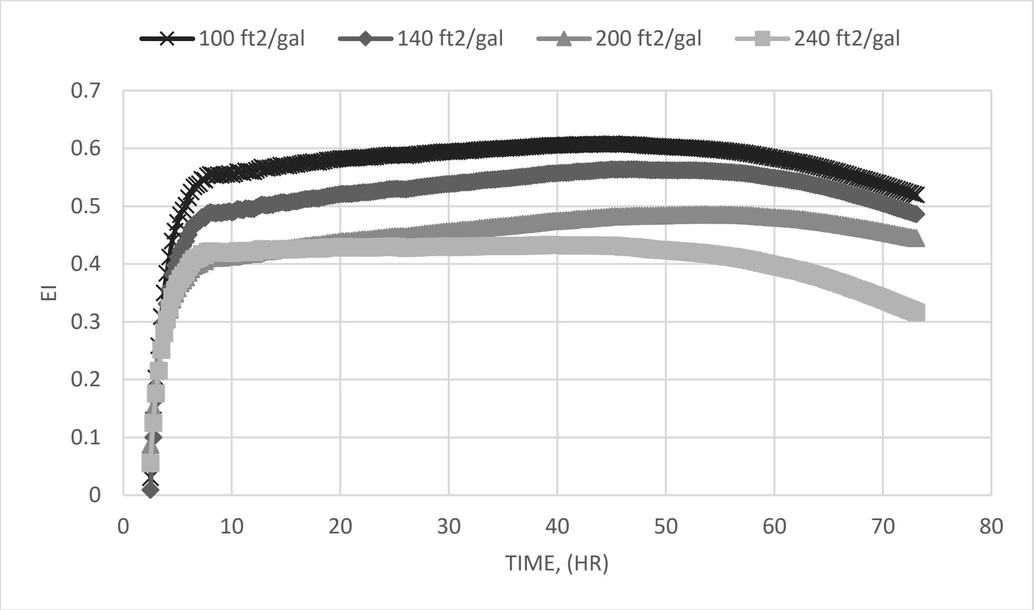

Figure 133. 2 EI measurement—Wind Speed 15 mph.

Analysis and Evaluation

In order to evaluate curing compounds effectiveness, moisture loss and abrasion resistance testing measurements from the surface were conducted. This data was useful to validate the utility of EI and the existence of a relationship between EI and the dielectric data.

The results are shown in Table 33 and EI plotted versus abrasion weight loss and moisture loss in Figure 134 and Figure 135. It can be concluded that as curing quality improves (as indicated by

EI) that hydration improved resulting in stronger concrete surface strength and a decrease in moisture weight.

Table 33. Moisture weight loss, surface abrasion weight loss, and EI.

Wind Speed	No			5			10			15		
	Moisture Loss	Abrasion, Weight Loss	EI	Moisture Loss	Abrasion, Weight Loss	EI	Moisture Loss	Abrasion, Weight Loss	EI	Moisture Loss	Abrasion, Weight Loss	EI
100	0.2265	0.374	0.865	0.272	0.41	0.838	0.3363	0.458	0.743	0.4552	0.517	0.519
140	0.2859	0.46	0.816	0.3398	0.492	0.697	0.406	0.539	0.591	0.5293	0.582	0.483
200	0.3701	0.555	0.708	0.413	0.585	0.699	0.4921	0.643	0.557	0.6155	0.6769	0.444
240	0.4554	0.709	0.67	0.4911	0.736	0.629	0.567	0.767	0.525	0.6849	0.809	0.316

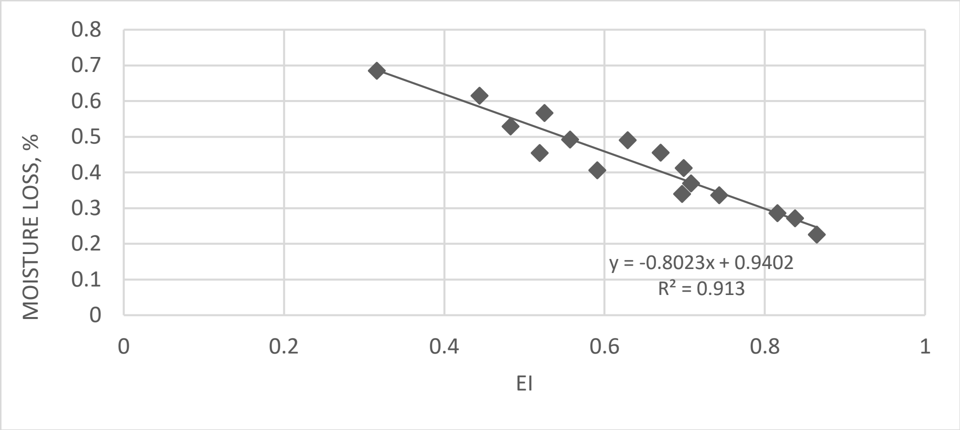

Figure 134. Moisture loss vs. EI.

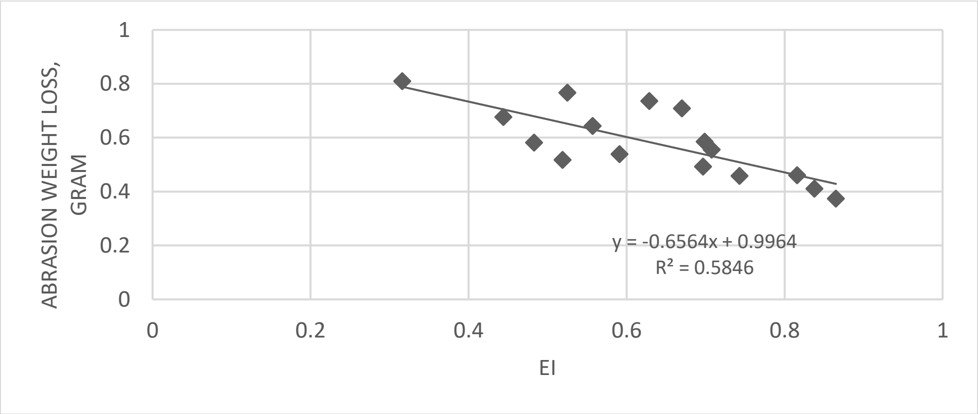

Figure 135. Abrasion weight loss vs. EI.

To examine the correlations of EI with abrasion weight loss and moisture loss, a correlation analysis is done by using the Pearson coefficient of correlation function. The correlation coefficient (a value between -1 and +1) identifies how strongly two variables are related to each other. A correlation coefficient of +1 indicates a perfect positive correlation (i.e., as variable X increases, variable Y increases or as variable X decreases, variable Y decreases). However, correlation coefficient of -1 indicates a perfect negative correlation. The statistical analysis is shown in Table 34.

Table 34. Correlation coefficients of EI with abrasion weight loss and moisture loss.

	Moisture loss, %	**Abrasion weight loss, gram**	**EI**
Moisture loss, %	1		
Abrasion weight loss, gram	0.897	1	
EI	-0.955	-0.764	1

If a correlation coefficient is greater than 0.8, it is classified as a strong correlation, whereas a correlation coefficient less than 0.5 would be classified as a weak correlation. The correlation coefficient between EI and the moisture weight loss measurements is -0.955. This correlation is considered a strong negative relationship, which means that by increasing EI, moisture loss will be decreased. In addition, the correlation coefficient between EI and the abrasion weight loss results is -0.764, which shows a moderate negative relationship. In this relationship, higher EI results in lower abrasion weight loss.

To validate the utility of EI to represent the effectiveness of a given curing practice, sensitivity analyses are conducted by comparing EI under different curing treatments, such as various wind conditions and application rates of curing. EI in various conditions is shown in Figure 136, which presents EI under four wind speeds and at four application rates (ARs).

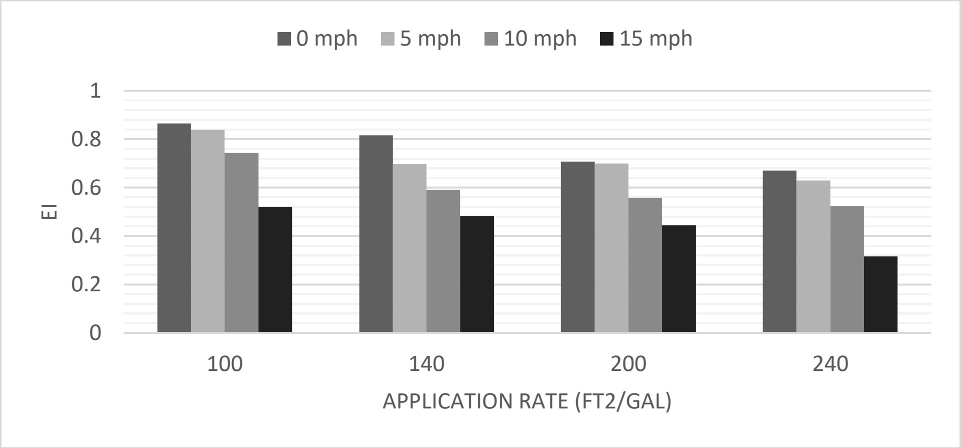

Figure 136. EI measurements comparison by different ARs.

The effect of wind condition on EI was investigated. It was observed that EI under no wind condition are consistently higher than under wind condition regardless of what the curing application rate was. The reason is curing practices were significantly influenced by the ambient wind conditions which caused more moisture evaporation at the surface of the concrete.

Dielectric Constant (DC) Measurement and Trends

Research has indicated that DC is highly sensitive to the moisture content at the surface of concrete where DC measurements indicate strong relationships with the volumetric change in free water content. In early-age concrete, when the volumetric moisture content is high, DC measurements are high but with time, due to moisture loss and hydration, the DC readings decline with a decrease of free water content proving that DC trends with curing quality. For example, sealed sections which were subjected to a better curing condition indicated a lower decreasing rates of DC measurements.

DC measurements were conducted at the surface of 6-in diameter and 2-in height concrete specimens under four different wind speeds and four ARs; Figures 137-140 illustrate the results.

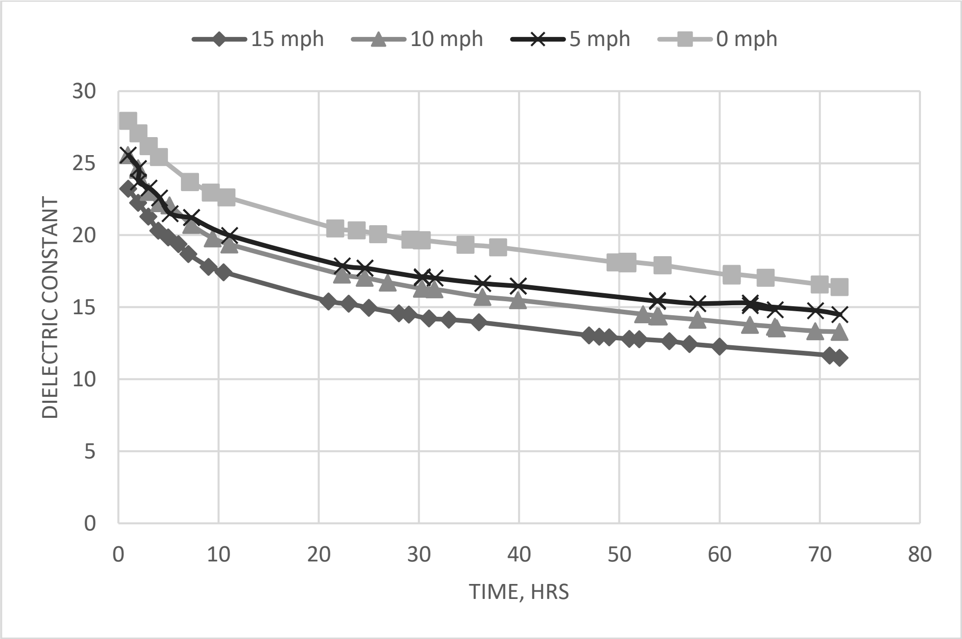

Figure 137. Dielectric constants for City White compound with AR100.

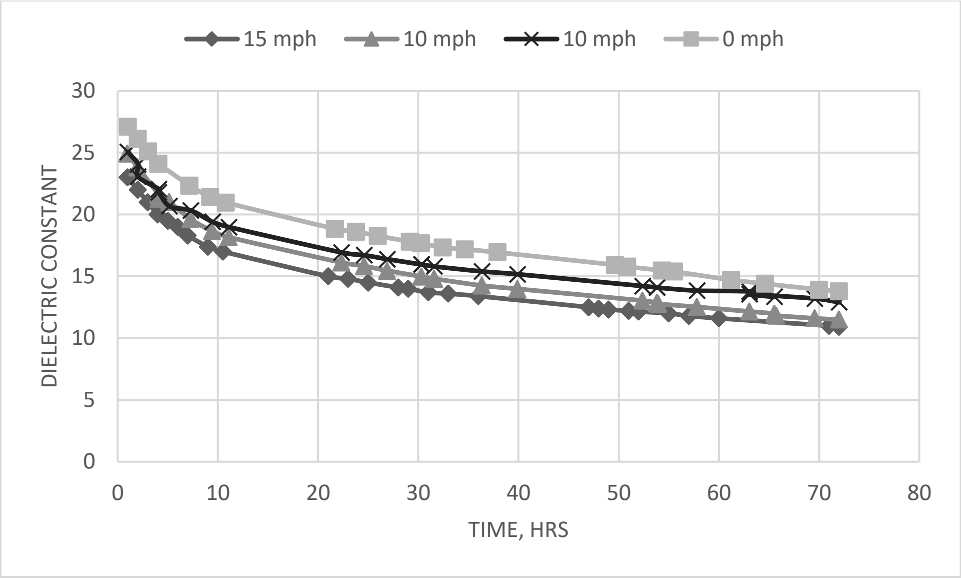

Figure 138. Dielectric constants for City White compound with AR140.

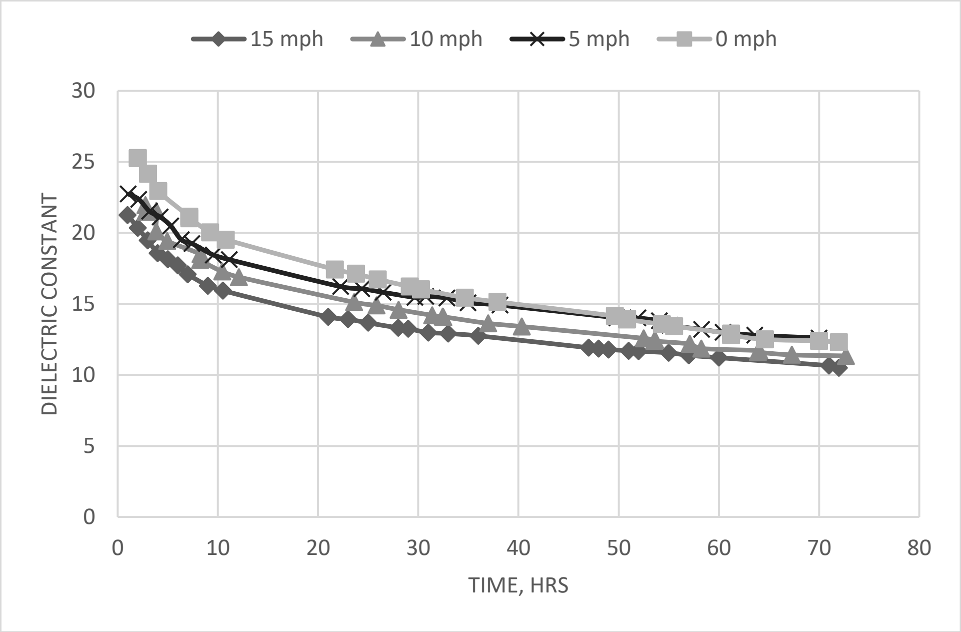

Figure 139. Dielectric constants for City White compound with AR200.

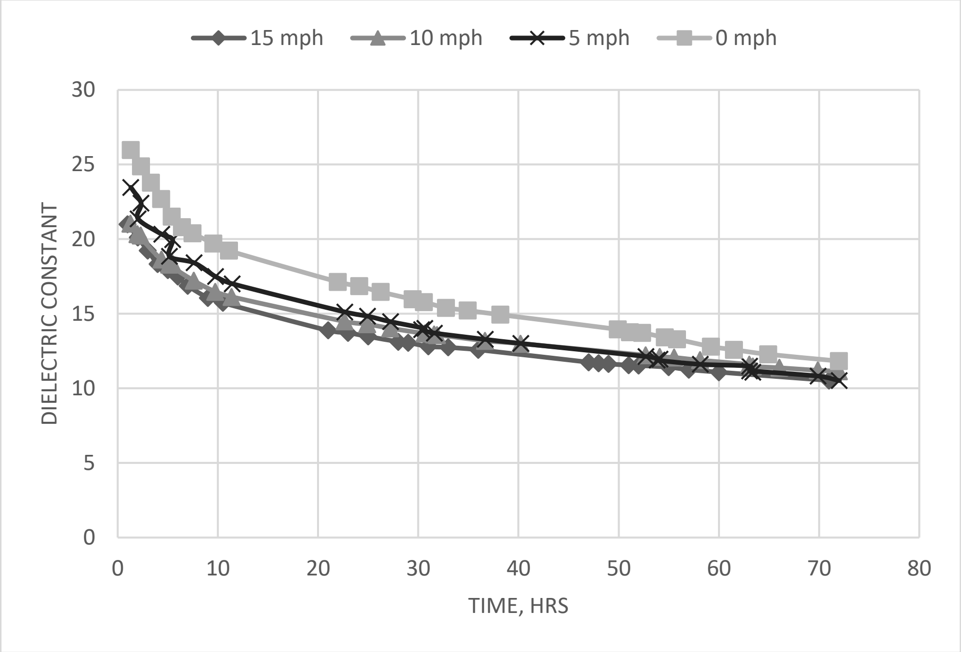

Figure 140. Dielectric constants for City White compound with AR240.

Figures 137-140 illustrate that the DC measurements for specimens treated with different ARs of curing compounds had similar sensitivity to wind conditions. Initially, the moisture content at the concrete surface was very high, so the DC measurements were correspondingly high as well. Gradually, DC measurements began to decrease over 72 hours. The most significant changes in DC occurred under higher wind conditions. It is noteworthy that rates of change in DC values for all specimens treated with wind conditions were very similar although some trends exhibited minor differences between specimens applied with different ARs. Higher ARs showed a little bit higher DC measurements over time. It could be concluded that DC measurements were sensitive to the wind condition and the rate of application.

Thin Sections

Sample images were analyzed with a microscopy imaging computer program that maps the quantity and density of voids found in the image field area. The images are shown in Figure 141 at various magnifications to indicate how different void sizes were identified. The voids were distinguished visually and their corresponding areas were measured using the image analysis software. The results of the image analysis relative to the rate of application (AR) and the depth from the cured surface are shown in Figures 142 and 143.

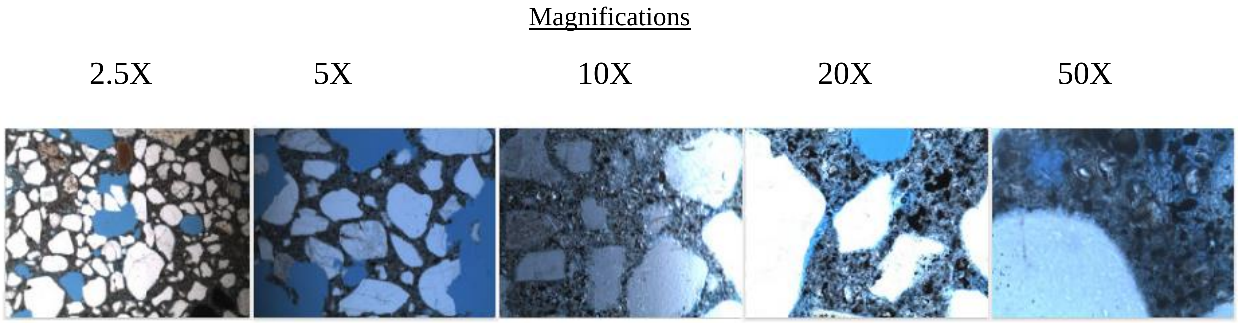
Magnifications
2.5X
5X
10X
20X
50X

A. Control Sample (No curing compound)

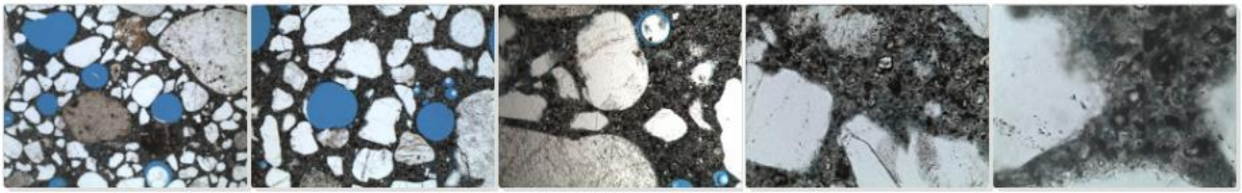

B. Application Rate = 200 ft^2/gal

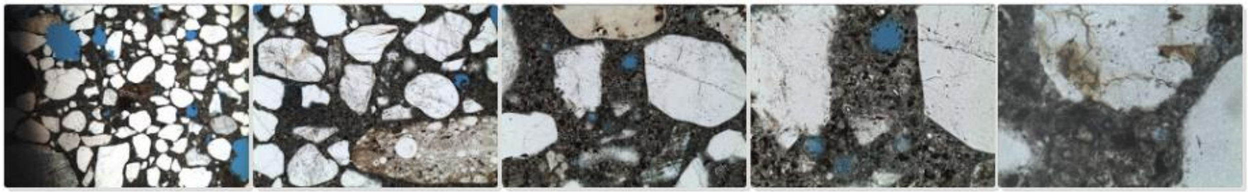

C. Application Rate = 100 ft^2/gal

Figure 141. Effects of curing compound rate on porosity of specimens.

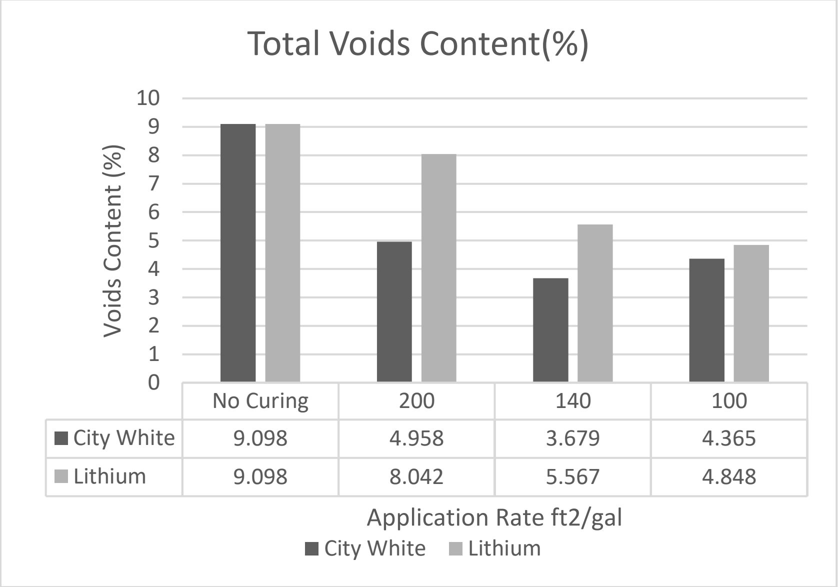

	No Curing	200	140	100
■ City White	9.098	4.958	3.679	4.365
■ Lithium	9.098	8.042	5.567	4.848

Figure 142. Total voids content for different AR.

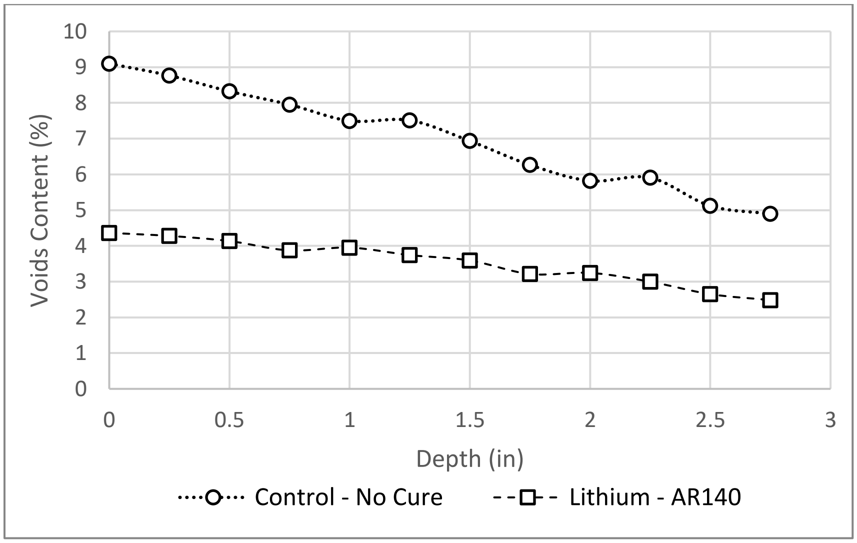

Figure 143. Total voids profile content versus depth from the cured surface.

Figures 142 and 143 indicate that total void space reduces as the quality of curing improves or as the distance from the cured surface increases, thereby suggesting the role that bleeding action can have on the quality of the cured concrete. As shown in Figure 143, the total void's volume diminishes with depth suggesting the bleed induced void space is closer to the evaporative surface. The lower the amount of change from the surface the more likely the higher the curing quality is. Furthermore, due to the effects on the pH of the pore water, lithium as curing medium likely results in greater reduction of the bleed induced pore space than non-lithium alternatives.

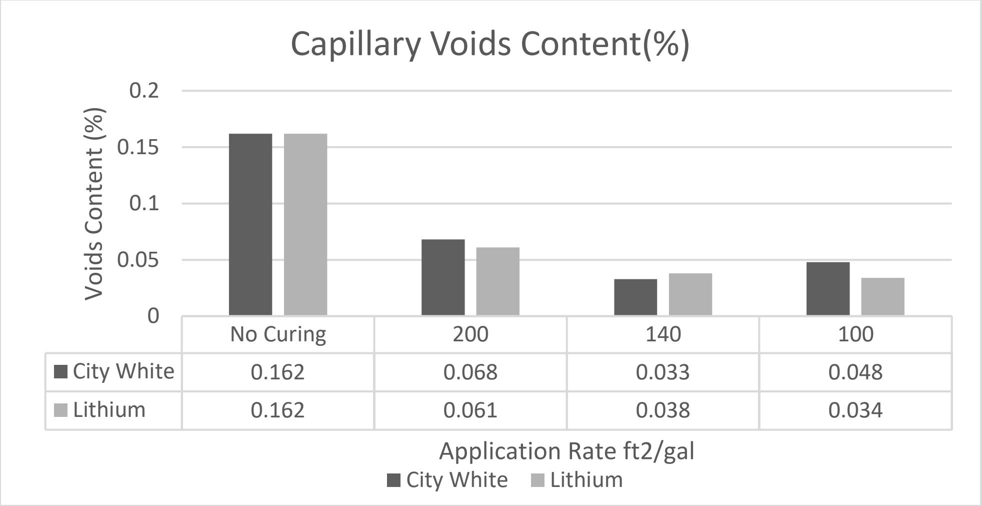

Figure 144. Capillary voids content for different AR.

The smallest class of optically visible voids noted in the thin sections is the capillary voids although limited range of capillary sizes were detectable in the image analysis. A few of the larger capillary voids (Figure 144) may be seen at the higher magnifications reported in the Figure 141. Capillary voids are spaces formed in part with the mixing water in the hydration process. They were occupied by water when the concrete was fresh and are likely larger and more abundant in concretes with a high water-cement ratio.

The amounts of the capillary pores are controlled by the water-cement ratio and the degree of maturity of the concrete. Lower quality curing may increase the total void content near the evaporative surface, since moisture content tends to increase at that location. As the concrete matures, some of the capillary space may become filled with the products of hydration and the products of any reactions occurring between the chemicals of the paste, so keeping moisture inside the body of concrete by applying a curing compound retains enough water in the pores for the cement to hydrate.

Shrinkage Test

The common cause of cracking in concrete is shrinkage due to drying. This type of shrinkage is caused by the loss of moisture from the cement paste constituent, which can shrink by as much as 1 percent per unit length. These moisture-induced volume changes are a characteristic of concrete. Curing compounds may prevent moisture loss and mitigate adverse effects of this incident. In Figure 154, shrinkage is plotted for SINAK (Lithium Cure) and City White curing compounds in two water-to-cement ratios, respectively:

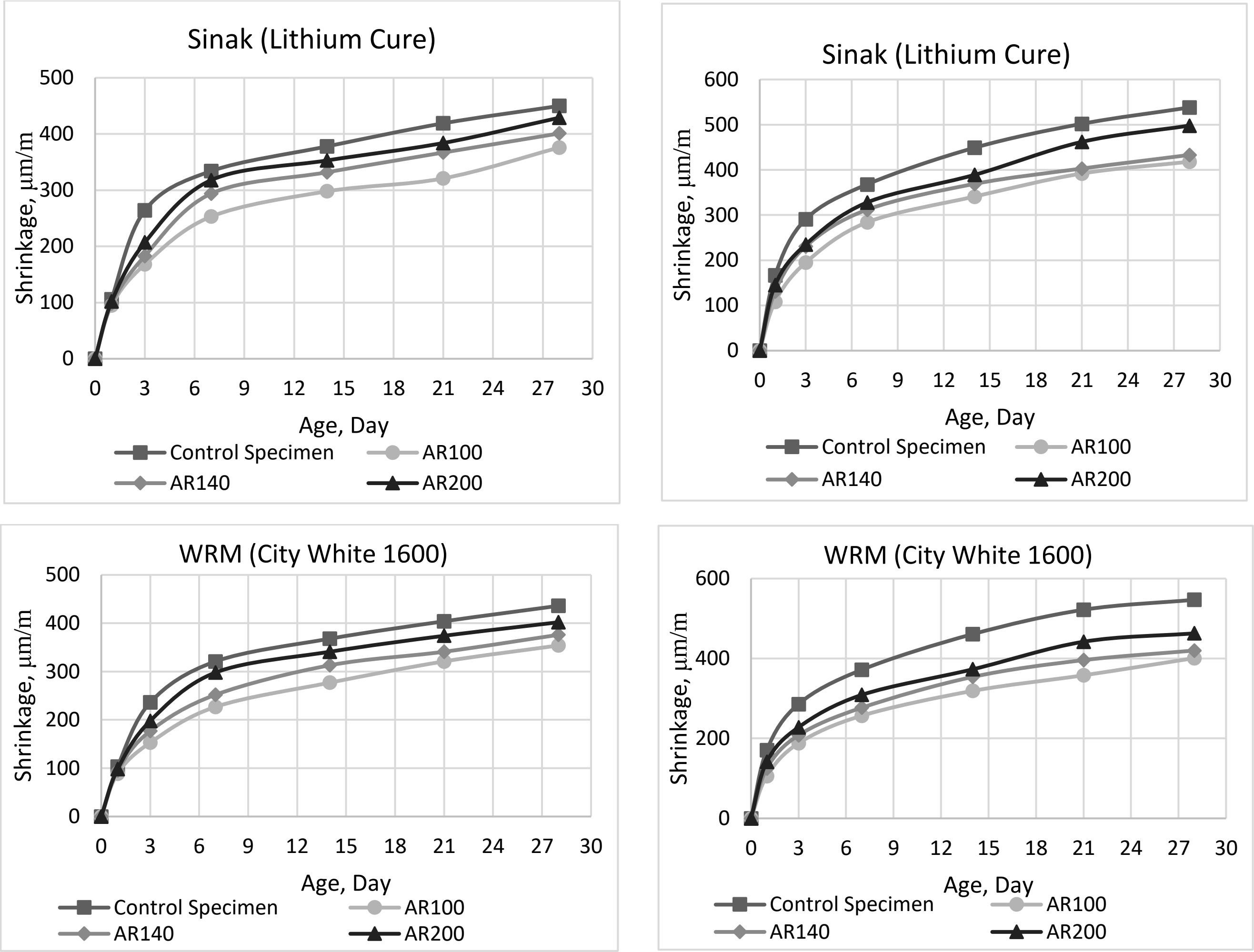

Figure 145. Effect of application rate on drying shrinkage in W/C=0.40 and 0.45.

The results show that the shrinkage potential of a particular concrete is influenced by the amount of curing compound, the elapsed time after the addition of water, and water-to-cement ratio.

Curing Protocol

In order to understand the utility of the DC measurements, a modified Weibull distribution function was used to generate regression curves fitting the DC measurements. The following expression was used to carry out the regression:

$$\varepsilon_r = \tau\left\{1 - e^{-\left[\frac{\beta}{t}\right]^{\alpha}}\right\}$$

where:

ε_r = DC

t = elapsed time, hours

τ = amplifying parameter

β = scaling parameter, and

α = shift parameter

The key parameter is the β term, which was found to correlate to EI. A summary of the laboratory data yields the following table and figures:

Table 35. Laboratory data summary.

Data Set	β	PE	EI
1	0.091	0.11274	0.828
2	0.064	0.11274	0.989
3	0.055	0.10025	0.946
4	0.206	0.15457	0.738

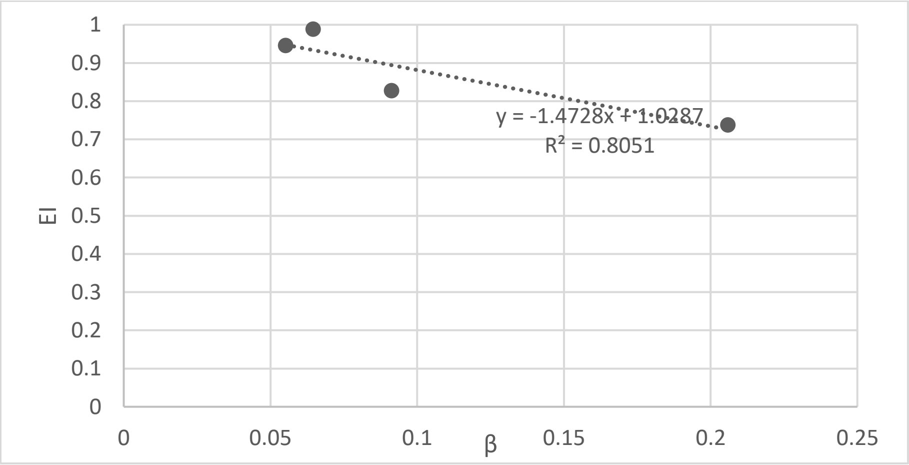

Figure 146. EI versus β based on laboratory data.

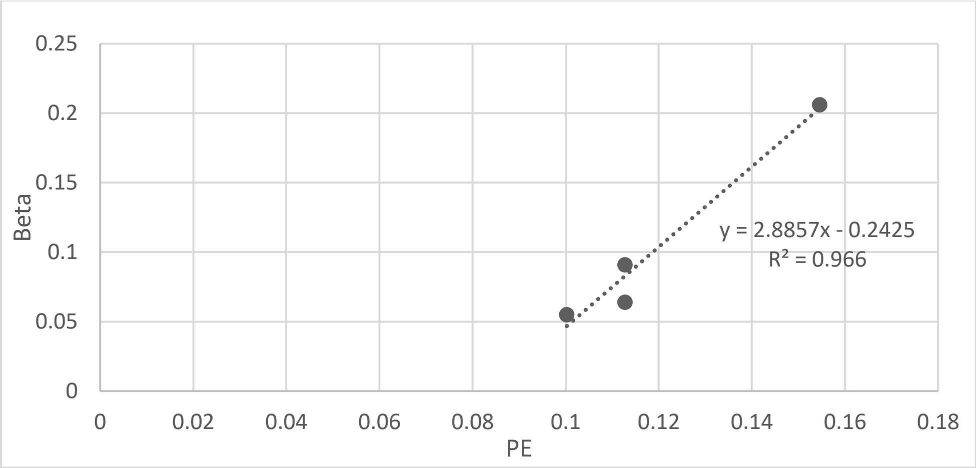

Figure 147. β versus PE based on laboratory data.

These figures indicate that there is a promising relationship between β and EI and between PE and Beta for a given curing compound, and consequently, the determination of β or EI under field conditions should provide a means to infer the required application rate to yield a desired EI.

Curing Effectiveness Laboratory Reference Curves

As previously elaborated, the laboratory data was used to develop a relationship between EI, the PE of the ambient conditions, and the application rate of the curing compound plotted in Figure 148. It provides an empirical method to predict the application rate of a curing compound for a given ambient environment condition of a new construction project. Further, three-dimensional figures display the relation among EI, PE, and the application rate, as shown in Figure 149. The PE in this figure is calculated for the environmental conditions in the laboratory. With respect to correlation among these parameters, an equation is driven to calculate application rate. So, by knowing W/C, PE (ambient conditions), and minimum EI that is appropriate curing quality for site construction, the minimum amount of compound can be calculated.

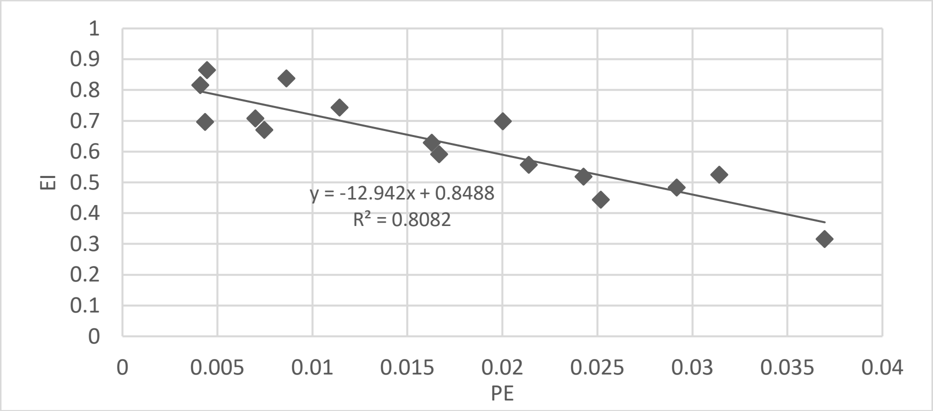

Figure 148. EI vs. PE in the laboratory.

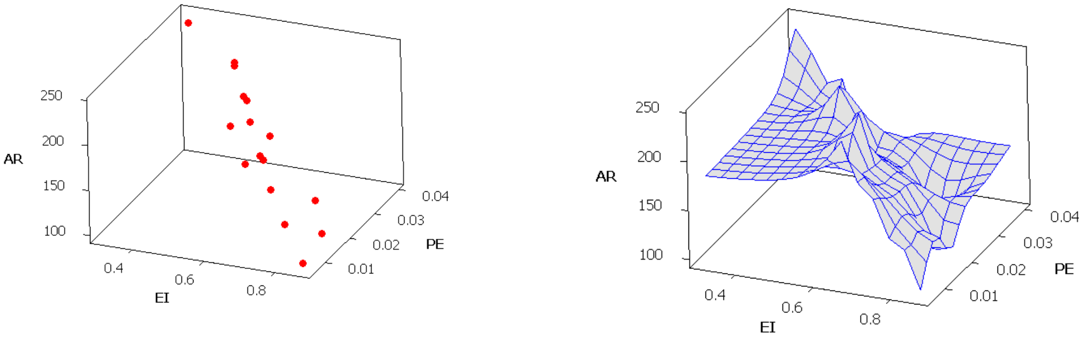

Figure 149. Diagrams from EI, PE, and the Application rate.

Special Comparative Studies

There are various criteria associated with performance of compounds in concrete curing. Each one of these parameters might present efficiency of compound and assist contactor to choose most appropriate one. In Table 36, a summary of two curing compounds, City White and Lithium, is presented. All the results show consistency with concept of applying curing compound might improve characteristics of concrete and summary of all these factors come in one index, which is called EI. Therefore, following EI trends for each curing practice could present performance of given compound.

Table 36. Comparison between two curing compounds in related parameters.

	Application Rate (ft2/gal)	Total Voids Content (%)	Capillary Voids Content (%)	Moisture Loss (%)	Beta	Shrinkage (μm/m)	Abrasion Resistance (%)
W. R. Meadows - 1600 City White	No Curing	0.161	9.098	0.194	0.182	436	0.709
	200	0.067	4.957	0.122	0.087	402	0.555
	140	0.033	3.678	0.097	0.082	376	0.46
	100	0.048	4.364	0.078	0.071	354	0.374
SINAK - Lithium	No Curing	0.161	9.098	0.194	0.182	436	0.709
	200	0.061	8.041	0.168	0.109	429	0.585
	140	0.038	5.566	0.139	0.091	401	0.492
	100	0.034	4.848	0.108	0.073	374	0.416

The EI for all four tested compounds under different conditions are shown in Table 37. As EI gets higher value, the compound performs better in curing. So normally compound with highest EIs are placed within top ranking curing compounds.

Table 37. EIs for four compounds under different conditions.

Ranking				#1	#2	#3	#4
	W/C	Application Rate	Wind Speed	W. R. Meadows - 1600 City White	SINAK - Lithium	DAYTON - DSSCC	W. R. Meadows - 1300 Clear
1	0.4	100	0	0.907	0.917	0.845	0.768
2			6	0.83	0.789	0.739	0.675
3			15	0.742	0.624	0.654	0.603
4		140	0	0.821	0.827	0.802	0.721
5			6	0.701	0.701	0.721	0.665
6			15	0.652	0.576	0.639	0.543
7		200	0	0.782	0.716	0.745	0.694
8			6	0.716	0.603	0.672	0.578
9			15	0.623	0.524	0.623	0.502
10	0.45	100	0	0.921	0.954	0.872	0.789
11			6	0.847	0.858	0.823	0.693
12			15	0.794	0.754	0.71	0.645
13		140	0	0.864	0.844	0.829	0.756
14			6	0.789	0.736	0.766	0.641
15			15	0.712	0.589	0.703	0.569
16		200	0	0.801	0.732	0.791	0.71
17			6	0.754	0.584	0.742	0.594
18			15	0.691	0.495	0.698	0.553

As it is shown in Figure 150, W. R. Meadows—City White and SINAK-Lithium have higher EI values under the similar situation which means that higher quality is expected from these compounds, while WRM Clear has lower values rather than other compounds.

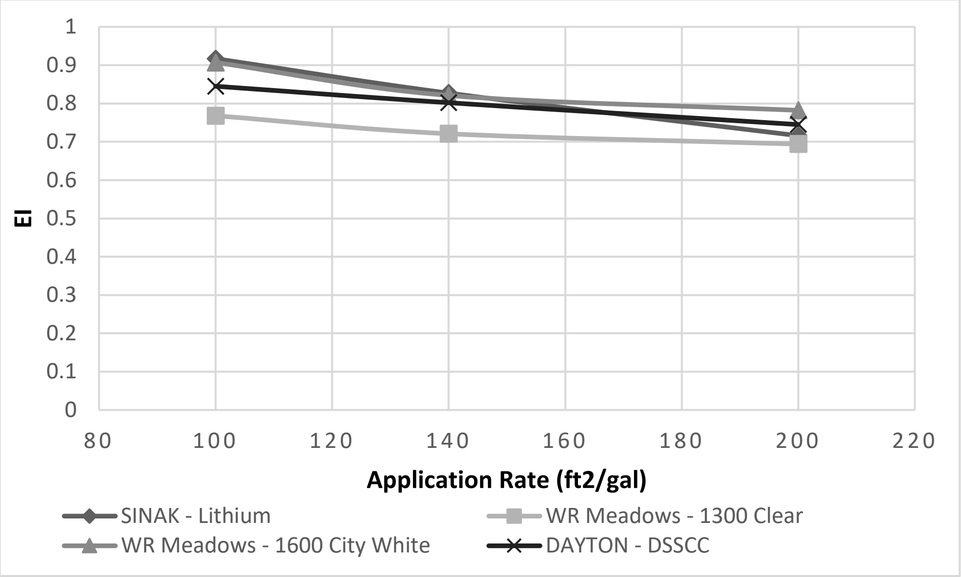

Figure 150. EI comparison among four curing compounds (W/C=0.4 - Wind speed=0).

Testing Program on John Stockbauer Dr.

Four sections were monitored by the ACMM the GPR systems previously described. The curing treatments for the four sections are shown in Table 38.

Table 38. Curing Treatments for the Victoria Test Sections.

Test Section#	Lithium Cure		Resin Cure	
	Type	Application Rate	Type	Application Rate
1	Transil	200 ft^2/gal	City White-E	200 ft^2/gal
2	Transil	200 ft^2/gal	City White-E	150 ft^2/gal
3	SINAK	200 ft^2/gal	City White-E	200 ft^2/gal
4	SINAK Mix	200 ft^2/gal	None	None

Lithium curing compounds were all sprayed manually. Once lithium was sprayed, the City White-E resin-curing compound served as a second layer of coating was applied by using a spraying machine.

DC measurements were taken for the four sections over a 43-hour period. The detailed results are shown in the following figures for the four fields. In the field study, five data points were taken for each time and averaged. The fitted regression parameters of the four sections are shown in Table 39 and the fitted regression curves for the four sections are shown in Figure 151.

Table 39. Regression parameters and EI for the four test sections in the field.

Test Section#	*α*	*β*	*τ*	EI
1	0.295	0.091	13.869	0.828
2	0.472	0.064	12.551	0.989
3	0.712	0.055	16.474	0.946
4	0.293	0.206	16.674	0.738

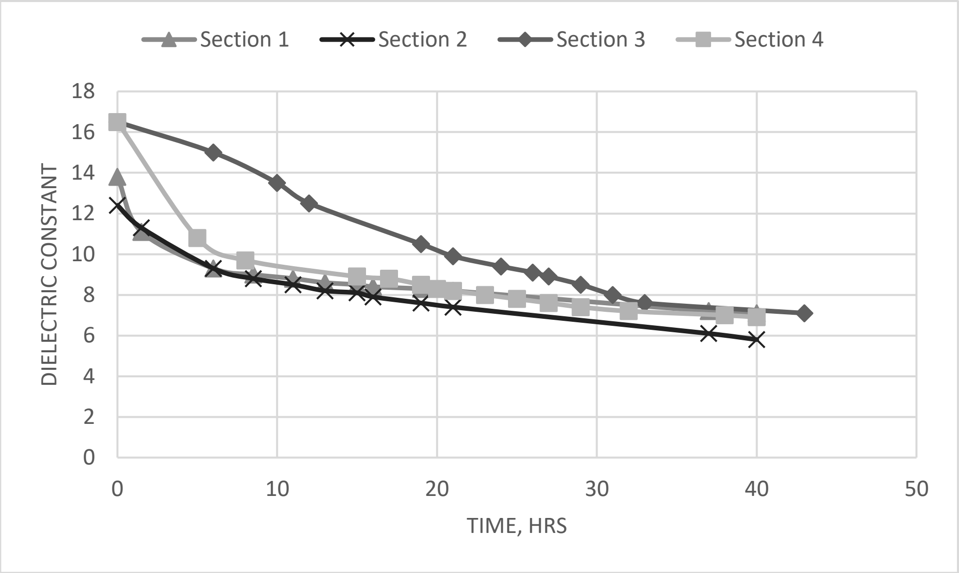

Figure 151. Regression Curves for DC Measurements in the Field Using the Percometer.

As shown in Figure 152, a direct relationship was found between EI and beta. A higher EI is generally associated with a lower beta, which represents a lower decreasing rate of DC measurements and a better moisture retention capability of the curing practice. Therefore, these results tend to validate the utility of using DC measurements to qualify curing quality. Though more results are needed to further understand the relationship between EI and beta, it still shows good potential for using beta and DC measurements to extend the evaluation of the effectiveness of curing compounds beyond the use of EI.

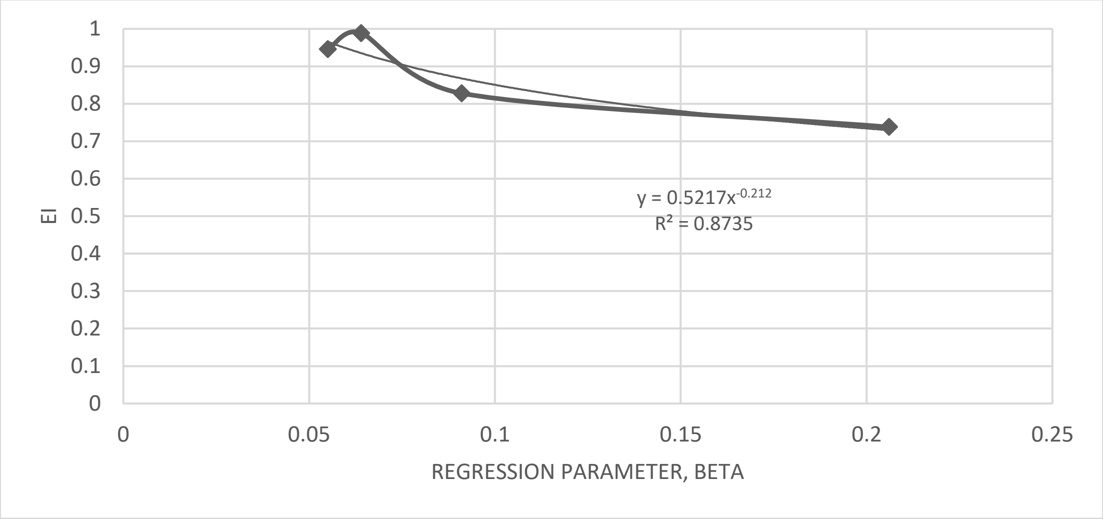

Figure 152. Regression parameters and EI for the four test sections.

Testing Program on Ball Airport Rd

Figure 153 shows typical sample data taken during the field study for a 45 ft. long test section. In spite of the poor curing condition, it is evident in Figure 153 is it possible to achieve good repeatability of the collected data. The data was collected three times after the curing compound dried to avoid disturbance to the sampling area. During the repetition of the data collection, the wheels on one side of the cart was pushed align with longitudinal joints. The data shows that the variance of the three repetitions at each location was very small; for all the positions in this section, the average of the standard deviation for three repetitions was only 0.68, which indicated that the repeatability of the data collection procedure was very high. The GPR device was calibrated each time before data were taken to insure the accuracy of the.

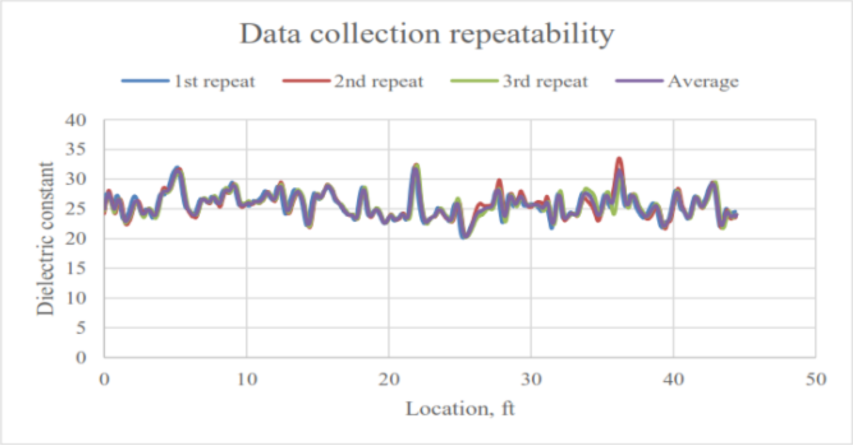

Figure 153. Sample DC data obtained with the GPR cart.

Another sample of the data collect is shown in Figure 154 with a time delay of 3 hours between the readings at the same locations. The shapes of the amplitude of the two data sets were almost the same, whereas the magnitudes of the "earlier readings" were greater comparing to those of the "later readings." This phenomenon is the key to the evaluation of curing effectiveness with this device. The decrease in the magnitude of DC as time elapsed was due to the evaporation of the unused free moisture in hardened concrete. Since more free moisture is held at the surface, the DC measurements are expected to stay at a higher level for a longer period of time compared to those of uncured concrete. The better the curing practice is, the longer it takes for DC to drop to lower levels.

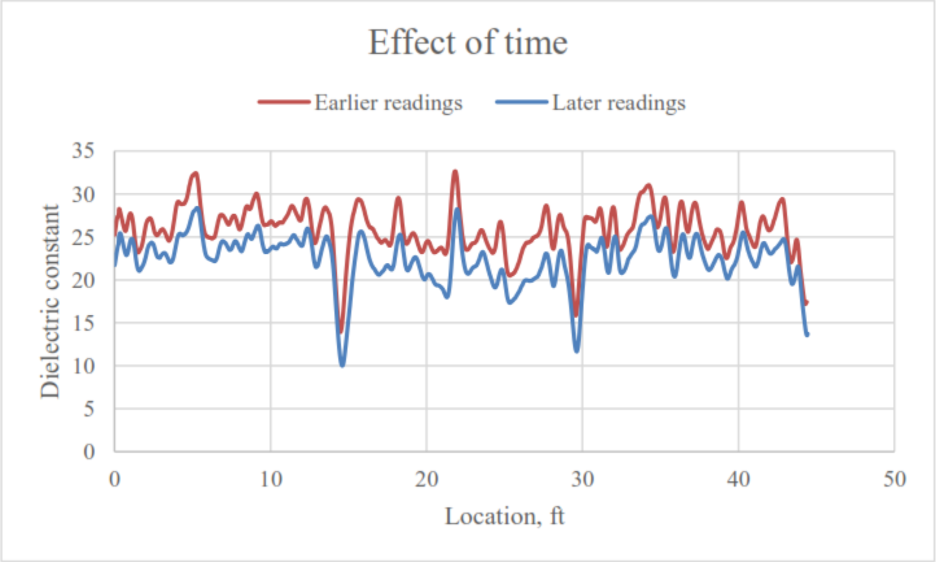

Figure 154. Two DC data traces at separate times.

The Proof of Concept behind Protocol

In order to prove the viability of the EI protocol, this study proposed the following:

- The establishment of a laboratory reference curve that covers the range of PEs and EIs expected under field conditions.
- The calibration of a field relationship between the EI and beta.
- The use of both of these curves to determine the appropriate rate of application of a given curing compound.

Field Reference Curves

As previously indicated, a relationship between beta and EI was established for the field sections where both the ACMM and percometer data collection sites were setup. If one wants to know the EI for broader areas of a paving project other than the position of the ACMM, DC measurements are necessary. Once DC measurements are taken and the beta is derived from the DC measurements (for areas where ACMM system is not positioned), the EI is predicted based on the known (or calibrated) relationship between EI and beta for a given ambient environment condition.

Once the field determined EI is calibrated against the field determined beta values; EI is taken from the beta values and used to determine the rate of curing. Therefore, in this manner, EI is used to predict the application rate of curing compounds for construction for a known ambient environment condition using the laboratory reference curves for the project approved curing compound.

Once the relationships are established, one could predict the best application rate of a curing compound under a given PE for a new construction project. If all the relationships are merged together a reference curve in the field created to infer the value of EI based on beta.

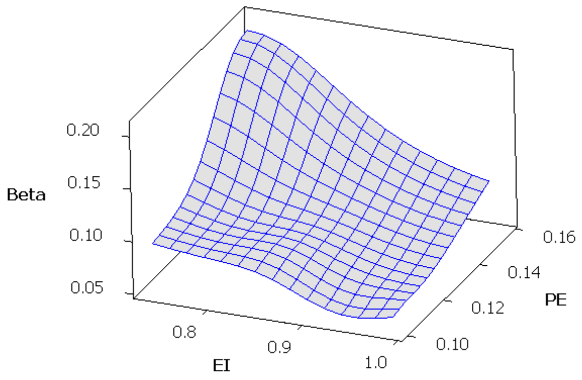

Figure 155. Diagram from Field EI, PE, and Beta Data.

Curing Monitoring Protocol

By knowing the field beta from the DC data, one can determine the EI from Figure 156. Given the field based EI, the application rate of the curing compound could be determined from this Figure for the given PE. It provides an empirical method to predict the application rate of a curing compound for a given ambient environment condition of a new construction project.

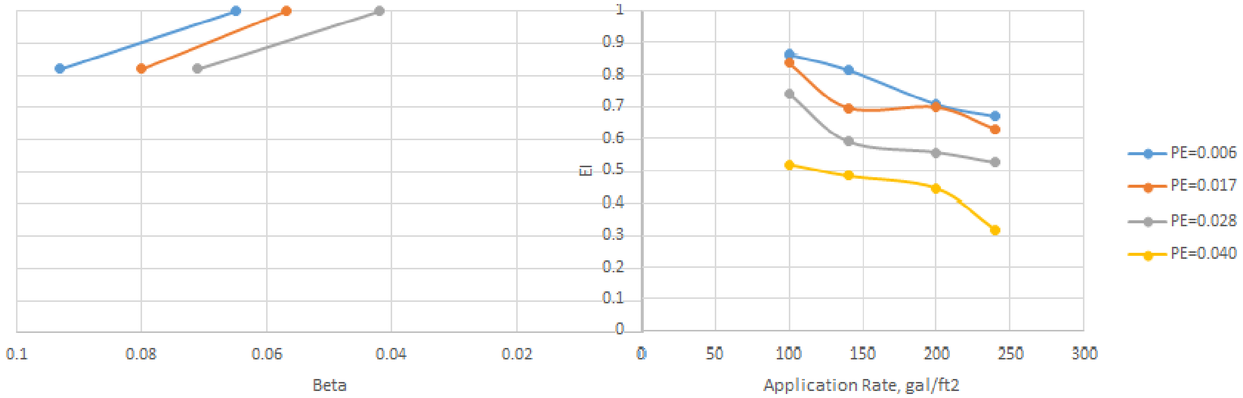

Figure 156. Curing Monitoring Protocol.

CONCLUSIONS

In conclusion, several considerations regarding implementation of the EI concept are subsequently addressed to emphasize how EI can be utilized to assess curing quality. From the results obtained in this investigation, the following conclusions can be drawn:

- The results from the laboratory testing indicated that measures of moisture loss and strength were consistent with measures of EI, Beta, drying shrinkage, and total voids with respect to the type of curing compound. This finding supported the development of a protocol in which to assess the effectiveness of a curing compound applicable to both the laboratory and the field—meeting an important goal of this research.
- Implementation of the EI concept potentially provides several advantages for TxDOT and the related construction industry. A practical means to address the influence of field conditions on curing quality including a variety of combinations of temperature, solar radiation and wind, early-age water evaporation at the surface of a concrete pavement during construction on performance. Climatic effects such as these have been suspected for years as the source of insufficient hydration of the surface concrete resulting in impaired strength and durability. Other detrimental impacts, such as plastic shrinkage cracking and delamination (cause of spalling) that eventually affect the long life of a concrete pavement have also been concerns and the approach advanced in this research provides a path to address curing needs before it becomes too late.
- A new protocol for evaluating concrete curing effectiveness has been proposed in the first phase of this study. This protocol consists of the determination of the EI and using the change (β) in dielectric constant (DC) measurements with time at the concrete surface to qualify curing quality. EI is a calculated parameter based on the concrete maturity concept based on three different RH and temperature related measurements using a device especially configured for this purpose. The DC of a concrete surface measured by a GPR air-launched system to indicate the free moisture content on the surface of concrete is also considered as a rapid means to collect dielectric data over an extensive area.
- Potential benefits of the EI concept include providing a means to rank effectiveness of various curing compounds, allowing determination of the minimum required curing compound application rate for environmental conditions, and through the use of GPR allowing near full-coverage verification of proper concrete curing. Since EI is a time-based factor, the concept could also help determine the proper timing for application of curing compound.

Further work is needed to increase the technology readiness of the EI concept in preparation for transition to stakeholders. Such work should include:

- Further validation of the EI concept through evaluation of the concrete mixture pore structure and early-age shrinkage.
- Validation of using GPR to measure EI in field conditions.
- Integration of real-time processing of GPR for EI into concrete paving operations.

- Modeling of temperature and moisture profiles in concrete pavements in different curing conditions.
- Developing draft construction specifications.
- Performing pilot implementation on construction projects.

REFERENCES

AASHTO (2007). "Standard method of test for resilient modulus of subgrade soils and untreated base/subbase materials." *AASHTO T307-99*, American Association of State Highway and Transportation Officials, Washington, D. C.

AASHTO (2008). "Mechanistic-Empirical Pavement Design Guide: A Manual of Practice." *AASHTO Designation: MEPDG-1*. Washington, DC.

Andrei, D., Witczak, M. W., Schwartz, C. W., and Uzan, J. (2004). "Harmonized Resilient Modulus Test Method for Unbound Pavement Materials." *Transportation Research Record: Journal of the Transportation Research Board*, No. 1874, pp. 29-37.

Cary, C., and Zapata, C. (2011). "Resilient Modulus for Unsaturated Unbound Materials." *Road Materials and Pavement Design*, Vol. 12, No. 3, pp. 615-638.

Choubane, B., P. B. Upshaw, G. A. Sholar, G. C. Page, and J. A. Musselman. *Nuclear Density Readings and Core Densitities: A Comparative Study*. Report FL/DOT/SMO/98-418, Florida Department of Transportation, Gainseville, FL, July 1998.

Drucker, D.C., and Prager, W. (1952). "Soil Mechanics and Plastic Analysis for Limit Design." *Quarterly of Applied Mathematics,* Vol. 10, No. 2, pp. 157-165.

Epps, J., Sebesta, S., Hewes, B., Sahin, H., Luo, R., Button, J., Lytton, R., Herrera, C., Hatcher, R., and Gu, F. (2014). "Development of a specification for flexible base construction." Final Report, *No. FHWA/TX-13/0-6621*, 414p.

Fredlund, D. G., and Rahardjo, H. (1993). *Soil mechanics for unsaturated soils*. John Wiley & Sons, New York.

Fredlund, D. G., and Xing, A. (1994). "Equations for the Soil-Water Characteristic Curve." *Canadian Geotechnical Journal,* Vol. 31, pp. 521-532.

Gauch, H. G., Hwang, J. T., Fick, G. W. (2003). "Model Evaluation by Comparison of Model-Based Predictions and Measured Values." *Agronomy Journal*, No. 95, pp. 1442-1446.

Gu, F., Luo, X., Luo, R., Lytton, R. L., Hajj, E., and Siddharthan, R. J. (2016). "Numerical Modeling of Geogrid-Reinforced Flexible Pavement and Corresponding Validation Using Large-Scale Tank Test." *Construction and Building Materials,* Vol. 122, 214-226.

Gu, F., Sahin, H., Luo, X., Luo, R., and Lytton, R. L. (2015). "Estimation of Resilient Modulus of Unbound Aggregates Using Performance-Related Base Course Properties." *Journal of Materials in Civil Engineering*, Vol. 27, No. 6, 04014188.

Gu, F., Zhang, Y., Droddy, C. V., Luo, R., and Lytton, R. L. (2016). "Development of a New Mechanistic-Empirical Rutting Model for Unbound Granular Material." *Journal of Materials in Civil Engineering,* 04016051.

Heath A. C., Pestana, J. M., Harvey, J. T., and Bejerano, M. O. (2004). "Normalizing Behavior of Unsaturated Granular Pavement Materials." *Journal of Geotechnical and Geoenvironmental Engineering*, Vol. 130, pp. 896-904.

Huang, Y. H. (1993). *Pavement analysis and design.* Prentice-Hall, Englewood Cliffs, NJ.

Juarez-Badillo, E. (1981). "General Compressibility Equation for Soils." *Proceedings of the International Conference in Soil Mechanics and Foundation Engineering,* Stockholm, Sweden, pp. 171-178.

Lekarp, F., Isacsson, U., and Dawson, A. (2000). "State of the Art: Resilient response of unbound aggregates." *Journal of Transportation Engineering*, Vol. 126, No. 1, pp. 66-75.

Liang, R. Y., Rabab’ah, S., and Khasawneh, M. (2008). “Predicting Moisture-Dependent Resilient Modulus of Cohesive Soils Using Soil Suction Concept.” *Journal of Transportation Engineering*, Vol. 134, No. 1, pp. 34-40.

Lytton, R. L. (1995). “Foundations and pavements on unsaturated soils.” Keynote Address, *Proceedings, First International Conference on Unsaturated Soils*, International Society of Soil Mechanics and Foundation Engineering, Paris, pp. 1201-1220.

Malla, R. B., and Joshi, S. (2007). “Resilient Modulus Prediction Models Based on Analysis of LTPP Data for Subgrade Soils and Experimental Verification.” Journal of Transportation Engineering, Vol. 133, pp. 491-504.

Maser, K. R. *Mapping the Density of New Asphalt Pavement with GPR*. In *BSCE News*, Boston Society of Civil Engineers, April 2014.

Maser, K. R. and A. Carmichael. *Ground Penetrating Radar Evaluation of New Pavement Density.* Report WA-RD 839.1, Inrasense, Inc, Woburn, MA, February 2015.

Matsuoka, H., and Nakai, T. (1985). “Relationship among Tresca, Mises, Mohr-Coulomb and Matsuoka-Nakai failure criterion.” *Soils and Foundations*, Vol. 25, No. 4, pp. 123-128.

Montgomery D. C., and Runger G. C. (2007). *Applied Statistics and Probability for Engineers*. John Wiley & Sons, New York.

Nazzal, M. D., and Mohammad, L. N. (2010). “Estimation of Resilient Modulus of Subgrade Soils for Design of Pavement Structures.” *Journal of Materials in Civil Engineering*, Vol. 22, pp. 726-734.

NCHRP (2003). “Harmonized test methods for laboratory determination of resilient modulus for flexible pavement design.” *Final Report. No. 1-28A*, National Cooperative Highway Research Program (NCHRP), Washington, D. C.

Pan, T., Tutumluer, E., and Anochie-Boateng, J. (2006). “Aggregate Morphology Affecting Resilient Behavior of Unbound Granular Materials.” *Transportation Research Record: Journal of the Transportation Research Board*, No. 1952, pp. 12-20.

Popik, M., K. Maser, and C. Holzschuher. *Using High-Speed Ground Penetrating Radar for Evaluation of Asphalt Density Measurements.* Toronto, ON Canada, October 2009.

Sahin, H., Gu, F., and Lytton, R. L. (2014). “Development of Soil-Water Characteristic Curve for Flexible Base Materials Using the Methylene Blue Test.” *Journal of Materials in Civil Engineering*, Vol. 27, No. 5, 04014175.

Sebesta, S. and T. Scullion. *Using Infrared Imaging and Ground-Penetrating Radar to Detect Segregation in Hot-Mix Overlays.* Report 4126-1, Texas Transportation Institute, Texas A&M University System, College Station, TX, May 2002.

Stroup-Gardiner, M. and E. R. Brown. *Segregation in Hot-Mix Asphalt Pavements.* NCHRP Report 441, Washington, D.C., 2000.

U.S. Environmental Protection Agency (n.d.). *Dielectric Permittivity.* Environmental Geophysics. http://www.epa.gov/esd/cmb/GeophysicsWebsite/pages/reference/properties/Electrical_Conductivity_and_Resistivity/Dielectric_Permittivity.htm. Accessed October 27, 2014.

Uzan, J. (1985). “Characterization of Granular Material.” *Transportation Research Record: Journal of the Transportation Research Board*, No. 1022, pp. 52-59.

Vivar, E. d. P. and J. E. Haddock. *HMA Pavement Performance and Durability.* FHWA/IN/JTRP-2005/14, Purdue University, Lafayette, IN, April 2006.

Williams, S. G. *Non-Nuclear Methods for HMA Density Measurements.* Department of Civil Engineering, Univeristy of Arkansas, Fayetteville, AR, June 2008.

Wilson, B. T. and S. Sebesta. Comparison of Density Tests for Thin Hot Mix Asphalt Overlays. In *Transportation Research Record: Journal of the Transportation Research Board*, Transportation Research Board of the National Academies, Washington, D.C., January 2015, pp. 148-156.

Yau, A., and Quintus, H. L. (2004). “Predicting Elastic Response Characteristics of Unbound Materials and Soils.” Transportation Research Record: Journal of the Transportation Research Board, No. 1874, pp. 47-56.

Zapata, C. E. (2010). “A National Catalog of Subgrade Soil-Water Characteristic Curve (SWCC) Default Inputs for Use with the MEPDG,” The National Cooperative Highway Research Program (NCHRP), *NCHRP Report 9-23A*, Arizona State University, Temple, AZ.

Zhang, Y., Bernhardt, M., Biscontin, G., Luo, R., and Lytton, R. L. (2014). “A Generalized Drucker-Prager Viscoplastic Yield Surface Model for Asphalt Concrete.” *Materials and Structures*, Vol. 48, pp. 3585-3601.

APPENDIX A. PC-BASED CMS INSTRUCTIONS

When turn on the CMS data-acquisition computer, on the desktop of the Widows 10 operation system (as see in Figure A-1), user can find the icon of “RollerGPS” . This is the CMS data-acquisition software icon. Double-clicking this icon will start the program, and Figure A-2 will show:

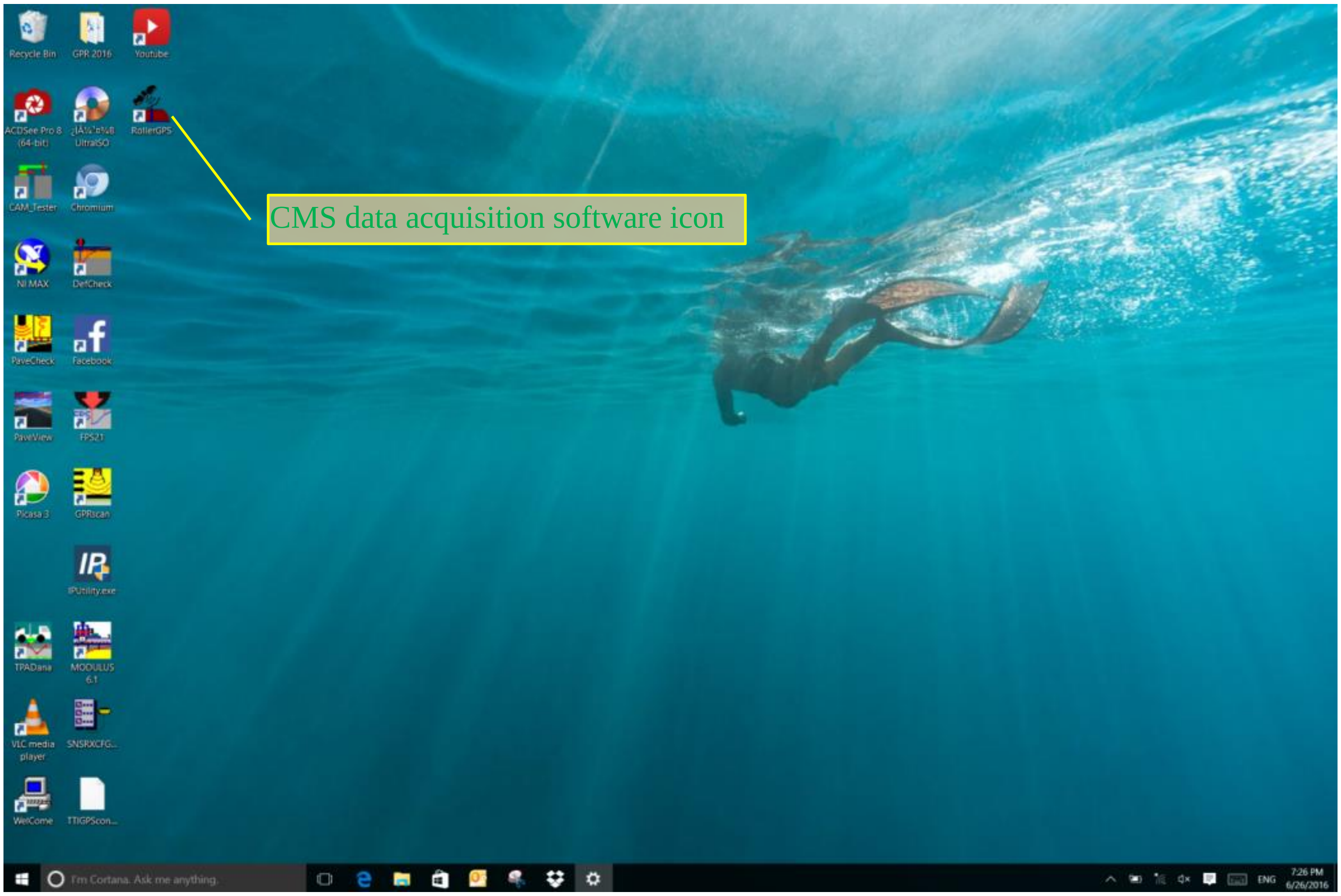
Recycle Bin
GPR 2016
Youtube
ACDSee Pro 8 (64-bit)
UltraISO
RollerGPS
CAM_Tester
Chromium
NI MAX
DefCheck
PaveCheck
Facebook
PaveView
FPS21
Picasa 3
GPRscan
IPUtility.exe
TPADana
MODULUS 6.1
VLC media player
SNSRXCFG...
WelCome
TTIGPScon...
I'm Cortana. Ask me anything.
ENG
7:26 PM
6/26/2016

CMS data acquisition software icon

Figure A-1. Computer desktop to find the icon of CMS data-acquisition software.

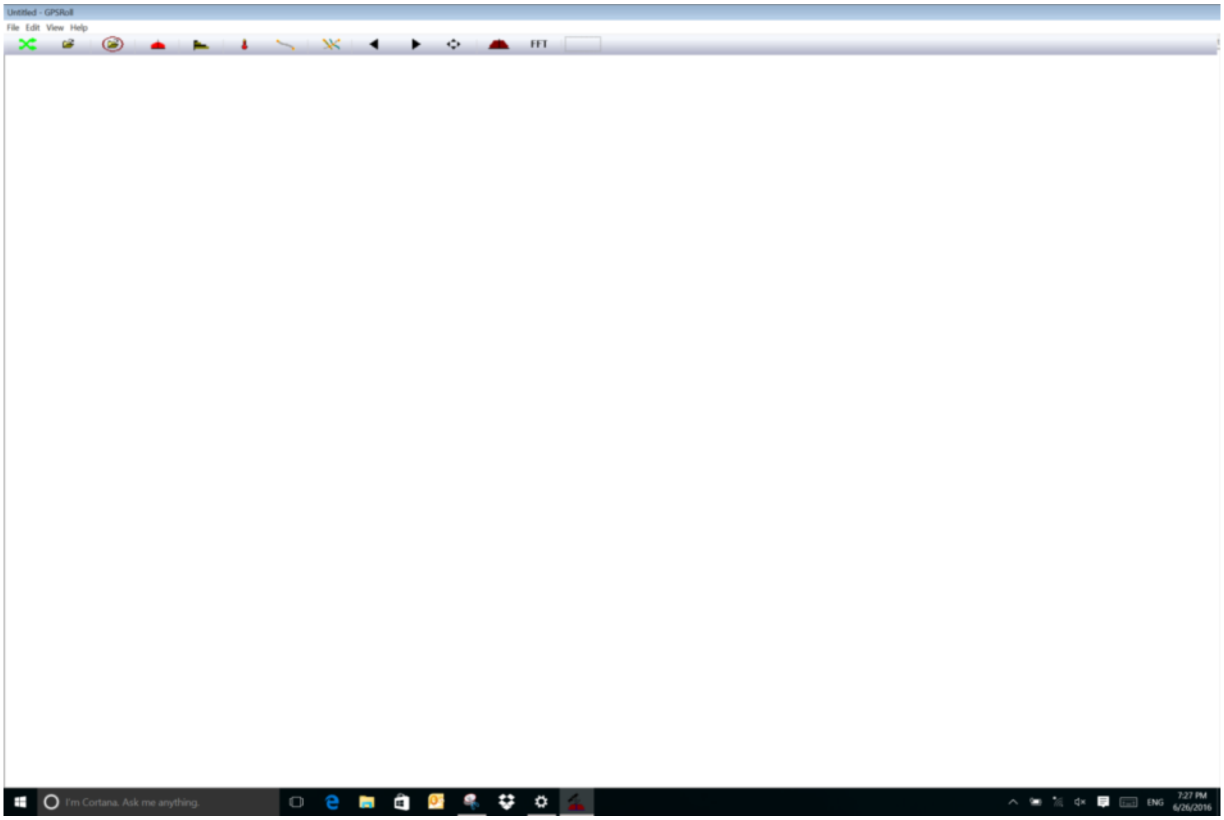
Untitled - GPSRoll
File Edit View Help
FFT
I'm Cortana. Ask me anything.
ENG
7:27 PM
6/26/2016

Figure A-2. First data post-processing interface screen.

Since this software package include the data-acquisition part and the data post-processing part, when starts the program, the first interface is data post-processing part. Click the first icon on the top toolbar 🔀 to switch another new toolbar for filed data acquisition as in Figure A-3:

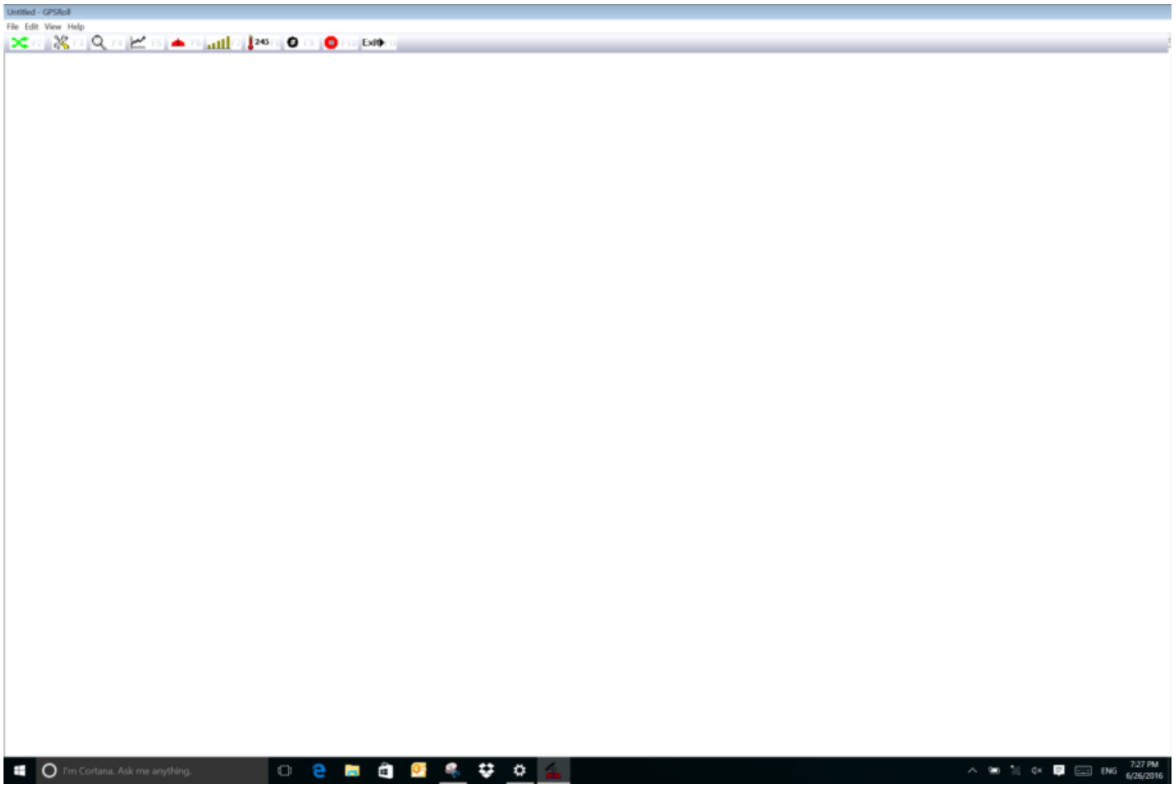

Figure A-3. Field data-acquisition interface of the software.

For each toolbar button on Figure A-3, user can see the following toolbar:

F2 F3 F4 F5 F6 F7 245 F8 F9 F10 Exit F11

F2 This button will switch the interface back to data post-processing interface

F3 This button will set the GPS communication parameters and check the GPS status

F4 This button will show the GPS raw data (for software debug)

F5 This button will show the GPS raw data and stationary chart check

F6 This button will begin to collect data and in real time show the compaction-effectiveness colormap

F7 This button will begin collect data and real time show the number of roller passes colormap

245 F8 This button will begin collect data and real time show the first time rolling temperature colormap

F10 For stop any above data-acquisition operation

Exit F11 This button will exit the program and go back to computer desktop

So following steps for running the data-acquisition software:

1. Click the icon on the desktop to start the software (Figure A-1).
2. Click the first toolbar button will go to data-acquisition interface (Figure A-2).
3. Click F3 if you need change the GPS parameters by the Figure A-4 interface:
4. When the user clicks the "OK" button on Figure A-4, then Figure A-5 will show the GPS status.
5. Click F4 screen will begin show GPS location and the raw data from GPS as Figure A-6.
6. Click F5 screen will show GPS raw data and chart showing how the stationary GPS reading is stable by showing Figure A-7, user can see the chart's longitude range is 5 meters, and latitude range is 2 meters. If the roller is not moving, we use this function to check the GPS reading's repeatability. The first point starts from the center of the chart.
7. Clicking F6 , F7 , 245 F8 is for collecting data, difference is that what kind of real-time information will show on screen. When these button be clicked, user need input file name and comment about the testing by Figure A-8.
8. User clicks the "Browse…."button to select file name for the final data we collected. Then input the comment about this test. Click "OK" will start to collect data. Figure A-9 showing the data-acquisition interface with real time showing compaction-effectiveness colormap. Also on the bottom left of the screen, this are GPS reading, IR temperature reading and the accelerometer data chart showing the roller vibration. At the same corner, the DMI showing the cumulated distance roller has run. This distance is created by the GPS distance, not the distance by the distance encoder.
9. When the paving job finished, user can click F10 button to stop the data acquisition and click Exit F11 to exit the program.

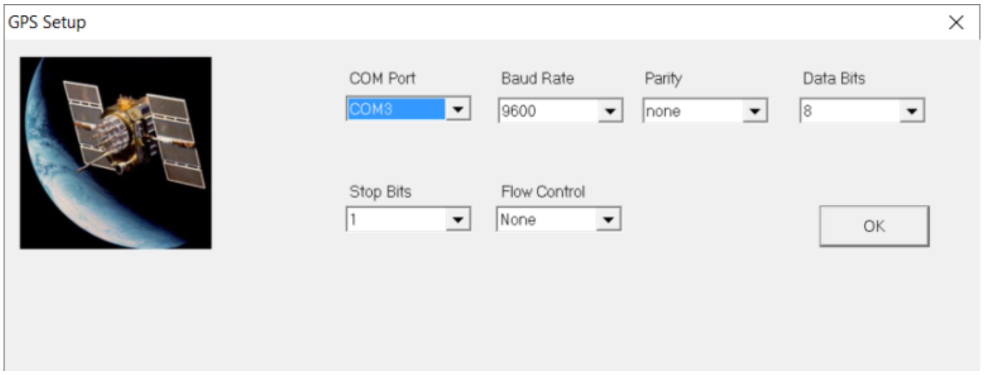
GPS Setup

COM Port: COM3

Baud Rate: 9600

Parity: none

Data Bits: 8

Stop Bits: 1

Flow Control: None

Figure A-4. Dialog box for changing GPS parameters.

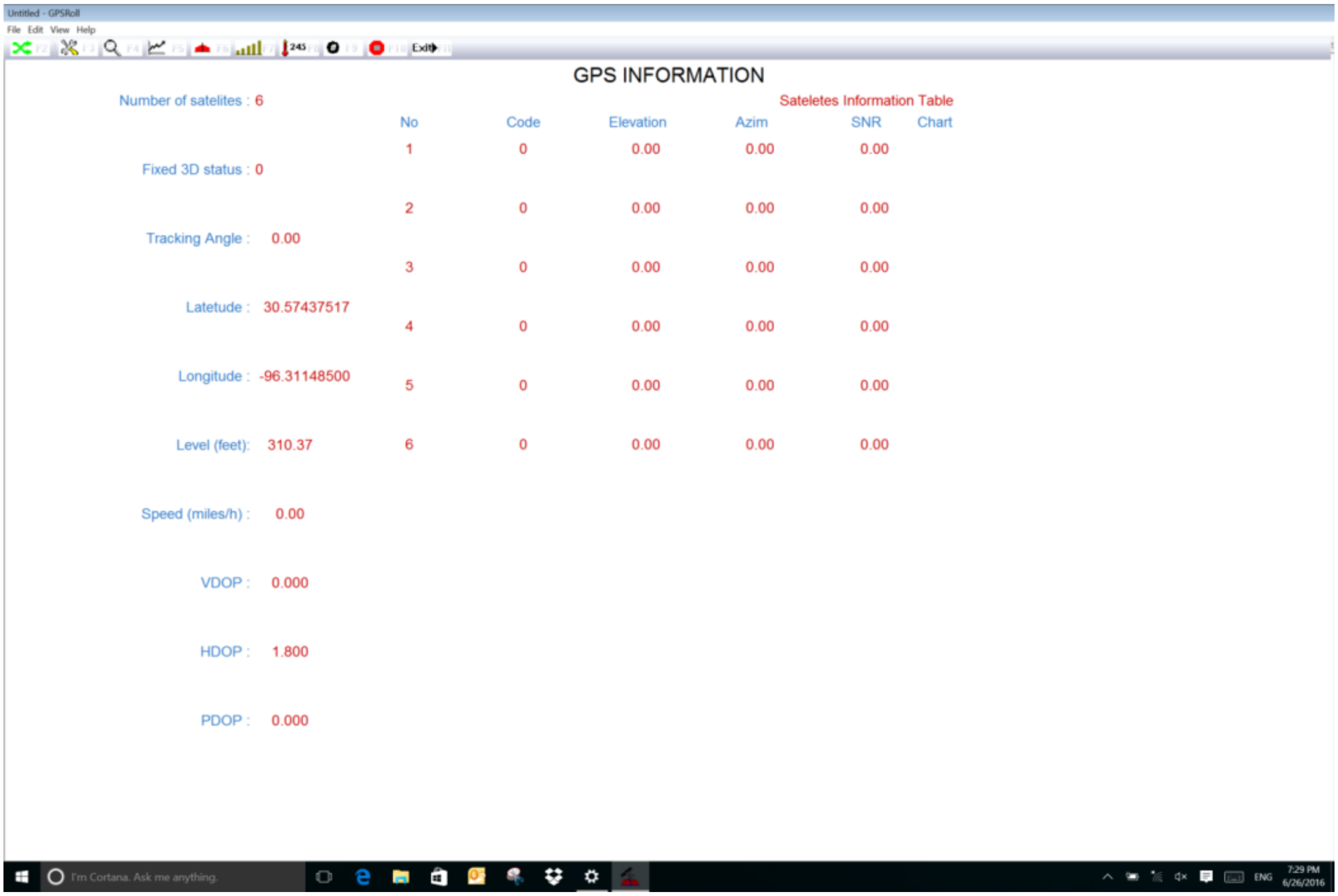
Untitled - GPSRoll
File Edit View Help
Exit
I'm Cortana. Ask me anything.
ENG
7:29 PM
6/26/2016

GPS INFORMATION

Number of satelites : 6

Fixed 3D status : 0

Tracking Angle : 0.00

Latetude : 30.57437517

Longitude : -96.31148500

Level (feet): 310.37

Speed (miles/h) : 0.00

VDOP : 0.000

HDOP : 1.800

PDOP : 0.000

Sateletes Information Table

No	Code	Elevation	Azim	SNR	Chart
1	0	0.00	0.00	0.00	
2	0	0.00	0.00	0.00	
3	0	0.00	0.00	0.00	
4	0	0.00	0.00	0.00	
5	0	0.00	0.00	0.00	
6	0	0.00	0.00	0.00	

Figure A-5. The GPS status screen.

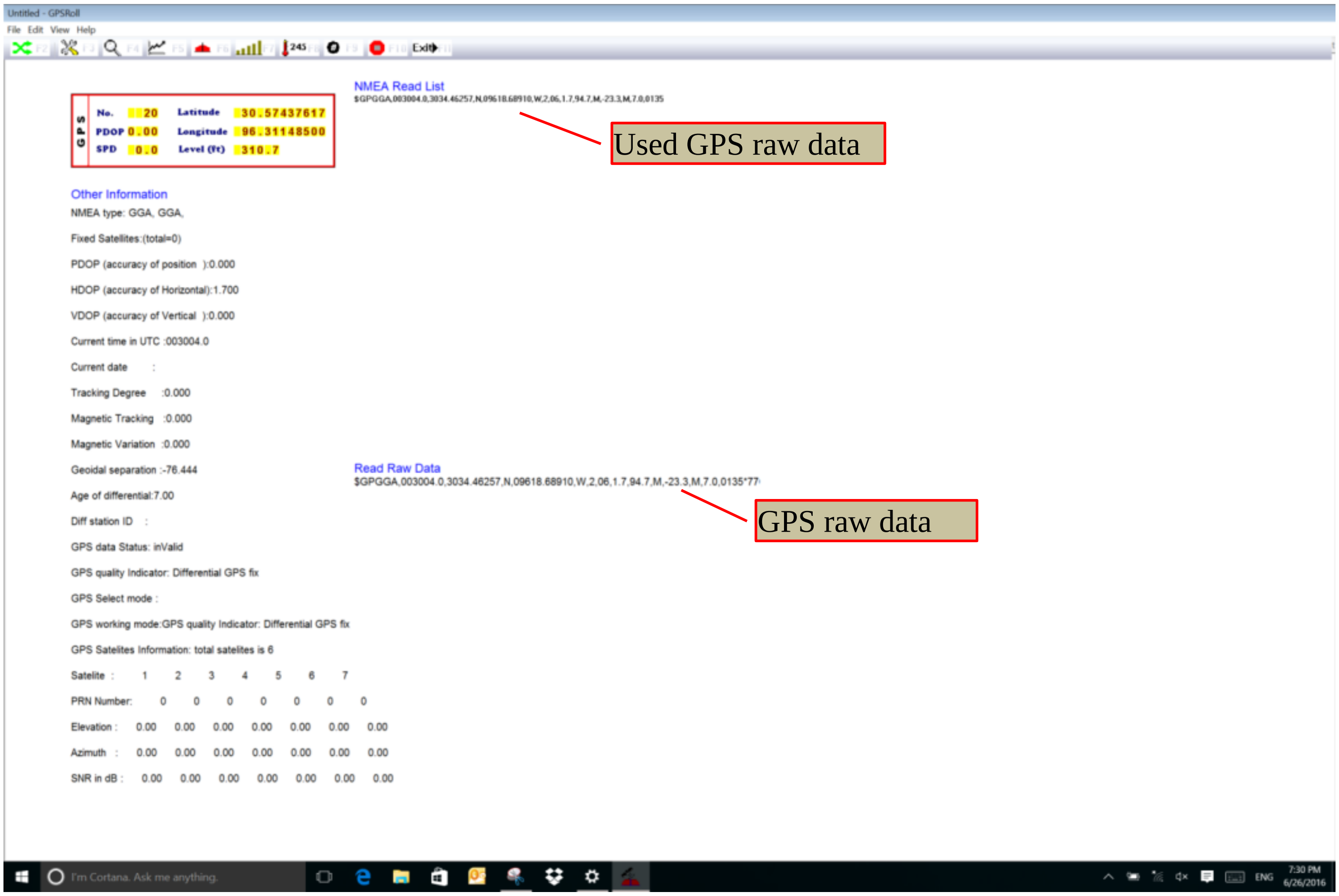
Untitled - GPSRoll
File Edit View Help
F2 F3 F4 F5 F6 F7 245 F8 F9 F10 Exit F11
GPS
Used GPS raw data
GPS raw data
I'm Cortana. Ask me anything.
ENG
7:30 PM
6/26/2016

```
No.     20     Latitude     30.57437617
PDOP  0.00     Longitude    96.31148500
SPD    0.0     Level (ft)   310.7
```

NMEA Read List

```
$GPGGA,003004.0,3034.46257,N,09618.68910,W,2,06,1.7,94.7,M,-23.3,M,7.0,0135
```

Other Information

```
NMEA type: GGA, GGA,

Fixed Satellites:(total=0)

PDOP (accuracy of position  ):0.000

HDOP (accuracy of Horizontal):1.700

VDOP (accuracy of Vertical  ):0.000

Current time in UTC :003004.0

Current date       :

Tracking Degree     :0.000

Magnetic Tracking   :0.000

Magnetic Variation  :0.000

Geoidal separation :-76.444

Age of differential:7.00

Diff station ID    :

GPS data Status: inValid

GPS quality Indicator: Differential GPS fix

GPS Select mode :

GPS working mode:GPS quality Indicator: Differential GPS fix

GPS Satelites Information: total satelites is 6

Satelite  :     1      2      3      4      5      6      7

PRN Number:     0      0      0      0      0      0      0

Elevation :   0.00   0.00   0.00   0.00   0.00   0.00   0.00

Azimuth   :   0.00   0.00   0.00   0.00   0.00   0.00   0.00

SNR in dB :    0.00   0.00   0.00   0.00   0.00   0.00   0.00
```

Read Raw Data

```
$GPGGA,003004.0,3034.46257,N,09618.68910,W,2,06,1.7,94.7,M,-23.3,M,7.0,0135*77
```

Figure A-6. The GPS location and raw data screen.

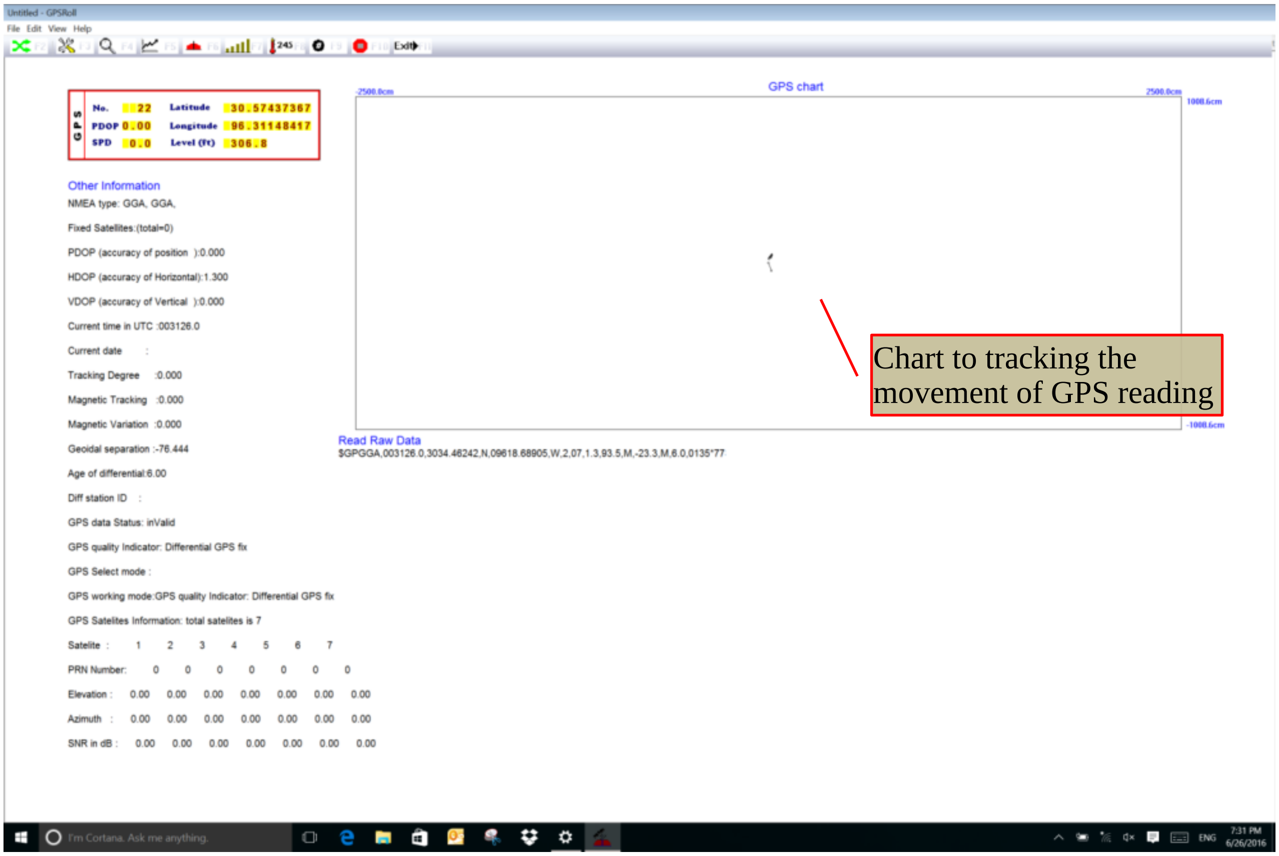
Untitled - GPSRoll
File Edit View Help
F2 F3 F4 F5 F6 F7 245 F8 F9 F10 Exit F11
GPS
GPS chart
-2500.0cm
2500.0cm
1000.6cm
-1000.6cm
I'm Cortana. Ask me anything.
7:31 PM
6/26/2016
ENG

No. 22
PDOP 0.00
SPD 0.0
Latitude 30.57437367
Longitude 96.31148417
Level (ft) 306.8

Other Information

NMEA type: GGA, GGA,

Fixed Satellites:(total=0)

PDOP (accuracy of position):0.000

HDOP (accuracy of Horizontal):1.300

VDOP (accuracy of Vertical):0.000

Current time in UTC :003126.0

Current date :

Tracking Degree :0.000

Magnetic Tracking :0.000

Magnetic Variation :0.000

Geoidal separation :-76.444

Age of differential:6.00

Diff station ID :

GPS data Status: inValid

GPS quality Indicator: Differential GPS fix

GPS Select mode :

GPS working mode:GPS quality Indicator: Differential GPS fix

GPS Satelites Information: total satelites is 7

Satelite :	1	2	3	4	5	6	7
PRN Number:	0	0	0	0	0	0	0
Elevation :	0.00	0.00	0.00	0.00	0.00	0.00	0.00
Azimuth :	0.00	0.00	0.00	0.00	0.00	0.00	0.00
SNR in dB :	0.00	0.00	0.00	0.00	0.00	0.00	0.00

Read Raw Data

```
$GPGGA,003126.0,3034.46242,N,09618.68905,W,2,07,1.3,93.5,M,-23.3,M,6.0,0135*77
```

Chart to tracking the movement of GPS reading

Figure A-7. GPS stationary stable check.

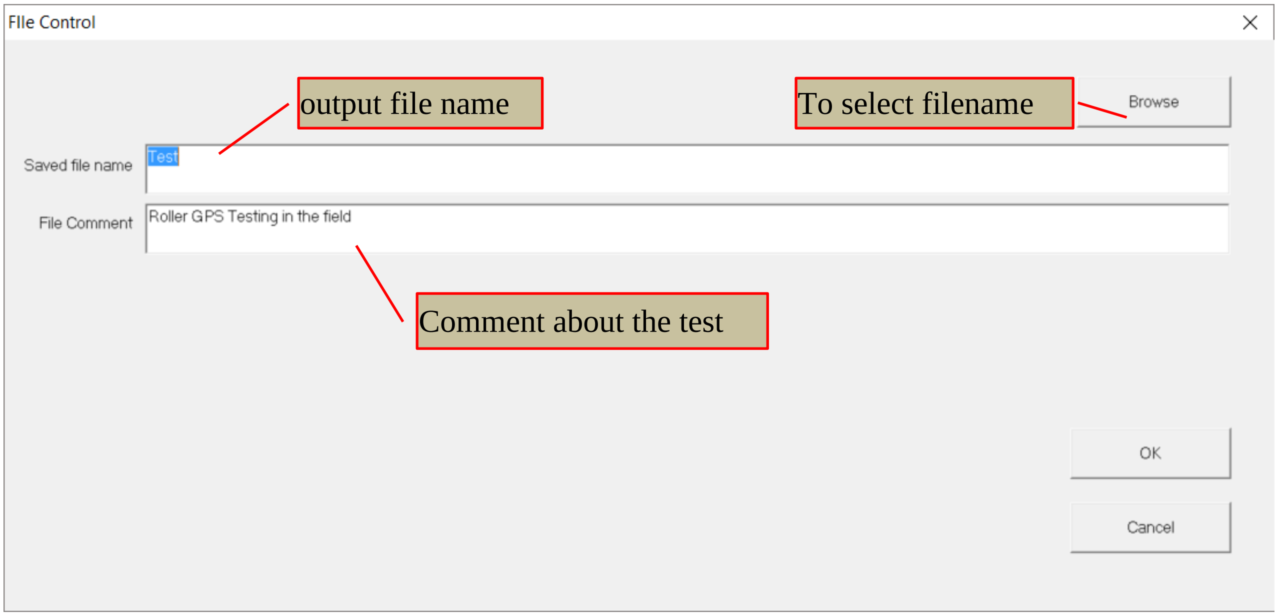
FIle Control
Browse
OK
Cancel

Saved file name: Test

File Comment: Roller GPS Testing in the field

output file name

To select filename

Comment about the test

Figure A-8. Dialog box for input filename and comment.

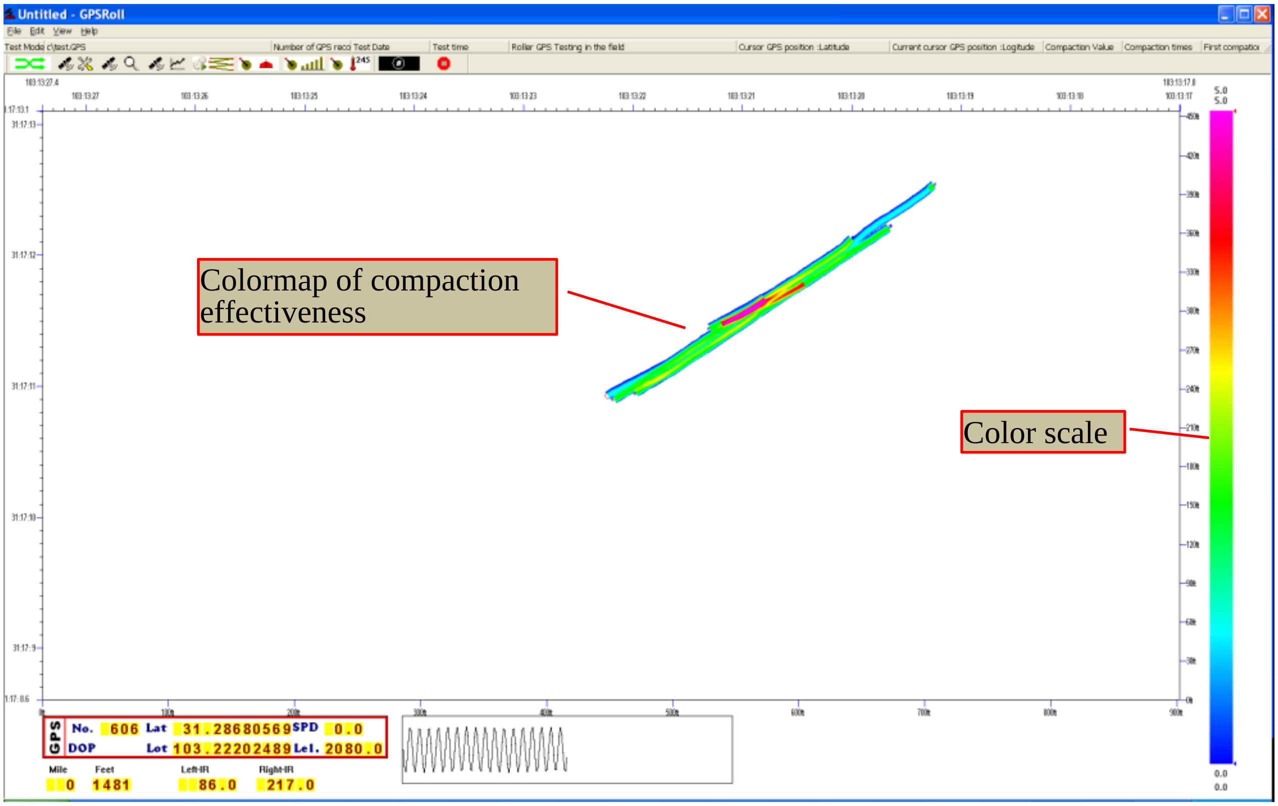

Test Mode c:\test.GPS | Number of GPS reco | Test Date | Test time | Roller GPS Testing in the field | Cursor GPS position :Latitude | Current cursor GPS position :Logitude | Compaction Value | Compaction times | First compactio

Colormap of compaction effectiveness

Color scale

GPS No. 606 Lat 31.28680569 SPD 0.0
DOP Lot 103.22202489 Lel. 2080.0

Mile 0 Feet 1481 Left-IR 86.0 Right-IR 217.0

Figure A-9. Real-Time Display of Compaction Effectiveness.

Figure A-9 is the most important interface for user collecting data. The right side of the screen is the scale for the color display. The numbers at the top and bottom of the scale (5 and 0) are the range of compaction-effectiveness values displayed in the figure. Any location with an EI (number of passes times effectiveness factor) of 5 on the effectiveness scale would be colored pink and values close to 0 would be dark blue. In the bottom left of the screen the user can see all the information from the infrared temperature sensors, accelerometer sensor and the GPS receiver. This display is shown below in Figure A-10.

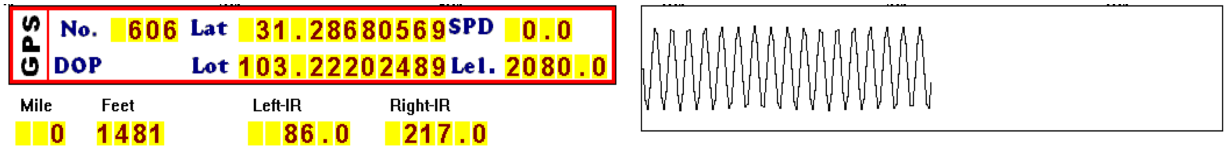

GPS No. 606 Lat 31.28680569 SPD 0.0
DOP Lot 103.22202489 Lel. 2080.0

Mile 0 Feet 1481 Left-IR 86.0 Right-IR 217.0

Figure A-10. Sensor display from data-acquisition screen.

In Figure A-10, the top box displays the GPS information showing both the latitude and longitude of the current position of the roller. The left and right side infrared temperature readings are shown in degrees Fahrenheit. This is a typical first pass of most overlay-compaction projects where the left side reading is 86°F and the right side is 217°F. As with most roller operations, the first pass runs down the edge of the mat, where the left hand sensor is not on hot asphalt. The analysis/display system takes this into consideration; if there is more than a 30°F temperature difference between the two sensors, then the system assumes that one sensor is off the mat. The high value is therefore used and displayed on the color plot. However if reasonable readings are found on both sensors then the system averages these values and saves and reports that value for the entire width of the roller (typically 7 ft) at that location. Under normal operations, a temperature reading is taken for every 8 inches of travel along the mat.

On the right side of Figure A-10 there is a sine wave showing the current vibration amplitude of the roller. If the operator turns off the vibration, this chart will show a flat line. Currently, accelerometer data are collected and save it to the data file; later in this report, we will process this accelerometer data in the frequency domain.

Figure A-11 is a blow up of the compaction-effectiveness display from Figure A-9. This information is displayed in real time for the roller operator to view the coverage on the mat. Displays such as this should be useful to ensure that a uniform effort is being applied to all areas on the mat. The red colors represent a compaction index (number of passes times compaction-effectiveness factor based on roller location) of 4 to 5, the green 2 to 3 and the blue 1 to 2. Under ideal conditions the map should be all a similar color, blue areas could be areas where the operator needs to apply more passes.

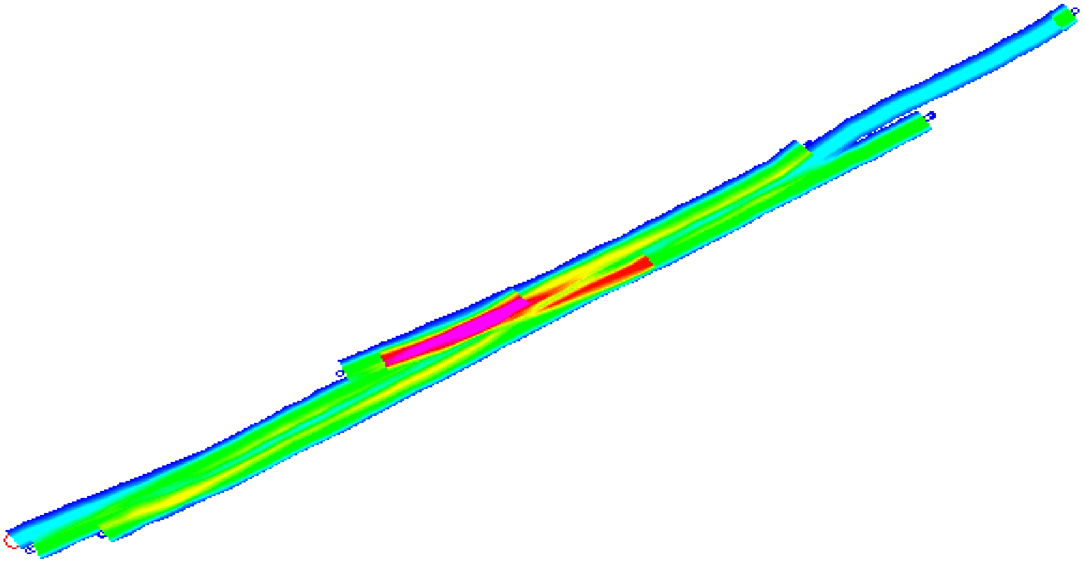

Figure A-11. Color-coded Compaction Effort map—real time displayed.

If the user starts the data acquisition by selecting either 📶F7 🌡245F8 buttons, then the real-time display viewed by the roller operator will be either the number of roller passes or the mat temperature at the first roller pass.

Post-Processing and display software

This section illustrates the steps required to post process the field data with the “RollerGPS” software. This software is also for field data acquisition. Initially was developed in Study 6992, and in this project, we did many updates.

First, click the icon of the software to start the “RollerGPS”; the main menu screen in the post-processing mode is shown in Figure A-12.

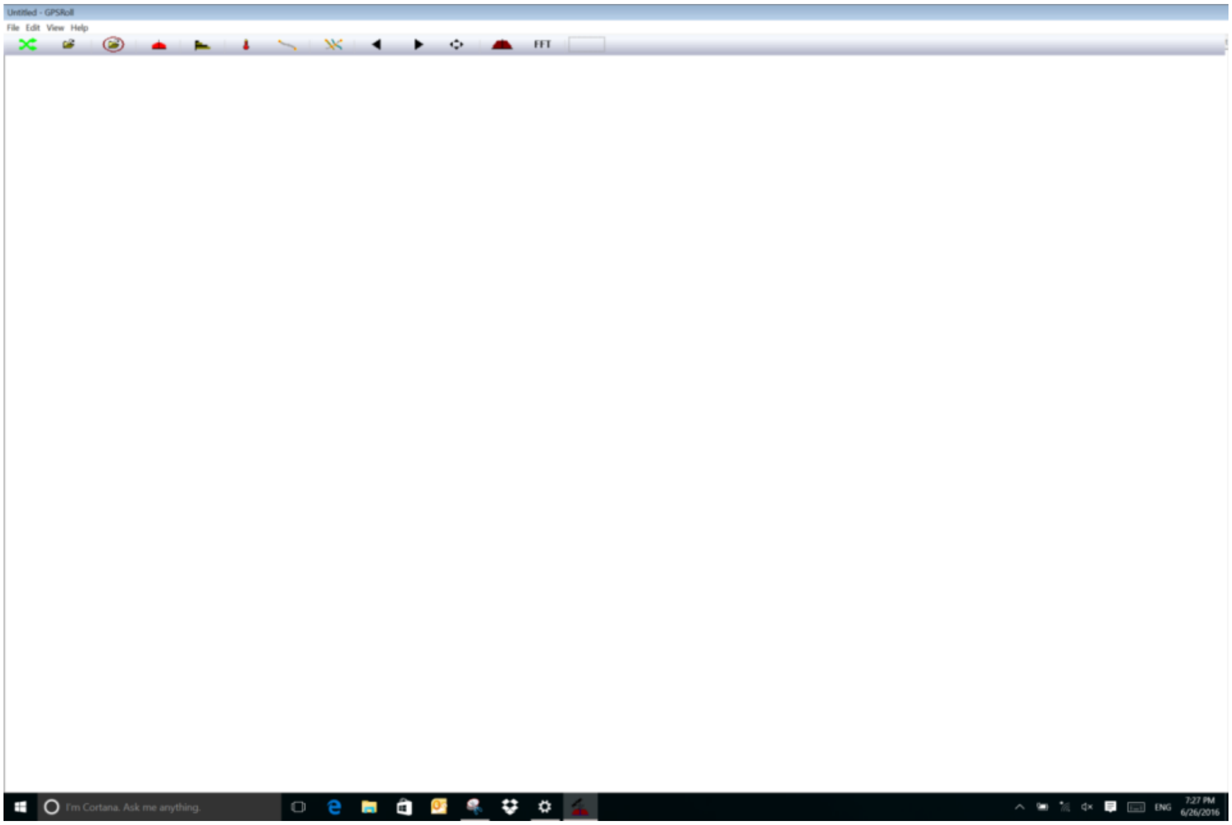
Untitled - GPSRoll
File Edit View Help
FFT
I'm Cortana. Ask me anything.
ENG
7:27 PM
6/26/2016

Figure A-12. Post-processing toolbar and main interface.

Table A-1 list the options available for post-processing the raw field data.

Table A-1. Explanation of the post-processing tool bar buttons.

Button image	Explanation of each button.
🔀	Switch to CMS data acquisition toolbar for collecting data.
📂	Load the single file to do the single file processing.
📂	Load one project folder and do the group files processing.
▲	Show the compaction-effectiveness color map chart on the display screen.
▬	Show the number of roller passes color map chart on the display screen.
🌡	Show the temperature at the first roller pass color map chart on the display screen.
∿	Show a line diagram of all the roller passes over the section.
✕	Show the rolling path chart for all files in the project folder.
◀	Show the previous file in the project.
▶	Show the next file in the project.
✥	Zoom the data to fit the screen.
▲	Change the roller compaction-effectiveness chart. These relate the compaction effectiveness for different lateral locations on the drum, where the edge is less effective than the center of the drum.
FFT	Show the Fast Fourier transform(FFT) of the accelerometer data, also user can show the raw accelerometer data on screen for each second.
Exit▶	Exit the program.

Based on Project 6992 lab and field testing, the researchers find that the center of the roller has better compaction effectiveness than the edge. This is believed to be based on the lack of confining of the mat at the edge of the roller. This non-uniformity of roller compaction effort will affect the final density of the mat. Pressing the ▲ icon displays the currently recommended compaction index profiles for steel wheel rollers. The recommended profile based on this study and earlier studies is the model shown in Figure A-13. From this profile for a 7 feet width roller drum, there is 3 feet in the middle part that gets full compaction (this value is defined as 1.0). At the edge of the roller drum, the effectiveness factor is only 0.3 or 30 percent of that in the middle of the drum. This is the key calculation made by the "RollerGPS" system. The accurate GPS tracks the position of the roller and for each pass calculates the compaction effectiveness for the entire roller width by multiplying the number of passes by the effectiveness factor index from Figure A-13. Therefore, locations that only receive passes with the edge of the roller will have a computed compaction index much less than those compacted under the center of the roller.

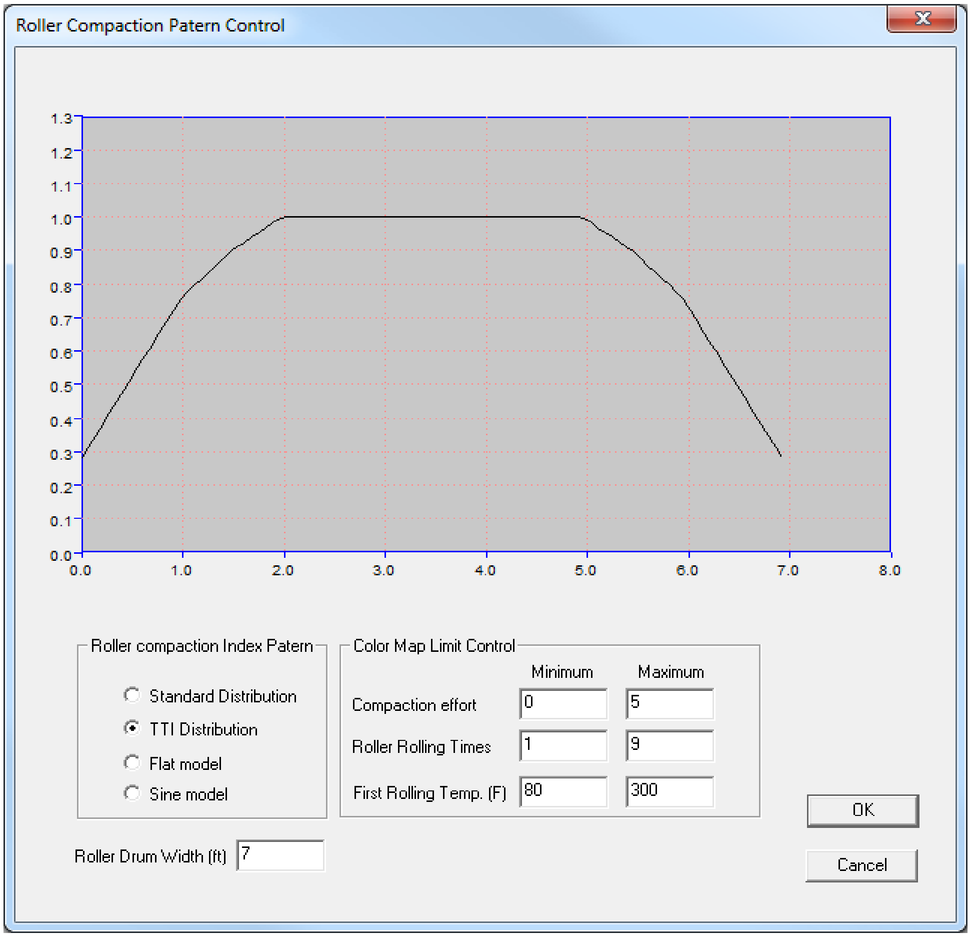

Roller Compaction Patern Control

Roller compaction Index Patern

○ Standard Distribution
● TTI Distribution
○ Flat model
○ Sine model

Color Map Limit Control

	Minimum	Maximum
Compaction effort	0	5
Roller Rolling Times	1	9
First Rolling Temp. (F)	80	300

Roller Drum Width (ft) 7

Figure A-13. Recommended Roller Effectiveness Distribution.

This dialog box also permits the user to control the graphical display of the color map, by changing the max and min limits on each of the color maps. For example for the temperature map the lower limits (blue color) is 80°F, and the upper-limit red color is 300°F. These values can be changed in this dialog box.

This software has two kinds of processing methods; one is single file, the other is a multiple files project within one folder. We will focus on the single file post-processing method.

Load file basic data processing. To process a single file the user clicks the toolbar 📂 button, then a file open dialog box permits the user to select the raw data file to open and display. All of the files collected have the "*.GPS" extension. Once selected the system displays the data for the complete section tested, which in the example shown in Figure A-14 is over 2500 feet on this section. As described below the user has the options to zoom into any location in the data set.

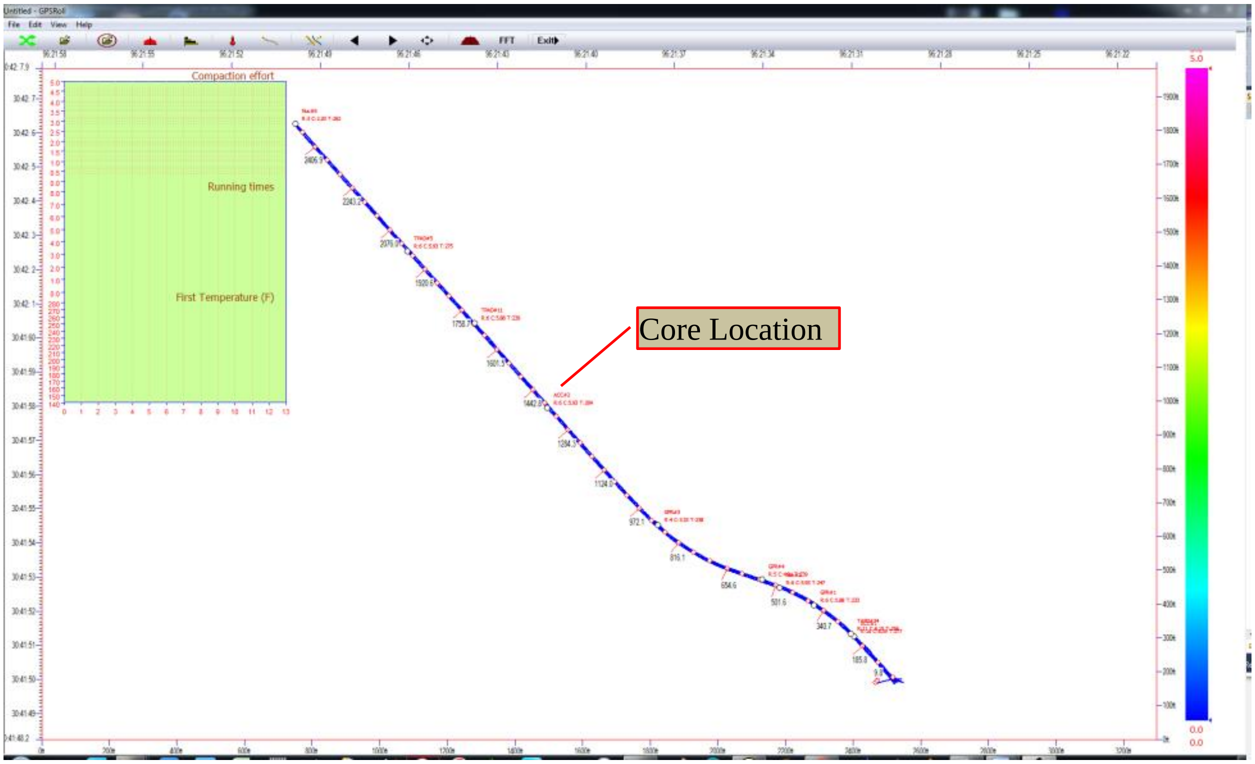
Untitled - GPSRoll
File Edit View Help
FFT
Exit
Compaction effort
Running times
First Temperature (F)
Core Location
5.0
0.0

Figure A-14. First display screen showing the entire section length.

The user can then click any one of the buttons to display ◓ (compaction effectiveness) , ▬ (number of passes) and 🌡 (first pass temperature). Figure A-15 is an example when user selects the ◓ button.

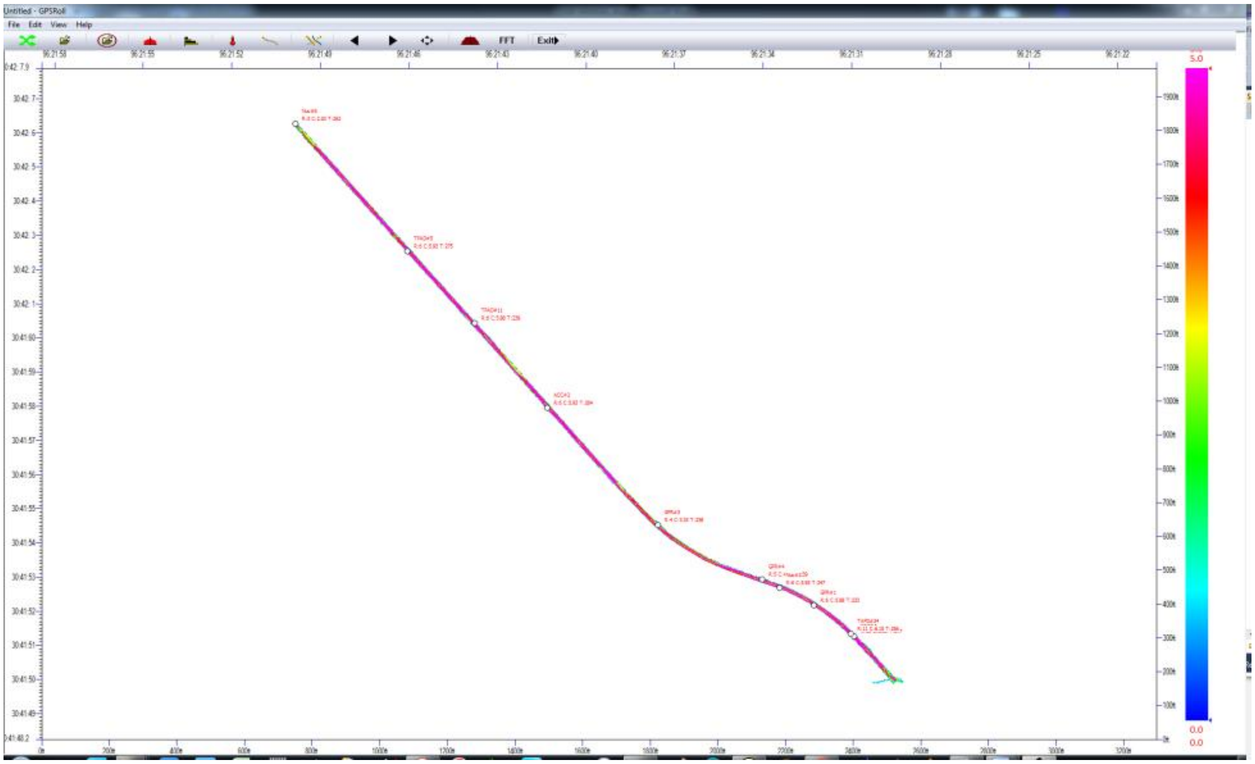

Figure A-15. Compaction effort color map view of the loaded data file.

Since the width of the paved lane is typically 12 feet, this distance compared to the length of the section is relatively small. Therefore, the display of the complete section is very difficult to review to find problem areas. For this reason, an option was included to permit the user to zoom into any part of the project. To zoom in, user puts the cursor in the required location and while holding down the left mouse button and drags the mouse, as shown in Figure A-16 a black rectangle is superimposed on top of the project. When the user releases the mouse button, the information only from this section is displayed as shown in Figure A-17.

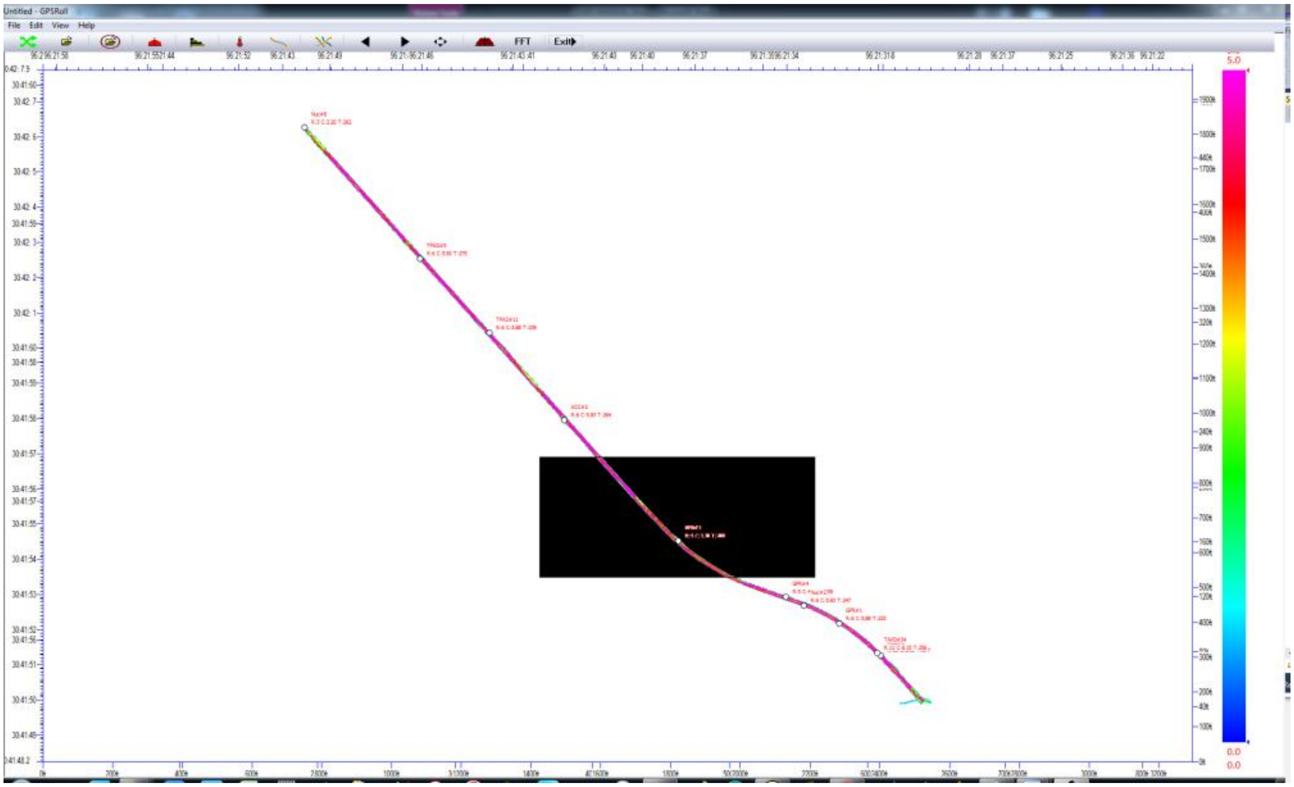
Untitled - GPSRoll
File Edit View Help
FFT
Exit
5.0
0.0
0.0

Figure A-16. Compaction effort color map view of the loaded data file.

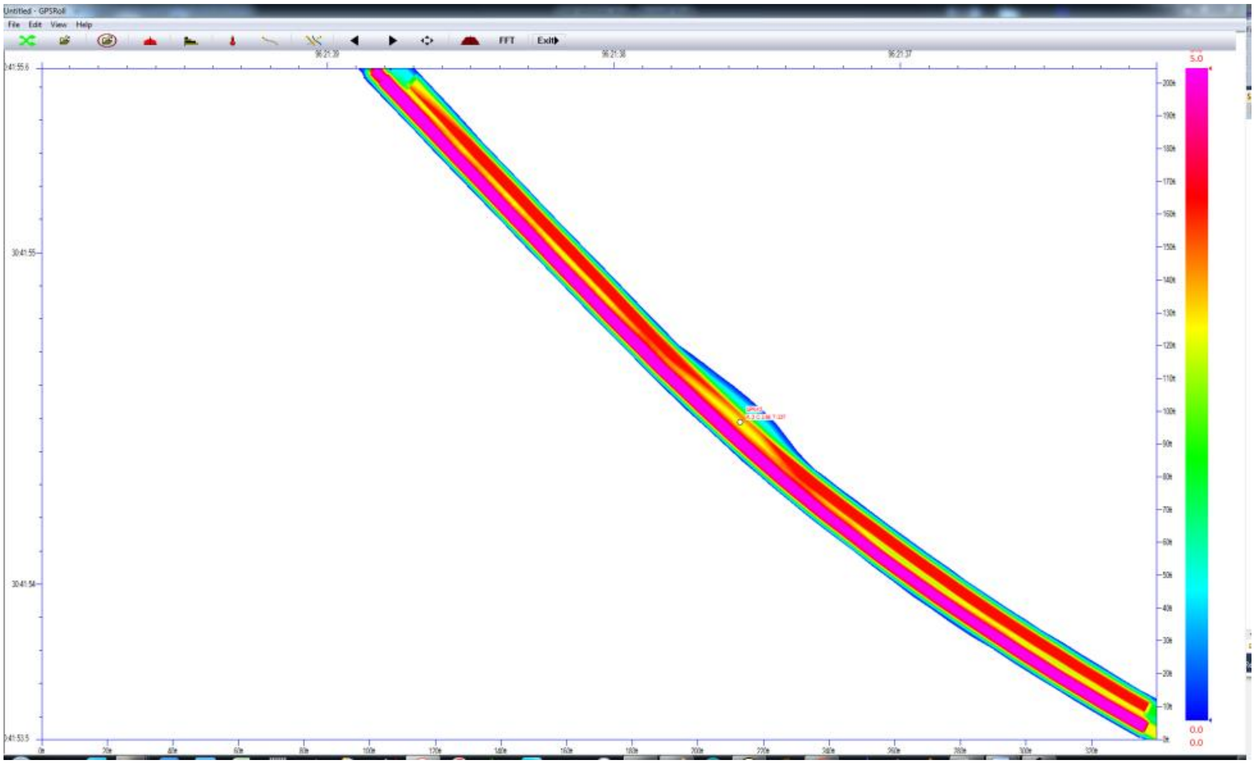
Untitled - GPSRoll
File
Edit
View
Help
FFT
Exit
96:21:39
96:21:38
96:21:37
30:41:55
30:41:54
5.0
0.0
0.0

Figure A-17. New zoomed view of color-coded compaction effort.

By placing the mouse cursor on any location on Figure A-17, some very useful information is displayed in the upper five boxes of the color plot. As shown below in Figure A-18 placing the cursor at the location of the “X” display the following data is shown in the boxes at the top of the screen:

- Longitudinal Position from GPS: -96.36318063 (96°21'47.45027W).
- Latitudinal Position from GPS: 30.70108765 (30°42'3.91555N).
- Compaction Effectiveness: 3.31.
- Number of passes of roller over this location: 11.
- Temperature at the first roller pass: 247°F.

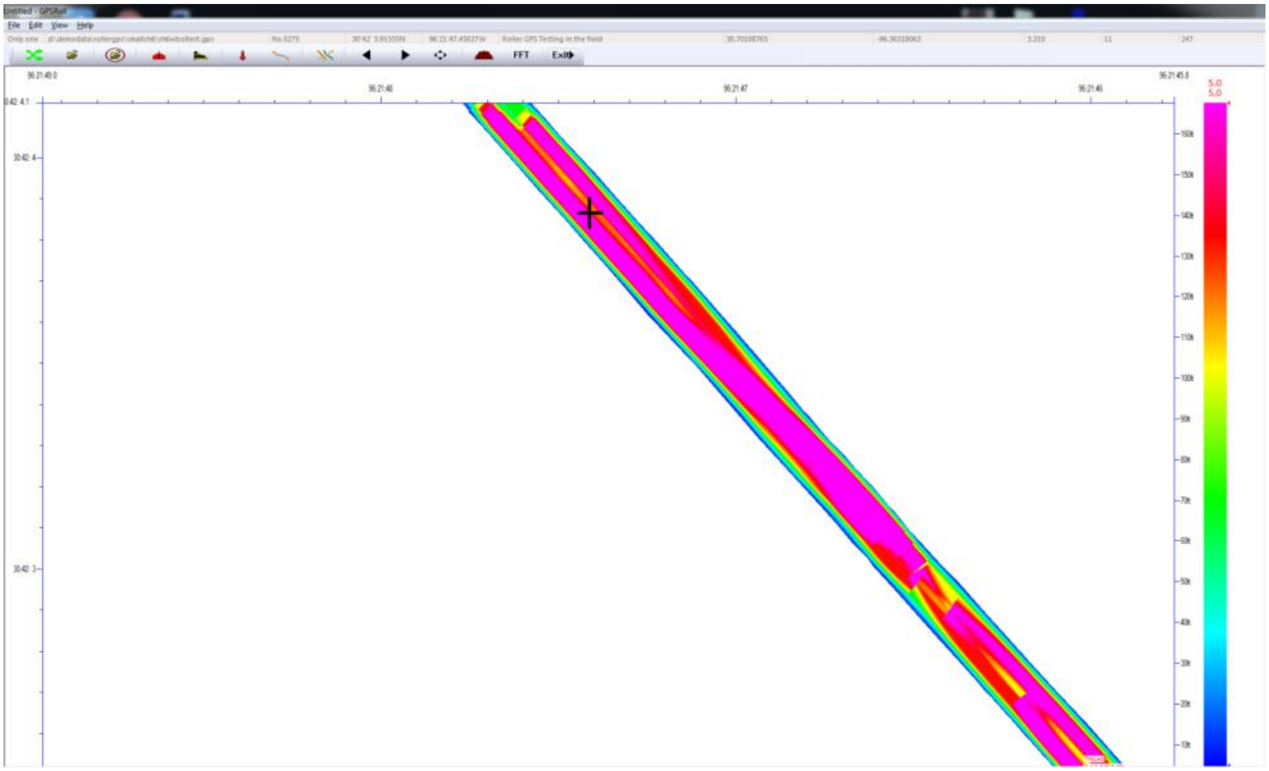

Figure A-18. Point-specific compaction data.

Moreover, by clicking the mouse at a location of interest, the transverse distribution of compaction and temperature data across the mat is displayed as shown in the box in the upper left corner of Figure A-19 and in detail in Figure A-20. The upper chart is the compaction-effectiveness index, the middle one is the number of passes placed across the mat and the lower one is the temperature profile during the first pass over the mat. The width shown in Figure A-20 is 13 feet but the paving width is only 12 feet. This means that there was at least a 0.5 feet overlap of the roller off each side of the mat.

Also in the upper right corner of Figure A-19, users can find the roller rolling temperature (for each pass) and temperature drop-rate bar chart by unit of F/minutes (the detail in Figure A-21). From this bar chart, we get first rolling temperature is 245 °F, after 2.6 minutes, second time rolling temperature is 230 °F, and temperature drop rate is 5.73 °F/minutes. Until eighth rolling, temperature drop to 194 °F, and drop rate is 10.34 °F/minutes. On this location, total rolling passes is eight, and total rolling time is 15.9 minutes.

If there is any uncertainty about the number of passes placed over any section of the mat, then clicking the path button from the main menu screen will display the path of the roller over that segment. An example of this is shown in Figure A-22 below. The normal rolling pattern is typically four passes on either side of the mat with a final pass down the center of the mat. Clearly, in this case, the center pass was not made, and at this location, the effectiveness of compaction in the middle of the mat is in question.

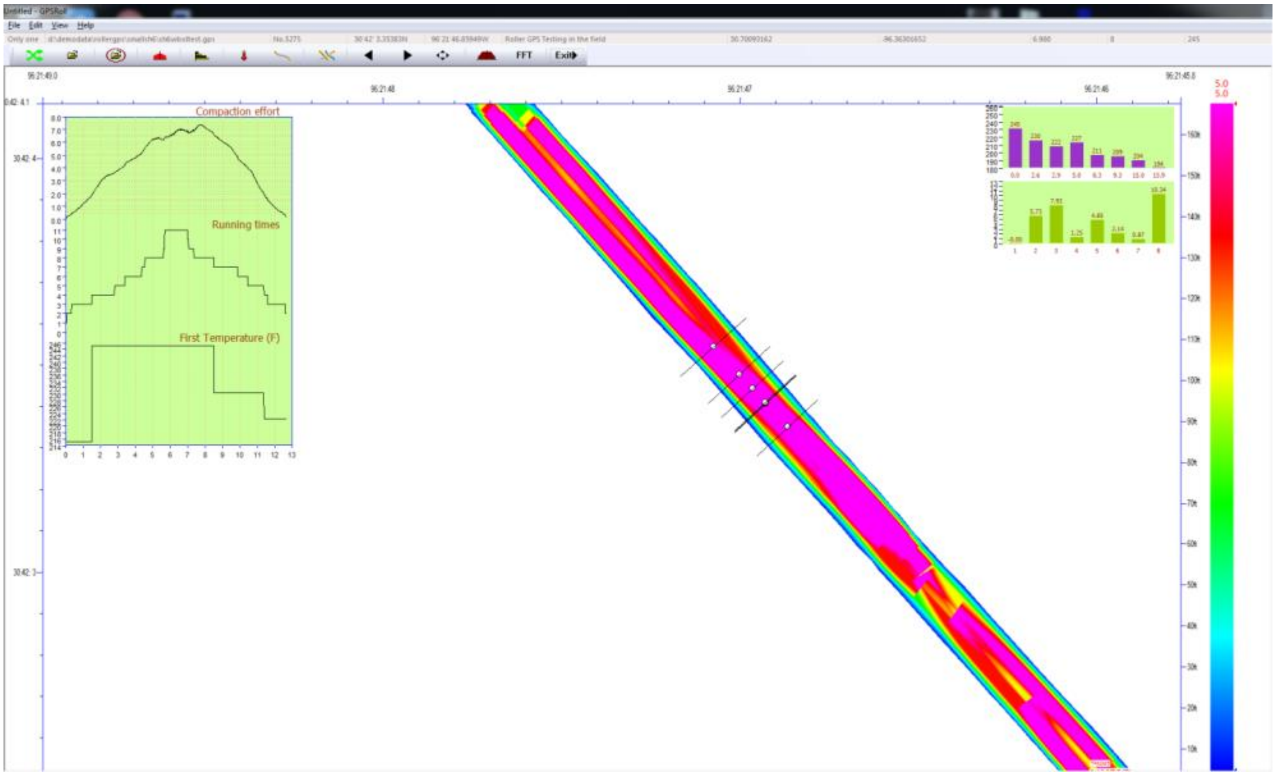
File Edit View Help
FFT
Exit
96:21:48
96:21:47
96:21:46
Compaction effort
Running times
First Temperature (F)
5.0
5.0

Figure A-19. Transverse distribution of compaction data at user selected location.

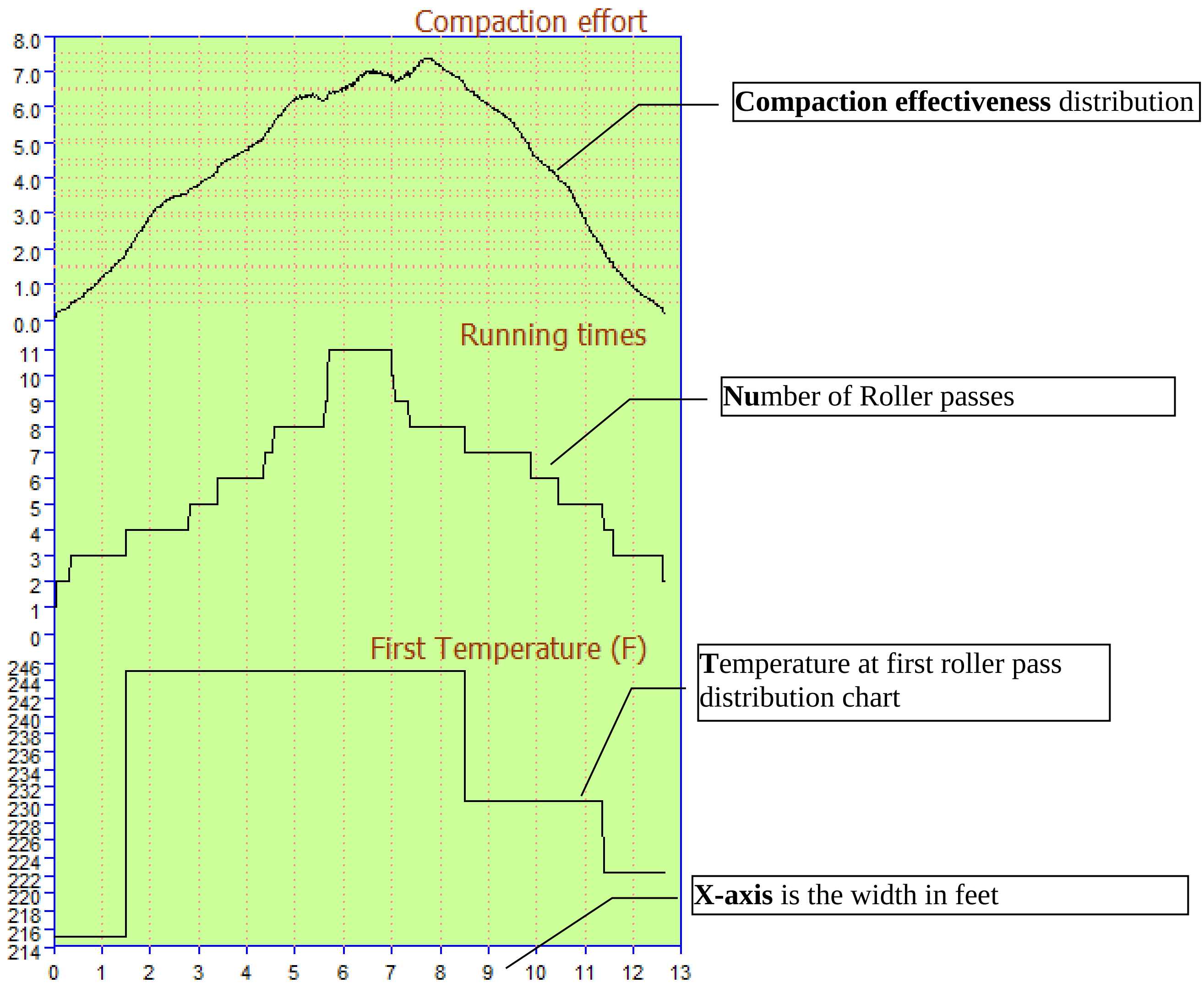

Compaction effectiveness distribution

Number of Roller passes

Temperature at first roller pass distribution chart

X-axis is the width in feet

Figure A-20. Details of the transverse distribution data.

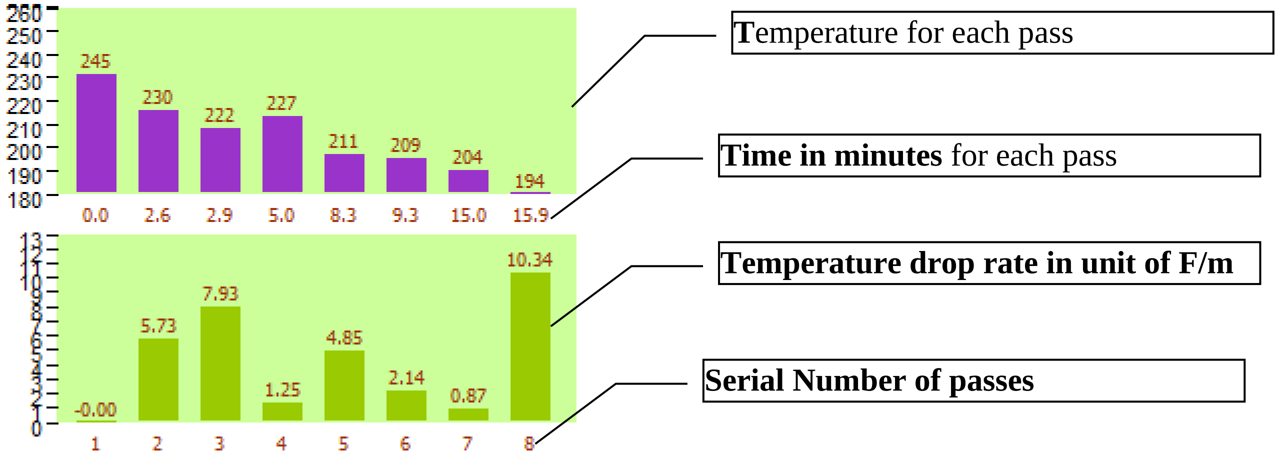

Temperature for each pass

Time in minutes for each pass

Temperature drop rate in unit of F/m

Serial Number of passes

Figure A-21. Details of the transverse distribution data.

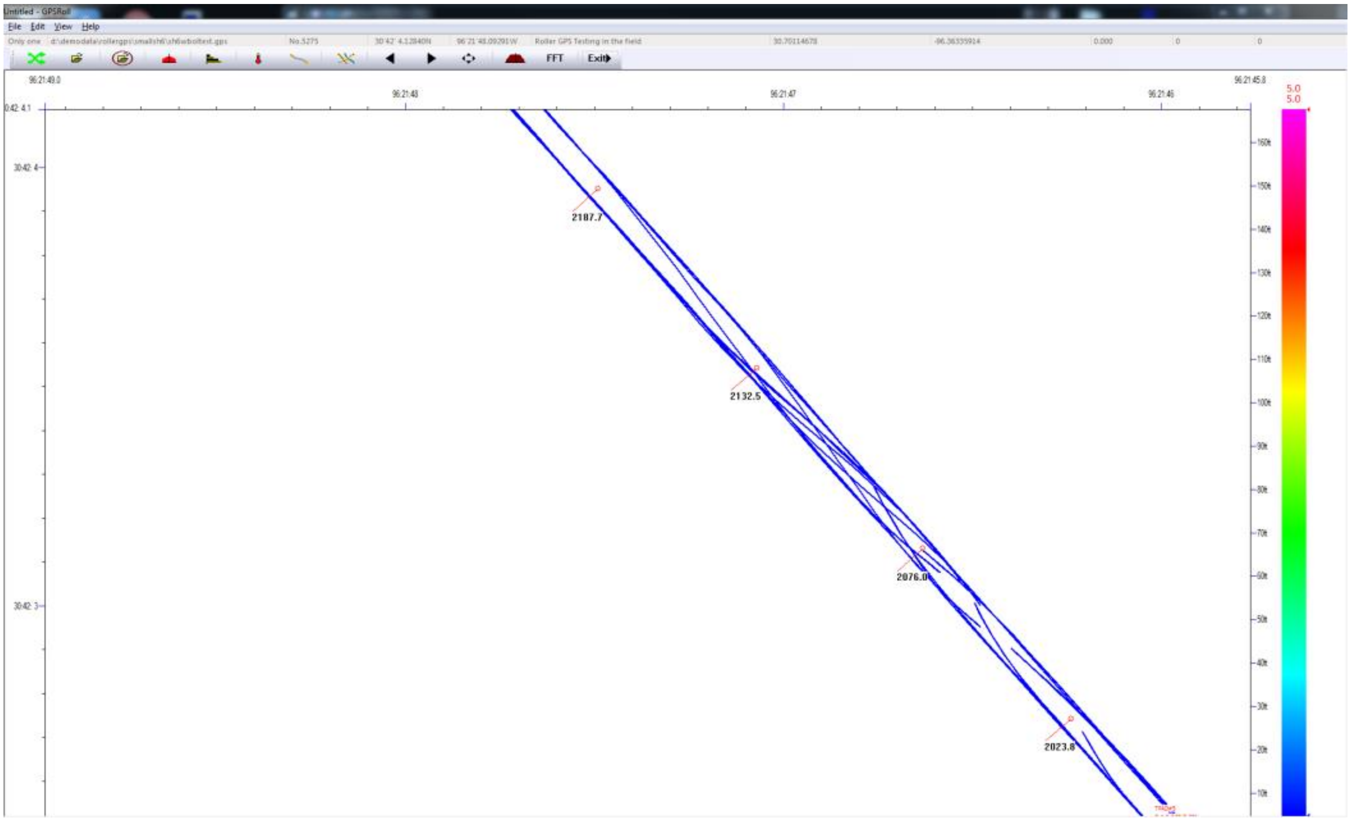
Untitled - GPSRoll
File
Edit
View
Help
Only one
d:\demodata\rollergps\smallsh6\sh6wboltest.gps
No.5275
30 42' 4.12840N
96 21' 48.09291W
Roller GPS Testing in the field
30.70114678
-96.36335914
0.000
0
0
FFT
Exit
96:21:49.0
96:21:48
96:21:47
96:21:46
96:21:45.8
0:42 4.1
30:42 4
30:42 3
2187.7
2132.5
2076.0
2023.8
5.0
5.0
160ft
150ft
140ft
130ft
120ft
110ft
100ft
90ft
80ft
70ft
60ft
50ft
40ft
30ft
20ft
10ft

Figure A-22. Paths taken by the roller in the compaction of this segment.

For all the colormap data view method, on the right side of the screen, user can find the color scale. One useful option available to the user is to modify the color display by using the mouse to change the upper limit on the color scale. To do this the mouse is placed over the red arrow and this arrow is dragged down to a different level, as shown in Figure A-23. The two numbers at the top of the screen are the maximum values set up in the initial set up menu screen. In this case, the max temperature (300°F) is the surface temperature at which the display is colored red. By moving the red triangle, the upper level has been reset to 260°F as shown. In this case, the red color will be associated with temperatures at or above 260°F. The color scale display is automatically changed to reflect the color associated with the new level. The lower end of the temperature scale can also be changed as can the compaction-effectiveness and number-of-passes charts.

Figure A-23. Resetting the color scale.

Accelerometer data FFT processing. The last new feature of this software is to show the raw accelerometer's Fast Fourier transform(FFT), or the raw acceleration data, by clicking the FFT button. Then, the user can use the right arrow key to turn to other pages. Figure A-24 depicts one of the pages that shows the FFT of the accelerometer data. At the beginning, the roller is rolling without vibration on, and the FFT chart is low and only low components showed on the chart. Later the FFT chart gets bigger and bigger. At around 30 Hz, 60 HZ, there are peaks clearly showing the roller's vibration.

Using the up arrow key turns on the raw data view function, and Figure A-25 shows the raw accelerometer data. We also noticed that at the beginning, the acceleration is low, and later, when the vibration is on, the acceleration is much bigger.

In the next software update, we will add a feature to divide the rolling passes into vibration and non-vibration rolling passes according to FFT calculation.

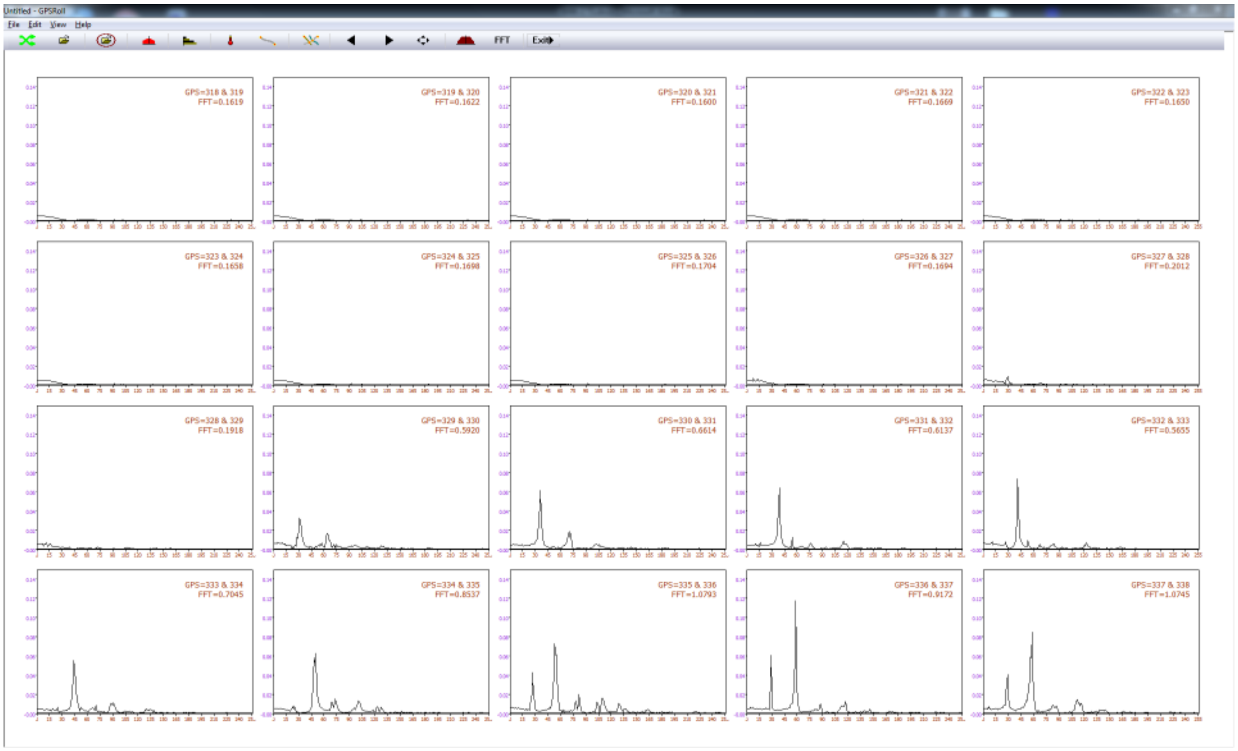
Untitled - GPSRoll
File Edit View Help
FFT
Exit
GPS=318 & 319
FFT=0.1619
GPS=319 & 320
FFT=0.1622
GPS=320 & 321
FFT=0.1600
GPS=321 & 322
FFT=0.1669
GPS=322 & 323
FFT=0.1650
GPS=323 & 324
FFT=0.1658
GPS=324 & 325
FFT=0.1698
GPS=325 & 326
FFT=0.1704
GPS=326 & 327
FFT=0.1694
GPS=327 & 328
FFT=0.2012
GPS=328 & 329
FFT=0.1918
GPS=329 & 330
FFT=0.5920
GPS=330 & 331
FFT=0.6614
GPS=331 & 332
FFT=0.6137
GPS=332 & 333
FFT=0.5655
GPS=333 & 334
FFT=0.7045
GPS=334 & 335
FFT=0.8537
GPS=335 & 336
FFT=1.0793
GPS=336 & 337
FFT=0.9172
GPS=337 & 338
FFT=1.0745

Figure A-24. Resetting the color scale.

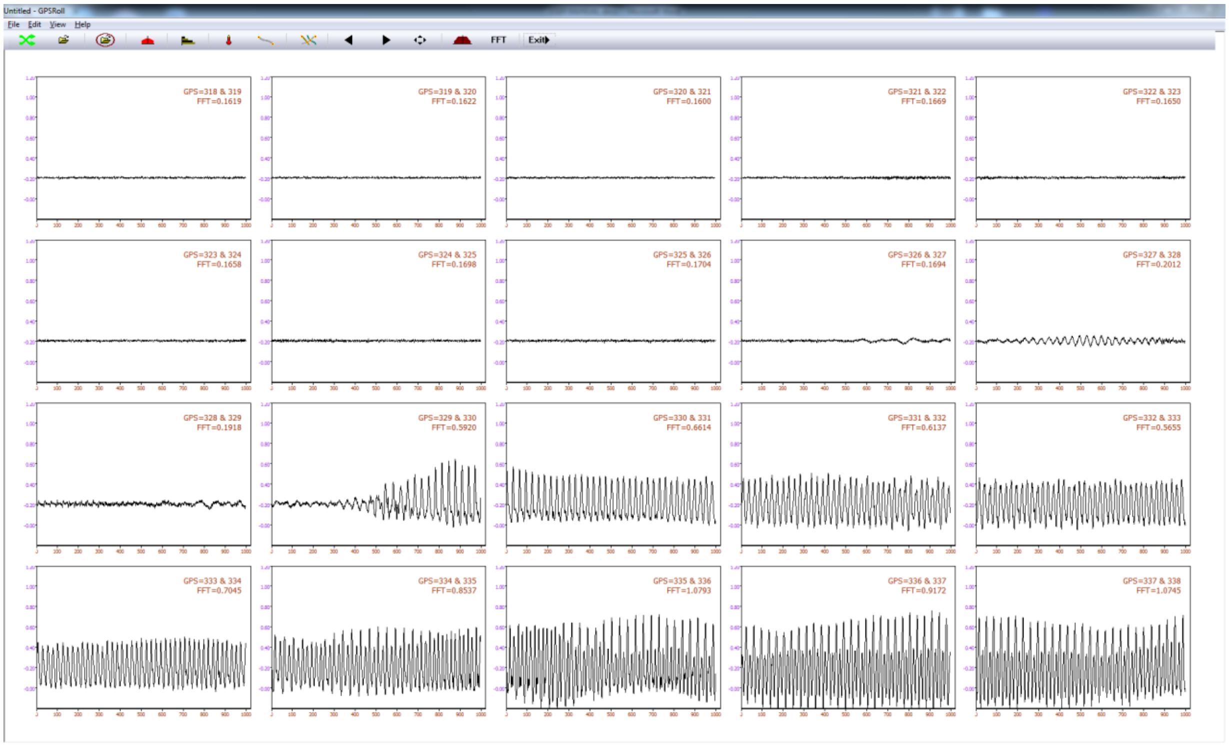
Untitled - GPSRoll
File Edit View Help
FFT
Exit
GPS=318 & 319
FFT=0.1619
GPS=319 & 320
FFT=0.1622
GPS=320 & 321
FFT=0.1600
GPS=321 & 322
FFT=0.1669
GPS=322 & 323
FFT=0.1650
GPS=323 & 324
FFT=0.1658
GPS=324 & 325
FFT=0.1698
GPS=325 & 326
FFT=0.1704
GPS=326 & 327
FFT=0.1694
GPS=327 & 328
FFT=0.2012
GPS=328 & 329
FFT=0.1918
GPS=329 & 330
FFT=0.5920
GPS=330 & 331
FFT=0.6614
GPS=331 & 332
FFT=0.6137
GPS=332 & 333
FFT=0.5655
GPS=333 & 334
FFT=0.7045
GPS=334 & 335
FFT=0.8537
GPS=335 & 336
FFT=1.0793
GPS=336 & 337
FFT=0.9172
GPS=337 & 338
FFT=1.0745

Figure A-25. Resetting the color scale.

On the toolbar, there are project data processing method, and these toolbar are 📂, ✕, ◀, ▶. Sometimes on the same road, there are several paving days, and user colect several GPS files. On the previous manul, only one file is loaded. Now we have several files in one project.

First we load the folder by click 📂, then the software load the first file. As the same way to analyze the data as before. Then ◀ and ▶ buttons will allow user to load previous or next file in the project. The ✕ button will drawing all the GPS files' path on the screen.

Core-location data processing. When we monitor the compaction with this CMS device, we also do some core, GPR, or other testing on some selected location. Therefore, on each field trip for CMS testing, we will use the same GPS unit to get the core location. The steps below will instruct the reader on how to add the core location on the final data presentation:

1. After select the core location in the field, use the CMS device to measure the core location. Make sure the GPS antenna is directly over the center of the core location. Also, make sure there are no objects to block the GPS signal. Write down the GPS reading and give a specific core ID for this location.
2. Use any ASCII edit to create a "Core" file for loading this core-location data integrated to the system.
3. The "Core" file has the same file name as the GPS data file, but the extensive name is ".COR."
4. As in Figure A-26, this file is a sample-core data file. First line must be "CORE DATA."
5. Second and third line is for comments, Generally, the second line is for comments, and the third line is the data list title.
6. The core data start from fourth line, the format is comma delaminated.
    - Serial number of the core.
    - Core code or ID, any string.
    - Usage text, text for showing the usage for this core location.
    - Latitude of the core location in degrees.
    - Longitude of the core location in degrees.
    - Lever over the see in meters.
    - Comment about this core location.
7. After this file is edited and saved to the same folder as other GPS files.
8. When first load the GPS data, the core data file is also loaded. As in Figure A-14, the red line showing the core location.
9. When zoomed in on one of the core locations, Figure A-27 shows the core location on the compaction-effectiveness colormap output screen. This core is the No. 6 core, and at this location, the roller running pass is 3, the compaction effectiveness is 2.96, and the first running temperature is 237°F.

```
CORE DATA
Core Location with GPS for showing on the Final Result
No.   Core Code,  Usage Text,  Latitude,      Longitude,      Level, Comment
1,      ACC#1,     GPR,      30.69756750 ,  -96.35858817  ,  359.58, GPR Test Location
2,      TAPD#34,   TPAD,     30.69758783 ,  -96.35862100  ,  358.92, Lee collect core
3,      GPR#4,     GPR,      30.69802750 ,  -96.35945450  ,  353.67, Racky collect core
4,      Nuc#2,     Nuc,      30.69796050 ,  -96.35928800  ,  354.99, Bryan collect core
5,      GPR#1,     GPR,      30.69781950 ,  -96.35896417  ,  356.96, Lee collect GPR
6,      GPR#3,     GPR,      30.69846817 ,  -96.36043317  ,  349.74, Lee collect nuclear Device
7,      ACC#2,     ACC,      30.69942433 ,  -96.36147100  ,  344.16, Lee run TPAD
8,      TPAD#11,   TPAD,     30.70011083 ,  -96.36215533  ,  342.19, Lee run GPR
9,      TPAD#5,    TPAD,     30.70069533 ,  -96.36278717  ,  345.80, Bryan run GPR test
10,     Nuc#6,     Nuc,      30.70173150 ,  -96.36384550  ,  348.10, Final core location
```

Figure A-26. Sample-core data file.

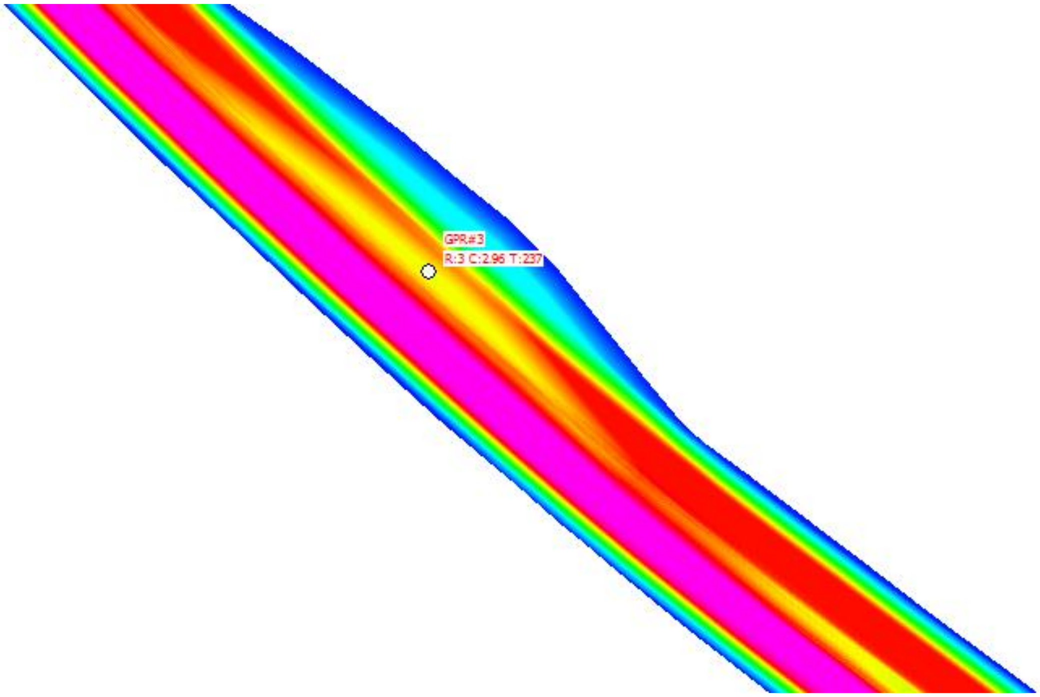

Figure A-27. Sample-core data view.

APPENDIX B. LABORATORY EFFECTIVE INDEX (EI)

SINAK—LITHIUM

Table B.1. Laboratory Experiment Data for SINAK, Lithium.

SINAK - Lithium						
	W/C	Application Rate	Wind Speed	EI	PE	Beta
1	0.4	100	0	0.917	0.002139	0.073
2	0.4	100	6	0.789	0.007271	0.088
3	0.4	100	15	0.624	0.01497	0.100
4	0.4	140	0	0.827	0.002139	0.091
5	0.4	140	6	0.701	0.007271	0.105
6	0.4	140	15	0.576	0.01497	0.116
7	0.4	200	0	0.716	0.002139	0.109
8	0.4	200	6	0.603	0.007271	0.129
9	0.4	200	15	0.524	0.01497	0.131
10	0.45	100	0	0.954	0.002139	0.084
11	0.45	100	6	0.858	0.007271	0.097
12	0.45	100	15	0.754	0.01497	0.106
13	0.45	140	0	0.844	0.002139	0.099
14	0.45	140	6	0.736	0.007271	0.109
15	0.45	140	15	0.589	0.01497	0.119
16	0.45	200	0	0.732	0.002139	0.116
17	0.45	200	6	0.584	0.007271	0.128
18	0.45	200	15	0.495	0.01497	0.136

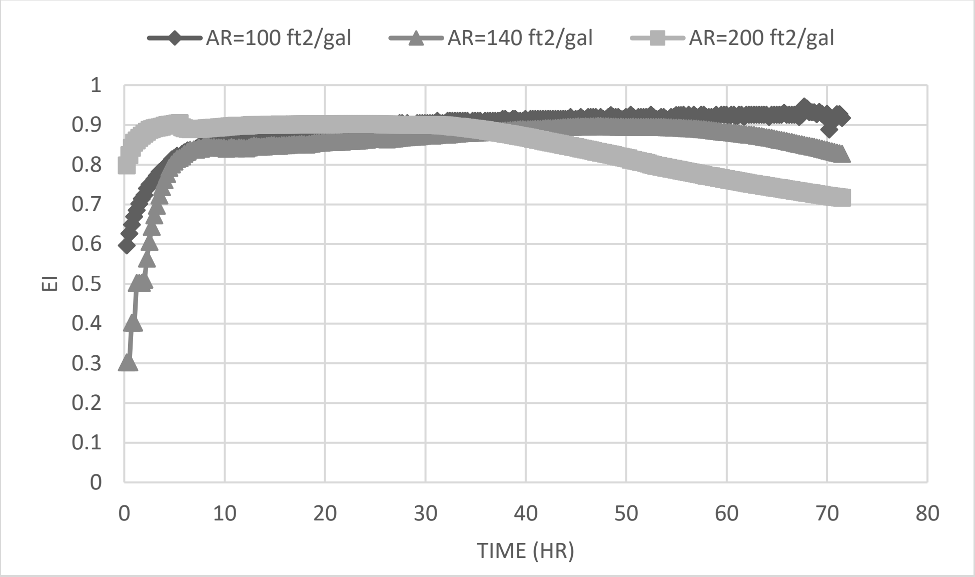

Figure B-1. Comparison of EI for 100, 140, and 200 ft^2/gal application rate.

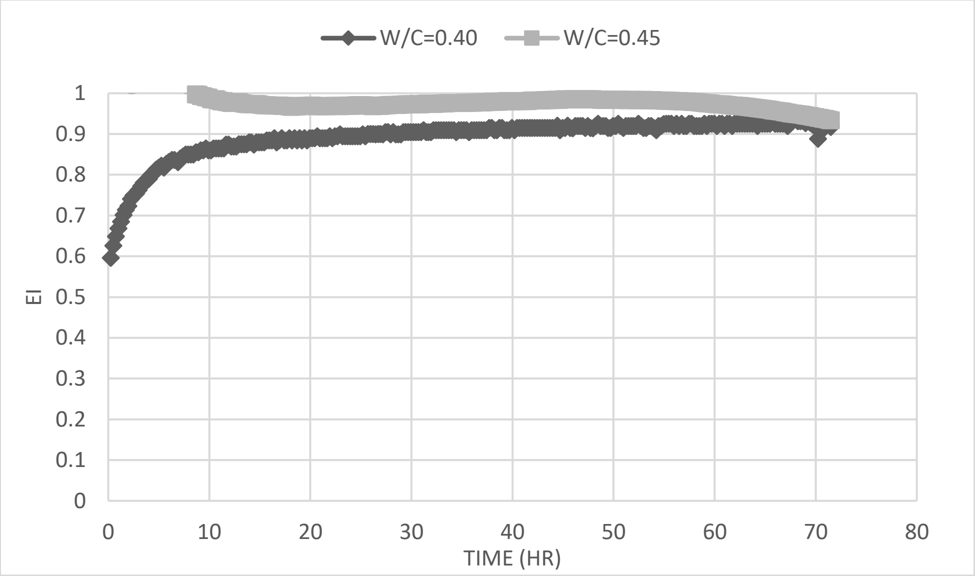

Figure B-2. Comparison of EI for 0.4 w/c and 0.45 w/c specimens under 100 ft^2/gal application rate.

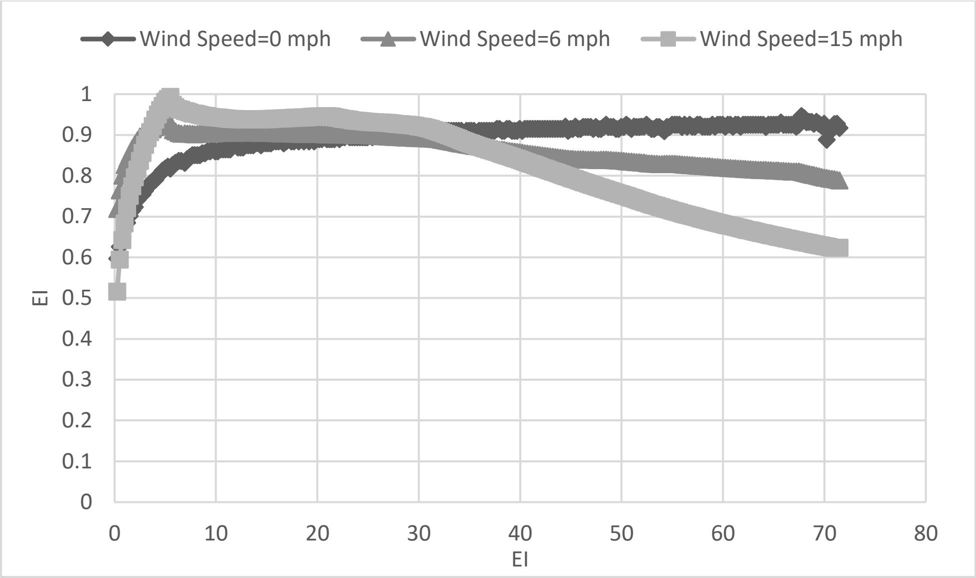

Figure B-3. Comparison of EI for 0, 6, and 15 mph wind speed under 100 ft^2/gal application rate.

W. R. MEADOW—1300 CLEAR

Table B-2. Laboratory Experiment Data for W. R. Meadow—1300 Clear.

W. R. Meadows - 1300 Clear						
	W/C	Application Rate	Wind Speed	EI	PE	Beta
1	0.4	100	0	0.768	0.002886	0.062
2	0.4	100	6	0.675	0.009812	0.083
3	0.4	100	15	0.603	0.020201	0.105
4	0.4	140	0	0.721	0.002886	0.083
5	0.4	140	6	0.665	0.009812	0.099
6	0.4	140	15	0.543	0.020201	0.119
7	0.4	200	0	0.694	0.002886	0.096
8	0.4	200	6	0.578	0.009812	0.118
9	0.4	200	15	0.502	0.020201	0.142
10	0.45	100	0	0.789	0.002886	0.076
11	0.45	100	6	0.693	0.009812	0.095
12	0.45	100	15	0.645	0.020201	0.106
13	0.45	140	0	0.756	0.002886	0.085
14	0.45	140	6	0.641	0.009812	0.111
15	0.45	140	15	0.569	0.020201	0.117
16	0.45	200	0	0.71	0.002886	0.097
17	0.45	200	6	0.594	0.009812	0.121
18	0.45	200	15	0.553	0.020201	0.128

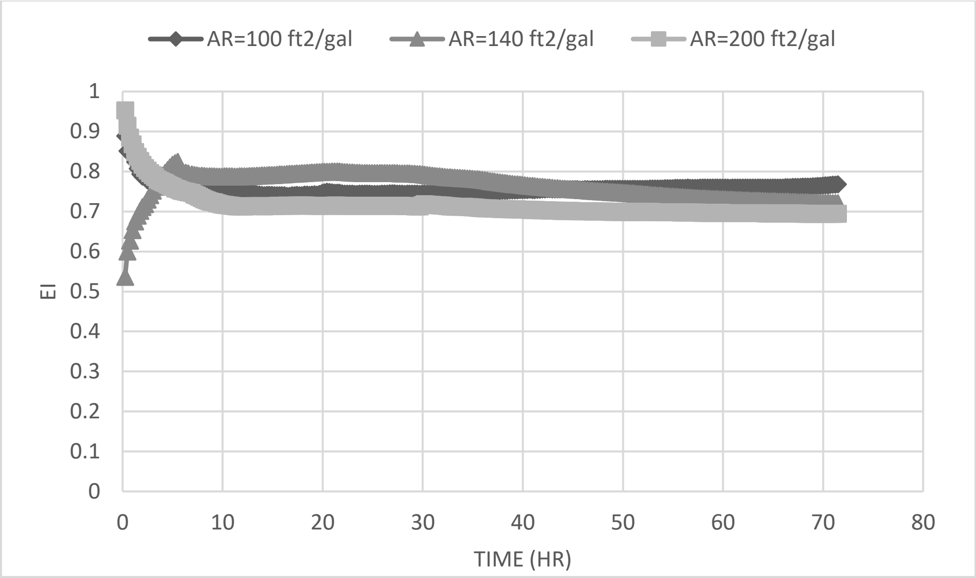

Figure B-4. Comparison of EI for 100, 140, and 200 ft^2/gal application rate.

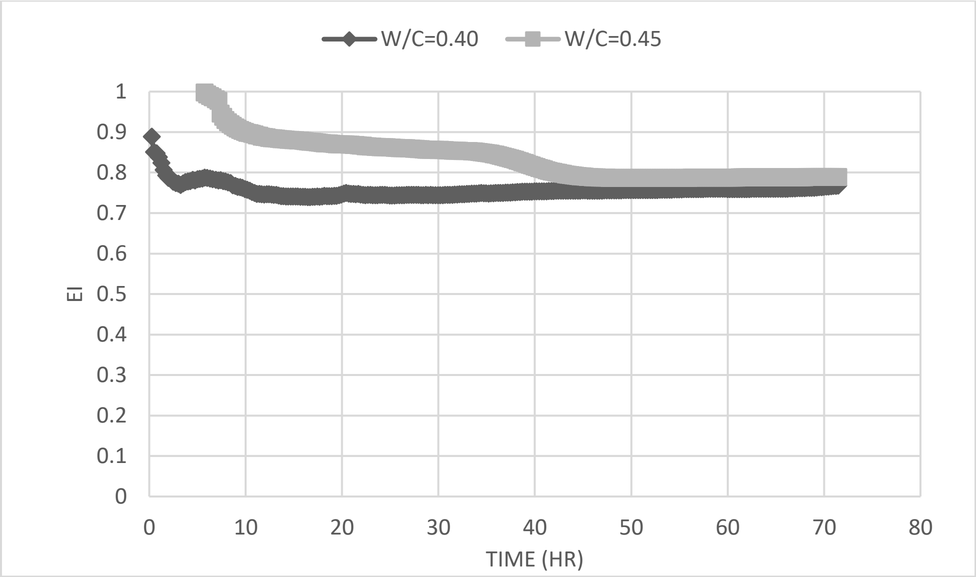

Figure B-5. Comparison of EI for 0.4 w/c and 0.45 w/c specimens under 100 ft^2/gal application rate.

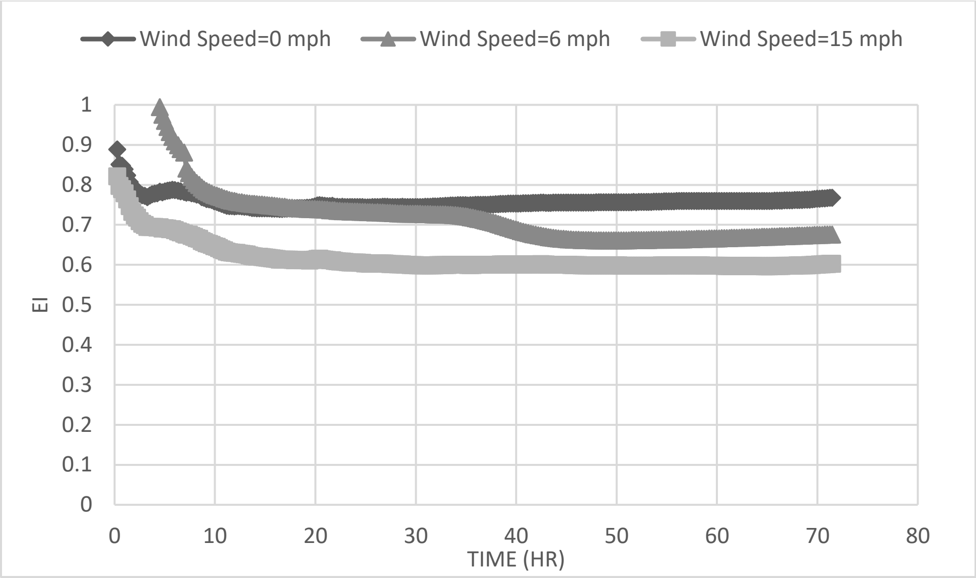

Figure B-6. Comparison of EI for 0, 6, and 15 mph wind speed under 100 ft^2/gal application rate.

W. R. MEADOW—CITY WHITE

Table B-3. Laboratory Experiment Data for W. R. Meadow—City White.

W. R. Meadows—1600 City White						
	W/C	Application Rate	Wind Speed	EI	PE	Beta
1	0.4	100	0	0.907	0.002886	0.071
2	0.4	100	6	0.83	0.009812	0.083
3	0.4	100	15	0.742	0.020201	0.119
4	0.4	140	0	0.821	0.002886	0.085
5	0.4	140	6	0.701	0.009812	0.110
6	0.4	140	15	0.652	0.020201	0.121
7	0.4	200	0	0.782	0.002886	0.087
8	0.4	200	6	0.716	0.009812	0.104
9	0.4	200	15	0.623	0.020201	0.126
10	0.45	100	0	0.921	0.002886	0.081
11	0.45	100	6	0.847	0.009812	0.099
12	0.45	100	15	0.794	0.020201	0.110
13	0.45	140	0	0.864	0.002886	0.089
14	0.45	140	6	0.789	0.009812	0.108
15	0.45	140	15	0.712	0.020201	0.125
16	0.45	200	0	0.801	0.002886	0.097
17	0.45	200	6	0.754	0.009812	0.114
18	0.45	200	15	0.691	0.020201	0.124

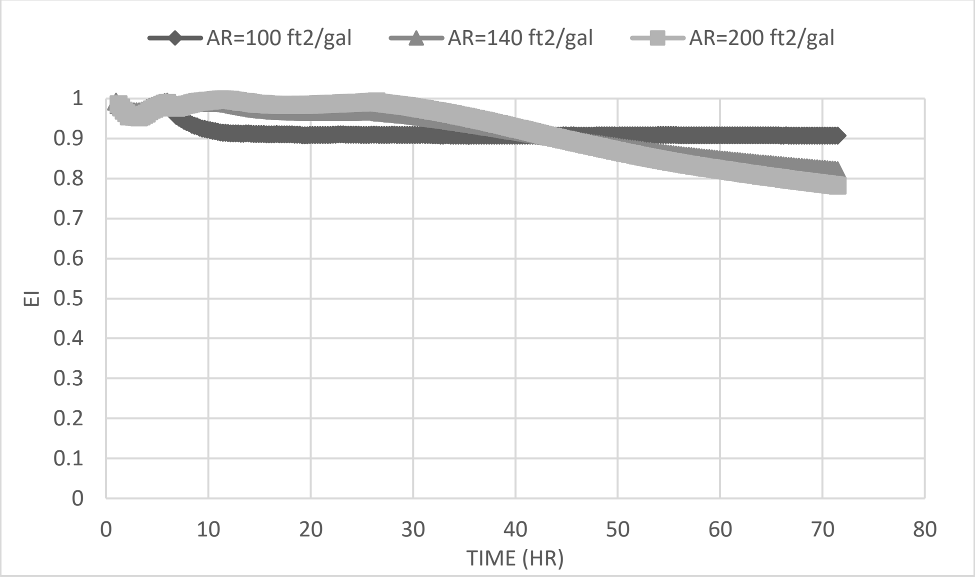

Figure B-7. Comparison of EI for 100, 140, and 200 ft^2/gal application rate.

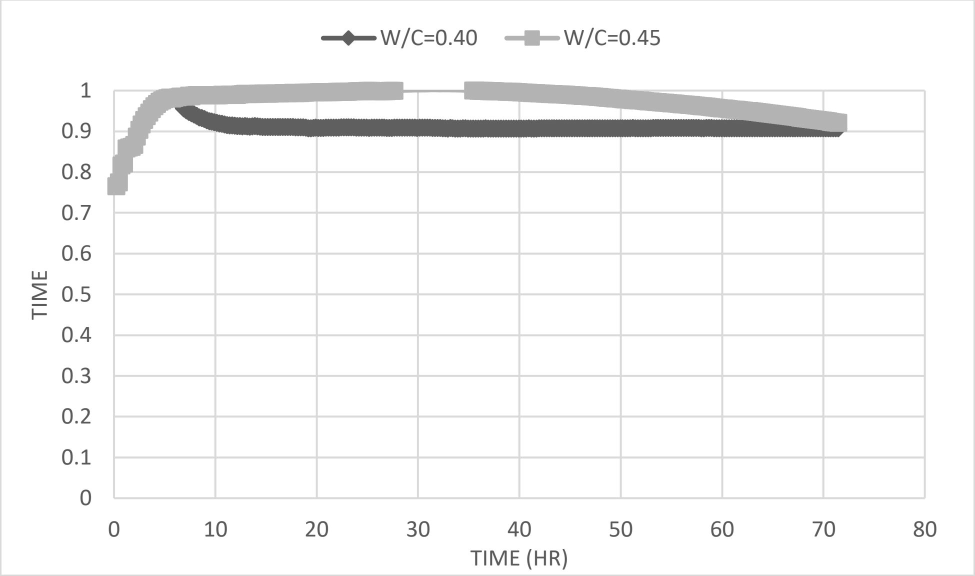

Figure B-8. Comparison of EI for 0.4 w/c and 0.45 w/c specimens under 100 ft^2/gal application rate.

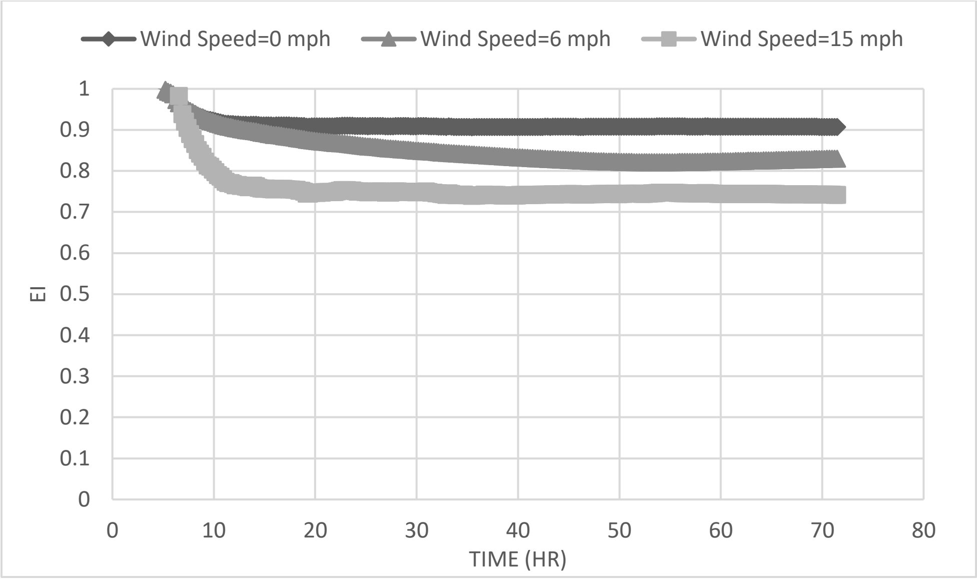

Figure B-9. Comparison of EI for 0, 6, and 15 mph wind speed under 100 ft^2/gal application rate.

DAYTON, DSSCC

Table B-4. Laboratory Experiment Data for Dayton—DSSCC.

DAYTON—DSSCC						
	W/C	Application Rate	Wind Speed	EI	PE	Beta
1	0.4	100	0	0.845	0.00159	0.068
2	0.4	100	6	0.739	0.005408	0.091
3	0.4	100	15	0.654	0.011133	0.113
4	0.4	140	0	0.802	0.00159	0.075
5	0.4	140	6	0.721	0.005408	0.098
6	0.4	140	15	0.639	0.011133	0.112
7	0.4	200	0	0.745	0.00159	0.102
8	0.4	200	6	0.672	0.005408	0.114
9	0.4	200	15	0.623	0.011133	0.124
10	0.45	100	0	0.872	0.00159	0.079
11	0.45	100	6	0.823	0.005408	0.095
12	0.45	100	15	0.71	0.011133	0.103
13	0.45	140	0	0.829	0.00159	0.096
14	0.45	140	6	0.766	0.005408	0.102
15	0.45	140	15	0.703	0.011133	0.114
16	0.45	200	0	0.791	0.00159	0.105
17	0.45	200	6	0.742	0.005408	0.119
18	0.45	200	15	0.698	0.011133	0.128

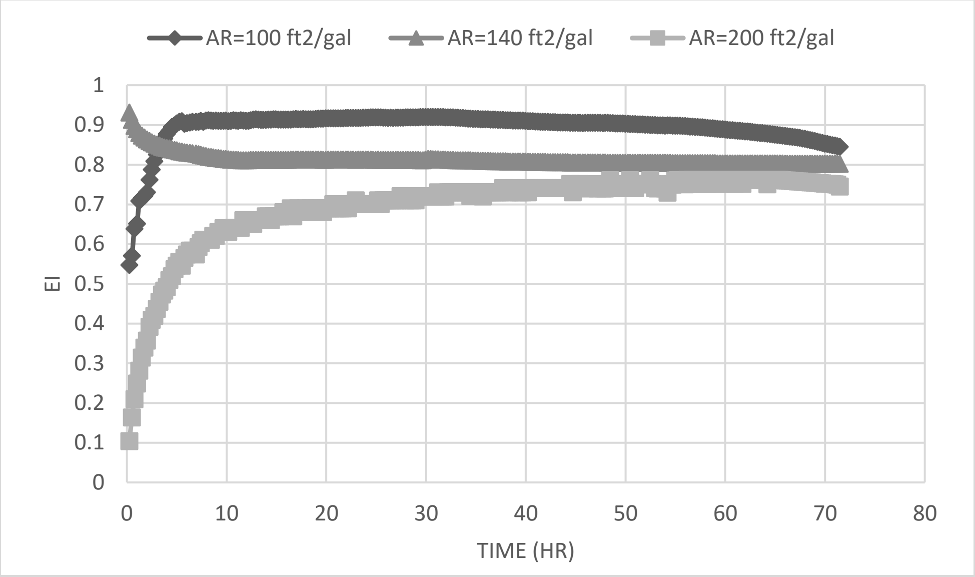

Figure B-10. Comparison of EI for 100, 140, and 200 ft^2/gal application rate.

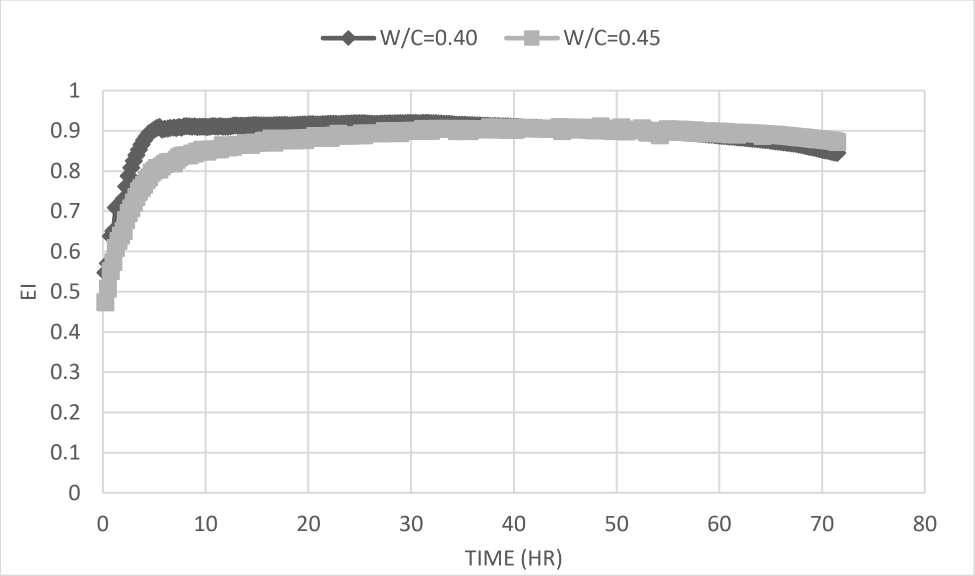

Figure B-11. Comparison of EI for 0.4 w/c and 0.45 w/c specimens under 100 ft^2/gal application rate.

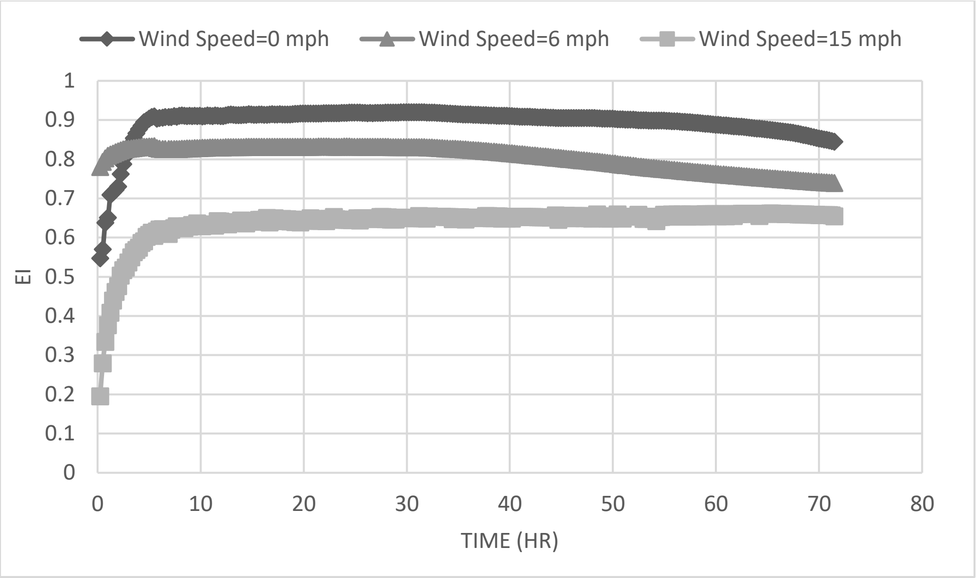

Figure B-12. Comparison of EI for 0, 6, and 15 mph wind speed under 100 ft^2/gal application rate.

APPENDIX C. LABORATORY REFERENCE CURVES

SINAK—LITHIUM

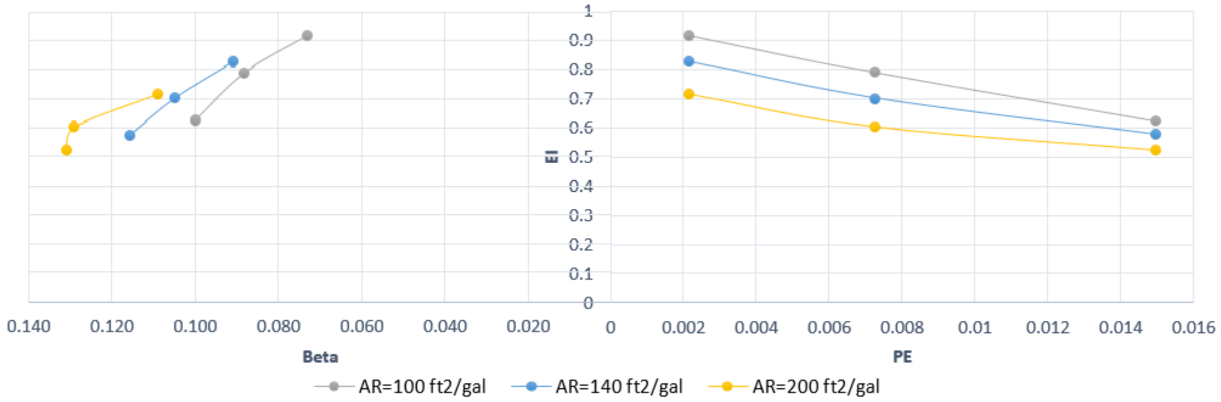

A) W/C= 0.40

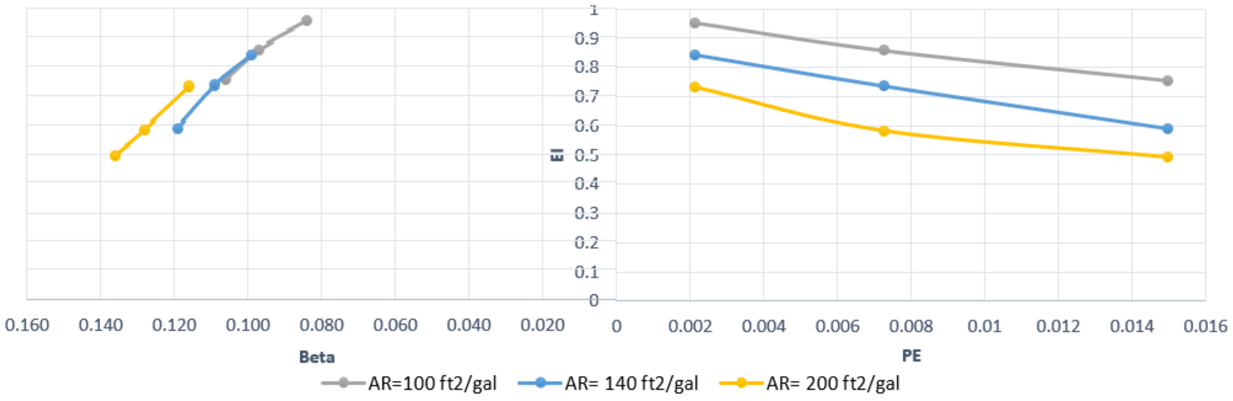

B) W/C = 0.45

Figure C-1. EI vs. PE vs. Beta in SINAK-Lithium compound.

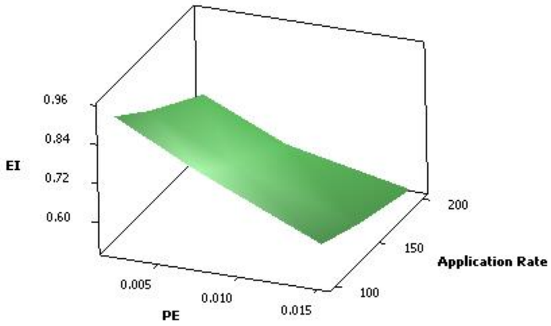

Figure C-2. Diagram from EI, PE, and Application rate in SINAK-Lithium compound.

$$EI = PE^{-0.079} + 0.598 \times \frac{W}{C} - \frac{AR}{500} - 0.739 \qquad \text{R2} = 0.945$$

W. R. MEADOW—1300 CLEAR

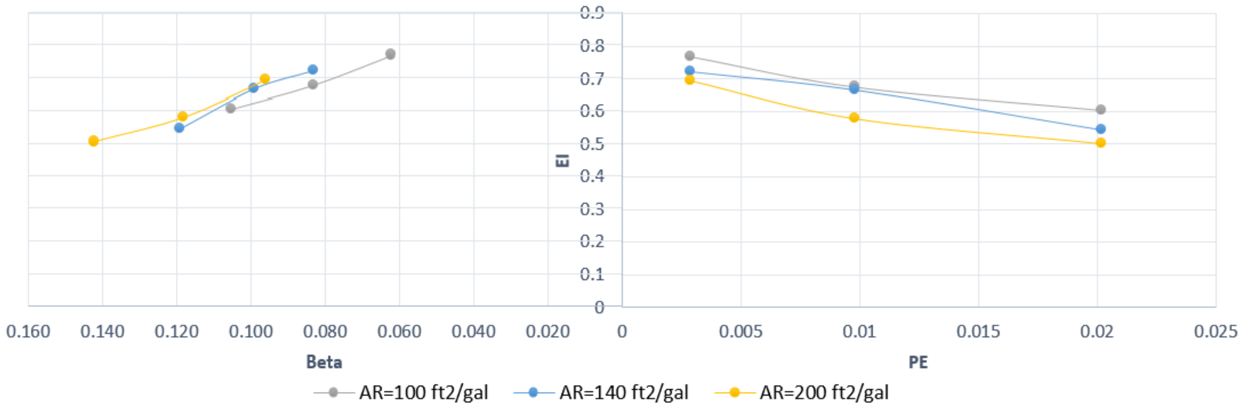

W/C= 0.40

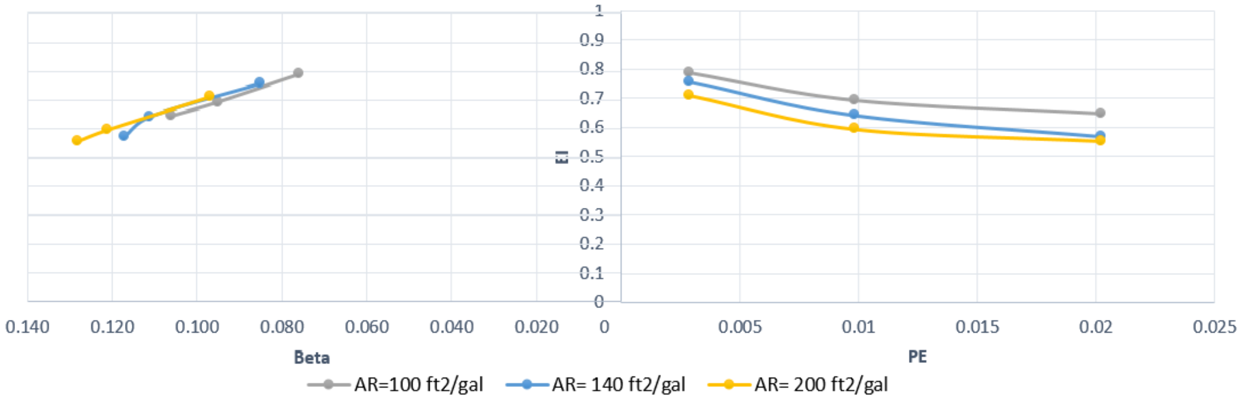

W/C= 0.45

Figure C-3. EI vs. PE vs. Beta in W. R. Meadow—1300 Clear compound.

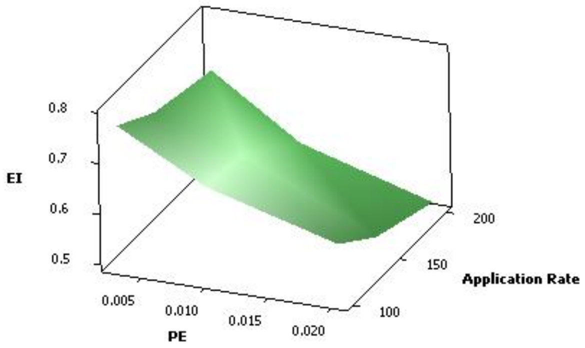

Figure C-4. Diagram from EI, PE, and Application rate in W. R. Meadow—1300 Clear compound.

$$EI = PE^{-0.063} + 0.447 \times \frac{W}{C} - \frac{AR}{1000} - 0.766 \qquad R2 = 0.967$$

W. R. MEADOW—CITY WHITE

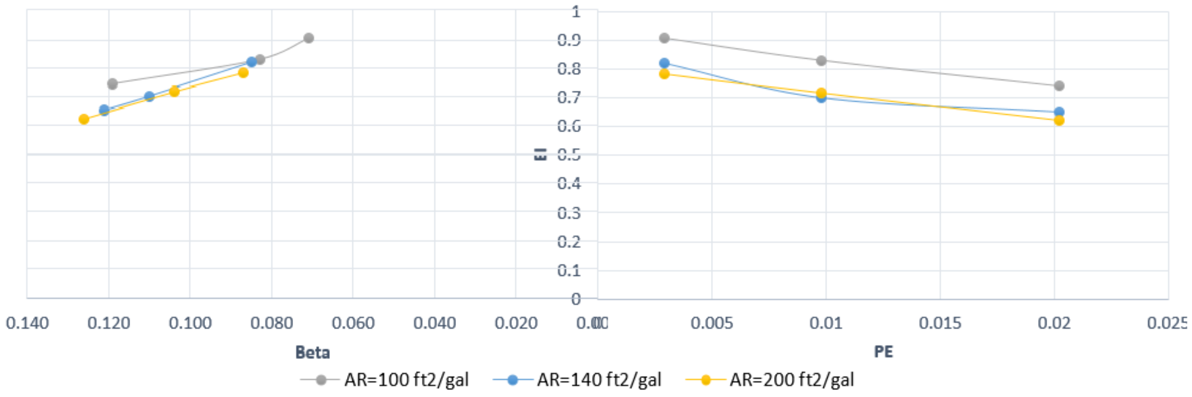

A) W/C= 0.40

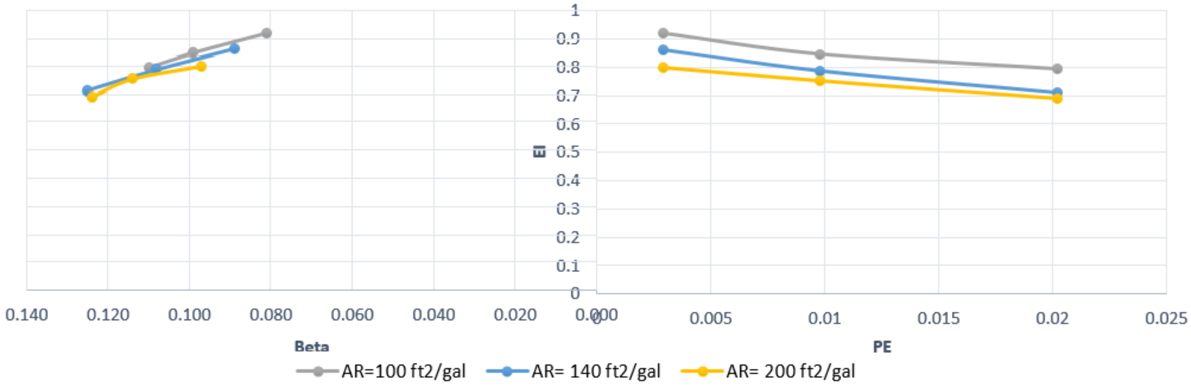

B) W/C= 0.45

Figure C-5. EI vs. PE vs. Beta in W. R. Meadow—1600 City White compound.

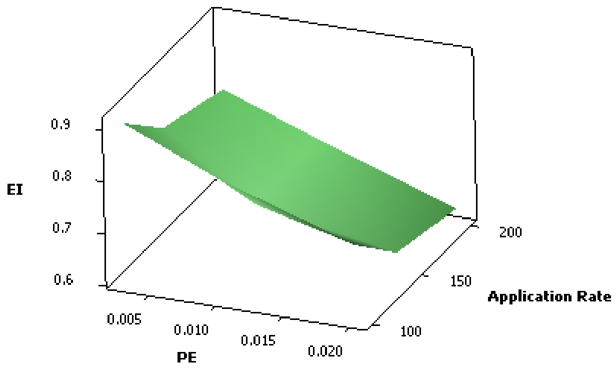

Figure C-6. Diagram from EI, PE, and Application rate in W. R. Meadow—1600 compound.

$$EI = PE^{-0.056} + 0.887 \times \frac{W}{C} - \frac{AR}{1000} - 0.754 \qquad R2 = 0.910$$

DAYTON, DSSCC

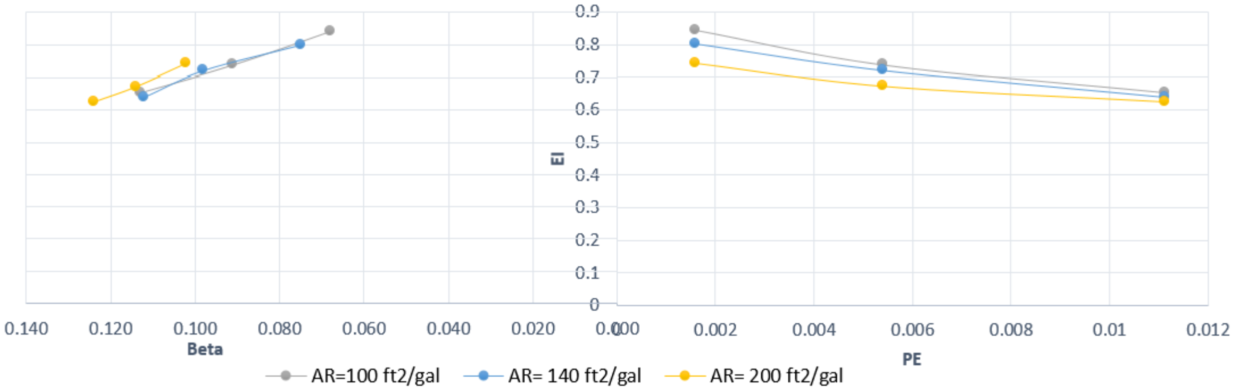

A) W/C= 0.40

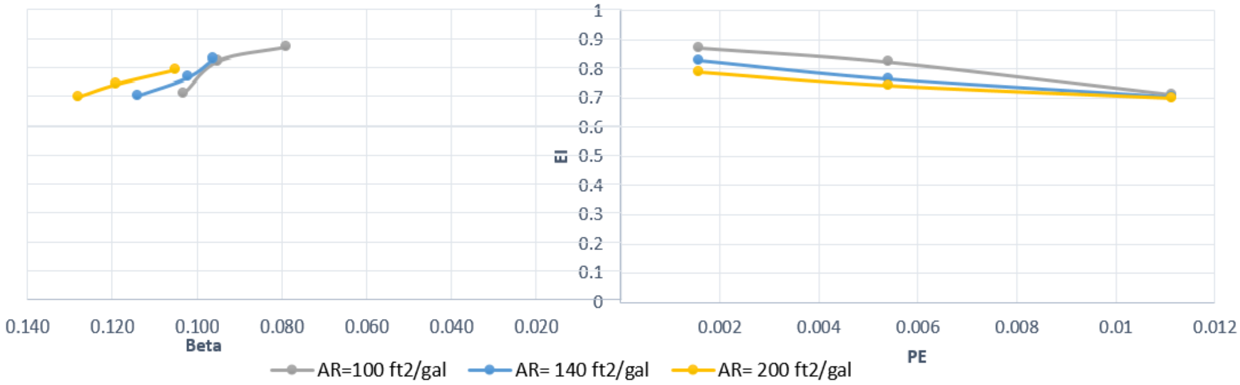

B) W/C= 0.45

Figure C-7. EI vs. PE vs. Beta in DAYTON—DSSCC compound.

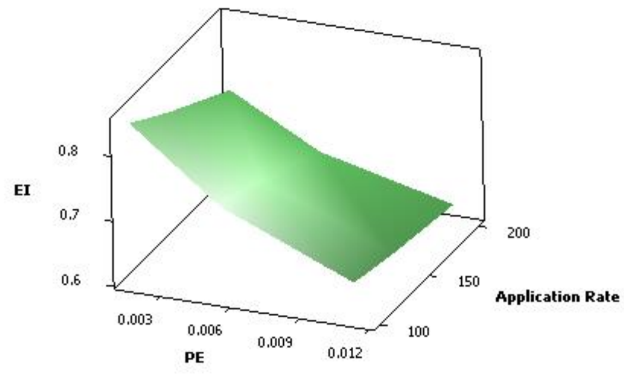

Figure C-8. Diagram from EI, PE, and Application rate in DAYTON—DSSCC compound.

$$EI = PE^{-0.053} + 1.098 \times \frac{W}{C} - \frac{AR}{1000} - 0.967 \qquad \mathrm{R2} = 0.932$$